Development and performance evaluation of detectors in a Compton camera arrangement for ion beam range monitoring in particle therapy

Silvia Liprandi

München 2018

Development and performance evaluation of detectors in a Compton camera arrangement for ion beam range monitoring in particle therapy

Silvia Liprandi

Dissertation
an der Fakultät für Physik
der Ludwig-Maximilians-Universität
München

vorgelegt von
Silvia Liprandi
geboren in Milano

München, den 26. September 2018

Erstgutachter: Priv. Doz. Dr. Peter G. Thirolf
Zweitgutachter: Prof. Dr. Taiga Yamaya
Tag der mündlichen Prüfung: 30.10.2018

Alla mia mamma e al mio papá.

Al mio fratellino Luca.

A Davide.

Credere nella scienza significa credere nel futuro.
(Umberto Veronesi)

Zusammenfassung

Das zunehmende Interesse an der Teilchentherapie zur Tumorbehandlung wird durch die Möglichkeit zur hochpräzisen Dosisverabreichung voran getrieben. Dies jedoch verlangt nach hoher Genauigkeit bei der Bestimmung der gut lokalisierten Dosisabgabe (Bragg Peak), die sich innerhalb des Tumorgewebes befinden muss. Weltweit werden verschiedene Ansätze zur Reichweitenbestimmung des Teilchenstrahls verfolgt. Die Compton-Kamera ist einer dieser Ansätze, deren Ziel die, in-vivo und in Echtzeit realisierte Protonen- bzw. Ionenstrahl-Reichweitenbestimmung durch die Detektion von sekundären, prompten Gammastrahlen ist, die durch Anregung und unmittelbare Abregung von Atomkernen im Gewebe bei der Wechselwirkung mit dem Teilchenstrahl entstehen. Die Zielsetzung unseres Projekts ist die Entwicklung und der Aufbau eines auf dem Prinzip der Compton-Kamera basierenden bildgebenden Verfahrens, das (letztendlich) in Echtzeit die Reichweite eines Ionenstrahls sichtbar macht. Im Kontext dieser Arbeit wurde ein Compton-Kamera-Prototyp mit jeweils einer mehrlagigen und einer einlagigen Streukomponente charakterisiert, verbessert und betrieben. Der erstgenannte Aufbau gehört zum LMU Compton-Kamera Prototyp: die Detektorkomponenten wurden umfassend charakterisiert, um Limitierungen durch ihren Aufbau zu ermitteln und die benötigte Konfiguration für eine optimale Leistungsfähigkeit festzulegen. Die Komplexität der Signalverarbeitung und Datenaufnahme konnte mit Blick auf eine zukünftige klinische Anwendung vereinfacht werden. Die Streukomponente wird von einem Stapel aus sechs hochsegmentierten doppelseitigen Silizium-Streifenzählern gebildet. Dazu fungiert ein monolithischer $LaBr_3(Ce)$ Szintillator als Absorberkomponente und ist an eine segmentierte positionssensitive Multi-Anoden-Photoelektronenvervielfacherröhre (PMT) gekoppelt. Der ursprünglich verwendete 256-fach segmentierte PMT wurde durch einen 64-fach segmentierten PMT ersetzt, für den eine vergleichbare bzw. höhere Leistungsfähigkeit gezeigt werden konnte. Der selbe Trend einer Verbesserung der Ortsauflösung mit zunehmender Energie des absorbierten Photons, der mit dem 256-fach segmentierten PMT beobachtet werden konnte, wurde auch in diesem Szenario beobachtet: bei der ^{137}Cs Energie wurde ein Wert von 3.4(1) mm erhalten, während bei den 1173 keV und 1332 keV Photopeaks von ^{60}Co die Ortsauflösung Wer-

te von 2.9(1) mm erreichte und somit unterhalb der durch das Compton-Kamera-Design anvisierten 3 mm Ortsauflösung des Absorbers lagen. Desweiteren wurden erste Tests im Hinblick auf einen möglichen Ersatz des $LaBr_3$(Ce) Szintillatonsmaterials durch einen kostengünstigeren und untergrundfreien $CeBr_3$-Szintillator unternommen und erscheinen vielversprechend ($\Delta E/E \sim 4$ % bei 662 keV und vergleichbare zeitliche Eigenschaften wie $LaBr_3$(Ce)). Die Signalverarbeitung und das Datenauslesesystem für die Streukomponente wurde von einer ASIC-basierten Auslese zu einer flexibleren und leistungsfähigeren Elektronik auf der Basis diskreter Komponenten umgerüstet. Volle Übereinstimmung der neuen Elektronik mit den Anforderungen des Streudetektor wurde erreicht: die Akzeptanz von beiden Signalpolaritäten wurde genauso eingeführt wie die Möglichkeit des Triggerns mit der Streukomponente, was zuvor nicht möglich war. Weiter wurde die Umrüstung der Signalverarbeitung und Datenaufnahme durch Anpassung der ursprünglich nur zum Ersatz der veralteten ASIC-basierten Module der Streudetektoren entwickelten Front-End Elektronik an die Signaleigenschaften des Absorberszintillators und seine segmentierte Auslese auf die gesamte Compton-Kamera ausgedehnt. Dies erlaubte die Verringerung der Komplexität des Systems und schließlich das Erreichen einer Zählrate von bis zu 1 Mcps, wie es in einem klinischen Szenario benötigt wird: die VME-basierten Module wurden in die neue DAQ-Software eingebunden und die Datenströme von Streuer und Absorber wurden zusammengeführt. Die verringerte Pixelierung der PMT-Signalkanäle, kombiniert mit der neuen Signalauslese und dem neuen Datenaufnahmesystem, basierend auf optischen Fasern macht den Compton-Kamera-Aufbau weniger komplex und flexibler. Sämtliche Detektoren können in einen neu entworfenen Faradaykäfig eingebaut werden, der außerdem eine aktive Kühlung zur Verringerung des Dunkelstroms der Siliziumdetektoren enthält. Das verbesserte System wurde im Labor sowie unter Online-Bedingungen mit Teilchenstrahlen am Tandem-Beschleuniger in Garching getestet. Eine Validierung mit prompten Gammastrahlen, die durch den Beschuss eines Wasser- bzw. PMMA-Targets mit einem 20 MeV Protonenstrahl entstehen, wurde durchgeführt und die selben Resultate konnten ebenfalls mit dem neuen Signalverarbeitungssystem gezeigt werden. Die erreichbare Triggerrate wurde um eine Größenordung erhöht und wegen der effizienten Auswahl an Compton-gestreuten Ereignissen durch das Triggern mit der Streukomponente konnte das Verhältnis an registrierten Compton-Ereignissen um circa drei Größenordnungen im Vergleich zum vorherigen Aufnahmesystem erhöht werden. Das Kamerasystem wurde außerdem mit einem auf ein Wassertarget auftreffenden, gepulsten Deuteronenstrahl getestet, um die zeitliche Leistungsfähigkeit beurteilen zu können. Mit einer geplanten verbesserten Version des Implantationsprofils der segmentierten Silizium-Streifenzähler, wird das mehrlagige Compton-Kamerasystem für eine vollständige Charakterisierung der Leistungsfähigkeit des bildgebenden Systems bereit sein. Unter Verwendung des leistungsfähigen monolithischen $LaBr_3$(Ce) Szintillators als Absorber wurde auch ein Compton-Kameraaufbau mit einer einlagigen Streukomponente zusammengestellt, bestehend aus einer gepixelten 22×22 Anordnung aus GAGG Szintillationskristallen. Eine Studie zum Beweis der Funktionsfähigkeit des Konzepts wurde mit ^{137}Cs und ^{60}Co Kalibrationsquellen durchgeführt: die Rekonstruktion der Quellposition wurde mit der MEGAlib Software durchgeführt und die daraus resultierenden rekonstruierten Bilder aus experimentellen Daten wurden mit

rekonstruierten Bildern aus Simulationen verglichen. Eine Verschiebung der Quelle von 2 mm konnte von dem System mit sub-Millimeter Genauigkeit aufgelöst werden. Ein Trend zu verbesserten Winkelauflösungen mit höherer Energie des einfallenden Photons spiegelt die verbesserte Leistungsfähigkeit des Detektors (Energie- und Ortsauflösung) bei höheren Energien wider. Das System wurde in unterschiedlichen geometrischen Anordnungen charakterisiert, um nicht nur einer möglichen Prompt-Gamma Bildgebungsanwendung gerecht zu werden, sondern auch einem multimodalen Detektorsystem mit der Möglichkeit zur Anwendung in PET- oder gamma-PET-ähnlichen Bildgebungsszenarien.

Summary

The growing interest in particle beam therapy for cancer treatment is driven by the ability to provide high precision dose delivery. However, this benefit demands a high accuracy on the determination of the well-localized dose deposition (Bragg peak), which has to be located within the tumor volume. Different approaches for the beam range monitoring are worldwide being evaluated. The Compton camera is one of the proposed techniques, which aims at providing real-time, in-vivo proton (or ion) beam range monitoring by means of the detection of secondary prompt gamma rays, resulting from nuclear reactions between the particle beam and the biological tissue. The purpose of our project is to develop and commission an imaging system based on a Compton camera detector arrangement which could monitor in (ultimately) real-time the ion beam range. In the context of this thesis a Compton camera detector prototype was characterized, consolidated and commissioned with both a multi-layer and a mono-layer scatter component. The first detector arrangement belongs to the LMU Compton camera: the detector components were extensively characterized in order to determine the limitations imposed by their internal structure and the required configuration for an optimum performance. The complexity of the signal readout and processing could be reduced in view of facilitating an envisaged clinical applicability of the system. The scatter component (tracker) is formed by a stack of six highly segmented double-sided Si-strip detectors, whereas a monolithic $LaBr_3$(Ce) scintillator ($5 \times 5 \times 3$ cm^3) acts as the absorber component and is coupled to a segmented position-sensitive multi-anode photomultiplier tube (PMT). The initially applied 256-fold segmented PMT was replaced by a 64-fold segmented PMT, and similar or even superior performance was demonstrated for the latter one. The same trend of an improving spatial resolution, with an increasing energy of the incoming photon, which was observed when using the 256-fold segmented PMT, was also preserved: at ^{137}Cs energy a value of 3.4(1) mm was obtained, while at the 1173 keV and 1332 keV ^{60}Co photopeaks the spatial resolution reached values of 2.9(1) mm, thus below the 3 mm absorber resolution envisaged by the Compton camera design. Moreover, first tests in view of a possible replacement of the $LaBr_3$(Ce) scintillation material with the cost-effective and radio-pure $CeBr_3$ scintillator

material were pursued and seem promising ($\Delta E/E \simeq 4\%$ at 662 keV and comparable timing properties as $LaBr_3(Ce)$). The signal processing and data readout system for the scatter component was upgraded from an ASIC-based electronics to a more flexible and higher performing electronics based on discrete components. Full compliance of the new frontend electronics with the detector signal specifications of our camera prototype was achieved: an acceptance of both signal polarities was introduced as well as a trigger capability for the scatter component, which previously did not exist. Furthermore, the upgrade of the signal processing and data acquisition was extended to the whole Compton camera setup, adapting the new frontend electronics designed initially for replacing the outdated ASIC-based modules of the scatterer also to the signal properties of the absorber scintillator and its segmented readout. This allowed for reducing the complexity of the system and finally achieve a 1 Mcps count rate capability as required in a clinical scenario: the VME-based readout modules were implemented into the new DAQ software and the data streams of scatterer and absorber were merged. The reduced granularity of the PMT signal channels combined with the use of the new signal processing and data acquisition system based on optical fibers makes the Compton camera setup less complex and more flexible. All detectors can be mounted in a newly designed Faraday cage, which includes also an active cooling, capable of reducing the dark current in the silicon detectors. The upgraded system was tested in the laboratory as well as under online conditions with particle beams at the Tandem accelerator in Garching. A validation with high energy prompt-γ rays was performed, bombarding water and PMMA targets with a 20 MeV proton beam and the same detector performance could be demonstrated also with the new signal processing system. The achievable trigger rate was increased by one order of magnitude and due to the efficient selection of Compton scattered events by triggering on the scatter component, the ratio of registered Compton events could be increased by about three orders of magnitude compared to the previous data acquisition system. The camera system was also tested by hitting a water target with a pulsed deuteron beam in order to allow for assessing the timing performance. With an envisaged improved version of the internal implantation structure of the segmented silicon scatter modules, the multi-layer Compton camera system will be ready for a full performance characterization of the imaging system's capabilities.

By using the high performing $LaBr_3(Ce)$ monolithic scintillator as absorber, a Compton camera setup was also arranged with a mono-layer scattering component consisting of a pixelated 22 $\times$ 22 array of GAGG scintillator crystals. A proof of principle study was carried out using ^{137}Cs and ^{60}Co calibration sources: the source position reconstruction was performed with the MEGAlib software and the resulting reconstructed images from experimental data were compared to images reconstructed from simulated data. A source shift of 2 mm could be resolved by the system with sub-millimeter accuracy. A trend of improving angular resolution with the incoming photon energy reflects the detectors' (energy and spatial resolution) performance improvements with increasing energy. The system was characterized in different geometrical configurations, in order to address not only a possible prompt-gamma imaging application, but also a multi-modality detector system able to be applied also in PET- or gamma-PET-like imaging scenarios.

List of Acronyms and Abbreviations

2D / 3D	2 Dimension(al) / 3 Dimension(al)
AC	Alternate Current
ADC	Analog to Digital Converter
APD(A)	Avalanche Photodiode (Array)
Bq	Bequerel
CFD	Constant Fraction Discriminator
CPU	Central Processing Unit
CSA	Charge Sensitive Amplifier
CT	Computed Tomography
DAQ	Data Acquisition
DC	Direct Current
DOI	Depth of Interaction
ENC	Equivalent Noise Charge
eV	elettronvolt
FBP	Filtered Backprojection
FE board	Front-End board
FIFO	First In First Out

FOV	Field of View
FPGA	Field Programmable Gate Array
FWHM	Full Width at Half Maximum
GSI	GSI Helmholtzzentrum für Schwerionenforschung, Darmstadt, Germany
HIMAC	Heavy Ion Medical Accelerator in Chiba, Japan
HU	Hounsfield units
HZDR	Helmholtz-Zentrum Dresden-Rossendorf
ICRU	International Commission on Radiation Units and Measurements, Inc., Bethesda, MD, USA
IMPT	Intensity − modulated Proton Therapy
IMRT	Intensity − modulated Radiotherapy
KES	knife-edge slit
LET	Linear Energy Transfer
LINAC	Linear Accelerator
LLUMC	Loma Linda University Medical Center
LOR	Line of Response
MBS	Multi Branch System
MCA	Multichannel Analyzer
MCNPX	Monte Carlo N-Particle Transport Code System for Multiparticle and High Energy Applications
MCS	Multiple Coulomb Scattering
MGH	Massachusetts General Hospital
MLEM	Maximum Likelihood Expectation Maximization
MPS	multi-parallel slit
NIM	Nuclear Instrument Module

NIST	National Institute of Standard and Technology
NTCP	Normal Tissue Complication Probability
OAR	Organ at Risk
PCB	Printed Circuit Board
PCI	Peripheral Component Interconnect
PET	Positron Emission Tomography
pin	p-doped, intrinsic region, n-doped
PMMA	Polymethylmethacralate, Lucite, $C_5O_2H_8$
PMT	Photomultiplier Tube
RBE	Radiobiological Effectiveness
SI	International System of Units
SOBP	Spread Out Bragg Peak
STP	Standard Temperature (273.2 K) and Pressure (101.3 kPa)
TAC	Time to Amplitude Converter
TCP	Tumor Control Probability
TPS	Treatment Planning System
ToF	Time of Flight
TU	Technical University
UFH	University of Florida Health Proton Therapy Institute
UPTD	Universitäts Protonen Therapie Dresden
VMEbus	Versa Module Europa bus

Contents

List of Figures

List of Tables

CHAPTER 1

Introduction and Motivation

This first chapter introduces the topic of the research framework of this thesis. We first focus on giving an introduction to the problem of range uncertainty in proton therapy. The sources of uncertainties and their management during treatments are presented, highlighting the *in vivo* range control, highly desiderable to deliver safer treatments. The range control in proton (or ion) therapy is presently an extremely vivid topic, being investigated by several research groups in the field of medical physics. We present a brief overview on the various methods under investigation, categorizing the different approaches on the basis of the measurement technique. The current status of each technique is also discussed. Finally, the motivation and the objectives of this thesis will be given.

1.1 Particle therapy: advantages and challenges

Cancer is a generic term for a large group of diseases that can affect any part of the body. One defining feature of cancer is the rapid creation of abnormal cells that grow beyond their usual boundaries, and which can then invade surrounding parts of the body and spread to other organs, the latter process is referred to as metastasizing. Metastases are a major cause of death from cancer.

Between all the principal causes of death, cancer incidence is rising and is becoming a leading cause of death worldwide, accounting for 8.8 million deaths in 2015 [6]. In Fig. 1.1 data from [6] are considered to show estimated age-standardized rates for cancer incidence and mortality worldwide in 2012. The higher cancer incidence in more developed countries is mostly correlated to the higher possibilities to perform a cancer diagnosis.

Between 30% and 50% of cancers can currently be prevented by avoiding risk factors and implementing existing evidence-based prevention strategies. Many cancers have also a high chance of being cured if diagnosed early and treated adequately ([7] for Europe and

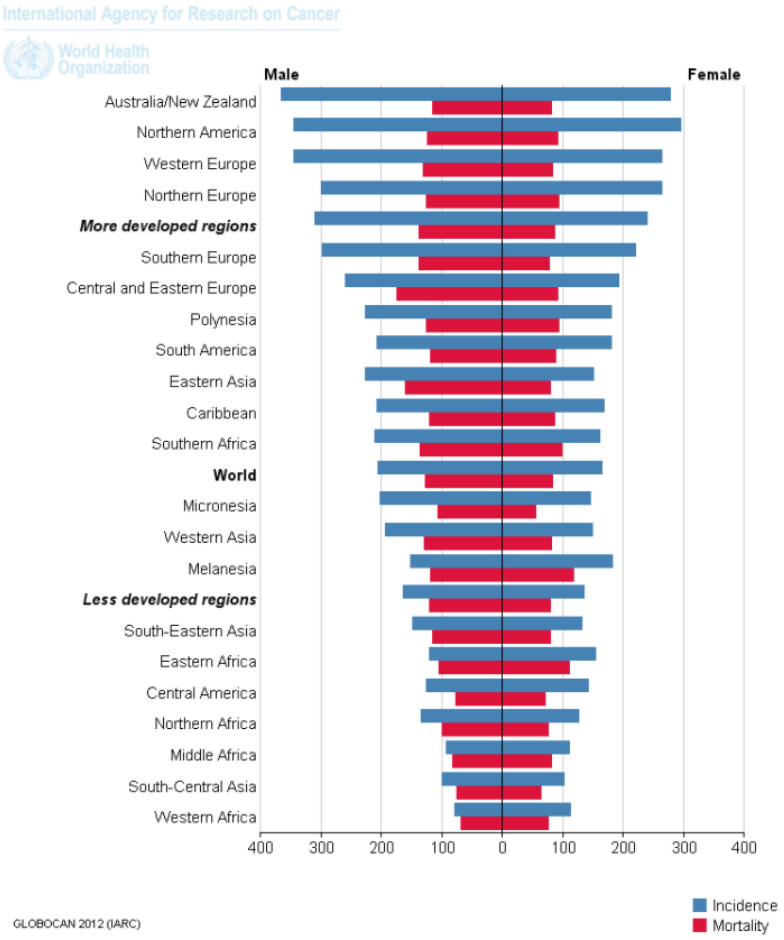

Figure 1.1: Estimated age-standardized rates for cancer incidence and mortality worldwide in 2012. All cancers (excluding non-melanoma skin cancer) are considered [6].

[8] for USA).

But, unfortunately, a non-negligible number of cases reach a stage in which surgery or treatment (chemotherapy or radiation therapy) is necessary. Radiation therapy plays a major role in cancer treatment. The principle of radiotherapy is to give the dose to the target volume, sparing as much as possible the surrounding healthy tissues [9], in order to kill only the diseased cells. In Fig. 1.2 dose-effect curves relative to local control of the tumor and to the probability of inducing complications are indicated.

With the same value of dose released, the probability of inducing complications (red solid line in Fig. 1.2) must be lower than the probability related to the local control of the tumor (blue solid line in Fig. 1.2). The therapeutic window, planned to be as large as possible, is the differential response between tumor and normal tissue, taking in consideration safety margins as well (red and blue dotted lines in Fig. 1.2). In this way local tumor control can be ensured by delivering a prescribed dose of radiation to cancerous tissues while minimizing radiation-induced side effects in surrounding healthy

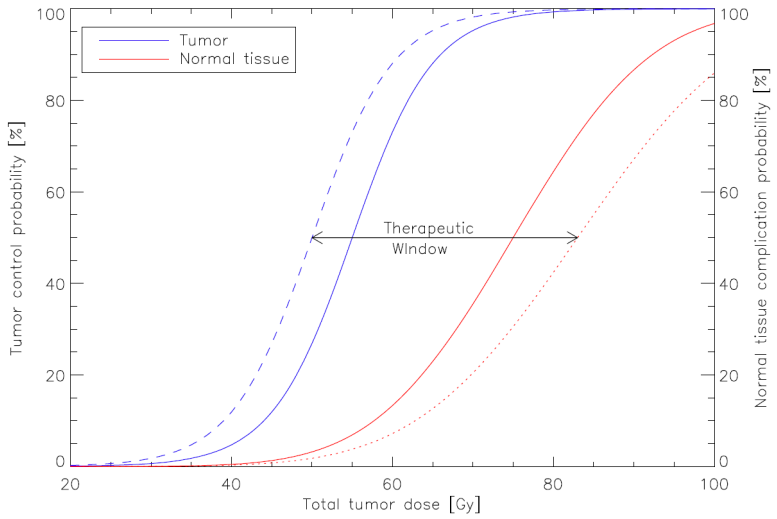

Figure 1.2: Illustration of a typical tumor control probability (solid blue line) and normal tissue complication probability (NTCP, red solid line) curve as a function of total dose delivered to the tumor [10].

tissues [11, 12].

Conventional radiation therapy is performed with either photon [13, 14, 15] or electron beams [16]. The development of this therapy approach started immediately after the discovery of the X-rays by Röntgen in 1896 [17]. In all these years photon therapy has become more and more conformal to the tumor volume by using sophisticated treatment planning with different beam incidence directions and modulated intensities (intensity modulated radiation therapy, IMRT [18]).

However, it is intrinsic in the definition of this method that a considerable amount of dose will be deposited before and after the tumor volume. An ideal radiotherapy treatment would deliver the dose precisely in the localized area of the tumor target volume, without affecting the surrounding healthy tissues. In 1946, Wilson was the first to demonstrate the physical and dosimetric properties of a proton beam [19] for a therapeutic scenario and founded the field of proton therapy. The straight beam trajectory, the finite particle range as well as the increase of the ionization density close to the stopping point (Bragg peak) increased the interest of the medical community and opened new planning and treatment possibilities [20, 21, 22].

Today, the most commonly used charged particles for radiotherapy are protons and carbon ions. Carbon ions present the advantage of having a high radiobiological effectiveness (RBE) towards the end of their range, making their profile even more peaked in terms of biological dose rather than physical dose [23]. They also present ballistic advantages, being subject to less multiple scattering and less longitudinal straggling. Their main drawback is the production of fragments along the path that have a longer range than the initial carbon ion, leading to a tail dose distribution beyond the Bragg peak. Figure 1.3 shows the potential dose benefit of a charged particle therapy treatment compared to a conven-

tional radiotherapy treatment. The dose release in tissues for photons and electrons has an exponential trend, depositing most of the energy in the first part of the path, whereas protons and carbon ions are releasing most of their energy at the end of the path, in the so-called *Bragg peak*.

Supporters of proton therapy claim that, by their very nature, protons are bound to lead to dose distributions that are superior to any that are achievable with photons and that photon therapy has reached its limit in terms of catching up dosimetrically with protons. But, while the available freedom given by the current photon machine design and treatment methods has largely been exhausted, new designs and treatment techniques can inject new freedom and drastically improve the quality of plans [24]. For example Trofimov et al. [25] present a treatment planning comparison with intensity-modulated photon radiotherapy (IMRT) and proton therapy, for early-stage prostate cancer. This comparison is performed in terms of dose conformity to the target, dose homogeneity and sparing of heatlhy tissues. Dose to healthy tissues in the range lower than 50% of the target prescription was, as it is clear from the physics of these particles, substantially lower with proton therapy.

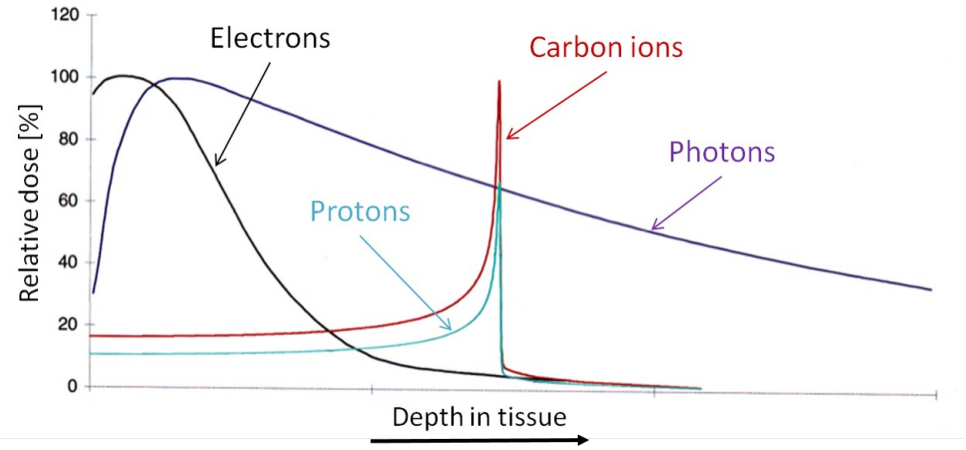

Figure 1.3: Dose release in tissue for different charged particles compared to photons.

In particle therapy, as the peak of the dose distribution for a single particle energy is too sharply peaked to adequately cover the whole depth of the tumor in almost all cases, dose distributions at different energies are superimposed, combining into what is called a spread out Bragg peak (SOBP). In this way, an almost flat dose distribution throughout the depth of the treatment volume can be created. First studies on that were conducted by Bortfeld and Schlegel [26] who derived a simple analytical approximation for the proximal part of the depthdose distribution of a spread-out Bragg peak (SOBP) proton beam. An example of SOBP calculation from these studies in shown in Fig. 1.4. Defining the correct energy range to cover the tumor area is very important and further studies are being conducted: for example in [27], satisfactory SOBP curves were created by arbitrary varying the parameter that relates the range of protons to their energy.

The first human patient was treated in 1954 at the Lawrence Berkeley Laboratory in

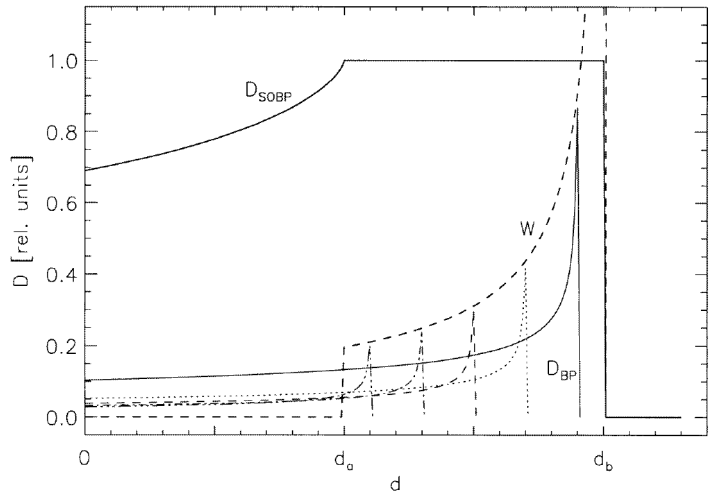

Figure 1.4: Weighted superposition of elementary Bragg peaks D_{BP} in different depths. The weighting function W must be determined such that the resulting dose distribution D_{SOBP} is uniform in a given depth interval $[d_a; d_b]$ [26].

the United States of America (USA) [28, 29]. The development of the cyclotron particle accelerator at this laboratory was led in 1930 by E.O. Lawrence, who received the Nobel Prize for this work in [30]. Still in the '50s, the first patient was treated in Uppsala, Sweden, for a cervical cancer [31, 32]. However, the first hospital-based proton facility was created only in 1990 in Loma Linda University, USA [33]. Since that time, the number of facilities for proton therapy has kept increasing [34], and carbon ion facilities have been also introduced. After many years of development, proton therapy is finally reaching the point of mass adoption in clinical practice [35]. The progress in particle accelerator technology and the improvement in dose delivery techniques have provided strong driving forces for a large scale use. Up to now, a total of around 170000 patients have been treated in around 80 facilities worldwide [32]. In Tab. 1.1 the total number of treatments delivered by the end of 2016, according to the particle therapy cooperative group, are indicated: 86% with protons, 12% with carbon ions and 2% with other ions. Details about neutron treatment facilities can be found in [36]; the patient treated are much less compared to the numbers shown in Tab. 1.1, but still a not neglibile number of them can be listed.

When using particle therapy, in order to fully use the potential of these particles, the range of proton/ion beams needs to be predicted and verified as accurate as possible both in the treatment planning and in the delivery process. A plan is robust if the calculated and the delivered dose are in agreement, even in the case of different uncertainties. The current practice is to use safety margins, expanding the clinical target volume sufficiently enough to account for treatment uncertainties. This, however, might not be ideal for proton therapy [37]. That is why it is very important to be able to define range uncertainties: about 30 years ago Gotein [38] suggested that error-bars should be associated with any calculated dose distribution as "at every point within the patient there is in fact a range

Particles	Number of treatments
He	2054
Pions	1100
Carbon ions	21580
Other ions	433
Protons	149345
Total	174512

Table 1.1: Total number of treatments delivered with various (charged) hadron therapy modalities worldwide as of the end of 2016 according to the particle therapy cooperative group [32].

of possible doses that may be delivered". In the next paragraph the main cause of range uncertainties will be presented, followed by the current research areas on beam range verification methods.

1.2 Range uncertainty in particle therapy

As already described in the previous section, the major advantage of particle therapy is related to the energy deposition in the depth of the tissue: the total energy deposited in the patient is reduced compared to photon techniques and it is localized in the Bragg peak (Fig. 1.3). Despite the higher accuracy reachable with particle therapy compared to conventional radiotherapy, some external uncertainties may affect the range of the depth-dose distribution in the tissue of the patient. Due to the steep dose gradient at the distal edge of proton (ion) beams, the consequences of these range uncertainties are particularly severe in particle therapy, as at the end of the ion path the linear energy transfer (LET) reaches its maximum and increases the ionization density. In Fig. 1.5(a) the nominal situation for both photons and charged particle, in terms of dose release in the tissues, is shown. In 1.5(b) the level of uncertainties for both treatment modalities is shown: being the circle the indicator of the end of the particle range, where the tumor area is supposed to be located, it is clear that uncertainties have a much higher effect on ion beams treatment modalities.

This is problematic, even with small errors, both in "undershoot" as well as in "overshoot" cases. In the latter case the ion beam range has a shift beyond the expected Bragg peak region and therefore an organ-at-risk (OAR) located behind the tumor may get a very high dose. On the other hand, in the first case, part of the tumor receives no dose, compromising the effectiveness of treatment.

Before having a look at the current state of the art on ion beam range verification, an overview of the causes of range uncertainties will be given. A way to categorize the uncertainties in particle therapy can be the following:

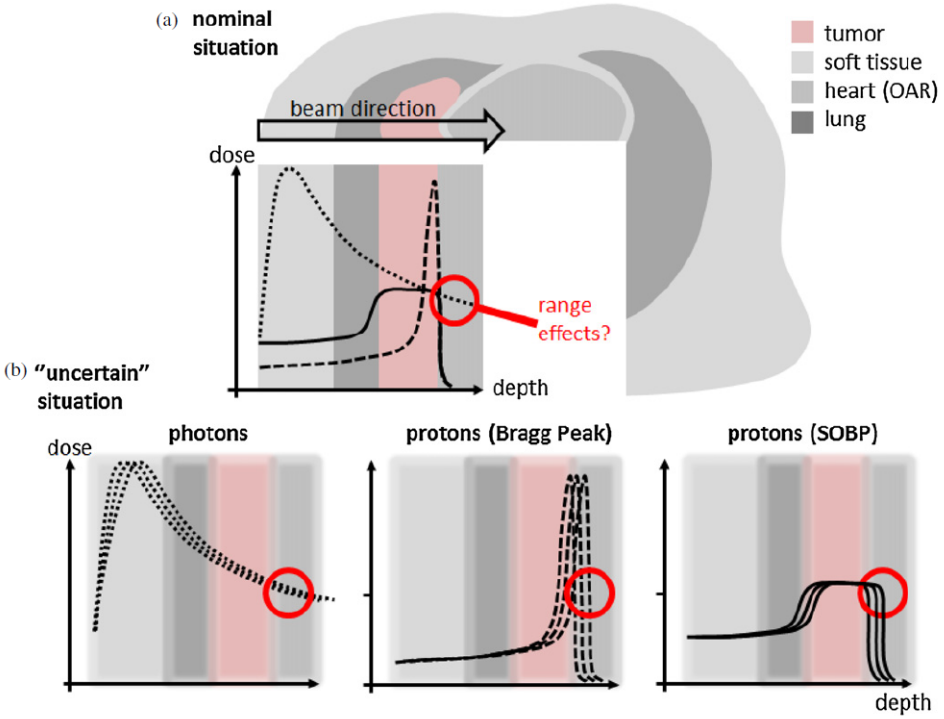

Figure 1.5: (a) Potential dose benefit of a proton treatment compared to a photon treatment (dotted line: photon depth dose curve; dashed line: mono-energetic proton depth dose curve known as Bragg peak; straight line: spread out proton Bragg peak (SOBP) to cover the whole tumour). (b) Influence of uncertainties to these depth-dose curves [39].

- **Systematic uncertainties:** a treatment plan is based on a single computed tomography (CT) acquisition. CT numbers are expressed in Hounsfield units (HU), which give the relative X-ray attenuation of a specific tissue in relation to the attenuation in water. To calculate ion ranges for treatment planning, HU must be first converted to the relative stopping powers; calibration curves are generated using sophisticated algorithms, but it is unavoidable that uncertainties will be associated with these curves, considering also that the actual conversion is dependent on the chemical composition of the material [40]. An uncertainty is also associated to the relative biological effectiveness (RBE): proton therapy has been based on the use of a generic RBE and therefore the dependencies of the RBE on different physical and biologcal properties are not taken into account. This uncertainty corresponds to an uncertainty in biological range of a few mm [41]. The uncertainties just described will likely be the same for every delivered fraction of a treatment.

- **Random uncertainties:** they include the unpredictable uncertainties, that could be different every day and for each different patient. The most important source for this kind of uncertainty is the patient mis-positioning relative to the beam, in particular when treating areas with large density heterogeneities and patient surfaces

that are oblique to the beam direction. Another obvious nor negligible uncertainty example is organ motion, which is being tried to be accounted for by implementing sophisticated modelling for the motion of the organs. Finally, the change in the patient anatomy should be also taken into account: over the weeks of treatment, the anatomy may change due to weight loss or gain and daily changes may occur due to the filling of internal cavities and the reduction of the tumor mass as well.

In Tab. 1.2 the sources of uncertainty in particle therapy are presented in detail, based on a systematic study and classification done by Paganetti [5], in which is also brought up the importance of Monte Carlo simulations. Different studies, for example [42], have been carried out to model at best all the contributions to range uncertainties. A promising option is to incorporate uncertainties directly into the optimization algorithm for treatment planning. The question remains as to whether adaptive therapy can become an integral part of a proton therapy, to allow re-optimization during the course of a patient treatment. The challenge of ensuring that plans are robust to range uncertainties in proton therapy remains, although these methods can provide practical solutions [43].

As a robust treatment planning is not capable to fully override range uncertainties, all these effects can add up to non negligible range errors. To cure this, normally safety margins are applied around the tumor volume and therefore a larger volume is irradiated in order to ensure full dose delivery to the whole tumor (in Fig. 1.6 clinically applied safety margins as routinely applied in some proton treatment facilities worldwide are displayed).

However, this consequently leads to the irradiation of healthy tissues and limits the ability to use the finite particle beam range to shield organs-at-risk. Any method that can verify the range, ideally in real time during the course of the treatment, is extremely desirable. Such a technique could not only reduce the side effects of the treatment, but also potentially provide quality assurance for particle therapy and improve the treatment outcomes. Driven by this desire, over the last years, many different approaches for in-vivo range verification have been proposed and investigated. An overview of the state of the art is presented in the next section.

1.3 Beam range verification

As already mentioned, a direct way of reducing range uncertainties could be through an in-vivo verification of the beam range [39]. Range verification can either be performed prior to the treatment (using test beams), after the treatment or during the treatment, the latter case being the most preferable one [47]. The treatment plan could then be adjusted based on information gained with the range verification measurements, ensuring a good tumor coverage, while still maintaining reasonably reduced margins. In-vivo range verification would therefore also be an excellent quality assurance method to confirm that the range calculated with a treatment planning system (TPS) is reproduced during the treatment itself. During the last decades, several research groups have been heavily working

Source of range uncertainty in the patient	without Monte Carlo	with Monte Carlo
Independent of dose calculation		
Measurement uncertainty in water for commissioning	±0.3 mm	±0.3 mm
Compensator design	±0.2 mm	±0.2 mm
Beam reproducibility	±0.2 mm	±0.2 mm
Patient setup	±0.7 mm	±0.7 mm
Dose calculation		
Biology (always positive)[1]	+∼0.8%	+∼0.8%
CT imaging and calibration	±0.5%	±0.5%
CT conversion to tissue (excluding I-values)	±0.5%	±0.2%
CT grid size	±0.3%	±0.3%
Mean excitation energy (I-values) in tissues	±1.5%	±1.5%
Range degradation; complex inhomogeneities	-0.7%	±0.1%
Range degradation; local lateral inhomogeneities[2]	±2.5%	±0.5%
Total (excluding [1],[2])	±2.7% + 1.2 mm	±2.4% + 1.2 mm
Total (excluding [1])	±4.6% + 1.2 mm	±2.4% + 1.2 mm

Table 1.2: Estimated proton range uncertainties and their sources and the potential of Monte Carlo for reducing the uncertainty [44, 45, 46]. The estimations are average numbers based on 1.5 standard deviations. Extreme cases, such as lung treatments, might show bigger uncertainties [5].

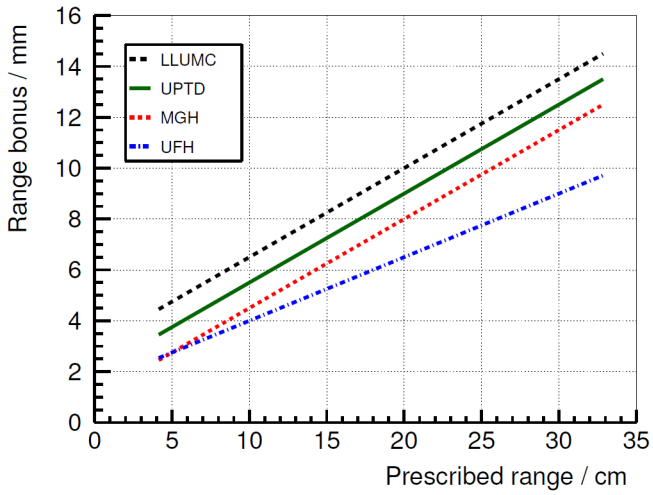

Figure 1.6: Safety margins applied at different clinical proton therapy facilities [3]: (3.5% + 3 mm) at Loma Linda University Medical Center (LLUMC), (3.5% + 2 mm) at Universitäts Protonen Therapie Dresden (UPTD), (3.5% + 1 mm) at Massachusetts General Hospital (MGH) and (2.5% + 1.5 mm) at University of Florida Health Proton Therapy Institute (UFH). "Range bonus" refers to the margin added to the prescribed range to ensure full tumour coverage even in the case of an undershoot. These centres may apply bigger margins in specific treatment scenarios [5].

on possible tools that could measure the particle range and the dose profile. Most of the methods are still in a research and consolidation phase [48], and, even if some of the methods have been tested and implemented on individual clinical treatments, at the moment there is no systematic method used in all the clinical facilities worldwide [39]. The current section is dedicated to the explanation of different approaches of in-vivo ion beam range verification being evaluated. These are based on nuclear techniques, using different kinds of secondary emissions that are generated due to the interaction of the ion beam with the tissues of the patient: ionoacoustic ultrasound signals (created via the thermoacoustic effect), positron annihilation γ rays and prompt γ rays. The nuclear reactions on which these techniques are based are schematically indicated in Fig. 1.7.

1.3.1 Ionoacoustics

The so-called *Ionoacustic method* is a non-nuclear approach to monitor the beam range. This approach makes use of the well-studied thermoacoustic effect, in which pressure waves are generated due to the expansion process of an irradiated medium in response to the temperature increase during the local absorption of light pulses. This phenomenon is similarly occuring for impinging ion beam pulses, in a stronger way at the Bragg peak region, where most of the ion energy is transferred to the surrounding tissue. The created (iono)acoustic signal is therefore directly correlated to the Bragg peak position and can be exploited, by detecting the thermoacoustic waves with high-frequency transducers, for

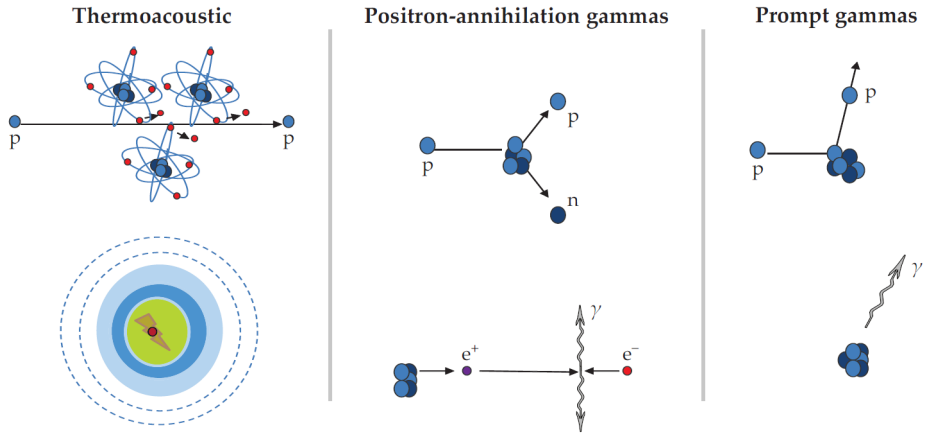

Figure 1.7: Scenarios of interaction between a proton/ion beam in therapeutical relevant samples, creating secondary signals that are used in the various techniques for ion-beam range verification (ultrasound-detectable thermal pressure shock waves, positron annihilation photons and prompt deexcitation γ rays) [49].

its precise localization ([50] and [51]). Ionoacoustic for proton beam range monitoring was initially proposed in 1991 by Tada et al. [52] and demonstrated in 1995 during hepatic cancer proton therapy [53] at the Proton Medical Research Center Tsukuba in Japan. In Fig. 1.8 the schematical setup for an ionoacoustic measurement during an ion beam irradiation in a water phantom is shown.

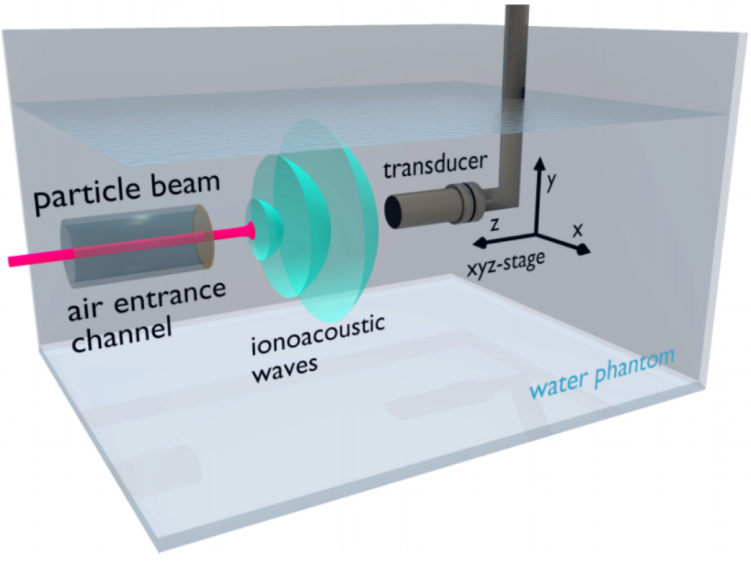

Figure 1.8: Setup used for ionoacoustic experiments: water phantom with air-filled entrance channel, separated by a polyimide entrance foil to water, and ultrasound transducer mounted onto a remote controlled xyz-stage [54].

For some years the interest for this technique decreased, but in the recent years the activity around this topic has renewed and increased thanks to improvements in ultrasound imaging as well as in ion irradiation techniques. Different groups around the world are presently carrying out simulation and experimental studies on the applicabilty of the ionoacoustic technique with a pencil proton beam, as well as with heavier ions using a water phantom. For example at the Medical Physics department of LMU Munich ([50, 54, 55]), and in the USA at the University of Pennsylvania [51], the University of Milwaukee [56] and the University of Stanford [57] such studies are conducted. This approach promises a cost-effective and direct way to characterize the dose distribution in particle therapy. The correlation between the ultrasound images of the irradiated region and the ionoacoustic signal is received quasi in real-time. This has been recently demonstrated in various phantoms and ex-vivo targets at 20 MeV and 50 MeV proton energy ([54] and [56]). In [55], data from ionoacoustic range measurements in water at proton energies between 145 MeV and 227 MeV, using a clinical synchrocyclotron (by its acceleration principle delivering an intense and short-pulsed proton beam with a width below 10 μs and 1 kHz repetition rate, optimally suited for ionoacoustics), are also presented. The approach looks promising and less complex compared to other techniques (that will be described in the next sections), but its applicability to heterogeneous tissue has to be further investigated.

1.3.2 Positron emission tomography (PET)

The first technique that was used in clinical routine for hadron therapy monitoring is positron emission tomography (PET) imaging [58]. When a particle (proton or ion) beam passes through a biological tissue, it undergoes inelastic nuclear collisions and fragmentation reactions that produce radioactive isotopes. Some of these isotopes are β^+ emitter, with half-lives ($T_{1/2}$) of the order of minutes. The PET technique is based on the detection of the photons originating from the electron-positron annihilation. In Tab. 1.3 the main β^+ emitting isotopes are listed, together with their corresponding half-lives for the case of nuclear reactions between a proton beam and tissue target nuclei [59]. Parodi et al. calculated with Monte Carlo simulations, taking into account realistic acquisition strategies at different ion beam facilities, the integral yield of several species of radionuclides (^{15}O, ^{11}C, ^{30}P, ^{38}K, etc.) for clinically planned treatment fields [60]. The activation depends on the composition of the tissue. This dependance could possibly be used in gaining information about the elemental composition of the tissue [61, 62]. ^{15}O and ^{11}C are the species that are generated most abundantly in soft tissues, with half-lives of 2 min. and 20 min., respectively [59], being therefore the dominant contribution to the PET measurement during or immediately after irradiation (^{15}O) and after few minutes (^{11}C). β^+ γ-decaying isotopes like ^{10}C and ^{14}O are generated as well: the daughter isotope is in an excited state, which then promptly de-excites to the ground state via the emission of a third photon in addition to the two annihilation photons. This feature could be used for a so called *triple coincidence* that will be further discussed in the proposed γ-PET technique in Sect. 1.3.3.5.

The PET imaging technique was first proposed by Maccabee et al. in 1969 [63], as

Isotope	Decay mode	Half-life [min]	Nuclear reaction channels
^{15}O	β^+	2.04	^{16}O(p,pn)^{15}O
^{11}C	β^+	20.39	^{12}C(p,pn)^{11}C
			^{14}N(p,2p2n)^{11}C
			^{16}O(p,3p3n)^{11}C
^{13}N	β^+	9.97	^{16}O(p,2p2n)^{13}N
			^{14}N(p,pn)^{13}N
^{10}C	$\beta^+ + \gamma$	0.32	^{12}C(p,p2n)^{10}C
			^{16}O(p,3p4n)^{11}C
^{14}O	$\beta^+ + \gamma$	1.18	^{14}N(p,n)^{14}O
			^{16}O(p,p2n)^{14}O

Table 1.3: Main β^+ emitting isotopes induced from nuclear reactions during the passage of a proton beam through an organic tissue.

well performing experimental tests using α particle beams. Since then, many groups have investigated PET for range control in heavy-ion therapy [58, 64] and proton therapy [65].

In heavy-ion therapy, having for example a mono-energetic ^{12}C beam, fragmentation reactions happen both in the projectile and in the target and therefore an activity maximum close to the Bragg peak can be found. For proton therapy instead only target fragmentation reactions are possible and the PET activity is considerably different from the dose distribution, with almost no activities produced within ∼1 cm before the Bragg peak due to the energy thresholds of the relevant nuclear reactions [66]. Therefore, in this case a direct comparison is not possible, but instead a comparison with predicted activity distributions or other reference images is needed. These are mainly calculated with Monte Carlo simulations using particle transportation packages such as Fluka [67, 68], Geant4 [69, 70], SRIM [71, 72] and MCNPX [73, 74], based on assumptions and prior knowledge of the beam parameters and CT images from the treatment plans.

The workflow typically applied is shown in Fig. 1.9 for a patient case with a one-field proton irradiation [75]. The planned dose (first panel) is compared to the Monte-Carlo predicted dose (second panel) and the simulated PET activity distribution is then determined (third panel). The latter is then compared to the measured PET activity distribution (fourth paneln) to obtain a treatment verification.

There are three operational modalities for PET-based verification of proton/hadron therapy (Fig. 1.10), where only the first is applied online during the treatment, while the other two modalities are applied after the treatment. A comparison can also be found in [76].

In-beam PET (Fig. 1.10(a)) profits from the highest photon emission rates, due to the exponential activity decrease in time. The disadvantages of this technique relate to the costs and to the physical space available in the treatment room: to accomodate the beam nozzle, the couch robot, the cone-beam CT etc., usually only a limited-angle dual-head

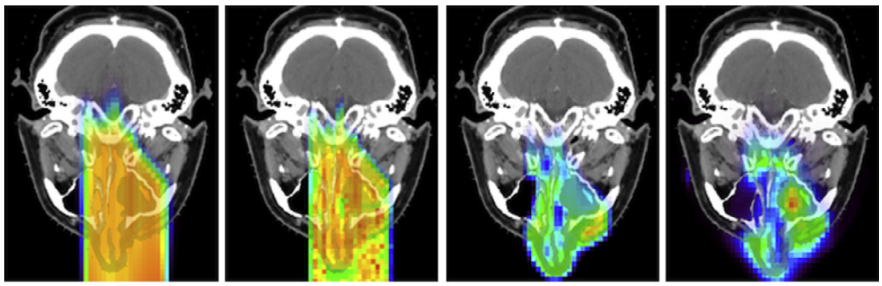

Figure 1.9: Planning dose (first panel), Monte-Carlo predicted dose (second panel), Monte-Carlo predicted PET (third panel) and measured PET (fourth panel) for a patient treated in the nasal cavity/sinus. The range of the color display is from blue (minimum) to red (maximum) [75].

PET acquisition system can be installed. This reduces the field of view and the system sensitivity, reducing the data collection efficiency. The correlation between the distribution of positron emitters and the dose distribution for in-beam PET data can be found for both carbon ions and protons [61, 77]. This approach has been used in some carbon or proton facilities around the world, such as the Gesellschaft für Schwerionenforschung (GSI) in Darmstadt, Germany [58] and the Heavy Ion Medical Accelerator Center (HIMAC) in Chiba, Japan [78].

Offline PET (Fig. 1.10(b)) makes use of already commercially available and dedicated PET or PET/CT scanners. The patient is relocated in a nearby room immediately after the treatment, where the scanner is located: this can lead to delays between treatment and scan of up to 30 minutes with drawbacks on the reconstructed PET images due to signal losses from the short-lived β^+-emitters. A further drawback is the occurrence of biological washout, occuring during the patient transportation. This reduces the activity in the target region, and the effect on the relative activity distribution can lead to image blurring, especially in well-perfused areas such as muscles. Clinical studies considering also washout effects have been conducted by Nishio et al. in [79]. The different half-lives of the relevant isotopes lead to changes in emission rates for different tissues over time.

In-room PET (Fig. 1.10(c)) uses a stand-alone PET scanner placed in the treatment room. It can be considered to be a compromise between in-beam and off-line PET: the cost of a stand-alone PET scanner is significantly lower compared to the installation of a PET system integrated into the beam delivery system and there is no geometrical constraint associated with the beam delivery and the patient positioning. However, there is still a delay between treatment and PET scanning; but since the time gap is much shorter than in the offline PET case, the collection of signals from ^{15}O ($T_{1/2}$=2.04 min.) is also possible. Complications present in offline PET, caused by biological washout, repositioning errors, anatomical changes, etc., are also greatly reduced or eliminated. In-room PET can be an economical option for most hospital-based proton centers that use a cyclotron for proton beam generation, but the time required for each patient treatment is likely to be longer than for in-beam PET.

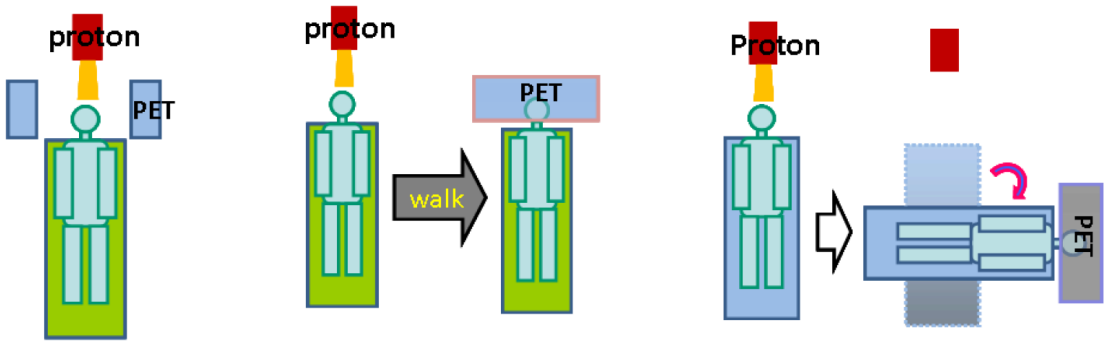

(a) (b) (c)

Figure 1.10: Three operational modalities for PET verification in proton therapy. (a) in-beam PET, which uses PET detection panels integrated into the beam delivery system; (b) off-line PET, where the patients walk to a nearby PET facility for the verification scan; (c) in-room PET, which uses a stand-alone, full-ring PET scanner positioned in the treatment room to scan the patient (still in the treatment bed) soon after the treatment [59].

Currently, PET is still the most widely used technique for verifying the range in hadron therapy, especially in the case of offline acquisition for which commercial scanners are already available. A great advantage of using PET is the fact that no additional dose is needed to be provided to the patient and it can be performed during treatment or in a relatively short time after, providing direct feedback about the treatment. On the other hand, a great challenge in PET imaging is related to the need of a sufficiently high signal-to-noise ratio for image reconstruction, which is limited by the relatively low emission rates and the presence of prompt-γ rays and neutrons. Currently, at the National Institute of Radiological Science (NIRS) in Japan, a huge effort is being made to overcome these limitations by developing the OpenPET system that is able to reconstruct data from all angular directions [80, 81].

1.3.3 Prompt gamma imaging

This category of techniques is based on the detection of prompt γ rays emitted from the nuclear reaction of the ion beam with the tissues of a patient. The gamma energies generated from nuclear reactions of a particle beam with ^{12}C and ^{16}O (the main components in the tissues) are shown in Fig. 1.11 in terms of their cross sections [82].

For many years this was not considered as an in-vivo range verification approach, but as background radiation challenging the quality of in-beam PET imaging for ion therapy monitoring [84]. In 2003, Stichelbaut and Jongen proposed the usefulness of these energetic photons as valuable information correlated to the position of the Bragg peak [85]. In the next section different methods based on the detection of prompt γ rays with the use of passively collimated systems will be presented.

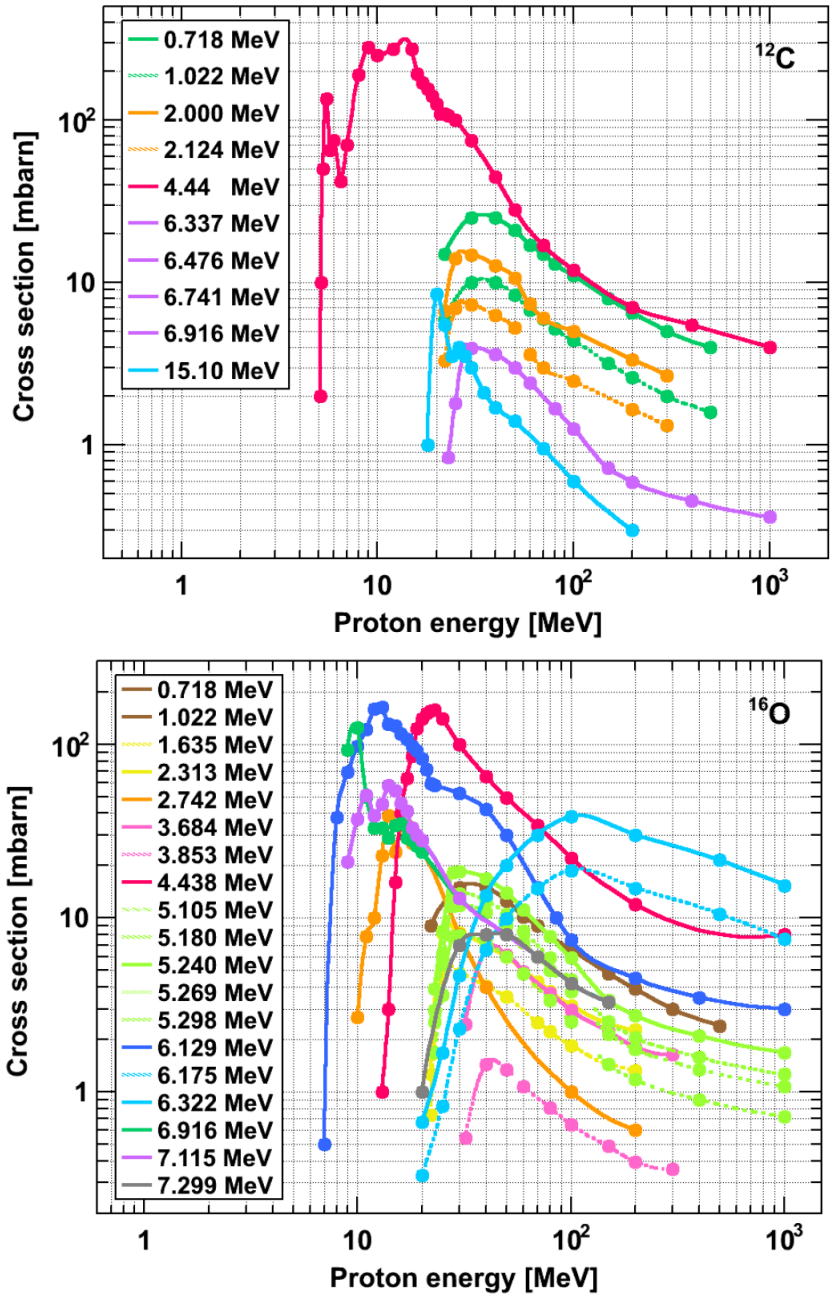

Figure 1.11: γ-ray transition cross sections from proton-induced reactions with ^{12}C (top) and ^{16}O (bottom). Plotted from data of [82]. Cross sections are drawn in the same color when they use the same data multiplied by different factors. For a ^{12}C projectile, the 4.438 and 4.444 MeV peaks are merged as the 4.44 MeV peak [83].

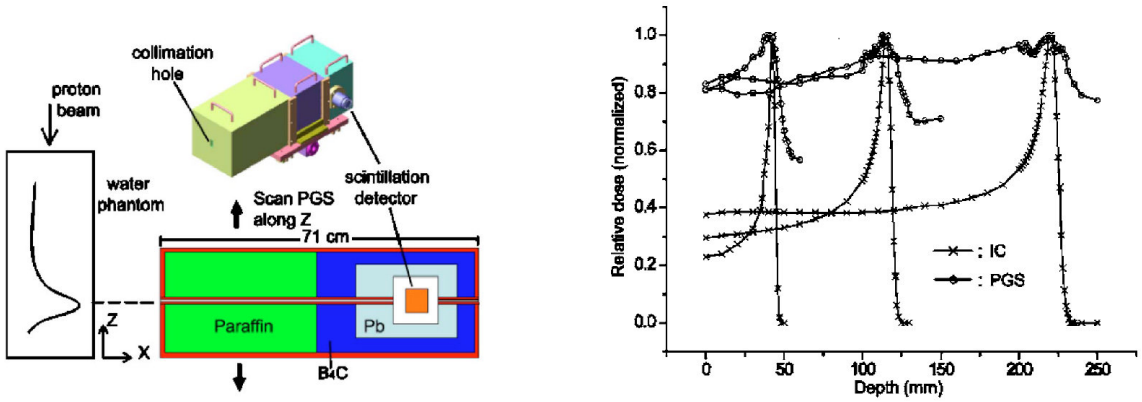

(a) (b)

Figure 1.12: (a) Experimental design of the prompt γ-ray scanning system of [86]. (b) Correlation between the prompt γ-ray scanning (PGS) profile and the depth-dose distribution, measured by an ionization chamber (IC), for 100 MeV, 150 MeV and 200 MeV proton beams, respectively.

1.3.3.1 Passively collimated systems

The experimental confirmation of Stichelbaut's and Jongen's proposal followed few years later [48] with measurements of prompt gamma depth profiles induced by proton [86] and carbon [87] ion irradiation of homogeneous phantoms, using **scanning systems**. These two groups used different setups but common features as they both used scintillation crystals (CsI or NaI) properly shielded by lead for 90° photon collimation from the incident beam direction and used passive (paraffine and B_4C powder) or active (by time-of-flight) neutron suppression techniques, respectively. The setup of [86] will be presented here in more details.

The system was composed of a CsI(Tl) scintillator placed behind a collimator hole. The collimation was created by three layers of shielding material against neutrons, generated from the phantom (Fig. 1.12(a)). The paraffin layer moderates the high-energy neutrons, the B_4C powder captures the neutrons by the B(n,γ) reaction and the lead layer blocks the undesired γ rays. The prompt γ rays were observed in small steps along the lateral path of the proton beam while irradiating a water phantom, using different proton beam energies. As shown in Fig. 1.12(b), the profile of the prompt γ rays has a direct correlation with the Bragg-peak position, and therefore with the proton range. To observe a correlation, a minimum γ-ray energy of 4 MeV was chosen, based on results in which the steepestt fall-off was obtained for the 4 MeV case as minimum energy value [86]. The γ-ray energies for the major decay channels, as it can be extracted from Fig. 1.11, start above 2 MeV. Although the scanning method was useful to demonstrate the existence of this correlation, it would not be fitting to a clinical routine, as the required time for scanning along the particle beam range in the patient would take much longer than the actual treatment time.

The use of position-sensitive cameras was subsequently investigated. In 2008 it was

reported by Min et al. [88] on the feasibility of a **Multi-Slit Camera**, composed of an array of scintillators collimated to detect prompt photons emitted at 90° along the proton track without a scanning process. A scheme of the setup is shown in Fig. 1.13: the system is composed of an array of lead-collimated slots filled with CsI(Tl) scintillators coupled to photodiodes, as readout sensors.

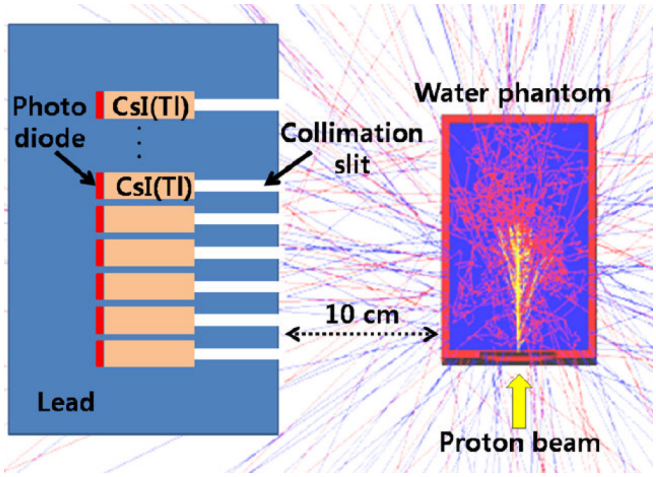

Figure 1.13: Scheme of the array of (collimated) scintillators from [88] to detect prompt γ-rays emitted from a water target after proton irradiation.

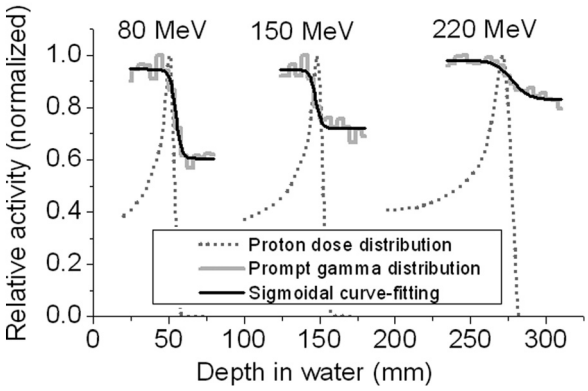

Figure 1.14: Prompt γ-ray profiles measured with a multi-slit camera and fitted with a sigmoidal curve for 80, 150, and 220 MeV proton beams. The measured proton dose distributions are shown for comparison [89].

Lateron, a Monte Carlo optimization study was performed with MCNPX [89], determining the sizes of the scintillator blocks. The tests were realized using a simplified system composed of a single CsI(Tl) scintillator: it was moved behind a multi-slit collimator at the National Cancer Centre in Korea and profiles were acquired with 4 mm bins along the beam axis.

The γ-rays detected were produced by proton irradiation of a water target at different beam energies. A clear correlation was observed (Fig. 1.14): the events selected were those in an energy range between 4 and 10 MeV and the fall-off of the detection profiles around the Bragg peak was fitted with sigmoidal curves, whose half-values were found to be located within 4 mm of the distal dose edge.

A multi-slit camera system was also investigated by the group in Lyon for both carbon ion [90] and proton [91] beams. This setup consists of LYSO scintillators and a multi-slit collimator made of tungsten alloy. A further implementation is the use of time-of-flight (ToF) discrimination between prompt γ-rays and neutrons, the latter being a background signal: using simplified systems for the first tests, it was concluded that ToF discrimination is necessary to observe any correlation with carbon ion beams [90], and that it improves the contrast with proton beams [91].

The **Pinhole Camera** is an alternative geometry that, instead of acquiring the prompt-γ profile, aims at retrieving a 2D image. In 2009 first measurements using a pinhole camera were performed under proton beam irradiation of a water target [92], but, to simplify the analysis, only a 1D distribution was considered. The scintillator used was again a CsI(Tl) crystal (1.5 cm wide, 3 cm high and 4 cm deep), in front of which 1 cm thick lead plates with a pinhole aperture were placed; the camera was moved along the beam axis to get a 1D image. The experiment was performed using the 50-MeV cyclotron at the Korea Cancer Center Hospital. The choice of beam energy was driven by the feasibility of empirical verification and by considering the results that can be reasonably extended to a beam energy of around 70 MeV, at which high-precision eye therapy is performed. The beam energy was varied in steps of 1 MeV by using an energy degrader and aluminum plates, placed as part of the beam vacuum window. The prompt-γ distribution was measured at three different proton energies, for which the gamma energy ranged approximately from 1 to 4 MeV. The profiles revealed a decrease of detected events as the beam energy decreased, but no clear spatial correlation with the beam particle range. As far as we know, this geometry is presently not investigated anymore due to the small counting statistics achievable with prompt γ-rays passing through a pinhole aperture.

Another alternative approach, which is capable of acquiring prompt-γ profiles, is the **Slit Camera**, also called **Knife-Edge Slit Camera**, based on a slit collimation system. In a recent study, cameras with a knife-edge slit (KES) design and a multi-parallel slit (MPS) design were optimized using Monte Carlo simulations and experimentally tested, acquiring data with proton pencil beams of 100, 160 and 230 MeV bombarding a PMMA target. According to this study, in order to reach a given level of statistical precision on the Bragg peak depth retrieval, the KES collimator requires only half the dose the MPS collimator needs, making the KES collimator a preferred option for a compact camera device aimed at imaging the Bragg peak position. On the other hand, the MPS collimator studied in [88] is more efficient at retrieving the entrance of the beam in the target in the context of an extended camera device that aims at imaging the whole proton track within the patient [93]. The slit camera that will be described in the following, based on the above mentioned study, was designed according to simulation studies by Smeets [94, 83] and built by Perali et al. [95] with joint forces between Politecnico di Milano and the company XGlab

[96], within a project also involving the manufacturer of proton accelerators, the Belgium company IBA [97].

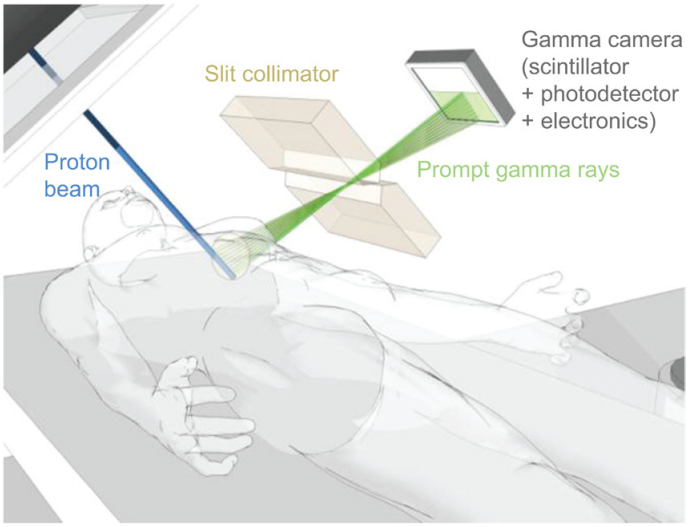

Figure 1.15: Conceptual design of the slit camera: a slit collimation gives a 1D projection of prompt gamma emissions along the beam path on a scintillation detector [95].

The concept of this camera is shown in Fig. 1.15: the aim is to detect the emitted prompt γ rays that are passing through the slit collimation. In order to do that, 20 LYSO scintillator slabs (4 x 31.5 x 100 mm^3 each) are arranged in two rows and placed behind the mechanical collimator [98]. The 1D profile of prompt γ rays is sensitively changed by proton range shifts also due to the design of the tungsten slit collimator that defines the acceptance angle of 53°. The camera is now located at the OncoRay treatment facility [99] at the Universitäts Protonen Therapie Dresden (UPTD), where it was first tested by irradiating water and head phantoms with pencil-beam scanning (PBS) proton beams of different energies. It was then finally brought to real clinical cases [100], demonstrating for the first time that prompt gamma-ray based range verification can be applied for clinical treatments of patients. The knife-edge shaped slit camera was intentionally developed for range verification in pencil-beam scanning proton therapy. The applicability of this system for a passively double-scattered (DS) treatment proton beam, where neutron-induced background is relatively high and can affect the profile quality, was as well evaluated with a proof-of-principle study that demonstrated the capability of detecting global range shifts of 25 mm in this scenario [101]. Further and deeper evaluations are ongoing: in [102] further tests using both PBS and DS were performed and it was demonstrated that global shifts can be detected with an accuracy of 1 mm for all treatment modalities.

1.3.3.2 Electronically collimated systems

A **Compton camera system**, which is the main subject of this thesis, is a device which aims at the detection of prompt-γ rays, in this context for ion beam range monitoring, by

exploiting the Compton scattering kinematics of the impinging radiation without the use of a mechanical collimation. The complete description of the system will be given in Sect. 4.1, where the device being developed at LMU will be also described. A brief description and overview on the state of the art for prompt-γ imaging using Compton camera devices will be now given. In contrast to the previous approaches, a Compton camera detector system is in principle able to provide up to three-dimensional images. This versatile tool for position-sensitive detection of prompt-γ rays is composed of two main parts: a scatterer and an absorber detectors. The primary γ ray interacts in the first component undergoing a Compton scattering, and is then absorbed by the absorber detector. By measuring both energy and position of the two interactions (the scattering and the photoabsorption) in the two camera components, and by applying the Compton kinematics formula, the Compton scattering angle θ between the direction of the primary photon and the scattered photon can be derived. The Compton cone, which is the surface spanned by all the possible directions related to θ, can thus be obtained as shown in Fig. 1.16 (for details see Sect. 4.1).

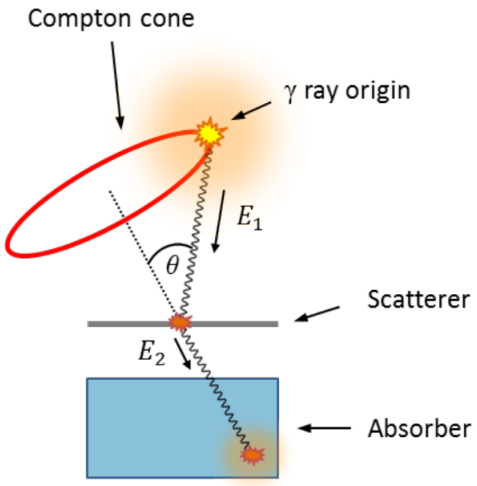

Figure 1.16: Scheme of the operational principle of a Compton camera. The primary photon interacts in the scatter component of the device and undergoes a Compton scattering interaction, depositing a fraction ΔE of the initial energy E_1. The scattered γ-ray is absorbed by the second component, thus releasing the rest of the energy ($E_2 = E_1 - \Delta E$). The angle θ is derived by measuring the two deposited energies and the interaction positions, and thus the *Compton cone* is obtained.

The Compton kinematics can be exploited for the reconstruction of the initial photon source position, either based on the scattered photon (γ-*tracking*) or the recoil electrons (*electron tracking*). The design of a Compton camera is based on a mono-layer or multi-layer scatter component, for γ- or electron- tracking purposes, respectively. From the latter one, which is the design chosen for the LMU Compton camera, a *Compton arc* instead of a *Compton cone* can be defined from the energy and position information registered in

the detector components. The purpose of this section is to show the state of the art in Compton imaging, thus the concept will be explained for a mono-layer Compton camera scenario. More details about the multi-layer scenario can be found in Sect. 4.1.

Once the angle θ is derived, in order to identify the source position, the reconstruction procedure has to be carried out for many registered photon events, emitted from the same origin. The different Compton cones (or arcs) which can be derived are then projected onto the same plane, and their intersection is assigned as the prompt-γ origin, as illustrated in Fig. 1.17.

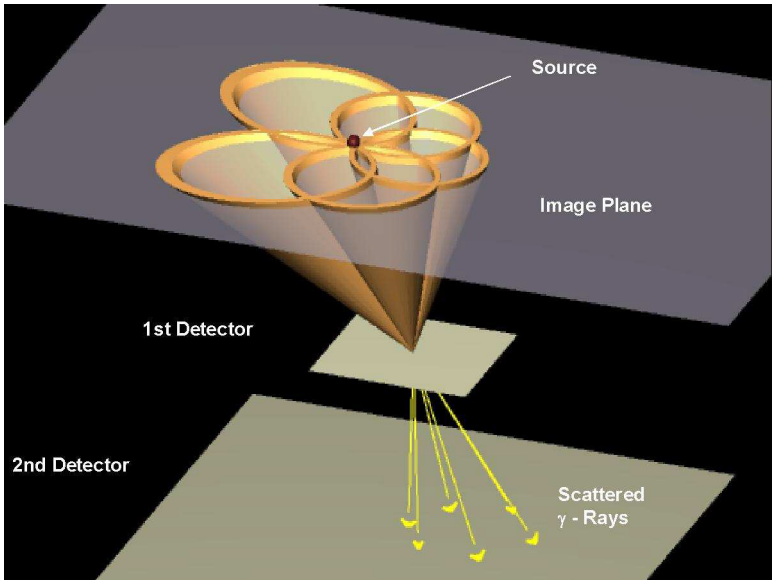

Figure 1.17: Schematic drawing of a source position reconstruction with a Compton camera. Each event corresponds to a cone of possible initial photon directions. Intersections of several cones yield the position of the photon source [103].

The Compton camera approach has been applied and tested for diverse applications including Compton telescopes for balloon and satellite gamma-ray astronomy [104], radioactive waste management [105] and medical imaging, which is the framework of our interest. The use of a Compton camera for medical imaging was first proposed in [106]. Many groups around the world have been investigating this approach using different detector configurations in terms of detector materials and geometrical arrangements: some of them design their Compton camera setup making use of the γ-tracking, some others make use of electron tracking.

In Lyon a Compton camera prototype is under development, in combination with an ion beam hodoscope in order to restrict the γ-ray source position to the intersection between the incoming ion trajectory and the Compton cone [107]. The hodoscope identifies the incident ions and the Compton camera detects the emitted prompt gamma rays, allowing the prompt-gamma origin to be reconstructed [108]. This Compton camera prototype is formed by a stack of 10 double-sided silicon-strip detector (DSSSD) layers ($90 \times 90 \times 2$

mm^3, 2 × 64 strips) acting as scatterer and 100 BGO blocks (38 × 35 × 30 mm^3 for each block [109]) or alternatively LYSO scintillators (300 × 300 × 40 mm^3 [110]) as absorber. The ion beam range verification was simulated showing promising results [109] The Lyon prototype is in a preparatory phase for tests with a clinical proton beam and it is currently being evaluated as well for energy ranges of interest in Single Photon Emission Tomography (SPECT) [111].

At the OncoRay-National Center for Radiation Research in Oncology in Dresden [99] a prototype was designed based on a pixelated CdZnTe detector array (20 × 20 × 5 mm^3, 16 × 16 pixels) working as a scatterer and an LSO scintillator (54 × 54 × 20 mm^3, 13 × 13 pixels) as an absorbing component. The camera was also experimentally tested with monoenergetic 4.4 MeV γ-rays at the HZDR Tandetron facility, revealing a promising ability for proton beam range verification. However, the count-rate capability may present limitations for a clinical scenario application [112]. Further extensive studies on the performance of a Compton camera were then conducted at OncoRay [113]. Simulation studies were also conducted for a scenario with more than one Compton camera, which allows for a 3D image reconstruction.

At the Istitut de fisica corpuscolar (IFIC) in Valencia [114] a Compton camera prototype is also being investigated for prompt-γ imaging in hadron therapy. The MACACO prototype is a three-plane Compton camera [115]: the first layer is a 27.2 × 26.8 × 5 mm^3 $LaBr_3$(Ce) crystal, whereas the second and the third one are $LaBr_3$(Ce) crystals with an area of 35 × 36 mm^2 and a thickness of 5 mm and 10 mm, respectively. The light from all these scintillation crystals is read out by position-sensitive SiPM arrays. Results from experimental data have been obtained using ^{22}Na and ^{88}Y gamma-ray sources, employing both two and three detector planes. In this energy range the device yielded better resolution for increasing photon energies, showing that gamma energy is a relevant parameter in Compton imaging [116]. The two-stages camera arrangement was also tested with a 150 MeV clinical proton beam.

A four stages Compton camera based on semiconductor detectors has been developed at the University of Maryland in Baltimore [117]. Each stage consists of a 2 × 2 array of pixelated (11 × 11 in x and y directions) CdZnTe crystals (2 × 2 × 1.5 cm^3), covering an area of 4 × 4 cm^2. The camera capabilities were tested first using laboratory point sources [118] and later at real clinical scenarios [119]. In the latter scenario shifts of the beam as small as 2 mm for the delivery of 2 Gy (6.29 × 10^8 protons) could be detected. For the delivery of a single distal energy layer (1 10^8 protons) shifts as small as 3 mm could be identified.

A Compton camera prototype with Compton recoil electron tracking capability is under development in Kyoto. The system is composed of a micro-TPC (10 × 10 × 15 cm^3, filled with air + C_2H_6 gas) acting as a scatterer and a 8 × 8 array of GSO(Ce) scintillators (6 × 6 × 26 mm^3 for each crystal) forming the absorber component. This camera was also investigated with a clinical proton beam, exhibiting a correlation between the imaged prompt γ rays and the Bragg peak position [120].

Finally the Compton camera prototype under development at LMU Munich in the framework of this thesis should be mentioned. This Compton camera was designed in

order to have electron tracking capabilities: it consists of a stack of six DSSSD layers, each with an area of 50 × 50 mm^2 and a thickness of 500 μm, followed by a monolithic $LaBr_3$(Ce) scintillator (50 × 50 × 30 mm^3) which acts as absorber component. The design specifications were initially simulated in [121], resulting in an expected spatial resolution of 1.5 mm for a 3 MeV point source placed at 5 cm distance from the first DSSSD layer.

1.3.3.3 Prompt-γ spectroscopy

The idea of this method, being investigated at the Massachusetts General Hospital in Boston (MGH) [122], is to directly match the detected discrete prompt γ-ray lines, originating mainly from $^{12}C^*$ and $^{16}O^*$ (and related fragmentation products), with the experimentally acquired reaction cross sections. The measurement of high-energy gamma rays is challenging, and simulation studies play also an important role in these developments. Prompt gamma-ray emission during proton therapy is dominated by proton-induced nuclear reactions on ^{12}C, ^{16}O and ^{14}N, that are the most abundant elements in human tissues, therefore it is very important to incorporate as precise knowledge as possible for these reactions.

In [123] an extensive simulation study of prompt γ-ray emission during proton therapy was performed using the Monte Carlo codes GEANT4 and MCNP6 and the dedicated nuclear reaction codes TALYS [124] and EMPIRE [125]. In particular, a focus was set on incident proton energies up to about 50 MeV aiming at the correlation with γ-ray energies emitted near the end-of-range of the proton beam. All results obtained by these simulations are compared to data previously reported, as the values reported in Tab. 1.4.

This range verification method was then tested experimentally [1], using the setup shown in Fig. 1.18, by applying two phantoms with different elemental concentrations.

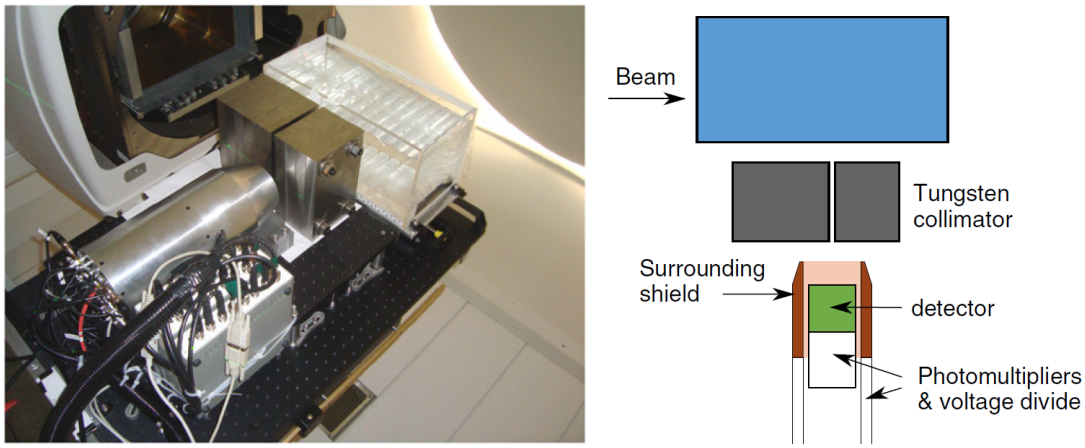

Figure 1.18: Experimental setup showing the prompt gamma-ray detector, tungsten collimator and a water phantom in the proton therapy gantry [1].

The measurement plane is positioned near the distal end of the target. The imaging system shown in Fig. 1.18 is based on a cylindrical $LaBr_3$(Ce) scintillator with a length

Target	Emitter	E_γ [MeV]	Transition	Study	E_{proton} [MeV]
^{12}C	^{12}C	4.44	$2^+4.44 \rightarrow 0^+$g.s.	[126]	5-23
				[127]	40, 65, 85
				[128]	9-50
				[129]	5-25
	^{11}C	2.00	$\frac{1}{2}^-4.44 \rightarrow \frac{3}{2}^-$g.s.	[127]	40, 65, 85
^{16}O	^{16}O	6.13		[130]	23.7, 44.6
		20.39		[126]	5-23
				[127]	40, 65, 85
				[128]	9-50
		9.97		[129]	20.0, 22.5, 25.0
		6.92	$2^+6.92 \rightarrow 0^+$g.s.	[131]	9-19
		7.12	$1^-7.12 \rightarrow 0^+$g.s.	[131]	9-19
		2.74	$2^-8.87 \rightarrow 3^-6.13$	[127]	40, 65, 85
				[131]	9-19
	^{12}C	4.44	$2^+4.44 \rightarrow 0^+$g.s.	[126]	14-23
				[127]	40
				[128]	20-50
				[129]	20.0, 22.5, 25.0
	^{15}N	5.27	$\frac{5}{2}^+5.27 \rightarrow \frac{1}{2}^-$g.s.	[127]	40, 65, 85
				[128]	30, 33, 40
^{14}N	^{14}N	1.64	$1^+3.95 \rightarrow 0^+2.31$	[126]	5-20
				[128]	9-40
				[132]	6-26
		2.31	$0^+2.31 \rightarrow 1^+$g.s.	[126]	4-23
				[127]	40, 65, 85
				[128]	9-40
				[132]	6-26
		5.11	$2^-5.11 \rightarrow 1^+$g.s.	[132]	7-26
		0.73	$3^-5.83 \rightarrow 2^-5.11$	[132]	7-26
		3.38	$1^-5.69 \rightarrow 0^+2.31$	[132]	7-14
		2.79	$2^-5.10 \rightarrow 0^+2.31$	[132]	7-14
		3.89	$1^+6.20 \rightarrow 0^+2.31$	[132]	8-14

Table 1.4: Experimental studies of γ-ray emission during proton-induced reaction on ^{12}C , ^{16}O and ^{14}N [122]. The cross-sections related to these γ-emissions were reported by Dyer et al. (1981) [126], Narayanaswamy et al. (1981) [130], Lang et al. (1987) [127], Lesko et al. (1988) [128], Kiener et al. (1998) [131], Belhout et al. (2007) [129] and Benhabiles-Mezhoud et al. (2011) [132] (g.s. = ground state).

and diameter of 7.5 cm, placed behind a collimation system of 13 cm thick tungsten and a slit opening of 9.5 mm. Based on five pencil beams with different ranges delivering 5 x 10^8 protons, the absolute particle range was determined with a standard deviation of 1.0 - 1.4 mm. Discrete gamma lines were resolved and proton- and neutron-induced contributions were separated ([1], shown in Fig. 1.19).

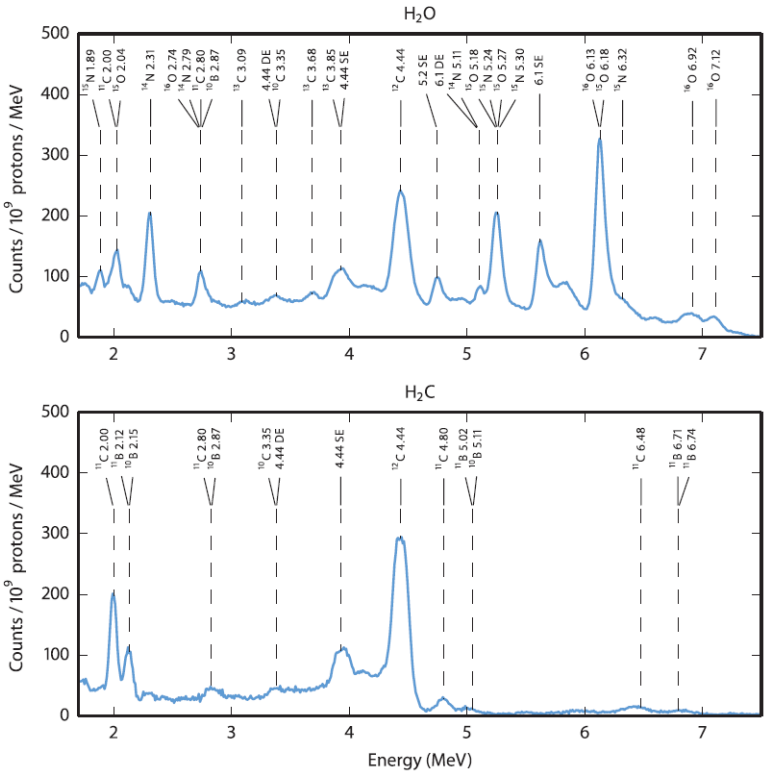

Figure 1.19: Energy spectra of prompt-γ rays induced by a 165 MeV proton beam impinging on a water and polyethylene target, respectively, measured along the last 30 mm of the particle range. Neutron-induced contributions were removed. The lines are named by the residual nucleus and the energy of the emitted gamma ray in MeV (SE: single escape; DE: double escape) [1].

This method can provide a 2D measurement at the detector position. Only a single detector is required, but it would be possible to use multiple detectors to improve statistical precision and to obtain simultaneous measurements at different positions along the beam path.

Recently, the same approach is being evaluated in Dresden as well, using $CeBr_3$ detectors [2]. Preliminary tests using an IBA C230 cyclotron to accelerate protons up to 165 MeV and 224 MeV, respectively, were performed at the OncoRay treatment facility [99] at the Universitäts Protonen Therapie Dresden. The setups used in three different scenarios under investigation is shown in Fig. 1.20(a), together with visible gamma lines obtained with three different targets (b).

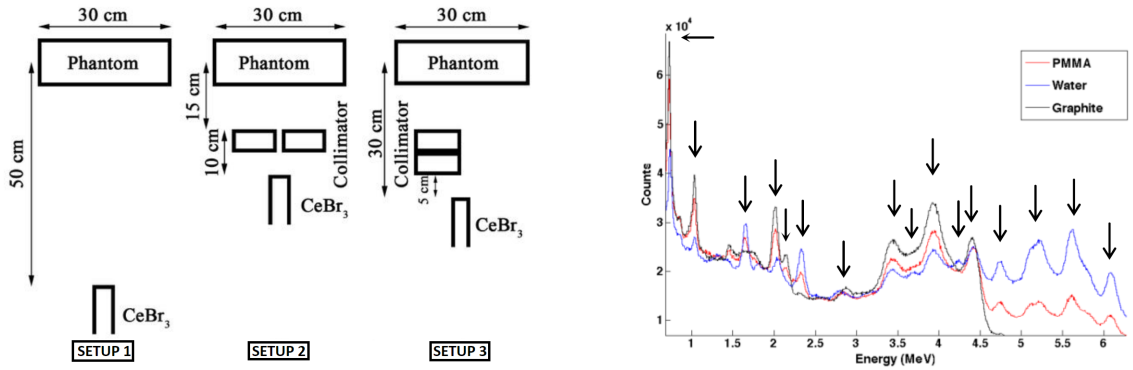

(a) (b)

Figure 1.20: (a) Schematic drawing of the three setups for the different campaigns evaluated (b) Energy spectra corresponding to prompt γ-rays resulting from the irradiation of PMMA, water and graphite for the interval 5-6 ns [2].

1.3.3.4 Prompt-γ timing

The prompt gamma-ray timing (PGT) method aims at obtaining information about the proton beam range by determing the gamma-ray emission time along the proton path, using a conventional time-of-flight detector setup (as indicated in Fig. 1.21).

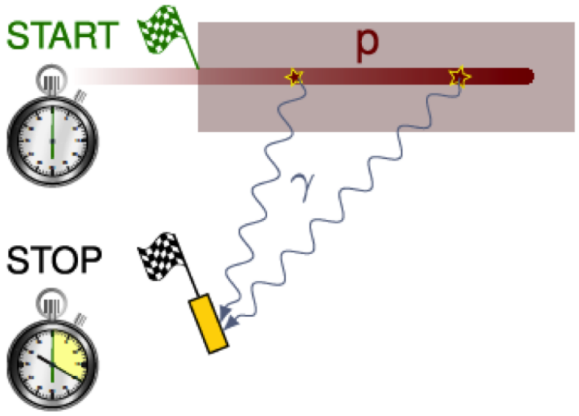

Figure 1.21: Schematic description of a typical setup for beam range verification via the prompt γ-ray timing imaging technique [3].

The approach is based on retrieving the transit time of the protons/ions in the tissues of a patients. This time can be measured indirectly by using the time-of-flight (ToF) technique: the start and stop signals are given by the accelerator RF signal and the timing signal from the detected prompt γ-rays emitted along the beam path. Clearly fast detectors, with a time resolution well below μs, are required in order to successfully be able to accurately correlate the time-of-flight information with the emission position along

the particle trajectory [133]. The more the ion interaction is located deeply in the target volume, the larger becomes the transit time (with a detector position like in Fig. 1.21).

The PGT technique for ion beam range verification is intensively under investigation by the Dresden group and first results were obtained in [134]. First tests of PGT at a clinical proton accelerator were performed, using different phantoms and detectors [135]. The PGT method appears to be feasible in a clinical scenario with a pencil beam, but challenging mostly in terms of data acquisition rate and modelling for time spectra and background. Measurements of the microbunch time structure of the commonly used clinical proton cyclotron C230 were performed [136]: the obtained data were required to understand the limitations of the prompt gamma-ray timing method and to design a bunch phase monitor to be used during patient treatments. In [137] tests under clinical conditions were performed and preliminary results demonstrated that range variations of 5-20 mm are detectable. Phase oscillations between RF and proton bunches were identified as the main factor presently limiting the accuracy of the method, together with load effects on the detector timing. The introduction of a bunch phase monitor and the use of the actual detector gain as a measure of possible timing shifts are expected to improve the accuracy of this method: an accuracy of 2-3 mm using prompt-gamma timing in clinical scenarios seems achievable.

1.3.3.5 γ-PET

As already mentioned in Sect. 1.3.2, besides the 511 keV positron annihilation photons, some of the β^+ emitters, which are produced along the proton beam path in the organic tissue (e.g. ^{10}C and ^{14}N, shown in Tab. 1.3), simultaneously emit a third (prompt) photon. This photon comes from the de-excitation of the excited β-decay daughter nucleus. The principle of the γ-PET technique is based exactly on this resulting triple coincidence: it requires an arrangement of at least three combined Compton camera configurations (or a hybrid system built from a conventional PET scanner plus at least one additional Compton camera system). With this idea, the line-of-response (LOR) can be reconstructed by detecting the two opposite annihilation γ rays following the principle of PET, while the third photon can be used with its kinematics information to reconstruct a Compton cone (or arc segment). The origin of the radiation emission, corresponding to the point in which the initial proton beam interacted in the tissue, is represented by the intersection of the LOR and the Compton cone/arc. The combination of two different pieces of information provided by the different trajectories of LOR and Compton cone in each considered event can improve the image reconstruction sensitivity compared to the performance of the standard PET technique (in Fig. 1.22 the setup studied in [4] is displayed).

The γ-PET technique can be used as a hybrid imaging technique for ion beam range verification during treatment irradiation: the information could be retrieved online using the prompt γ-rays acquired by using the Compton camera principle and the detector system can afterwards switch immediately to PET or γ-PET mode in order to measure the delayed activity distribution of the β^++γ emitters.

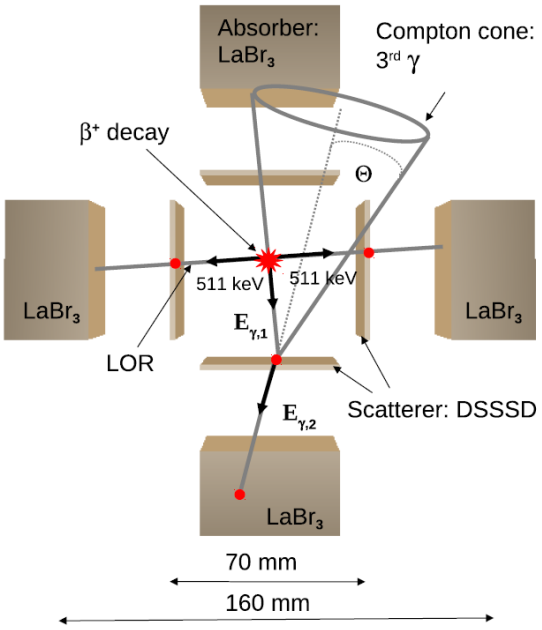

Figure 1.22: Principle of the γ-PET technique in the setup evaluated in [4].

1.4 Contents and organization of the dissertation

At the Chair of Medical Physics at the Ludwig-Maximilians Universität (LMU) of Munich, a Compton camera prototype is under development and is treated in this thesis. The prototype aims at performing prompt-γ imaging for a (ultimately) real-time ion beam range monitoring during hadron therapy in a small-animal irradiation scenario. In particular, its application can be in the framework of laser-accelerated proton beams, since such beams will become available soon at the Center of Advanced Laser Application (CALA) in Garching [138]. The design of this Compton camera prototype was simulated and defined in a previous thesis project [121], when the detectors and the geometry of the camera were chosen: a detector arrangement with a multi-layer scattering component was selected, in order to allow for an electron tracking capability and the detector dimensions were adapted for a small-animal irradiation scenario. First characterization tests for the detectors and the full camera system were performed offline and online [139]. The two components of the prototype are the scatterer, which is comprised of six layers of customized double-sided silicon strip detectors (DSSSD) and a monolithic scintillation detector which acts as absorber component. The aim of this thesis was to upgrade the system in terms of performance of the detector components and in terms of signal processing and data acquisition system, working in the direction of a future real-time application. First of all the silicon scatter detector layers were extensively investigated, in order to identify the reason, previously observed, of an unpredicted behaviour. The explanation of the internal structure of these detectors (and of the absorber as well) can be found in Chap. 3, following the description

of the interaction of photons and particles with matter, which will be presented in Chap. 2. Furthermore, the initial signal processing and data readout system was upgraded: after various assessment studies, a solution was defined and implemented. These characterization and evaluation tests are presented in Chap. 5. First tests with this readout system were performed at the Tandem accelerator in Garching with a 20 MeV proton beam and with a pulsed 20 MeV deuteron beam, which are presented in Chap. 7. Parallel to that, a new design for the scatterer component was studied in order to improve its performance. Concerning the absorber component, the achievements which could be reached during this thesis work can also be divided in detector design and readout system. The originally applied monolithic $LaBr_3$(Ce) scintillator [139] was coupled to a 256-fold segmented photomultiplier (PMT). In order to reduce the complexity of the readout system, a 64-fold segmented PMT was coupled to a second monolithic $LaBr_3$(Ce) scintillator crystal and better performances were achieved, also thanks to an improvement which was implemented in the algorithm for the photon interaction position determination in the monolithic crystal (k-NN algorithm, from which the improved CAP version is used). The procedure needed for the acquisition of the reference library (which is the input of the position reconstruction algorithm of the monolithic absorber) and related results are presented in Chap. 6. In addition satisfactory results could be obtained from first characterization studies with a monolithic $CeBr_3$ scintillation crystal, which is considered an alternative to $LaBr_3$(Ce) as absorber material, as it is a cheaper solution, which still preserves comparable performance. The signal processing of the absorber component was also upgraded to a more compact and flexible electronics and data acquisition system, which enabled a merging of the signal processing of the more than 2000 channels of the Compton camera system into a common homogeneous platform; furthermore, this solution allowed for setting the trigger to the scatterer component, thus improving the useful data rate via the ratio of recorded coincidence events. The system is described in Chap. 5 and first tests with it can be found in Chap. 7. Tests were also performed using prompt γ-rays induced via nuclear reactions generated by an irradiation of water or PMMA phantoms with a 20 MeV proton beam from the MLL Tandem accelerator in Garching. These tests include as well a time-of-flight performance evaluation using the new signal processing and data acquisition electronics which was implemented in the framework of this thesis project. Chapter 8 is dedicated to an alternative Compton camera setup, which makes use of γ-ray tracking instead of electron tracking, therefore requiring just one, but thicker, scattering layer. This detector is a pixelated GAGG crystal, read out by an SiPM MPPC array using a customized signal processing frontend board from Hamamatsu [140]. The $LaBr_3$(Ce) crystal coupled to either the 256-fold or the 64-fold segmented PMT was also used as absorber component of this Compton camera system investigated in parallel in view of a possible application in the framework of prompt-γ or γ-PET imaging techniques in hadron therapy. First tests of this Compton camera detector arrangement were performed with radioactive laboratory point sources at different incident photon energies and in different geometrical configurations. Experimental and simulated data were generated and their outcome was compared. The data in coincidence between the two detectors were extracted and analyzed to be the input of the MEGAlib software toolkit to perform the source position image reconstruction. A

proof of principle of this Compton camera setup could be reached: in the results a good accuracy could be obtained and source shifts could be detected by the system. The thesis concludes with Chap. 9, where a summary of the work is given together with perspectives and impressions related to future plans for the tested and evaluated prototypes under development.

CHAPTER 2

The physics of direct and indirect ionization of matter

In order to develop a device which aims at a beam range control in particle therapy via the detection of prompt γ-rays, it is essential to fully understand the interaction between the beam particles or more generally between the radiation of interest with matter: by their detection they can provide therapeutical valuable information (see details in Chap. 3). The following chapter explains the basic physics behind the interactions that the radiation experiences when passing through matter. The chapter is divided into two parts, describing, respectively, direct ionization and indirect ionization of matter. The first part is dedicated to particles like electrons and ions. The second part considers the three main phenomena that occur when photons interact with matter, namely photoelectric effect, Compton scattering and pair production. In addition the interaction of neutrons with matter is discussed.

2.1 Particle interactions with matter

The operation of any radiation detector depends on the manner in which the radiation of interest interacts with the material of the detector itself. An understanding of the response of a specific type of detector must therefore be based on the knowledge of the fundamental mechanisms by which radiation interacts and loses energy in matter. For a clear classification, it is convenient to arrange the major categories of radiation, important for the topics treated in this thesis, as listed in Tab. 2.1.

In the left column of Tab. 2.1 charged particle radiation is listed. Those particles, because of their electric charge, continuously interact through the Coulomb force with the electrons present in any medium through which they pass.

The radiation listed in the right column is electrically neutral and is therefore not subject to the Coulomb force. Instead, this kind of radiation must first undergo an interaction

Charged particle radiation	Uncharged radiation
Heavy charged particles	Neutrons
Fast electrons	X-rays and gamma rays

Table 2.1: Particles and electromagnetic radiation that can create a direct (first column) or indirect (second column) ionization in matter [141].

that results in a full or partial transfer of energy of the incident radiation to electrons or nuclei of the constituent atoms, or to charged particle products of nuclear reactions.

2.1.1 Direct ionization of matter

In this section the interaction of charged particles with matter is discussed. A charged particle is surrounded by its Coulomb electric field that interacts with orbital electrons and the nuclei of all atoms it encounters, as it penetrates into matter [142]. When directly ionizing radiation interacts with matter, the charged particle's path may be altered (elastic or inelastic scattering) and it may transfer, partly or entirely, its energy to the absorbing material (collision loss) or to photons (radiation loss). All the possible interactions between the charged particle and the orbital electrons or the nucleus of the absorber atoms depend on the characteristics of both particle and absorber and they are characterized by a specific cross section (probability) σ for the particular interaction. Depending on the energy that the radiation deposits in the medium, an ionization track develops within the material. In the following section the discussion will cover the interaction mechanism of heavy (e.g. protons) and light (e.g. electrons) charged particles. The theory of stopping power played an important role in the development of atomic and nuclear models starting with the α particle scattering studies of Rutherford in 1908 [143] and the classical stopping power theory developed by Bohr in 1913 [144], and culminating with the quantum mechanical and relativistic theory of stopping power proposed by Bethe in the 1930s [145] and refined by Fano in the 1960s [146]. The interactions between a charged particle and an absorber can be divided into three cathegories depending on the size of the classical impact parameter b of the charged particle trajectory compared to the classical atomic radius a of the absorber atom with which the charged particles interact:

- Coulomb interaction of the charged particle with an orbital electron of the absorber atom for $b \approx a$ (hard collision).
- Coulomb interaction of the charged particle with an orbital electron of the absorber atom for $b >> a$ (soft collision).
- Coulomb interaction of the charged particle with the external nuclear field of the absorber atom for $b << a$ (Bremsstrahlung production).

The above described different kinds of collisions between a charged particle and an atom are sketched in Fig. 2.1

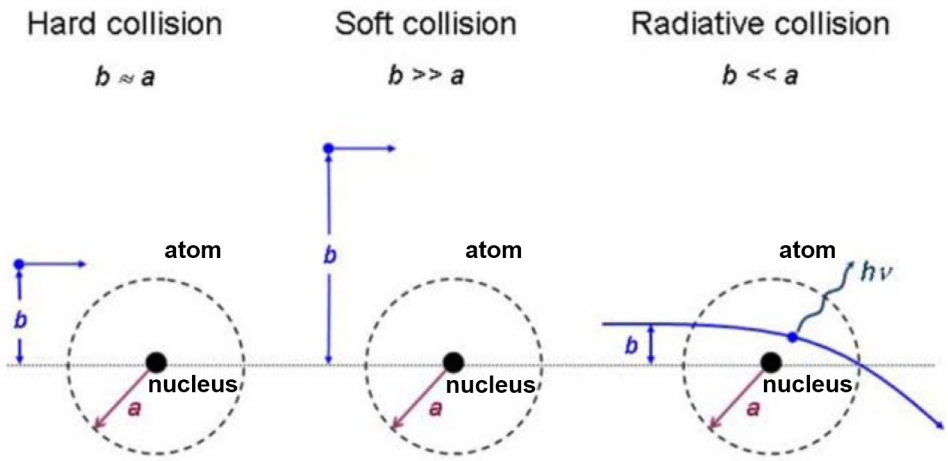

Figure 2.1: Three different types of interaction of a charged particle with an atom, depending on the relative size of the impact parameter b and the atomic radius a. Hard (close) collision for a; soft (distant) collision for $b>>a$; and radiation collision for $b<<a$ [147].

Each of these interactions with the medium is characterized by a specific cross section (probability) σ and makes the charged particle lose some energy. The rate of energy loss per unit of path length that a charged particle loses in a medium is called *linear stopping power* (-dE/dx). The *mass stopping power* is simply obtained by dividing the linear stopping power by the density ρ of the absorber material and it is expressed in units of MeV $\cdot$ cm^2 $\cdot$ g^{-1}. In general, the total stopping power S_{tot} for a charged particle travelling through an absorber is the sum of the radiation (nuclear) stopping power S_{rad} and the collision (electronic) stopping power S_{col}:

$$S_{tot} = S_{rad} + S_{col} \tag{2.1}$$

where the term S_{col} includes both S_{col}^{soft} and S_{col}^{hard}.

- *Radiation stopping power*: It is the result of the charged particle Coulomb interaction with the nuclei of the absorber. An appreciable energy loss through these interactions, normally called *bremstrahlung interactions*, is experienced by light charged particles (electrons and positrons). For heavy charged particles the radiation loss is negligible in comparison with the collision loss and only contributes significantly for very low initial particle energies of less than about 1 keV/u.

- *Collision stopping power*: It is the result of the charged particle Coulomb interactions with orbital electrons of the absorber. These interactions are experienced from both heavy and charged particles.

2.1.1.1 Ions in matter

Heavy charged particles interact with matter primarly through the Coulomb force between their positive charge and the negative charge of the orbital electrons within the absorber atoms. Interactions of the particle with nuclei are also possible, but those interactions occur only rarely and they are normally not significant in the response of radiation detectors. Therefore, the main contribution to the ion's stopping power originates from electronic stopping, where the impinging particles collide with atomic electrons, causing ionization or excitation. The expression for the stopping power for a heavy charged particle thus corresponds to the S_{col} term in Eq. (2.1). The behaviour of the (collision) stopping power can be explained by the Bethe-Bloch formula [142]:

$$S(E) = \frac{-dE}{dx} = 4\pi\frac{N_A}{A}\left(\frac{e^2}{4\pi\varepsilon_0}\right)^2\frac{z^2}{m_e c^2\beta^2}Z\left\{ln\left(\frac{2m_e c^2}{I}\right) + ln\left(\frac{\beta^2}{1-\beta^2}\right) - \beta^2 - \frac{C}{Z} - \delta\right\} \quad (2.2)$$

where N_A is the Avogadro number, A is the relative atomic mass of the absorber material, e is the elementary charge of an electron, ε_0 is the vacuum permittivity, z is the charge of the particle, m_e is the mass of an electron, c is the speed of light, $\beta = \frac{v}{c}$, Z is the atomic number of the absorber material and I is the mean excitation potential.

The Bethe-Bloch collision stopping power equation shown in Eq. (2.2) includes the Fano shell correction and density correction for heavy charged particles: $\frac{C}{Z}$ and δ are, respectively, the shell correction, dominating for slow particles, and the density correction, which is important for high energy particles. The expression in Eq. (2.2) can be summarized as $S(E) = C_0\frac{z^2}{\beta^2}\frac{Z}{A}B_{col}$. The atomic stopping power number (B_{col}), before the corrections introduced by Fano in the 1960s, can in various optimization steps be expressed as indicated in Tab. 2.2. When considering the last corrections, implemented of Fano, the stopping power S(E) can be calculated with an accuracy of a few percent.

In Fig. 2.2 a schematic plot of the mass collision stopping power for a heavy charged particle as a function of its kinetic energy E_K is shown. With increasing energy E_K, the heavy charged particle traverses three different regions, as can be seen in Fig. 2.2:

Region 1: In the low energy region, S_{col} rises almost linearly and reaches a maximum at about 250·I, where I is the mean ionization/excitation potential of the absorber material.

Region 2: In the intermediate energy region beyond the peak, S_{col} decreases as $\frac{1}{v^2}$ or $\frac{1}{E_K}$, where v is the velocity of the charged particle, before reaching a broad minimum at $\sim 2.5 M_0c^2$ where M_0c^2 is the rest energy of the charged particle. Particles in this minimum of the energy loss curve are called "*minimum ionizing particles*" (MIPs)and the corresponding velocity range can be expressed as 3-4·$(\beta-\gamma)$ with $\gamma = 1/\sqrt{1-\beta^2}$. Thus minimum ionizing particles exhibit velocities of $\beta \approx 0.96$. For simply-charged particles (Z=1) an approximation can be given as $dE/\rho \cdot dx \approx 2MeV(g \cdot cm^2)$.

Derivation of S(E)	Atomic stopping number B_{col}
Classical Bohr - 1913	$\left\{ ln\sqrt{\frac{2m_e v^2}{I}} \right\}$
Non relativistic, quantum-mechanical Bethe - 1931	$\left\{ ln\frac{2m_e v^2}{I} \right\}$
Relativistic, quantum-mechanical Bethe - 1931	$\left\{ ln\frac{2m_e c^2}{I} + ln\frac{\beta^2}{1-\beta^2} - \beta^2 \right\}$
Relativistic, quantum-mechanical with shell correction (C/Z) and density correction	$\left\{ ln\left(\frac{2m_e c^2}{I}\right) + ln\left(\frac{\beta^2}{1-\beta^2}\right) - \beta^2 - \frac{C}{Z} - \delta \right\}$

Table 2.2: Expression for the atomic stopping number B_{col} for various energy ranges of heavy charged particle energy [142].

Region 3: In the relativistic region beyond the broad minimum, S_{col} rises slowly with increasing kinetic energy E_K as a result of the relativistic term $\left\{ ln\beta^2 - ln(1-\beta^2) - \beta^2 \right\}$.

After having introduced the topic, the focus can be narrowed down to particle types and energies of specific interest in the hadron therapy field, namely interactions of protons up to about 250 MeV and carbon ions up to about 450 MeV/u. For a particle of kinetic energy E_K, total energy E_{tot}, mass m_0 and momentum p, the particle velocity β in units of the velocity of light c is given by

$$\beta \equiv \frac{v}{c} = \frac{pc}{E_{tot}} = \frac{\sqrt{E_{tot}^2 - m_0^2 c^4}}{E_K + m_0 c^2} = \frac{\sqrt{E_K^2 + 2E_K m_0 c^2}}{E_K + m_0 c^2} \tag{2.3}$$

For a proton with kinetic energy E_K=250 MeV and given the proton mass of 938 MeV/c^2, the resulting velocity amounts to $\beta \approx 0.6$, while a carbon ion with an energy of 450 MeV/u has $\beta \approx 0.7$. Thus, in radiotherapy, we generally deal with relativistic particles, but still located on the low-energy side of the Bethe-Bloch minimum [47].

The electronic stopping power as a function of the kinetic energy of protons impinging on a water target is shown in Fig. 2.3, where the different regions are shown in details. At low energies, before the Bethe-Bloch region, the so-called regions of *Lindhard-Scharff* and *Anderson-Ziegler* can be found. Also indicated is the nuclear stopping power resulting from Coulomb interactions of the incident particles with the atomic nuclei, which only negligibly contributes to the total stopping power.

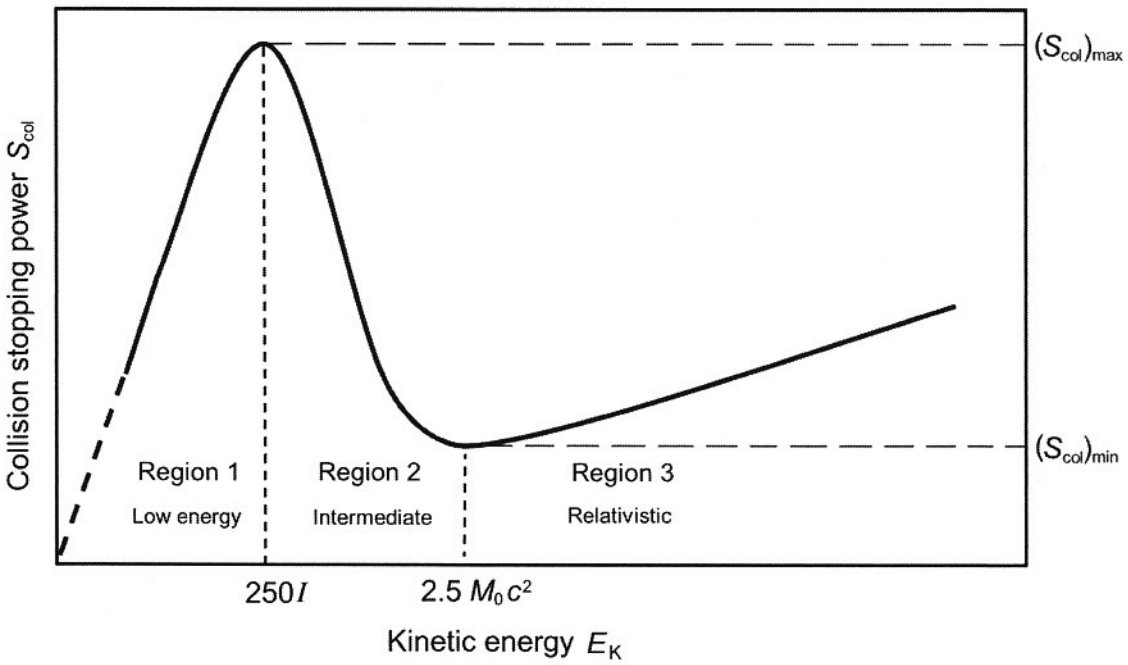

Figure 2.2: Schematic plot of the mass collision stopping power for a heavy charged particle as a function of its kinetic energy E_K; M_0 is the rest mass of the charged particle, I is the mean excitation/ionization energy of the target medium [142].

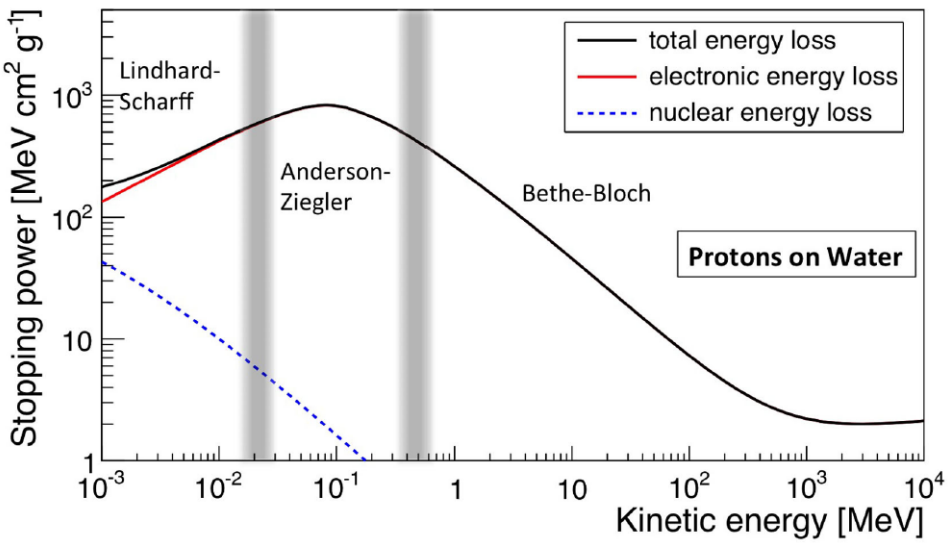

Figure 2.3: Stopping power (dE/dx), in [MeV cm^2 g^{-1}], for protons in water as a function of their kinetic energy. The total, electronic, and nuclear stopping powers are shown, as well as the characteristic regions. The plot is based on data from NIST [148, 47].

The data were obtained a data base maintained at the National Institute of Standard and Technology (NIST) [148], using the Bethe-Bloch collision stopping power equation (2.2) (including the shell and density corrections at high proton energies). At low proton energies the NIST data are determined from fitting formulas, which are largely based on experimental data. The NIST collision stopping power database uses mean ionization/excitation potentials recommended by the ICRU Report 37 [149].

The solid curve in Fig. 2.3 for the proton collision stopping power in water exhibits the standard collision stopping power behavior of an increase with E_K at low kinetic energies, reaching a peak and then decreasing as $\frac{1}{v^2}$ or $\frac{1}{E_K}$ at intermediate energies before reaching the minimum around $\frac{E_K}{E_0} \approx 2.5$. In the relativistic energy range the stopping power slowly rises with E_K, whereas it increases when the particle slows down: this relates to the increased interaction time of slow particles with the Coulomb field of the electrons of the absorber material.

All these considerations finally lead to the determination of a well-localized energy deposition of the heavy charged particles in the medium at the end of their stopping range. This well localized position, already mentioned in Sect. 1.1, is known as the *Bragg peak* and is of particular interest in hadron therapy for dose delivery in tumor treatment. The distance in the medium that a heavy charged particle needs to traverse in order to lose all its energy is called the particle *range* and it can be approximately calculated by the integration of the particle stopping power.

This corresponds to the R_{CSDA} range and is defined by the CSDA concept (continuous slowing down approximation) [150]:

$$R_{CSDA} = \int_0^{(E_K)_0} \frac{dE}{S_{tot}(E)} \tag{2.4}$$

where R_{CSDA} is the CSDA range (mean path length) of the charged particle in the absorber (typically in $cm^2 \cdot g^{-1}$), $(E_K)_0$ is the initial kinetic energy of the charged particle, and $S_{tot}(E)$ is the total mass stopping power of the charged particle as a function of the kinetic energy E_K.

The CSDA range is a quantity that represents the mean path length along the trajectory of the charged particle. In general, the range is an experimental concept that provides the thickness of an absorber medium that the particle is able to penetrate. This quantity depends on the kinetic energy of the particle, its mass and charge and the composition of the absorbing medium.

Since for heavy charged particles deflections due to elastic scattering are not much pronounced and the path of the particle is therefore essentially rectilinear, the R_{CSDA} is a very good approximation to the average range R of the charged particle in the absorbing medium

Figure 2.4 shows the energy - range relationship for monoenergetic proton beams. As the human body is mainly composed of water, the values obtained and shown in Fig. 2.4 can be considered as a good approximation to ranges of protons in inhomogeneous patient tissues. Values of interest are for example the 4 cm range at 70 MeV energy (used for eye

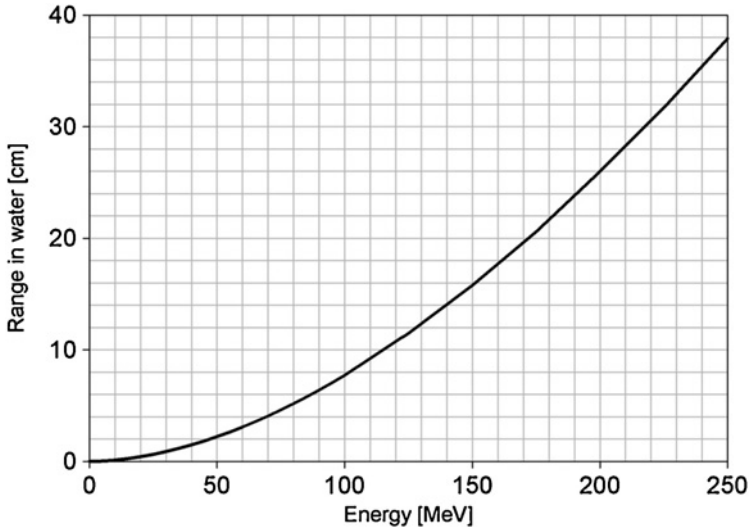

Figure 2.4: Range of a proton beam in water based on the continuous slowing down approximation as a function of proton energy [5].

therapy treatments) or 25 cm at 200 MeV corresponding to the energy used for treatment of organs located deeper in the patient's body. Of interest for this specific thesis work are also ranges of protons in water at lower energies which were used during some experimental campaigns at the local Tandem accelerator: a 4 mm range corresponds to a proton energy of 20 MeV.

However, for the needs in hadron therapy, the particle range is defined at the position where the dose has decreased to 80% of the maximum dose, i.e. in the distal dose falloff. The reason for this choice is that the 80% falloff position is independent of the beam energy spread and coincides with the range where 50% of the protons have stopped. More detailed studies, also empirical, on methods for range calculations, are being carried out by several groups: an example can be found in [151] by Krim et al.

2.1.1.2 Electrons in matter

When light charged particles like electrons and positrons pass through a medium, they can, elastically or inelastically, interact with the atom's Coulomb potential. When an elastic interaction happens, the electron direction is deflected by many small-angle scatterings caused by the electrostatic field of the target without affecting the electron energy. Unlike the heavy charged particles, a light charged particle like an electron is experiencing multiple elastic scatterings that are preventing the electron itself to follow a straight path. This multiple scattering is known as Molière scattering [152, 153]. In applications, like the LMU Compton camera, where the Compton-scattered electron needs to be tracked, it is important to take into consideration this type of interaction as well. The Coulomb scattering distribution is well represented by the Molière theory [154]. It is roughly Gaussian for small deflection angles [155], but at larger angles (greater than a few θ_0, defined

in Eq. (2.5)) it behaves like Rutherford scattering, exhibiting larger tails than a Gaussian distribution.

θ_0 is defined like

$$\theta_0 = \theta_{plane}^{rms} = \frac{1}{\sqrt{2}}\theta_{space}^{rms} \tag{2.5}$$

where θ_{plane}^{rms} is defined on a 2D plane, whereas θ_{space}^{rms} is defined in a 3D space.

For many applications it is sufficient to use a Gaussian approximation for the central 98% of the angular distribution projected on the scattering plane, with a width given by

$$\theta_0 = \frac{13.6MeV}{\beta cp} z\sqrt{x/X_0}[1 + 0.038 \cdot ln(x/X_0)] \tag{2.6}$$

where p is the momentum, βc is the velocity ($= (v/c) \cdot c$) and z is the charge number of the incident particle. X_0 is the radiation length of the material and it is defined as the mean length (in cm) to reduce the energy of an electron by the factor 1/e (21.82 $g \cdot cm^{-2}$ for silicon [156]). x represents the straight line between the start and the end point of the electron trajectory in the medium that is being traversed. When an electron is passing through different materials, the combined radiation length ist estimated with

$$\frac{m_T}{X_T} = \sum_i \frac{m_i}{X_i} \tag{2.7}$$

where m_T is the total mass of the sample in g, X_T is the combined radiation length of the sample in $g \cdot cm^{-2}$, m_i is the mass of each individual component in g and X_i is the radiation length of each individual material component expressed in $g \cdot cm^{-2}$. From Eq. (2.6) it can be derived that the smaller the electron energy is, the more dominant the Molière scattering will become.

The inelastic interactions which the electrons undergo when traversing a medium result in energy losses in the medium itself. These energy losses are dissipated in the medium either by radiative emission (Bremsstrahlung), coming from interactions with the field of the nucleus of the medium, or by collisions with the atomic electrons or the nucleus, causing ionization or excitation. Unlike heavy charged particles, for light charged particles like electrons the radiation component is not negligible anymore. Therefore the total mass stopping power can be expressed as given in Eq. (2.1), where both components are contributing. Within a broad range of kinetic energies below 10 MeV collision losses are dominant ($S_{col} > S_{rad}$); however, the situation is reversed at higher kinetic energies, where $S_{rad} > S_{col}$. In Fig. 2.5 the total mass stopping power S_{tot} for electrons in water, aluminum and lead is shown as a function of the electron kinetic energy.

The contribution of both components to the total energy loss is about equal if the critical kinetic energy ($(E_K)_{crit}$) of the light charged particle, expressed as

$$(E_K)_{crit} \approx \frac{800MeV}{Z} \tag{2.8}$$

is reached [142].

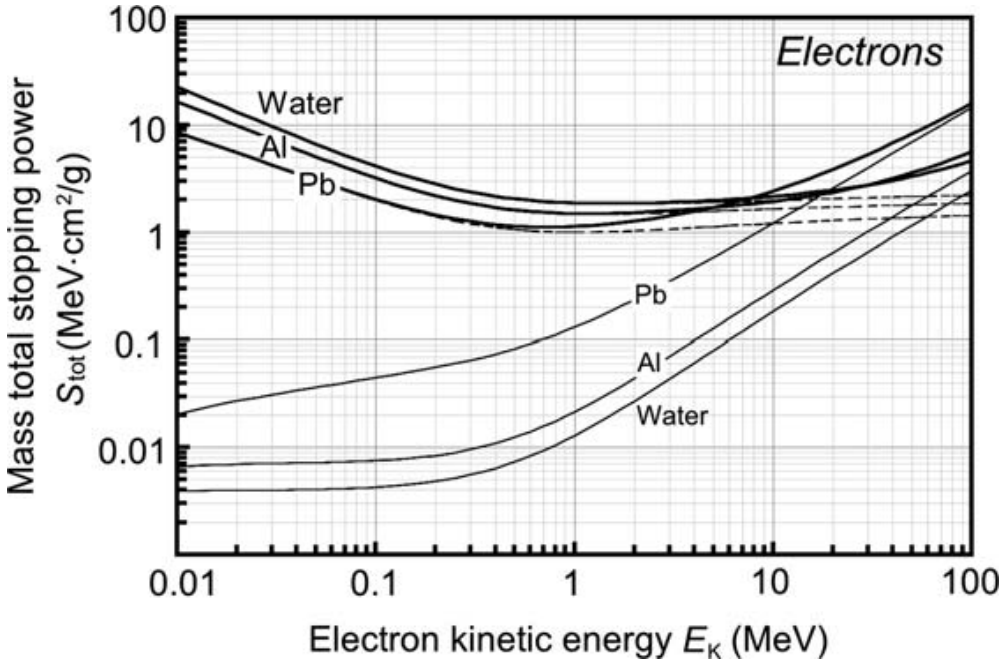

Figure 2.5: Total mass stopping power S_{tot} for electrons in water, aluminum and lead against the electron kinetic energy (thick solid curves). The mass collision stopping power S_{col} and the mass radiation stopping power S_{rad} are shown for comparison with dashed curves and thin solid curves, respectively [142]. Data were obtained from the NIST database [148].

The scatterer component of the LMU Compton camera is a silicon detector. This material has a $(E_K)_{crit} = 53$ MeV. The impinging γ rays which are detected by the LMU Compton camera have an energy up to above 6.1 MeV (which is the most energetic prompt γ-ray line (from $^{16}O^*$) to be expected from nuclear interactions of a therapeutic proton (ion) beam with organic tissue materials as it is shown in Fig. 1.19): as the average energy of the Compton electron generated is far below $(E_K)_{crit}$ and its maximum energy is less than 5 MeV, the contribution of the Bremsstrahlung radiation in the electron energy loss is negligible in our case, and the total energy loss can be expressed exclusively via the term S_{col}, referring to the collision processes. This feature is an advantage for our application, since the minimization of the radiative process leads to a cleaner condition for the tracking of the Compton electrons, which will lose their energy via collision processes.

An expression similar to the one in Eq. (2.2) can be also found for fast electrons and has been derived by Bethe, describing the specific energy loss due to ionization and excitation (=collisional losses):

$$-\frac{dE}{dx} = \frac{2\pi e^4 NZ}{m_e v^2}\left(ln\frac{m_e v^2 E}{2I^2(1-\beta^2)} - (ln2)\left(2\sqrt{1-\beta^2} - 1 + \beta^2\right) + (1-\beta^2) + \frac{1}{8}\left(1-\sqrt{1-\beta^2}\right)^2\right) \tag{2.9}$$

where e and v are the charge and the velocity of the electron, N and Z are the number of

Energy [MeV]	R_{CSDA} [g/cm^2]	R_{LISE} [g/cm^2]
0.01	$3.46 \cdot 10^{-4}$	$3.11 \cdot 10^{-4}$
0.1	$1.82 \cdot 10^{-2}$	$1.53 \cdot 10^{-2}$
1	0.54	0.46
2	1.18	1.06
3	1.81	1.69
5	2.99	2.94

Table 2.3: Electron range in Si for different energies of interest for the LMU Compton camera. The range was calculated using the *CSDA* concept and with an empirical formula [157, 158].

atoms and the atomic number of the medium traversed, m_e is the rest mass of the electron, $\beta = v/c$ and I is the average excitation and ionization potential of the material. The latter has to be determined experimentally for each element [141].

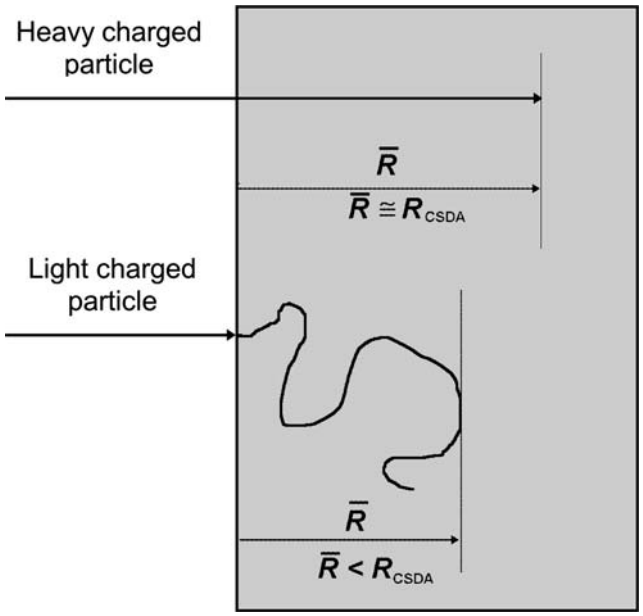

Figure 2.6: Schematic diagram of charged particle penetration into an absorbing medium. The *bottom* part shown is for the light charged particle case as treated in this section, compared to the case of heavy charged particles (*top* part) [142].

The concept of range has been already introduced in Sect. 2.1.1.1. As deflections due to elastic scattering in the medium are much more pronounced for light charged particles (a schematic diagram of the charged particle penetration into an absorbing medium is shown in Fig. 2.6), for these particles the R_{CSDA} range can be used as an approximation, but the real trajectory can also be up to twice the average range R.

In Tab. 2.3 the range of an electron in silicon was calculated at different energies of interest for the LMU Compton camera. Two methods were used: the R_{CSDA} formula that

is based on the *continuous slowing down approximation* and a calculation obtained from the LISE code package [157], that is based on an empirical formula developed by Tabata et al. [158].

2.1.2 Indirect ionization of matter

In this section the interaction of radiation with matter will be described for non-charged radiation that can only indirectly ionize the matter. In these cases, the incident radiation transfers its energy to the traversed medium in more than one step. The ionization of matter happens via secondary reaction products, such as light or heavy charged particles, generated from the incident primary radiation. The mechanism of interaction with a medium, specific for neutral radiation like photons or neutrons, will be discussed in the following section.

2.1.2.1 Photon interaction

The term photon denotes electromagnetic radiation comprising both X- and γ-rays. As in our application nuclear reactions are involved, we are interested in the γ-ray production and their interaction with matter. γ radiation is defined as electromagnetic radiation generated during nuclear processes (in contrast to X-ray radiation that is created from atomic processes). It is mostly produced in nuclear de-excitation processes or in positron-electron annihilation, therefore its energy range varies between 100 keV and few tens of MeV.

The main difference between the way γ rays and charged particles interact with matter is the fact that photons do not lose fractions of their energy in a continuous way along their path, as it is the case for charged particles, but rather their intensity decreases. This phenomenon is called "attenuation": the number I of transmitted photons is given in terms of the number I_0 of initial photons as:

$$I(x) = I_0 \cdot e^{-\mu \cdot x} \tag{2.10}$$

where I(x) is the intensity at the traversed matter thickness x, I_0 is the initial intensity and μ is the linear attenuation coefficient, which is defined as

$$\mu = \tau(photoelectric) + \sigma(Compton) + \kappa(pair) \tag{2.11}$$

The three factors (μ, σ, κ) in Eq. (2.11) are the cross sections of the three major interaction processes that a gamma ray undergoes when interacting with matter: photoelectric effect, Compton effect and pair production. For each linear attenuation coefficient, a mass attenuation coefficient can be obtained by

$$\mu_{mass} = \frac{\mu}{\rho} \tag{2.12}$$

where ρ is the density of the absorbing material considered.

In Fig. 2.7 the energy dependence of the mass attenuation coefficient, related to the three major processes between a gamma-ray and an absorbing medium, is shown. These cross sections have been calculated for γ-ray interactions with sodium iodide (NaI), that is one of the most frequently used scintillator materials for the detection of γ rays. In the low energy range, the photoabsorption cross section reveals a sharp discontinuity, or "absorption edge". These discontinuities appear at gamma-ray energies that correspond to the binding energies of electrons in the different shells of the atoms of the absorber material. For example the edge labeled as *K edge* corresponds to the K-shell binding energy. For gamma-ray energies slightly higher than the gamma-ray energy at the edge, the photon energy is just sufficient to undergo a photoelectric interaction in which a K electron is ejected from the atom, whereas for lower energies the process is energetically not possible and the cross section drops. Similar absorption edges appear at lower energies for the L, M ... electron shells of the atom.

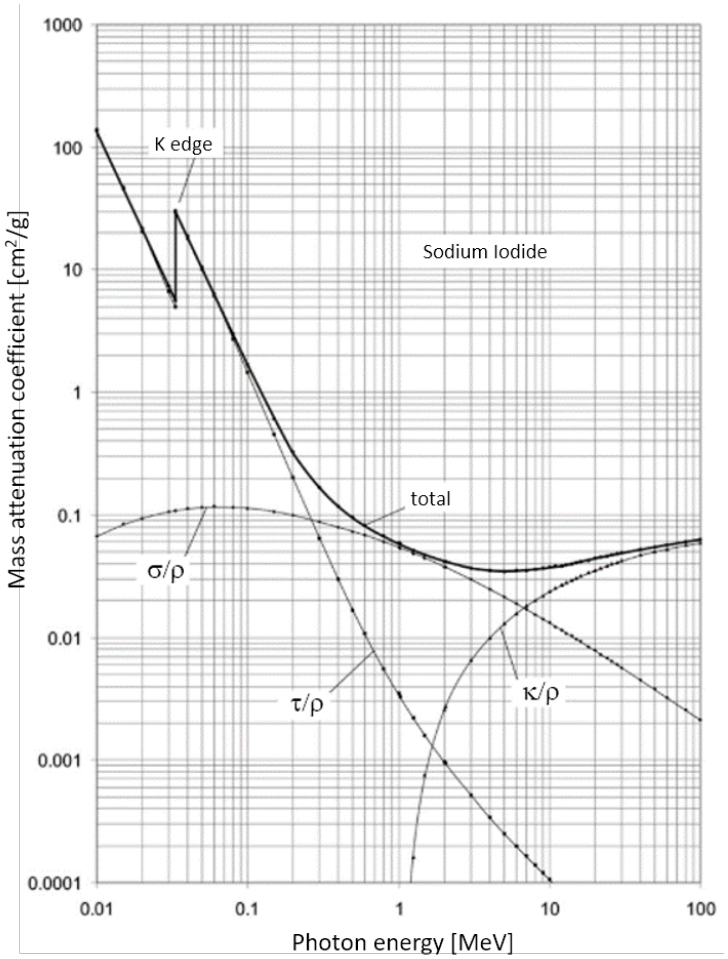

Figure 2.7: Energy dependence of the mass attenuation coefficient of NaI, showing contributions from photoelectric absorption, Compton scattering and pair production [159].

As it is visible from Fig. 2.7, photoelectric absorption dominates for low-energy gamma rays (up to several hundred keV), while pair production dominates for high-energy gamma rays (above 5-10 MeV), and Compton scattering is the most probable process in the range of energies between these two other phenomena.

This characteristic can be also observed in Fig. 2.8, in which the relative dominance of the three mentioned types of gamma-ray interaction is shown. They are represented as a function of the γ-ray energy $h\nu$ and of the atomic number Z of the absorbing material. The two solid lines separate the regions of the Z-$h\nu$ plane in which each phenomenon dominates over the other two. The line at the left represents the energy at which photoelectric absorption and Compton scattering are equally probable ($\sigma = \tau$), whereas the curve at the right represents the energy at which Compton scattering and pair production are equally probable ($\sigma = \kappa$) [141]. Three different areas are thus defined in this plot, and in each of them one of the three phenomena dominates.

This plot can be very useful when comparing different materials that are being taken into consideration for γ-ray detectors: for a given value of Z, the energy range in which a certain process is dominating can be defined and identified. In the plot in Fig. 2.8 the different colored dashed lines which were drawn indicate the atomic numbers of the detector materials which were chosen for the different Compton camera detector arrangement evaluated. Si (red line) and GAGG crystals (orange line) were used as scattering component of, respectively, a multi- and a mono-layer Compton camera. As materials for the absorber detector, $LaBr_3$(Ce) (blue line) and $CeBr_3$ (green line) were used.

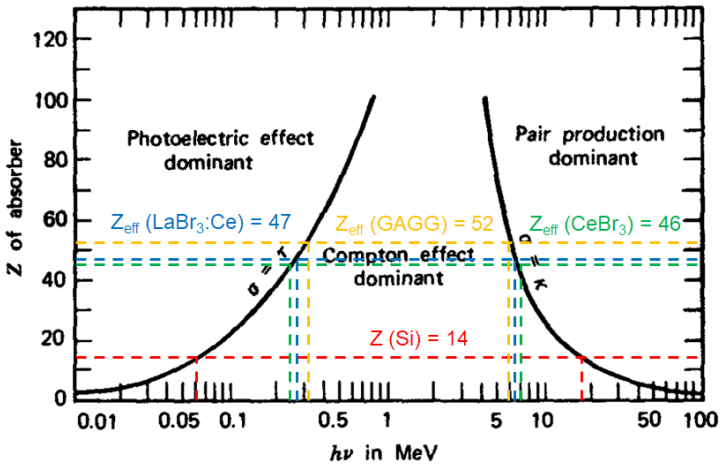

Figure 2.8: The relative importance of the three major types of gamma-ray - matter interaction. The lines show the values of Z and $h\nu$ (i.e. photon energy) for which the two neighboring effects are just equal [160].

Photoelectric effect The photoelectric effect (colloquially also photoeffect) is defined as an interaction between a photon and a tightly bound orbital electron of an absorber atom. In this kind of interaction the photon, if its energy exceeds the binding energy of the

electron, is completely absorbed and the orbital electron is ejected with E_K kinetic energy. The orbital electron that has been ejected is called *photoelectron* and its kinetic energy (E_e) is equal to the difference between the incident photon energy ($h\nu$) and the electron binding energy E_b

$$E_e = h\nu - E_b \tag{2.13}$$

Figure 2.9 is a schematical representation of a photoelectric interaction between a photon of energy hν and a K-shell atomic electron.

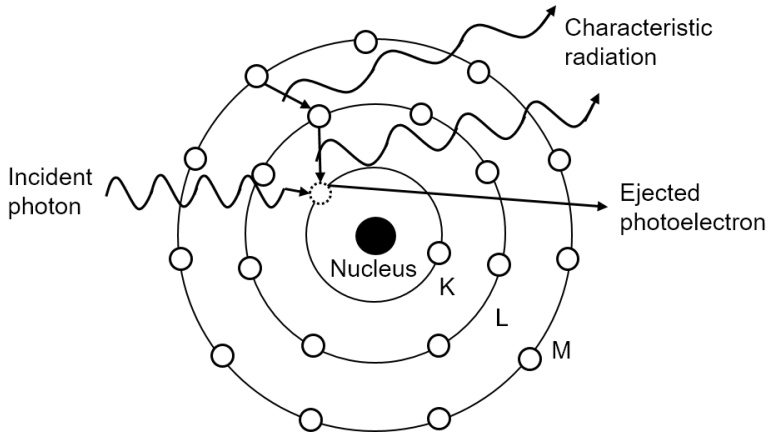

Figure 2.9: Schematic representation of the photoelectric process.

When the photoelectron is emitted, the vacancy that is created at its place is rapidly filled by an electron from a higher atomic shell: the energy of this transition is then released by either characteristic X-ray radiation or by an Auger electron. It is important to highlight that photoabsorption can not occur with free electrons because of the momentum conservation requirement.

The photoelectric process dominates at low incident photon energies, as it was shown in Fig. 2.7. Furthermore, the probability of the photoelectric effect strongly depends on the atomic number Z of the absorber material (the dependence can be seen in Fig. 2.8).

There is no analytic expression for the cross section τ of the photoelectric effect that is valid over all ranges of E and Z, but an approximation can be expressed as

$$\tau \simeq constant \cdot \frac{Z^n}{E_\gamma^{3.5}} \tag{2.14}$$

where n varies between 3 and 5, depending on the incident photon energy [142].

From the expression of Eq. (2.14) it can be stated that the higher the atomic number of the absorbing medium, the higher the probability to absorb the photon will be. It is also clear that the photoabsorption cross section decreases with increasing γ-ray energy E. These aspects are very important when a γ-ray detector is designed and its material is chosen.

Compton scattering Compton scattering is very important for our application, since it is the principle on which is based a Compton camera (that will be presented and described in Chap. 4).

In 1922, Arthur H. Compton observed a new interaction mechanism of photons with matter [161], which gained him the Nobel prize in physics in 1927. This kind of interaction was accordingly named *Compton interaction*.

This process describes an incoherent or inelastic interaction between an incident photon and an electron located in one of the outer shells of an absorber atom. Typically the electron is assumed to be at rest when the photon is impinging. From this interaction a recoil electron and a scattered γ-ray photon are generated, as it is shown in the sketch in Fig. 2.10.

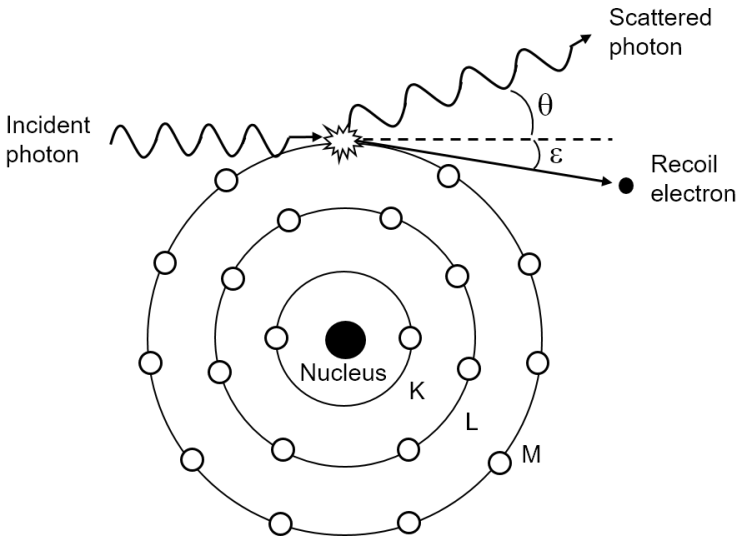

Figure 2.10: Schematic representation of the Compton scattering process.

The original energy of the incident gamma-ray photon is then divided between the components generated, depending on the scattering angle. The energy of the scattered gamma ray $h\nu'$ in terms of its scattering angle θ is given by

$$h\nu' = \frac{h\nu}{1 + (\frac{h\nu}{m_0c^2})(1 - cos\theta)} \tag{2.15}$$

where m_0c^2 is the rest mass energy of the electron (0.511 MeV). The kinetic energy of the recoil electron, calculated considering the energy conservation principle and rearranging Eq. (2.15), is therefore

$$E_e = h\nu - h\nu' = h\nu(\frac{(h\nu/m_0c^2)(1 - cos\theta)}{1 + (h\nu/m_0c^2)(1 - cos\theta)} \tag{2.16}$$

in which the electron binding energy has been neglected since it is very small compared to the photon and electron kinetic energies.

The photon Compton scattering angle θ can vary from 0° (forward scattering) to 90° (side scattering) up to 180° (back scattering), therefore, given a defined incident photon initial energy, the energy of the recoil electron is varying.

From Eq. (2.16) the minimum energy transfer to the Compton electron ($h\nu' \simeq h\nu$) is defined at $\theta \cong 0°$, meaning that the incident photon in this case is only negligibly deflected by the electron. On the other hand, when the scattered photon is back scattered ($\theta = 180°$) the maximum energy, equal to

$$(E_e)_{max} = h\nu\left(\frac{2\frac{h\nu}{m_e c^2}}{1+2\frac{h\nu}{m_e c^2}}\right) \tag{2.17}$$

is transferred to the recoil Compton electron.

The Compton scattering kinematics was calculated for an incident photon initial energy of 3 MeV and 6 MeV, respectively, as shown in Fig. 2.11(a) and 2.11(b). From the comparison depicted in Fig. 2.11 it can observed that at a fixed scattering angle with increasing initial energy of the photon the energy transferred to the recoil Compton electron is also increasing.

These considerations, based on the *Compton formula* in Eq. (2.15), are essential for the Compton camera system that will be presented in the next chapters.

The probability of Compton scattering per atom of the absorber depends on the number of electrons available as scattering targets and therefore increases linearly with Z [141]. The dependence on the gamma-ray energy was already illustrated in Fig. 2.8 for the case of NaI as target material.

The angular distribution of scattered gamma-rays is predicted by the *Klein-Nishina formula* [163] for the differential scattering cross section $d\sigma/d\Omega$

$$\frac{d\sigma}{d\Omega} = Zr_0^2\left(\frac{1}{1+\alpha(1-\cos\theta)}\right)^2\left(\frac{1+\cos\theta^2}{2}\right)\left(1+\frac{\alpha^2(1-\cos\theta)^2}{(1+\cos\theta^2)[1+\alpha(1-\cos\theta)]}\right) \tag{2.18}$$

where Z is the target material's atomic number, $\alpha = h\nu/m_e c^2$ and r_0 is the classical electron radius (=2.82 fm [142]). This equation is derived from the interaction between an incident photon and a free electron.

In Fig. 2.12 a polar plot of the number of photons that are Compton scattered at a given θ angle is shown, considering a unitary solid angle. The angular distribution is shown for initial photon energies of 0.1 MeV, 1 MeV and 10 MeV, respectively. At smaller photon energies the scattering angle becomes larger, leading also to a higher energy transfer to the recoil Compton electron, as deduced from Eq. (2.16). On the other hand, for higher incident photon energies, forward scattering is more pronounced and the photon is barely interacting with the electron.

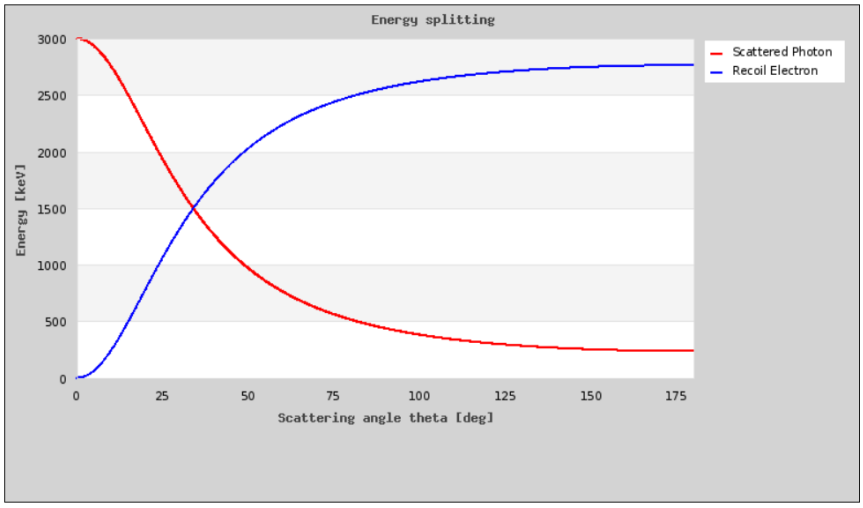

(a)

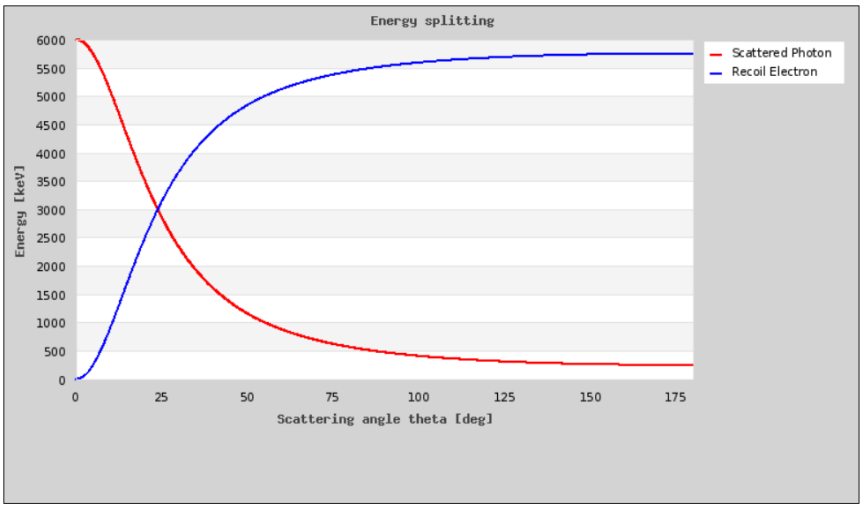

(b)

Figure 2.11: Compton scattering kinematics of 3 MeV (a) and 6 MeV (b) incident photon energy [162].

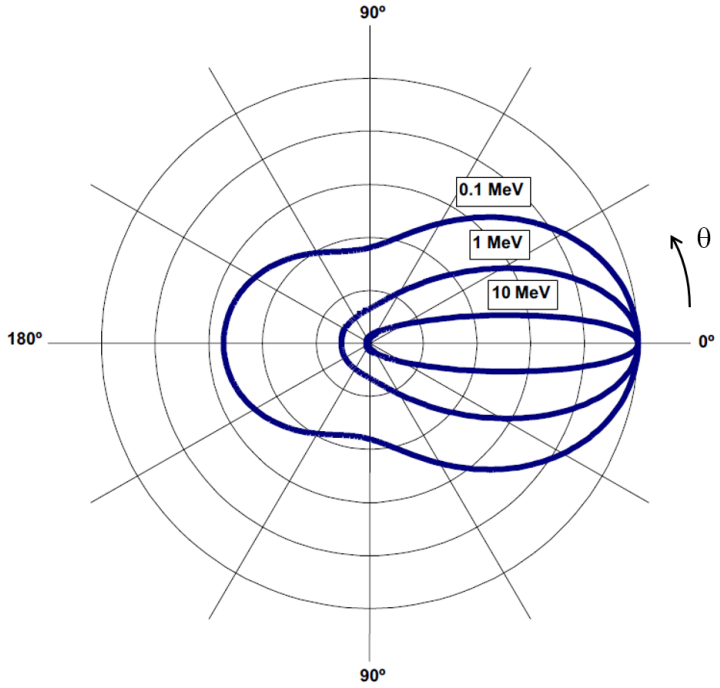

Figure 2.12: A polar plot of the number of photons (incident from the left) Compton scattered by a scattering angle θ. The curves are shown for the indicated initial energies.

Doppler effect in Compton scattering In a realistic scenario, when the Compton interaction happens in the detector material, the electron of interest is neither free nor at rest. J. DuMond in 1929 [164] experimentally observed a broadening in measured Compton spectra: this was due to the motional distribution of the electrons of the target. This effect was interpreted by him as a *Doppler broadening effect*. As all possible interaction angles should be considered when evaluating the consequence of this effect, the cross section of the Compton scattering has to take into account the momentum distribution of the bound electron. In 1975 Ribberfors included this effect and derived the following expression [165]

$$\left(\frac{d\sigma}{d\Omega}\right)_{bound,i} = \left(\frac{d\sigma}{d\Omega}\right)_{unbound,i} S_i(E_i, \theta, Z) \tag{2.19}$$

where S_i is the incoherent scattering function of the i-th shell electron, E_i is the incident photon energy, θ the Compton scattering angle and Z the atomic number of the target material. The first term of Eq. (2.19) represents the Klein-Nishina differential cross section (see Eq. (2.18)), which is derived for a free electron.

In the context of this tesis, the effect of the Doppler broadening should be considered for the detector components of the Compton camera system, in particular for the scatter component. The scatter detectors are silicon detectors (they will be introduced in Chap. 3 and described in more details in Chap. 4). As it is visible from Fig. 2.13, there is a slight deviation between the Compton scattering probability in silicon from bound and unbound electrons at low incident photon energies. In Fig. 2.14 the Compton scattering cross section

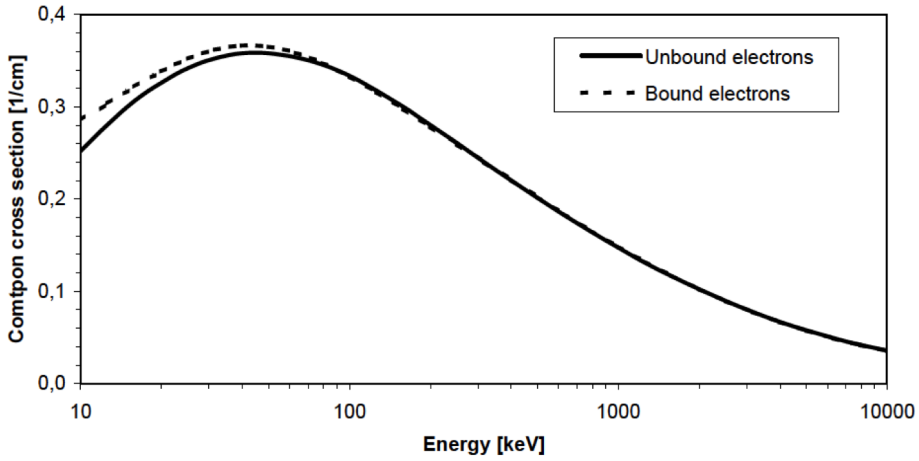

Figure 2.13: Compton scattering cross section for bound (dashed line) and unbound (solid line) electrons in silicon as a function of the initial photon energy. The probability of Compton scattering with bound electrons is slightly higher than the one predicted by the Klein-Nishina formula for low photon energies below 100 keV, while for higher energies the impact of the bound electrons is negligible and both models show an identical prediction of the cross section [166].

as a function of the scattering angle can be observed: for a bound electron, the interaction probability is slightly lower at small and large scattering angles, whereas between 40° and 130° the probability is higher than the one for free electrons. In our case, for a Compton camera system aiming at detecting prompt-gamma rays that are generated during hadron therapy, the energy of the photons is mainly between 3 and 6 MeV. Therefore, also the Compton electrons produced will have an energy higher than the energy range where the Doppler effect is relevant: in our case this effect can be neglected.

Pair production The third major gamma-ray - matter interaction process is pair production. This process takes place in the intense electric field near the nuclei of the absorbing material and it can occur when the incident photon energy exceeds $2m_ec^2 = 1.022$ MeV, with m_ec^2 being the rest energy of electron and positron.

If the incident gamma-ray energy exceeds this value, the energy of the incident gamma-ray minus $1.022MeV$ will be the excess energy that appears in the form of kinetic energy shared by the electron-positron pair. Thus it can be said that this process consists of converting the incident gamma-ray photon, that will undergo a complete absorption by the absorbing atom, into electron and positron kinetic energies, according to

$$E_{e^-} + E_{e^+} = h\nu - 2m_0c^2 \tag{2.20}$$

The pair production process is complicated by the fact that the positron is not a long-lived particle; once its kinetic energy becomes very low (i.e. after thermalization by

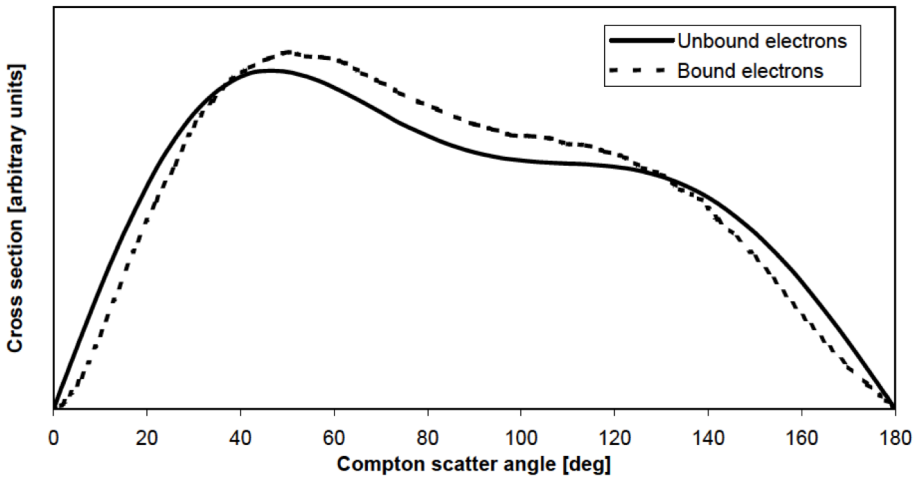

Figure 2.14: Evaluation of the angular dependence of the Compton scattering cross section for bound and unbound electrons at a fixed incident photon energy of 100 keV. At small and large scattering angles, the probability of the Compton scattering from bound electrons case is slightly suppressed [166].

collision), the positron will annihilate with a (bound) electron in the absorbing medium. Then they both disappear and are replaced by two annihilation photons of energy m_0c^2 (0.511 MeV) each. The time the positron needs to slown down and annihilate is small, so that the annihilation radiation appears in virtual coincidence with the original pair production interaction.

A schematic representation of the pair production process is depicted in Fig. 2.15.

The relative dominance of the pair production and dependence on the atomic charge Z of the absorber material can be observed in Fig. 2.8: the threshold at 1.022 MeV for the occurance of this process is clearly visible. It is also visible that the γ ray energy should exceed $\sim$ 6 MeV for this process to become dominant over the other two. For even higher photon energies, the pair creation probability is further increasing with energy, according to the (approximate) expression of its cross section:

$$\kappa \simeq Z^2 \cdot lnE_\gamma \tag{2.21}$$

2.1.2.2 Neutron interaction

Like photons, also neutrons carry no electric charge. Therefore they can approach the atomic constituents without direct interference with the Coulomb field. However, in contrast to photons that interact with orbital electrons as well, neutrons are mostly interacting with the atomic nucleus. They are depositing energy in the absorbing material through a two-step process: (1) the energy is transferred to protons or heavier nuclei and (2) these secondary products deposit their energy in the absorber through Coulomb interactions with atoms of the absorber.

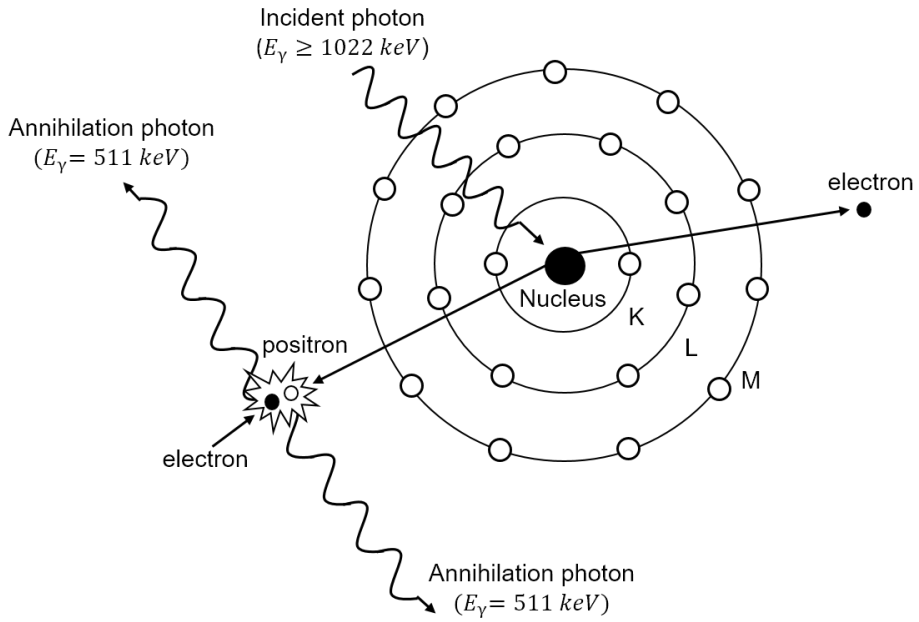

Figure 2.15: Schematic representation of the pair production process.

In terms of their kinetic energy E_K, neutrons are ordered into several categories:

- *Ultracold neutrons*: $E_K < 2 \cdot 10^{-7} eV$
- *Very cold neutrons*: $2 \cdot 10^{-7} eV < E_K < 5 \cdot 10^{-5} eV$
- *Cold neutrons*: $5 \cdot 10^{-5} eV < E_K < 0.025 eV$
- ***Thermal neutrons***: $E_K \approx 0.025 eV$
- ***Epithermal neutrons***: $1 eV < E_K < 1 keV$
- ***Intermediate neutrons***: $1 keV < E_K < 0.1 MeV$
- ***Fast neutrons***: $E_K > 0.1 MeV$

The energy range of interest for medical physics starts from the thermal neutrons energy range to higher energies; these neutrons are therefore used in medicine. Neutrons with an energy equal or higher than the energy of the thermal neutrons are Of all these listed categories, only thermal, epithermal and fast neutrons are in an energy range of interest for medical physics and are therefore used in medicine.

As neutrons pass through matter, they undergo elastic or inelastic scattering and they may as well trigger nuclear reactions such as neutron capture, spallation and fission.

In an **elastic scattering** process (schematically shown in Fig. 2.16) a neutron of mass m_n and velocity v_n collides with a nucleus of mass m_2 and velocity v_2.

The total momentum and energy are conserved. The target nucleus recoils with an angle ϕ with respect to the neutron initial direction of motion and the neutron flight path

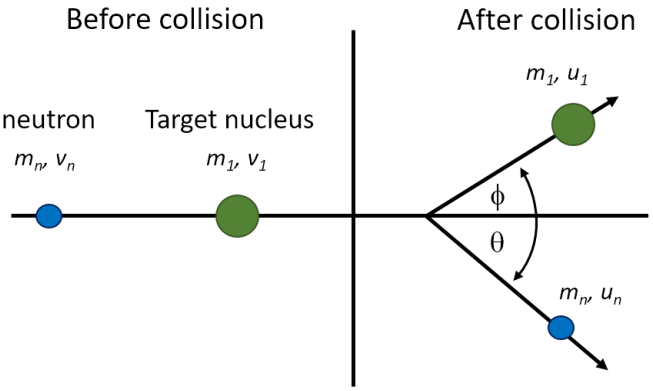

Figure 2.16: Schematic diagram of an elastic collision between a projectile with mass m_n and velocity v_n striking a stationary target m_1. The projectile is scattered with a scattering angle θ; the target recoils with a recoil angle ϕ. After the collision the velocity of the projectile m_n is u_n; the velocity of the target m_1 is u_1.

changes by an angle θ with respect to the initial neutron path direction, resulting in an energy transfer to the recoiling nucleus.

For a neutron of mass m_n and initial energy $(E_K)_i$, the kinetic energy ΔE_K transferred to the nucleus is in general given by

$$\Delta E_K = (E_K)_i \frac{4 m_n m_2}{(m_n + m_2)^2} \cos^2 \phi \tag{2.22}$$

where the parameters refer to the sketch in Fig. 2.16. From Eq. (2.22) it can be inferred that the neutron energy transfer strongly depends on the interaction angle. For example, when the scattering angle is equal to 0, the maximum energy of the incident neutron is transferred to the recoil nucleus. In general, the transfer of energy to the target nucleus is less efficient when $E_K << E_1$; when $E_K \approx E_1$ the neutron is transferring on average one half of its initial kinetic energy to the target nucleus and the maximum energy transferred is equal to the initial neutron energy. In this case the energy transfer to the medium is rapidly happening via the secondary particle generated: this has implications for shielding against neutron radiation in high-energy linear accelerator installations, where low atomic number materials are used in neutron barriers for shielding against neutrons produced by high-energy photons.

An **inelastic scattering** process is, on the other hand, governed by the following relation

$$n + {}^A_Z X \rightarrow {}^{A+1}_Z X^* \rightarrow {}^A_Z X^* + n' \Rightarrow {}^A_Z X^* \rightarrow {}^A_Z X + \gamma \tag{2.23}$$

where ${}^A_Z X$ is the stable target nucleus, ${}^{A+1}_Z X^*$ is an unstable compound nucleus and ${}^A_Z X^*$ is an excited target nucleus.

The neutron n is first captured by the target nucleus and then re-emitted as neutron n$'$, having a lower energy and a different direction. The nucleus is left in an excited state and is then de-exciting by the emission of high-energy γ rays [142].

Neutron capture describes a nuclear reaction in which a thermal neutron bombards a nucleus leading to the emission of a proton or γ ray: compared to the inelastic scattering process, in this case there is no neutron emission as secondary product since the n projectile is absorbed into the target nucleus. $^{14}N(n,p)^{14}C$ is an example of this kind of reaction. Extremely good n absorbing elements are B and Gd, which are, respectively, used as control rods in reactors and shielding material. It should also be mentioned that neutron capture cross sections are strongly energy dependent: $\sigma \sim 1/E_k$. Thermal neutrons are most efficient in reactors and therefore moderation is needed.

The **spallation** reaction consists of a fragmentation of the target into different and smaller components, such as particles and nucleons, resulted from an impact or stress event. An example of spallation is the following: $^{16}_{8}O + n \rightarrow 3\alpha + 2p + 3n$

Thermal or fast neutrons can also induce **nuclear fission reactions** with high-Z nuclei. The target nucleus is then fragmenting into two daughter nuclei of lighter mass. The fission process is also accompanied with the production of several fast neutrons and this can lead to further nuclear reactions, with the result of a self sustained nuclear chain reaction and a substantial release of energy. Controlled chain reactions are used in nuclear reactors for research purposes as well as for power generation. Three fissile nuclides are used in nuclear reactors: one is the naturally occurring ^{235}U and the other two are the artificially produced ^{233}U and ^{239}Pu (which is produced from a nuclear reaction from ^{238}U).

The total microscopic neutron cross section Σ_{tot} of all reactions, defined as the total cross section σ_{tot} multiplied by the number of nuclei per unit volume, can be expressed as follows [141]

$$\Sigma_{tot} = \Sigma_{scatter} + \Sigma_{rad.capture} + \cdots \tag{2.24}$$

The distance between two subsequent interactions is called *mean free path* and it is expressed by $\lambda = \frac{1}{\Sigma}$. This quantity is of the order of centimeters or less for slow neutrons, and tens of centimeters for fast neutrons.

CHAPTER 3

Detector technology

This chapter is dedicated to the detector technology relevant for the project of the LMU Compton camera prototype. The structure and operational principles of devices able to detect γ-ray and electron radiation will be described. The physics concepts explained in the previous chapter are exploited as a basis to understand what will be presented in the following sections.

3.1 Semiconductor detectors

This section reviews the basic concepts of semiconductor physics and related detector technology. As their name suggests, semiconductor materials have a conductivity that lies between the one of electrically conductive materials, like copper, and insulating materials, like glass. This characteristics can be observed in Fig. 3.1, where the electrical conductivity and resistivity for insulators, semiconductors and conductors is plotted.

In general there are two kinds of semiconductors: single-element semiconductors, such as germanium and silicon, which are in group IV of the periodic table; and compound semiconductors, such as gallium-arsenide, which are formed by combining elements from groups III and V or groups II and VI [168]. We will focus on the description of silicon, as it is the material from which the scatter detectors are made, which are used in the LMU Compton camera prototype.

3.1.1 Atomic and crystal structure

The electronic properties of semiconductor devices can be understood in the framework of quantum mechanics, since an electron is a quantum-mechanical particle. In order to

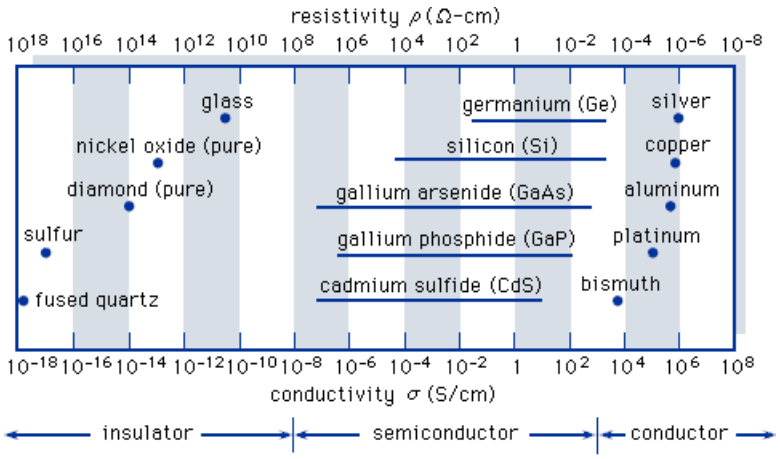

Figure 3.1: Typical range of electrical conductivity and resistivity for insulators, semiconductors and conductors [167].

understand the crystal structure of silicon, first the electronic states of isolated atoms are discussed.

From Bohr's atomic model [169], an atom consists of a nucleus of charge +Ze and mass M and one or more electrons of charge -e and mass m, that are attracted by a force F to the nucleus.

In this simplistic approach, the electron(s) is/are assumed to revolve in a circular orbit around the nucleus. If the mass of the electron is considered negligible compared to the mass of the nucleus, the electron orbit is expressed by:

$$\frac{1}{4\pi\epsilon}\frac{Ze^2}{r^2} = m\frac{v^2}{r} \tag{3.1}$$

where v is the speed of the electron in its orbit and r is the radius of the orbit.

The orbital angular momentum must be a constant (L=mvr), because the force acting on the electron is directed in the radial direction. By this condition and by applying the quantization condition on the momentum (mvr=n$\hbar$), the total energy (E=E_{kin}+E_{pot}, where E_{kin} is the kinetic energy and E_{pot} is the potential energy) of an orbital electron can be expressed as follows:

$$E = -\frac{mZ^2e^4}{(4\pi\epsilon_0)^2 2\hbar^2}\frac{1}{n^2} \qquad n = 1, 2, 3, \cdots \tag{3.2}$$

The quantized energy levels in Bohr's model are based on the concept of quantization of the energy postulated by Planck. Since the state of lowest total energy is the most stable state for the electron, the normal state of the electron in a one-electron atom is the state for which n=1. The integer n is called the *principal quantum number*. To label every atomic orbital and every electron in the orbitals, four quantum numbers are defined.

$\boldsymbol{n}$ is the principal quantum number. It gives the energy, size, shell and row of the orbital. It must be a positive integer and it can also be labeled as K, L, M, N, $\cdots$. $\boldsymbol{l}$ is the

angular momentum quantum number. It is related to the spatial probability distribution of the electron and therefore it provides the shape of the orbital. It is restricted by n: l = 0, 1, 2,$\cdots$, n-1 and it is classified, respectively, as *s*, *p*, *d*, *f*, $\cdots$ For a certain angular momentum quantum number, a maximum number of electrons can be stored in the orbital: 2, 6, 10 ,14, $\cdots$ for l = 0, 1, 2, 3, $\cdots$, respectively. $\boldsymbol{m}_l$ is the magnetic quantum number in the presence of an external magnetic field, defining a quantization axis. It specifies an orbital, gives orientation and direction of the orbital. It is restricted by l: m_l = -l, $\cdots$,0, $\cdots$, +l (or, m_l = 0, $\pm$1, $\pm$2, $\cdots$, $\pm$l). $\boldsymbol{m}_s$ is the spin orientation quantum number. It describes the non classical orientation of the electron spin, *up* or *down*. m_s can be +1/2 or -1/2.

With 3 quantum numbers (n, l, m_l) every *atomic orbital* can be labeled. With all 4 quantum numbers, a unique label to every electron in every atom can be given (since any electron orbital can only be filledd with max. two electrons, different in their spin orientation - Pauli exclusion principle [169]).

In order to determine the electronic configuration of an atom, the *Aufbau principle* is used and the maximum number of electrons in one orbital is constrained by the *Pauli principle*. If more orbitals with the same energy are available, the *Hund rule* says that the free orbitals will be filled (each with one electron and parallel spin) before partially filled orbitals will be completely filled (by electrons with antiparallel spin). In order to determine the order in which the electron orbitals are filled, the *n+l* rule, also called *Madelung rule*, is used [169].

The **silicon atom** is neutral and has 14 positively charged protons in its nucleus and 14 negatively charged electrons surrounding the nucleus (atomic number Z=14). As it can be observed from the scheme in Fig. 3.2, the silicon atom has ten of its electrons in the (filled) two inner shells (K, L: first and second) and four in its outer shell.

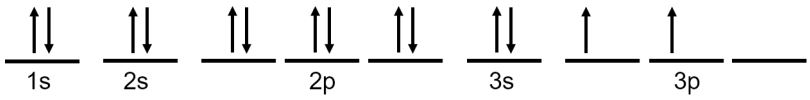

Figure 3.2: Electronic configuration of silicon.

The nucleus (Z=14) and the 10 (core) electrons together are considered the silicon ion core, with a net charge of +4e. The remaining four electrons of Si, located in the M shell, occupy the 3s orbitals (2x) and the 3p orbitals (2x). These four electrons are called the valence electrons. Their orbitals are spread out in a spatial configuration determined by the attractive Coulomb force between the Si^{4+} ion core charge and the four negatively charged electrons. Each orbital is described by a wave function ψ, indicating the position probability distribution of an electron. The valence electrons and the spatial distribution of the core electrons around the positive nuclear charge determine the properties of an atom as well as of a crystal formed by the atoms [170]. In Fig. 3.3 the atomic structure of silicon, with its ion core and its electron orbitals, is depicted.

A silicon atom requires other four electrons to complete its outermost shell, thus Si is

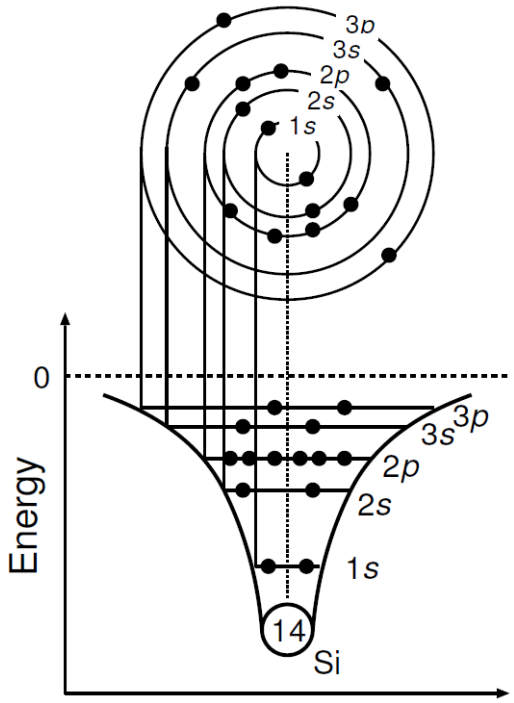

Figure 3.3: Atomic structure of silicon[170].

considered a 4-valent atom. This can be achieved by sharing one of its valence electrons with each of four neighboring atoms in case of a regular structure formed solely from Si atoms. Each pair of shared electrons forms a covalent bond. The result is that a crystal of pure or intrinsic silicon has a regular lattice structure, where the atoms are held in their position by the covalent bonds. Figure 3.4 shows a two-dimensional representation of such a structure [168].

The electron configuration explained above is valid only for a spatially isolated many-electron atom. A semiconductor crystal possesses about 10^{23} atoms per cubic centimeter and the atoms are closely spaced. Therefore, we have to consider the effects of the nearby atoms or their electrons and ion cores.

The position probability of an atomic electron is known as the electronic wave function, which is the solution of the Schrödinger equation for an electron in a central or 1/r Coulomb potential. The simplest configuration in the 1s orbital, considering two atoms, can be used to describe the many-body effects. Their two position probabilities are denoted by ψ_1 and ψ_2 referring on atom 1 and 2, respectively. The amplitude of the square of the wavefunction is the probability of finding the electron in the 3-dimensional space point (x,y,z) at the time t: $P_1(x,y,z,t) = |\psi_1|^2$. When the two isolated atoms come close, the two atomic wavefunctions overlap: they can then be represented by two other wavefunctions, which are known as the bonding and antibonding orbitals, which are linear combinations of the two atomic orbitals. They are known as molecular orbitals or *hybrid orbitals*. The simple picture of a diatomic molecule consisting of two one-electron atoms can be extended to

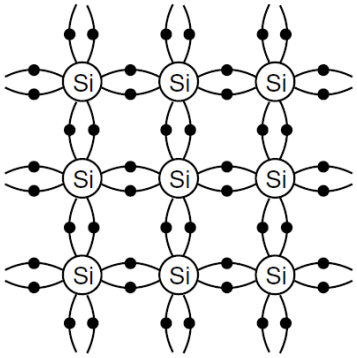

Figure 3.4: Two-dimensional representation of the silicon crystal. The circles represent the inner core of silicon atoms that has a positive charge of +4e, which is neutralized by the charge of the four valence electrons, which are forming covalent bonds with electrons of neighboring atoms [170].

explain the electrical properties of a silicon semiconductor crystal consisting of many silicon ion cores, each with four valence electrons in $(3s)^2$ and $(3p)^2$ configurations. The key point is the symmetry, determined by the spatial distribution of the Si^{4+} core charge: the electron distribution in the silicon crystal exhibits a tetrahedron symmetry. Therefore, with the four valence electrons in silicon crystal, there are four hybrid atomic orbital combinations from the four atomic orbitals, 3s, $3p_x$, $3p_y$, and $3p_z$, whose schematic wavefunctions are shown in Fig. 3.5 [170].

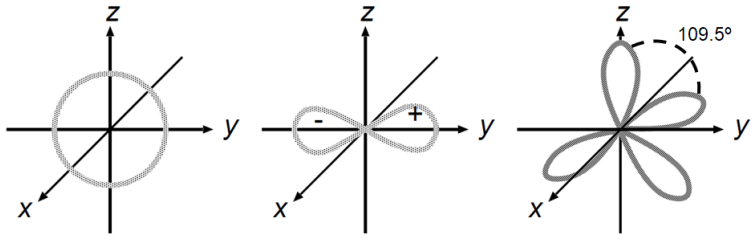

(a) s orbital (b) p_y orbital (c) sp^3 hybrid orbital

Figure 3.5: Schematic of wavefunctions of (a) s, (b) p_y and (c) sp^3 hybrid orbitals [170]. The binding angle of 109.5° for the sp^3 configuration is indicated.

When the complete crystal structure is built, the set of bonding orbitals forms groups of energetic states called the valence band(s), and the set of antibonding orbitals forms another group of energetic states called the conduction band.

3.1.2 Intrinsic semiconductors and band gap

As already mentioned in Sect. 3.1.1, when silicon material is exhibiting only instrinsic conductivity it shows a regular lattice structure (like in Fig. 3.4). Furthermore, at 0 K,

all bonds are active and no free electron is available for current conduction: at such low temperatures the intrinsic silicon crystal behaves as an insulator.

At room temperature, when sufficient thermal energy is available, some of the covalent bonds can be broken: this process is called *thermal generation*. When a covalent bond is broken, an electron becomes free: the electron leaving a specific atom creates, in its parent atom, a net positive charge (i.e. a hole), equal to the magnitude of the electron charge. Thus, another electron from another atom could be attracted: this will neutralize the hole previously created. The effective result of this process, that may occur repetitively, is a charge carrier moving through the silicon crystal structure, equivalent to electric current conductivity. This current, in silicon detectors, is part of the so called ***dark current***, because it is generated without the presence of an external source of signal, and it is therefore an undesired source of noise. As the temperature increases, more covalent bonds are broken and electron−hole pairs are generated. The increase in the numbers of free electrons and holes results in an increase in the conductivity of silicon.

When an electrical field is applied as well, the electrons and the holes are attracted to the oppositely charged electrodes, generating a *drift current*. The relation between the *drift velocity* and the electrical field can be defined as follows

$$\vec{\nu}_e = \mu_e \vec{E} \tag{3.3}$$

$$\vec{\nu}_h = \mu_h \vec{E} \tag{3.4}$$

where ν_e and ν_h are the drift velocities of the electron and hole, respectively, and μ_e and μ_h their mobilities. μ_e and μ_h are material-dependent values, and this is thus affecting the charge carrier drift velocity. It should be noted that the mobility of an electron is higher than the one of a hole. For example, in Si the mobility is 1350 $V/cm \cdot s^2$ for electrons and 450 $V/cm \cdot s^2$ for holes [171].

In intrinsic silicon, the electron and hole concentration, which refers to the number of charge carriers per unit volume, is equal. In the absence of an external electrical field, electrons may fill holes in the process of *recombination*. In thermal equilibrium, the recombination rate is equal to the generation rate, allowing to conclude that the concentration of the free electrons n is equal to the concentration of holes p

$$n = p = n_i \tag{3.5}$$

where all the variables represent charge carrier densities expressed in units of number / unit volume [cm^3].

n_i is the number of free electrons and holes in a unit volume (cm^3) of intrinsic silicon at a given temperature and is defined as

$$n_i = BT^{3/2} e^{-E_g/2kT} \tag{3.6}$$

where B is a parameter that depends on the material (7.3 x $10^{15} cm^{-3} K^{-3/2}$ for silicon), k is Boltzmann's constant (8.62 x 10^{-5} eV/K) and E_g is the ***band−gap energy***. The energy gap between the valence and the conduction band is equal to 1.12 eV for silicon

and it should be noted that the an energy quantity of $\sim 2.5 \times E_g$ is needed to create an e/h pair in silicon. The maximum energy level occupied by the charge carriers inside a semiconductor is defined as *Fermi energy*. In an intrinsic semiconductor, the Fermi energy is called *intrinsic level* (E_i).

From Eq. (3.6) it can be stated that the smaller the band−gap energy for a given material is, the higher will be the chance of a thermal excitation: therefore detectors from semiconductor materials like germanium, allowing a band−gap of $E_g = 0.67$ eV, need to be cooled during operation in order to reduce the dark current that would otherwise be generated as a source of unwanted noise. To substantially increase the electrical conductivity and operate a semiconductor detector, the concept of n- or p-doping is essential and will be introduced in Sect. 3.1.3.

In Fig. 3.6 a simple sketch of the energy band diagram in solids is depicted for a semiconductor ((a), here: Si), an insulator ((b), here: SiO_2) and (c) a conductor. E_g is the band−gap energy, E_c is the (lower edge) energy of the conduction band (where the freely movable electrons available for electrical conductivity are located) and E_v is the energy of the valence band (which is the energetically highest fully filled band). It is obvious that semiconductors, in general with a band−gap energy in the range around 0.7 eV to 3 eV, show a band configuration inbetween the conductor and the insulator energy configurations.

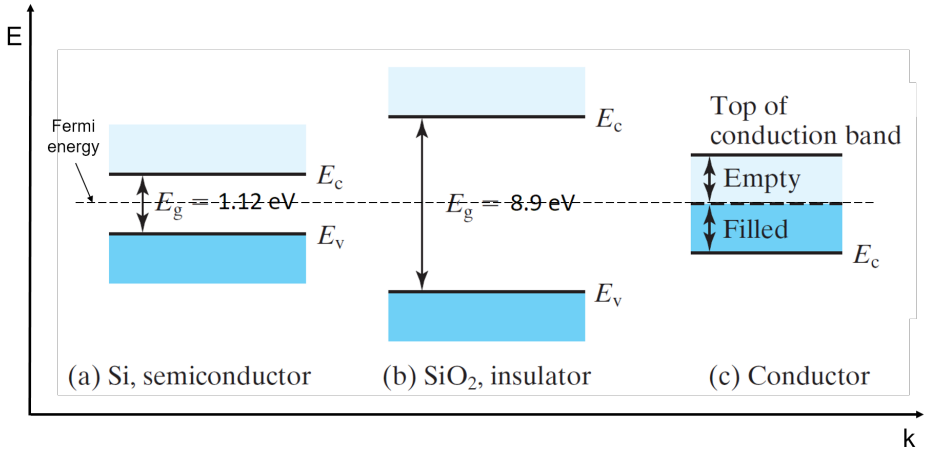

Figure 3.6: Simplified energy band diagram of a semiconductor (a), compared to the one of an insulator (b) and a conductor (c) [172]. k is the wave vector ($= 2\pi/\lambda$).

In real semiconductors, the band structure is more complex than the flat-band model suggested by Fig. 3.6. The energy of the valence and conduction bands varies depending on the momentum of the charge carriers and two types of semiconductor materials can be distinguished: *direct* and *indirect* semiconductors [173]. Silicon is an indirect semiconductor: the maximum of the valence band and minimum of the conduction band do not coincide for the same momentum value ($p = \hbar \cdot \kappa$). This means that for an electron to be promoted to the conduction band, a phonon must also be created to conserve momentum.

3.1.3 p-n doping

As mentioned in the previous section, the electrical conductivity of a semiconductor can be controlled by introducing specific impurities into the intrinsic semiconductor material, with concentrations in the range of $10^{12} - 10^{18} cm^{-3}$. If we consider silicon as the semiconductor material to be doped, elements of group 3 and group 5 have to be considered.

When considering a group 3 atom being inserted into a lattice site, like for boron in Fig. 3.7(a), bonds for all Si valence electrons are provided, but one covalent bond can't be formed because one electron is missing. An electron is then borrowed from a lattice atom nearby and for this reason the atom of group 3 is called *acceptor*. The borrowed electrons are missing from the valence band and form holes, which behave as an electron in the conduction band, i.e. they can move freely in the silicon crystal (although in opposite direction). As these charge carriers are positevely charged, the doped region of Si is called ***p-type***.

On the other hand, when considering a group 5 atom introduced into a Si lattice site, like phosphorus in Fig. 3.7(b), the situation is opposite to the p-type doping. All four covalent bonds can be formed for the Si atoms, leaving one valence electron of the dopant atom in excess. These electrons, being the reason for which this atom is called *donor*, become easily mobile charged particles in the conduction band. As these are negative charge carriers, the doped region of Si is called ***n-type*** in this case.

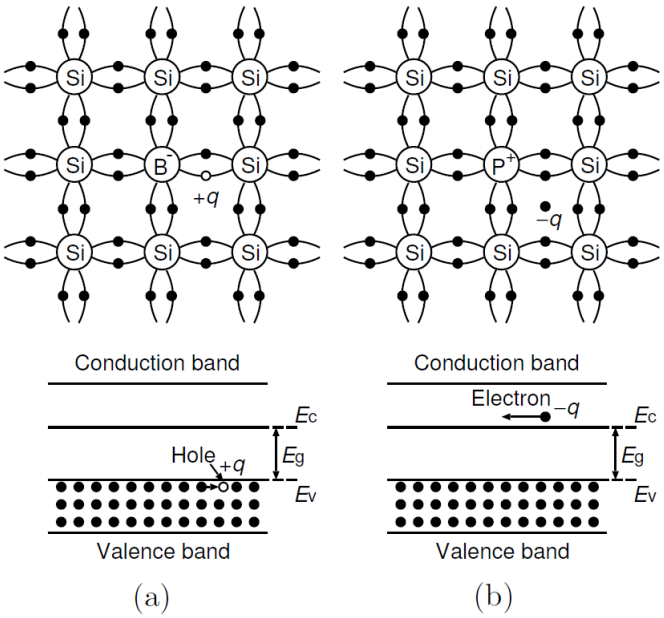

Figure 3.7: (a) a silicon crystal is doped with boron, which is a trivalent element; each dopant atom gives rise to a hole in the valence band, and the semiconductor becomes p-type. (b) a silicon crystal is doped with phosphorus, which is a pentavalent element; each dopant atom donates a free electron into the conduction band and is thus called a donor. The doped semiconductor becomes n-type [170].

pn junction

The p-n junction is the basic concept essential to understand the working principle of silicon detectors. It is formed by a p-type Si in contact with an n-type Si material. When a junction of p- and n-type semiconductors is formed, both electrons from the n-region and holes from the p-region diffuse across the junction into the other region, due to their concentration gradient. Due to this diffusion, electron and hole concentrations next to the p-n junction are reduced below their equilibrium: this creates a fixed positively charged region on the n-side and a fixed negatively charge region on the p-side. This region with fixed charges, which is void of free charge carriers, is called ***depletion region*** and creates an electric field oriented such that it prevents further diffusion of the mobile charges: the situation at thermal equilibrium is shown in Fig. 3.8, with N_A and N_D being the acceptor and donor impurities concentrations, respectively, W_{D_p} and W_{D_n} are the spatial boundaries of the region of fixed charges in p- and n-region ("depletion zone"), respectively, $\mathcal{E}$ is the electric field that is generated, and Ψ_{bi} is the built-in potential. The extension of this depletion region in each of the two doped regions depends on the doping concentration in the p- and n-region.

Since we are considering a situation in thermal equilibrium, with no external electric field being applied, the Fermi level E_F is constant. The energy bands E_V, E_C, E_i are bent due to the built-in potential created by the diffusion across the p-n junction.

3.1.4 Silicon detectors

The p-n junction described in the previous section is the basic concept needed to understand the working principle of a silicon detector. The incoming radiation has to be detected in the depleted region, where electron-hole pairs can be created and lateron attracted by the electrodes.

This means that for operating a detector, the depleted region should be extended as much as possible, until having a *fully depleted region*, to be able to detect all the incoming radiation without distorsion by intrinsic mobile charge carriers. In order to modify the depletion region, an external voltage has to be applied between the two electrodes of a p-n junction: the two possible cases are presented in Fig. 3.9. If a positive voltage is applied to the n-side (or a negative voltage is applied to the p-side) it is referred to as *reverse bias*, the opposite case is referred to as *forward bias*.

The built-in potential Ψ_{bi} is developed by the p-n junction itself, as previously presented, and it is a barrier voltage that renders the n-side more positive than the p-side (and limits the diffusion current to a value exactly equal to the drift current).

When applying a reverse bias to the junction (Fig. 3.9(a)), it adds to the barrier voltage and the potential difference between p- and n-side increases. This reduces the number of holes that diffuse into the n region and the number of electrons that diffuse into the p region, with the result that the diffusion current I_D is dramatically reduced and the drift current I_S dominates. As a consequence also the width of the depletion region increases: this is the scenario to operate a semiconductor detector, in particular applying a V_R large

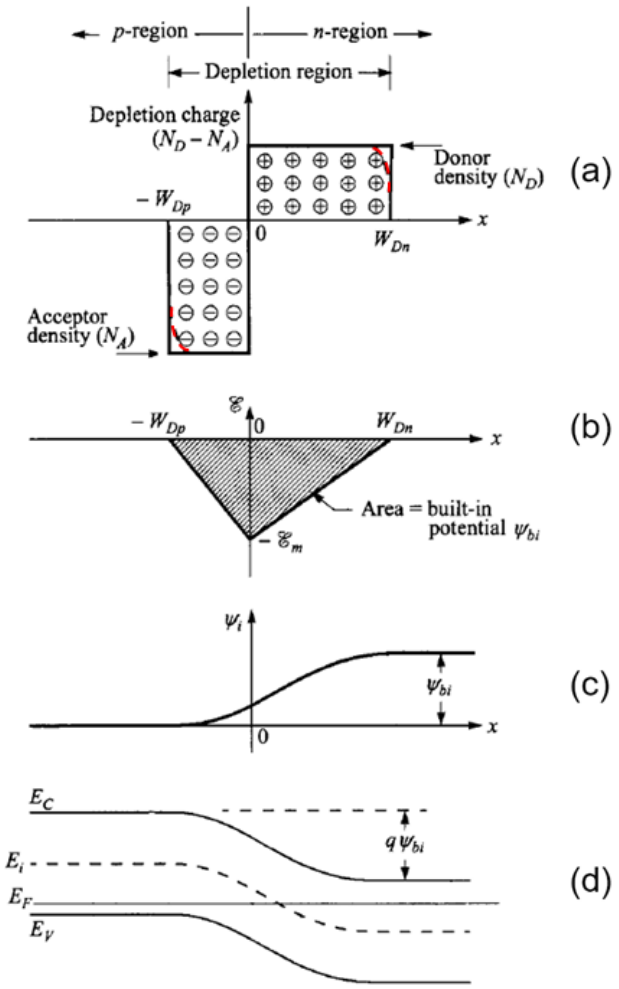

Figure 3.8: p-n junction in thermal equilibrium. (a) space charge distribution (red dashed lines indicate corrections to depletion approximation). (b) Electric field distribution. (c) Potential distribution, where Ψ_{bi} is the built-in potential. (d) Bent energy-band diagram [174].

enough to create a fully depleted region across the whole thickness (*bulk*) of the detector.

On the other hand, when applying a forward bias to the junction (Fig. 3.9(b)), V_F is subtracted from the built-in potential difference between p- and n-side. The consequence is opposite to the case of the reverse bias and therefore the depletion region size decreases, meaning that the diffusion current dominates the drift current.

Bulk and interstrip capacitance

With an increasing value of V_R, an increasingly larger region of the detector gets depleted. The therefore generated current (I_S) involves the presence of a *junction capacitance*. Referring to a simple geometry with plane and parallel plates, in which the distance between

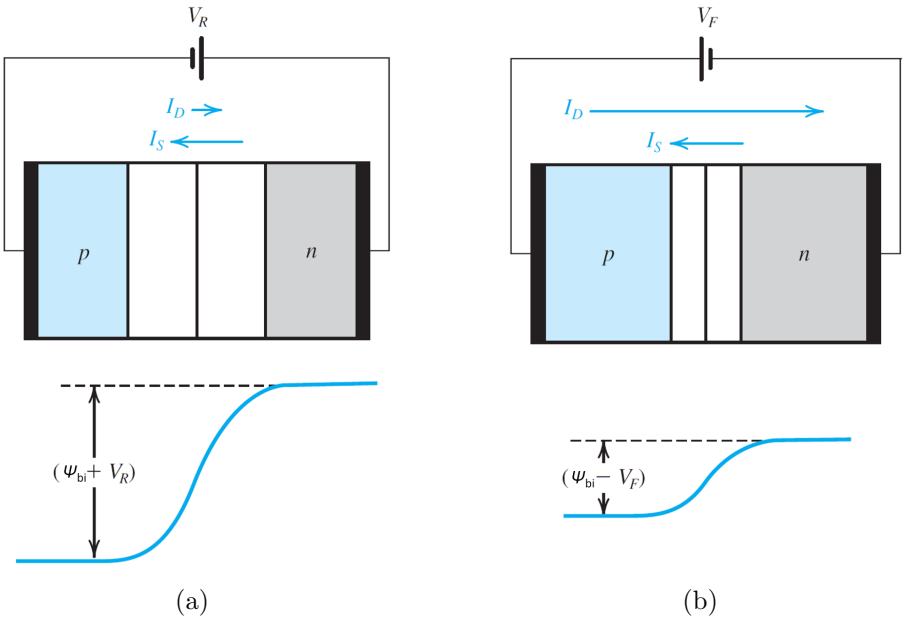

(a) (b)

Figure 3.9: The p-n junction in reverse bias with an external voltage V_R applied (a) and forward bias with V_F (b). Ψ_{bi} is the built-in potential, I_D is the diffusion current and I_S is the drift current [168].

the two plates is the extension of the depletion region, this capacitance can be described as follows:

$$C_j = \frac{C_{j0}}{\sqrt{1 + \frac{V_R}{\Psi_{bi}}}} \tag{3.7}$$

where C_{j0} is the junction capacitance when no voltage is applied

$$C_{j0} = A\sqrt{\frac{q\epsilon}{2\Psi_{bi}} \frac{N_A N_D}{N_D + N_A}} \tag{3.8}$$

and A is the area of the device perpendicular to the junction.

The electrodes of the sensor can also be segmented to provide position information, like it is the case for the detectors used in the LMU Compton camera prototype (see Chap. 4 for more details about the detector's system). In particular double−sided silicon strip detectors (DSSSD) are of interest and therefore will be described in the following.

In Fig. 3.10 a sketch of the structure of a DSSSD is presented. As it is not realistic to produce pure intrinsic silicon, also the bulk of a silicon detector is slightly doped, in this case n-doped: that is why it is referred to as *n-bulk*. On one side p+ strips are implanted, and on the other side, perpendicular to the p-strips, n++ strips are implanted (the ++ notation indicates that the concentration of dopant material is higher than in the + case). The width of one strip is of the order from (few) millimeters down to few tens of micro−meters. The length of a strip ranges from few centimeters to few tens of

centimeters. The smaller the strips, the lower the dark current due to the reduced strip capacitance. Observing Fig. 3.10 it can be noted that on the n side, also smaller p+ strips

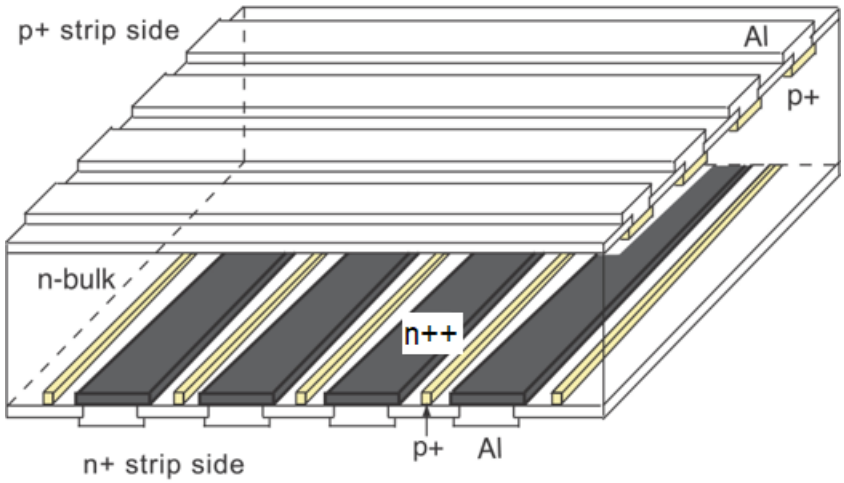

Figure 3.10: Double−sided silicon strip detector (DSSSD) structure: Subdividing both electrodes to form orthogonal strips provides two-dimensional imaging. This is also the structure used for the scatter component of the LMU Compton camera prototype.

are implanted: these are called *p stops*. As we have an n-bulk, the n-n++ junction is less abrupt than a p-n junction, therefore we have to make sure that neighboring strips do not connect to each other by a current flowing between them. The p-stop strips are much smaller in width compared to the n++ strips and they increase the resistivity between two neighboring n++ strips. Furthermore, as it can be seen in Fig. 3.10, on top of each strip on both detector sides a layer of aluminum is present: it is needed to achieve the electrical contact to the strip and to be able to read out its signal.

As the bulk and many strips are present, at each junction a capacitance can be calculated, considering Eq. (3.8) and (3.7) and depending on which electrode of the detector has been biased. In Fig. 3.11 a sketch of the capacitances that should be taken into account is depicted. C_B is the bulk capacitance, at the junction between the strips of one side of the detector and its bulk. C_{IS}^{DC} is an interstrip capacitance, calculated considering the junction(s) between two neighboring strips on one side of the detector. In order to reduce (or fully avoid) any current flowing between neighboring strips, the interstrip capacitance should be low enough and thus the resistivity should be high enough. Typical values for interstrip capacitances are below 1 pF/cm when the detector is fully depleted [175, 176].

Electronic noise

The term *noise* refers to spontaneous fluctuations in the current or voltage signals across semiconductor devices. Since such devices are mainly used to amplify small signals, the fluctuations set a lower limit to these signals. It is important to know the main factors

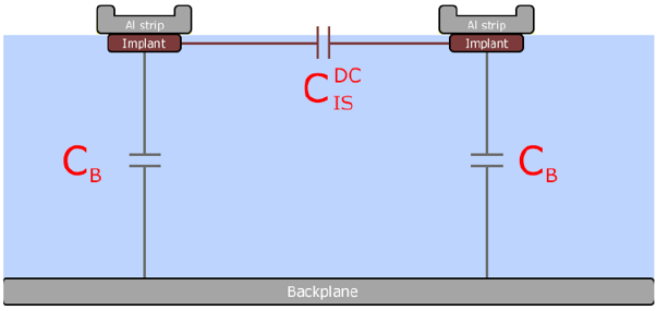

Figure 3.11: Sketch of the capacitances that should be taken into account in a Double Sided Silicon Strip Detector. C_B is the bulk capacitance and C_{IS}^{DC} is the insterstrip capacitance.

contributing to the electronic noise to optimize the operating conditions of a silicon detector.

Noise is typically given as *equivalent noise charge* (ENC, expresed in units of electrons), defined as the input charge that produces at the output a signal amplitude equal to the rms noise. It is the minimum charge detectable by the system, making the signal-to-noise ratio equal to 1. The signal-to-noise ratio (SNR) indicates the ratio between the signal (assumed to be noise free) and the rms noise. The most important sources of noise are *thermal noise*, *shot noise* and *1/f noise*.

Thermal noise is created by random motion of charge carriers due to their thermal excitation. This is the most common noise source in electronics and is present in all conductors and semiconductors. It is sometimes known as Johnson noise [177]. The current generated by the thermal noise is given by

$$i_{thermal}(rms) = \sqrt{\frac{4kT\Delta f}{R}} \tag{3.9}$$

where k is the Boltzmann constant, T is the absolute temperature [K] and R is the equivalent load resistor [Ω] in the detector and Δf is the effective noise bandwidth [Hz]. The different noise contributions are often expressed as a spectral density function: for thermal noise $S_{thermal} = 4kTR$. The thermal noise spectral density is independent of the frequency. Thermal noise can be reduced by acting on bandwidth, resistance and temperature.

Shot noise in semiconductor radiation detectors is associated with the discrete flow of charge carriers through a p-n junction (Sect. 3.1.3), when they have to overcome the potential barrier at the junction. This is a statistical effect of the random emission of electrons (and holes) or the production of photo-electrons [178]. Shot noise is given by

$$i_{shot}(rms) = \sqrt{2qI\Delta f} \tag{3.10}$$

where q is the electron charge, I is the forward junction current (it can be due to the signal, bias currents, background radiation and leakage) and Δf is the effective noise bandwidth. Like thermal noise, shot noise is proportional to $\sqrt{\Delta f}$, meaning that there is constant

noise power per Hz bandwidth, i.e. it is "white" noise. Its spectral density function is $S_{shot} = 2qI$.

1/f noise is the dominant noise in the low-frequency range and its spectral density function is proportional to 1/f [177], so it is the only contribution to the noise that is varying with frequency. It depends mainly on additional fluctuations caused by trapping and detrapping processes and its spectral density function is

$$S_{1/f} = \frac{\alpha_H \cdot I^{\alpha}}{f^{\gamma} \cdot N} \tag{3.11}$$

where $\alpha_H = 2 \cdot 10^{-3}$ is the Hooge constant [179], α and γ are material constants and N is the number of charge carriers. A current control and high-pass filter application can reduce the 1/f noise contribution.

3.2 Scintillation detectors

The basic principle of scintillating materials, in particular inorganic crystals, is the *absorption* of the incident high energy light (X- or gamma-rays) and subsequent *conversion* into multiple and low-energy photons, in the range of visible or UV light. A light sensor is then coupled to the scintillating material: in this way the light coming from the *emission* of the crystal is converted into an electrical pulse that can be read out and registered.

This section will mainly focus on different scintillator materials available and their performances, and will mention possible light sensors that can be used [141]. The ideal scintillator material should possess the following properties:

1. It should convert the kinetic energy of charged particles into detectable light with a high scintillation efficiency (i.e. light yield).

2. This conversion should be linear - the light yield should be proportional to deposited energy over a range as wide as possible.

3. The medium should be optically transparent to the wavelength of its own emission for efficient light collection.

4. The decay time of the induced luminescence should be short such that fast signals can be generated.

5. The material should be of good optical quality and allow to be grown in sizes large enough to be of interest as a practical detector.

6. Its index of refraction should be near that of glass ($\sim$1.5) to permit efficient coupling of the scintillation light to a photomultiplier tube or other light sensor.

The process of scintillation can be observed in organic or inorganic materials. Both types will be presented, with a special focus on inorganic crystals, since this type was chosen for the scintillators used in the LMU Compton camera.

In ***organic scintillators*** (e.g. plastic scintillators) the light-generating fluorescence process originates from transitions in the energy level structure of a single molecule and can therefore be observed in a given molecular species independent of its physical state. The incident radiation to the medium excites an electron that is promoted to a certain energy level that depends on the amount of energy that the radiation deposits. From this excited state, the electron rapidly de-excites to the ground state, emitting fluorescence light. As almost always only prompt fluorescence is observed, this process is very fast and takes about 1-2 ns [141], which reflects the superior timing performance of this class of materials. For molecules of interest as organic scintillators, the energy spacing between relevant levels is about 3 - 4 eV, (and somewhat smaller for higher lying states): this prevents thermal excitation processes at room temperature.

In ***inorganic scintillators*** the scintillation mechanism depends on the energy levels determined by the crystal lattice of the material. In Fig. 3.12 a sketch of the discrete bands of energy available for electrons is shown. The valence band, at lower energies, represents

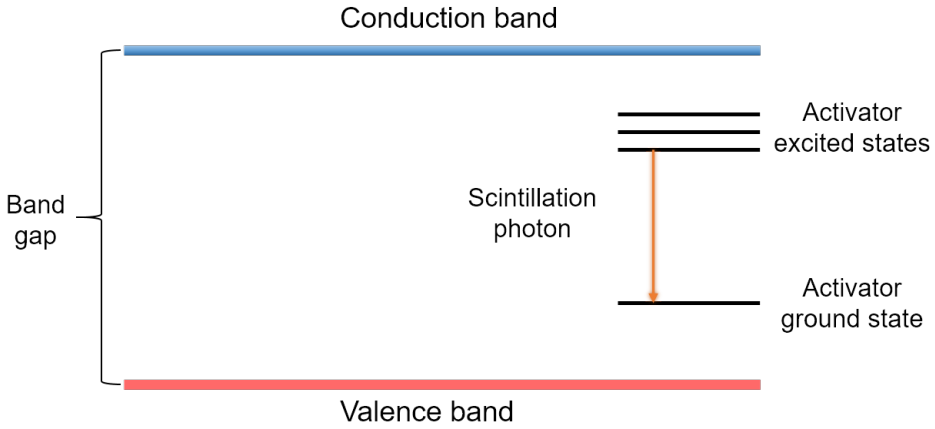

Figure 3.12: Energy band structures of an inorganic scintillator. Additional activator states (color centers) are introduced by doping the material with a small amount of specific impurities to enhance the probability of emitting photons in the visible or near-UV light range.

those electrons that are essentially bound to atoms located at lattice sites, whereas the conduction band represents those electrons that have sufficient energy to be free and move within the crystal. The band gap basically represents an intermediate band of energies that is forbidden to electrons in pure crystals. When the energy deposited in the crystal exceeds the minimum excitation energy, it promotes an electron from the valence to the conduction band. A direct de-excitation of this electron back to the valence band is associated with the emission of a photon with an energy that exceeds the visible or near UV spectral range. Therefore, in the lattice structure selected dopants can be inserted: they are called activators or color centers and they create new energy levels in the band gap, as shown in the sketch in Fig. 3.12. In this way the electrons, after being excited from the valence to

the conduction band, can be captured from an activator excited state before de-exciting directly to the valence band. They will then de-excite to a lower level emitting a visible or near-UV scintillation photon.

Scintillator crystal are characterized by a series of properties that should be taken into account when designing a new detector system, depending on the specific requirements. Table 3.1 lists the most important properties for those scintillation crystals that are relevant for the thesis project presented here.

Material	ρ **[g/cm^3]**	$\mathbf{Z}_{eff}$	τ **[ns]**	**Y [ph/MeV]**	λ_{max} **[nm]**	**hygr.**
$LaBr_3$(Ce) [180]	5.08	47	16	63000	380	yes
$CeBr_3$ [181]	5.2	46	17	68000	380	yes
GAGG [182]	6.7	52	<100	52000∼56000	520	no

Table 3.1: List of the most important properties for those scintillation crystals that are relevant for the thesis project presented here.

The probability of photon interaction in the crystal, and such its efficiency, is determined by the density ρ, expressed in [g/cm^3]. The effective atomic number Z_{eff} of the scintillator compound is the atomic number of the corresponding molecule. The decay time τ of a scintillator is defined by the time after which the intensity of the light pulse has returned to 1/e of its maximum value. It indicates the time needed for an excited electron to de-exite and emit light. The decay time is of importance for fast counting and / or timing applications. The *light yield* Y indicates the number of emitted secondary photons generated by an incoming photon per unit energy [ph/MeV]. It is an important parameter contributing to the efficiency of a detector. λ_{max} is the wavelength (in [nm]) of the spectral emission maximum of the scintillation light. It defines the choice of an appropriate photosensor able to efficiently read out the light produced in this spectral range. *Hygroscopy* is the phenomenon of attracting and holding water molecules from the surrounding environment: a hygroscopic scintillator always has to be encapsulated. The hygroscopicity of $LaBr_3$(Ce) and $CeBr_3$ scintillation crystals will be discussed in Sect. 4.4.2 in more details. Finally, the energy resolution achievable with a certain scintillation crystal is another important parameter when choosing a detector for a specific application; this property will be discussed in Sect. 3.3.1.

3.3 Detector system: scintillator and photo sensor

The photons emitted by a scintillator crystal have to be detected by a photo sensor, whose purpose is to convert the light into a detectable electronic signal. The principle of the photoelectric effect is used to convert photons into photoelectrons that can be amplified by the sensor and read out by the subsequent signal processing electronics.

When coupling the photo sensor to the scintillator crystal it is crucial to match the optical index of refraction between the two components by inserting a suitable optical grease or gel to act as light guide, in order not to lose light at the surface interface.

There are different types of photo sensors and their main requirement is to provide a high *photon detection efficiency* (PDE) in the wavelength region of interest, which is the ratio between the number of photoelectrons and incident photons. The two types of photo sensors that will be considered here are photomultiplier tubes (PMT), which are used throughout the experimental work of the presented thesis project, and (analog) silicon photomultipliers (SiPM), because their alternative use will be investigated in the continuation of the presented project.

A ***photomultiplier tube*** (PMT) is a highly sensitive photodetector. In the right-hand part of Fig. 3.13 its internal structure is shown: the PMT is coupled, via an optical light guide, to the scintillator. The entrance window of the PMT is typically the front face of an evacuated quartz-glass cylinder, directly followed by a photocatode made of a thin film of semiconductor or metallic material with a low work function for efficient photo-electron creation. The emitted photoelectrons are subsequently focused by focusing electrodes, and accelerated towards the first dynode (out of typically 10-12). If their energy is high enough to overcome the vacuum level barrier, they diffuse into the vacuum. This process happens with a certain probability, which directly influences the quantum efficiency (QE) of the device

$$QE(\nu) = (1 - R)\frac{P_\nu}{k} \cdot \left(\frac{1}{1 + 1/kL}\right) \cdot P_s \tag{3.12}$$

where R is the reflection coefficient, k the full absorption coefficient of photons, P_ν the probability that light absorption may excite electrons to a level higher than the vacuum level energy, L is the mean escape length of excited electrons, P_s the probability that electrons reaching the photocathode surface may be released into vacuum and ν is the frequency of the scintillation light.

Each dynode of the device generates δ secondary electrons: the photoelectrons emitted from the photocathode are multiplied starting from the first dynode throughout the sequence of dynodes and are finally sent to the collection anode. By using n dynodes a current amplification (or gain) of δ^n can be reached. The exact value depends linearly on the bias voltage (typically in the range of 1 kV) and is typically higher than 10^5. The last step is to collect all the secondary electrons at the anode and read out the electrical current by an external circuit [183].

Silicon photomultipliers (SiPM) are presently more and more popular as an alternative to standard PMTs, mainly because it is insensitive to magnetic fields. A SiPM is a silicon-based photodetector that uses multiple APD (Avalanche Photodiode) micropixels operating in Geiger mode [184]. These are called G-APD (Geiger-Avalanche Photodiode) or SPAD (Single Photon Avalanche Diode). Several hundreds up to a few thousands of these microcells are connected, sharing the same bias and ground, in a parallel circuit to build up one SiPM module. The pixels are electrically decoupled from each other by polysilicon resistors located on the same substrate. A sketch of the structure of a SiPM is shown in Fig. 3.14.

SiPMs are operated applying a reverse bias, specifically slightly above the breakdown voltage (V_{br}), which is the bias where the electrical field strength generated in the depletion region is sufficient to create a Geiger discharge. In Geiger mode, photons entering the

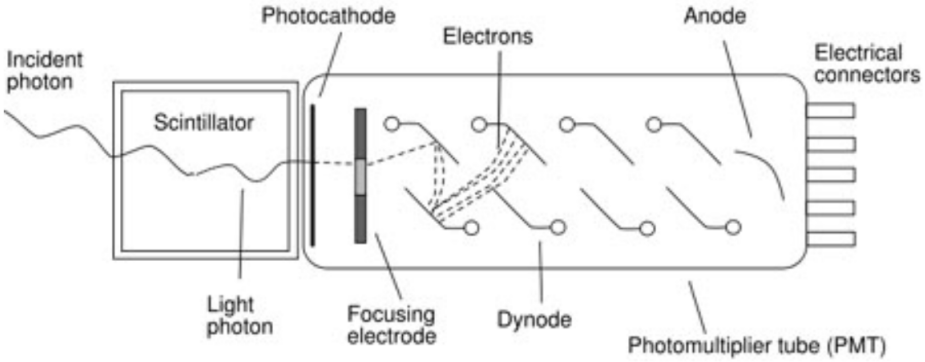

Figure 3.13: Sketch of a photomultiplier structure, coupled to a scintillator crystal.

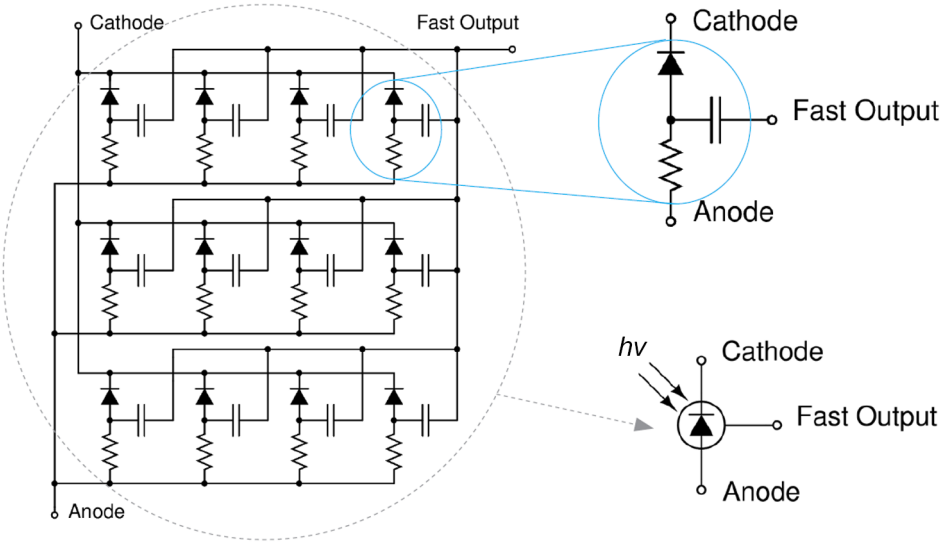

Figure 3.14: Simplified circuit schematics of a silicon photomultiplier, showing each microcell which is composed of a SPAD, quench resistor and fast output capacitor [184].

photodiode generate a self-sustaining avalanche current which is quenched and reset by use of either passive elements or active quenching circuits. Each SPAD pixel of the SiPM yields a pulse signal when it detects one photon; the summation of all SPADs pixel signals will generate the output of the SiPM. The gain of an SiPM is mainly determined by the overvoltage and is typically in the range of 10^5 to 10^7. On the surface of an SiPM pixel an antireflective layer is added in order to optimize the efficiency of the detector by increasing the number of photons reaching the depletion region at the p-n-junction. The PDE of a SiPM can be defined as

$$PDE(\lambda, V) = \eta(\lambda) \cdot \epsilon(V) \cdot F \tag{3.13}$$

where η is the quantum efficiency of silicon, ϵ is the avalanche initiation probability and F is the fill factor of the device. The PDE thus indirectly depends on the wavelength and

on the overvoltage that goes to the SiPM. Typical good values can be considered around 40 and 50 [184].

3.3.1 Energy resolution

In general the energy resolution is a detector property that can be specified for any kind of detection device. Since it defines the ability to resolve different detected energies, it has to be taken into account in the decision process on the type of scintillator material to be used when discrete photon energies have to be detected, as it is the case for our Compton camera. Even if a monochromatic photon is detected by a scintillator, due to the statistical nature of the physical processes that allow for the signal acquisition, the resulting measurement of the photon energy is affected by uncertainties. The factors that mostly influence this measurement are the statistical nature of the ionization process, the collection of the signal and the electronic noise introduced by the readout chain. Thus, the expected ideal sharp line in the energy spectrum is broadened, leading to a statistical distribution that can be approximated by a Gaussian with centroid E_0 and variance σ^2. The width parameter σ defines the full-width-at-half-maximum (FWHM) of the Gaussian distribution through the relation FWHM = 2.35σ. The relative energy resolution R of a detector is defined as the ratio between the width (expressed as FWHM) of the registered line in the γ-ray spectrum and the initial photon energy:

$$R = \frac{\Delta E(FWHM)}{E_0} \ [\%] \tag{3.14}$$

In particular, the total energy resolution can be assumed to be mainly affected by statistical fluctuations and by the electronic noise of the readout chain. These two factors can be considered by summing them up quadratically, meaning that an energy resolution measurement depends on all detector system components: the scintillation crystal, the photo sensor and the readout electronics. Details about the energy resolution of the Compton camera components will be given in Chap. 6.

3.3.2 Time resolution

When detecting γ rays from pulsed or coincident interactions and/or in the presence of particle-induced background, it is often also helpful to be able to achieve well defined temporal information about the detected radiation. This information can, e.g., be used for realizing time coincidence measurements in order to suppress background: in our case this means to be able to distinguish a (slow) neutron component from the (fast) gamma-ray component and suppress it to reduce the background. It is then fundamental to know the timing properties of the applied detector, namely the time resolution of the system, defined as the FWHM of a time spectrum. The latter is obtained by measuring the distribution of the time intervals between a start and a stop event, such as the detection of two coincident γ rays emitted by a calibration source or the arrival time of photon signals measured versus the short signal of an accelerator pulsing system in online applications. The overall

time resolution of a detector system depends on the timing properties of the scintillation material, on the photo sensor and on the electronic readout and signal processing chain.

CHAPTER 4

The Compton Camera system

This chapter will describe more in detail the detectors in use in the Compton camera prototype system being developed at LMU Munich. Some previous simulation results on which the design is based will first be shown and MEGAlib, the simulation toolkit used, will briefly be presented. The same toolkit can be used for the Compton image reconstruction of simulated and experimental data. Since the focus of this thesis is the experimental part of the project, the second part of the chapter will focus on the detectors in use. The description of the related hardware, readout electronics and mechanical setup will follow in the next chapter.

4.1 Compton camera concept and principle

As introduced in Chap. 1, the concept of a Compton camera system is based on the arrangement of two detector components: a scatter and an absorber component (as shown in Fig. 4.1(a)). The scatterer component can be constituted of either one or more than one detector layer (sketched in Fig. 4.1(b)). The latter is the setup of the LMU Compton camera (see the description of the detectors in Sect. 4.2). The sketch in Fig. 4.1 shows the principle of a Compton camera system and the information needed from each event to perform an image reconstruction, in a one-scattering-layer configuration (a) and in an arrangement that involves more layers as scatter component, thus including the electron tracking (b).

The aim of a Compton camera is to reconstruct the initial gamma-ray interaction position, without using any mechanical collimation. To perform the gamma-ray image reconstruction the position and energy information from successive interactions in both components are used. For each event, a Compton cone (or arc, in case also the information from the electron tracking is used) can be defined in a 3D space. As it is sketched in Fig.

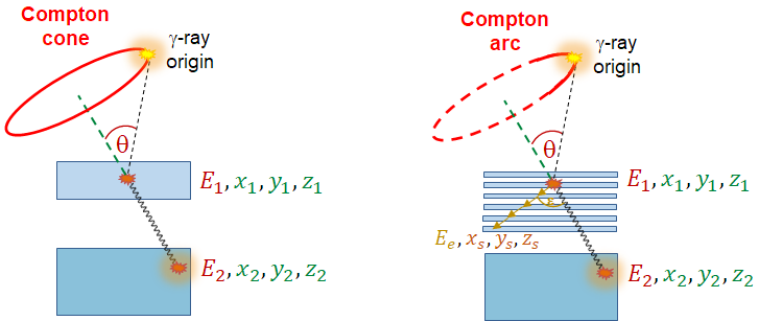

Figure 4.1: Working principle of a Compton camera system. From the energy and position information recorded in each detector component for each event, a Compton cone (a) can be derived. With the addition of the electron tracking (b) the Compton cone reduces to an arc. The intersection of more cones (arcs) will allow to reconstruct the initial source position.

4.1 the direction of the Compton cone is defined by the interaction positions determined in the two detector components and the aperture angle of the cone is given by

$$\cos\theta = 1 - m_e c^2 \left(\frac{1}{E_2} - \frac{1}{E_1 + E_2}\right) \tag{4.1}$$

where θ is the Compton scattering angle. E_1 is the energy deposited via Compton scattering in the scatter component and E_2 is the residual energy deposited in the absorber component. From the intersection of the cones (arcs) created by each event, the original gamma-ray position can be derived.

Figure 4.2 (taken from [185]) shows an example of the intersection process for a point source image reconstruction with a Compton camera setup using simulated data. The aim of these images is the explanation of the cones' (arcs) intersection behaviour and therefore the reconstruction is performed and shown using prototypically only one (upper row), two (middle row) and three (lower row) photon events. The images in Fig. 4.2(a) were reconstructed from a Compton camera setup with one scattering layer, whereas the images in Fig. 4.2(b) were reconstructed from a Compton camera setup that includes six scattering layers.

As mentioned before, when a camera device contains multiple scattering detectors it is possible to track the path of the Compton electrons being produced throughout the different layers. The electron tracking helps to recover those events that are not fully absorbed in the last stage of the Compton camera: by using the information of the electrons travelling over the different scattering layers, also these events can be included in the list of events used to reconstruct the initial source position, and the efficiency of the system can therefore be increased.

There are different groups presently working on the Compton camera concept applied in medical imaging (previously presented in Chap. 1.3.3.2), using different Compton camera

arrangements and mainly without utilizing electron tracking[109, 113, 116, 119, 120]. This concept presents many challenges, mainly affecting the efficiency: enough photon scattering events have to be recorded, and enough of them should fulfill the condition to be used for the source image reconstruction during a real-time acquisition ultimately targeted with the present concept. This motivated the choices made for the LMU Compton camera prototype design composed of a scattering part made of different detector layers that enable the electron tracking.

Before introducing in more detail the prototype that we are currently commissioning, an important parameter for the evaluation of the performance of every Compton camera setup will be presented.

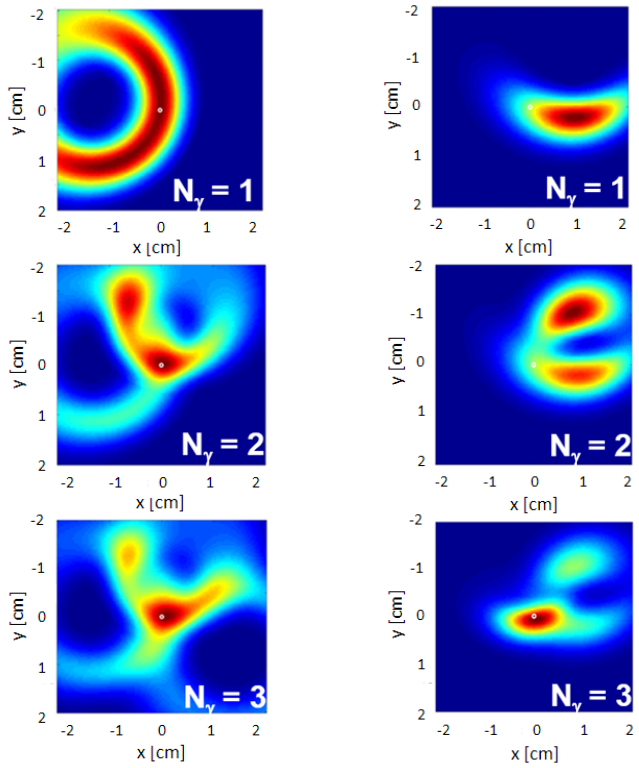

Figure 4.2: Simulated γ-ray source position reconstruction for the γ-ray tracking mode (a) and electron tracking mode (b) using the Megalib toolkit [186]. The three pictures for each of the two modes (from the top to the bottom) show the reconstruction based on different numbers of Compton scattering events, related to different numbers of primary photons (in this case 1, 2 or 3 photon events exemplifying the process of Compton cones (arcs) intersection) (taken from [185]).

The angular resolution measurement (ARM) is one of the most important parameters used to characterize the Compton camera system performance. There are different factors

that cause uncertainties in the scattering angle determination: as long as the Doppler broadening, caused by the nature of the Compton scattering interaction, can be neglected in our case (this concept was explained in Sect. 2.1.2.1), only the uncertainties affecting the information recorded from the detection system need to be considered. This corresponds to the position and energy resolution of the detectors that should be chosen accordingly to the envisaged angular resolution requirements.

The ARM is defined as the width of the Compton cone (arc) reconstructed from each photon event. As shown in Fig. 4.3 (here considering the simplified configuration with one scatter layer and an absorber detector), the incident gamma ray deposits its energy E_1 at r_1 and the rest of the energy E_2 at r_2. Because of the finite resolution in determining the energy and the interaction position in a detector, a measurement could also record values of E_{1m} at r_{1m} and E_{2m} at r_{2m}, respectively. The angle defined by the ARM is determined as the difference between θ_g and θ_e, where θ_g is calculated from measured interaction positions and the real direction of the source and θ_e is calculated from the measured energy deposits.

$$\cos\theta_g = \frac{(r_{1m} - r_0) \cdot (r_{2m} - r_{1m})}{|r_{1m} - r_0| \cdot |r_{2m} - r_{1m}|} \tag{4.2}$$

$$\cos\theta_e = 1 - m_e c^2 \left(\frac{1}{E_{2m}} - \frac{1}{E_{1m} + E_{2m}}\right) \tag{4.3}$$

The position uncertainty carries the error of θ_g and the energy resolution carries the error of θ_e. The angular resolution of a Compton camera is estimated by the width (FWHM) of the fitted distribution of the ARM value with a sufficient amount of Compton events. The values for the ARM measurement vary depending on the energy and on the setup and can typically be around 5°.

4.2 Simulations and prototype design

The work presented in this thesis is focused on the detector-oriented experimental part of the LMU Compton camera project. Simulation and image reconstruction studies can be found in different theses works and will be here partly commented as they are a complementary part of the same scientific project.

First simulation studies about the Compton camera prototype under development at LMU were carried out by C. Lang during his PhD studies [121]. These simulation studies were extended in [185] in the PhD work of I.I. Valencia-Lozano, in which she also benchmarked the prototype and evaluated images reconstructed from simulated and experimental data.

Simulations and reconstruction of the Compton images are obtained using the MEGAlib software package [186, 104]. This toolkit was developed to simulate and analyze data from a Compton telescope designed for Medium Energy Gamma-ray Astronomy (MEGA) [188] at the Garching Max-Planck-Institut für Extraterrestrische Physik. It is written in C++ and it is based on ROOT [189, 190]. The software is designed to be easily adaptable to different

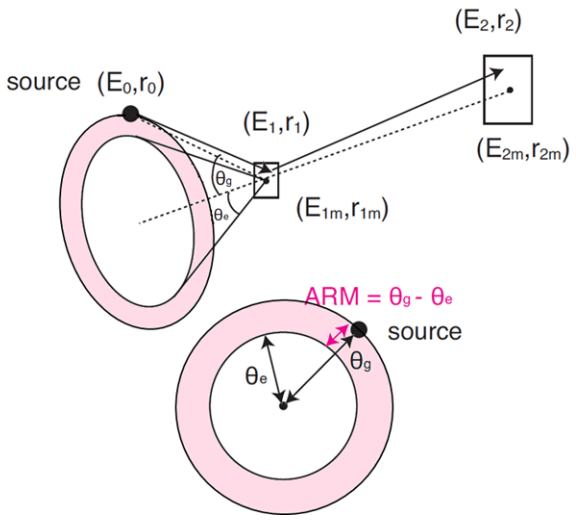

Figure 4.3: Sketch explaining the angular resolution measurement (ARM). A photon source in position r_0 emitting an energy E_0 is realistically depositing an energy E_{1m} at r_{1m} from the scattering and the rest energy E_{2m} at r_{2m}. The ARM is defined as $\theta_g - \theta_e$ [187], where θ_g is calculated from measured interaction positions and the real direction of the source and θ_e is calculated from the measured energy deposits.

detector designs by applying changes to the geometry and detector descriptions. A basic modular scheme representing the workflow of MEGAlib is shown in Fig. 4.4 [104]. As the work based on MEGAlib was performed in other theses ([121, 185]), in the present work this part is presented in a more general manner. A detailed description of the MEGALib software package can be found in the PhD thesis of Andreas Zoglauer [104], the developer of this software package.

After the definition of the geometrical design and the detector system, the data can be either simulated using the module *Cosima*, based on ROOT [190] and Geant4 [69], or imported as list-mode event files from experimental data. In this step of the reconstruction process the different interactions are recorded in each detector component of the system. Hence the data recorded are processed in the *Revan* module, where the hits are analyzed individually in order to classify the events: those which qualify as Compton scattering events can be reconstructed. The last step of the image reconstruction process is included in the *Mimrec* library: here the events can be selected depending on performance-relevant parameters for the Compton camera system. The image reconstruction is based on the list-mode maximum-likelihood expectation maximization algorithm (LM-MLEM) and can be performed in spherical as well as Cartesian coordinates (2D, 3D) for both simulated and experimental data. The angular resolution, the energy dispersion and the scattering angle distribution are taken into account and are influencing the imaging performances of the system.

The layout specification of the Compton camera is an essential part when designing such a complex system. First the image reconstruction technique on which the system will

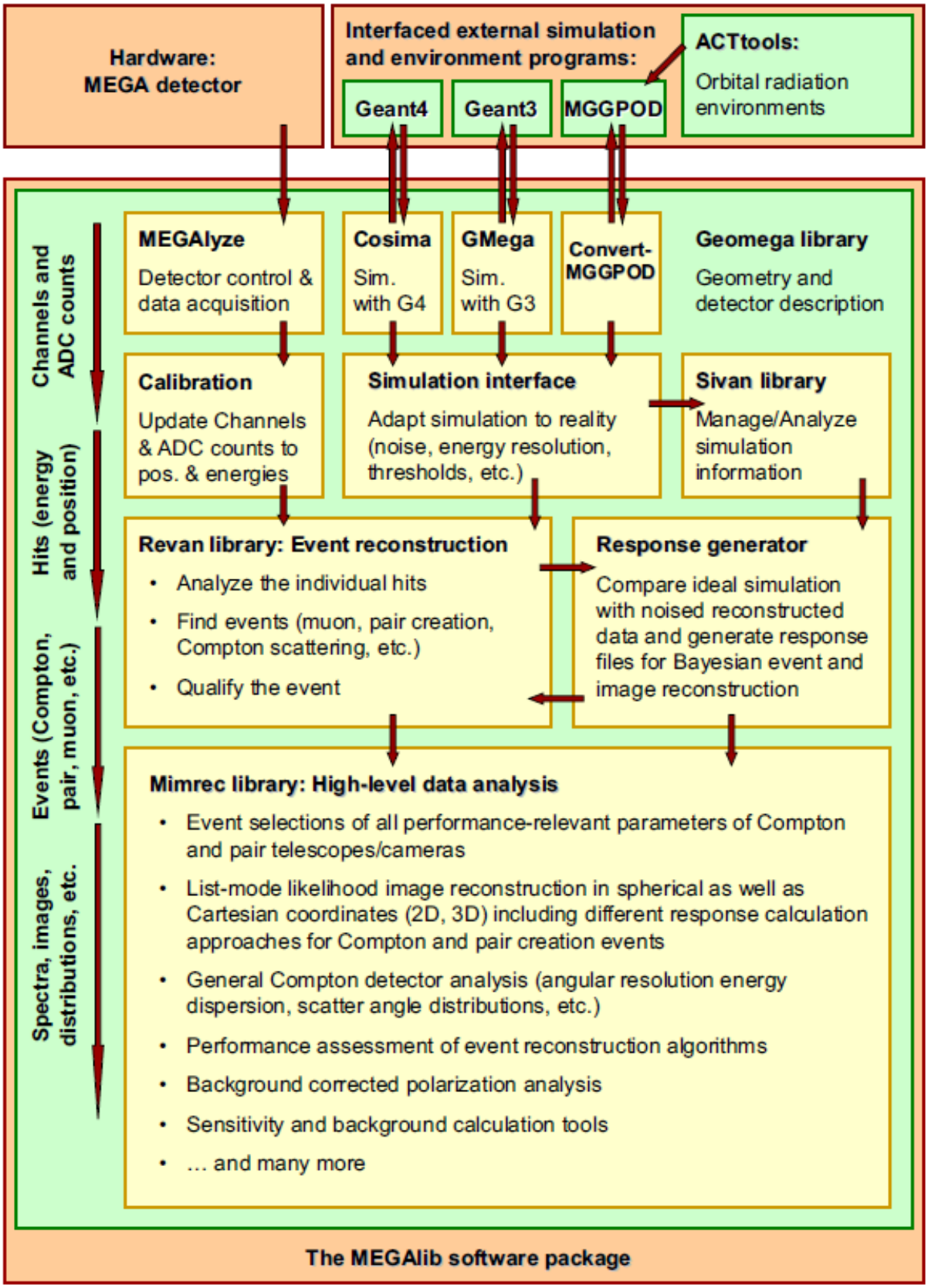

Figure 4.4: Overview of the various components of the MEGAlib software package for simulation and image reconstruction of Compton camera data. The data can be either simulated or experimental. The event reconstruction is performed by the Revan library, the image reconstruction and analysis by the Mimrec library. [104].

be based (photon tracking alone or in combination with recoil Compton electron tracking) should be decided, then the overall performance of the system should be evaluated and taken into account. The scatter detector of the LMU Compton camera was set up by multiple scatter layers to have the desired electron tracking capability: these layers should be thin enough to avoid the Compton electron to be absorbed already in the interaction layer, but still maintain a high enough scattering probability in order to produce sufficient Compton-scattered electrons to be included in the list of Compton events for the image reconstruction. In addition, and related to the ARM performance of the system, the scatter detector should provide a high segmentation for a precise localization of an interaction event. With these requirements semiconductor materials, like silicon (Si), cadmium zinc telluride (CdZnTe) or germanium (Ge), are good candidates for the scatter detector, with silicon exhibiting the most favorable linear attenuation coefficient as a measure for the scattering probability in the (multi-MeV) energy range of interest. The choice was made in favor of double-sided silicon strip detectors (DSSSD), as Si detectors can be operated at room temperature and exhibit a minimum Doppler broadening (0.4°) at 1 MeV incident photon energy, instead of a value of 0.85° for CdZnTe and 0.65° for Ge, at the same photon energy [104]. The Doppler broadening, if not negligible, affects the whole system's spatial resolution. Furthermore, a scintillation crystal is a good solution for the absorber component, as it can be produced in large volumes and this increases the absorption efficiency of the remaining energetic Compton-scattered photons. $LaBr_3$(Ce) was selected because of its excellent time resolution (few 100 ps) combined with one of the best energy resolution values amongst this kind of detectors (around 3.5% at 662 keV). During the course of the project a $CeBr_3$ scintillator also started to be taken into consideration, as it is a cheaper solution but still provides comparable values concerning time and energy resolution. Furthermore, it does not possess internal radioactivity (see details in Sect. 4.4.2). In Fig. 4.5 the chosen layout for the setup of the LMU Compton camera that has been simulated in a previous thesis work by C. Lang [121] is shown.

The system is composed of a scatter component that consists of six layers of DSSSD, each with an active area of $50 \cdot 50$ mm^2 and a thickness of 500 μm. In Fig. 4.6 the results in terms of reconstruction efficiency for different scatterer configurations evaluated in [121] are plotted, exhibiting best values for a camera with electron tracking capability and six layers of DSSSD, each of them with a thickness of 500 μm.

The scintillation crystal is acting as absorber component of the camera system. It was chosen to be monolithic in order to get the best energy resolution achievable also for the high photon energies of interest in prompt-γ imaging; its readout and data analysis will be later discussed in Chap. 5 and 6. The geometrical arrangement of the Compton camera was investigated and optimized for a small animal irradiation scenario, considering a photon source position 50 mm from the first DSSSD layer. From the initial study presented in [121] the distance between each DSSSD layer was decided to be 10 mm, as a compromise between the electron scattering angle and the geometrical constraints from the experimental setup. The distance between the front surface of the absorber and the first layer of DSSSD was defined in [121] to be 85 mm. After determining the geometrical setup of the camera, Lang performed some studies, by using simulated data from a point

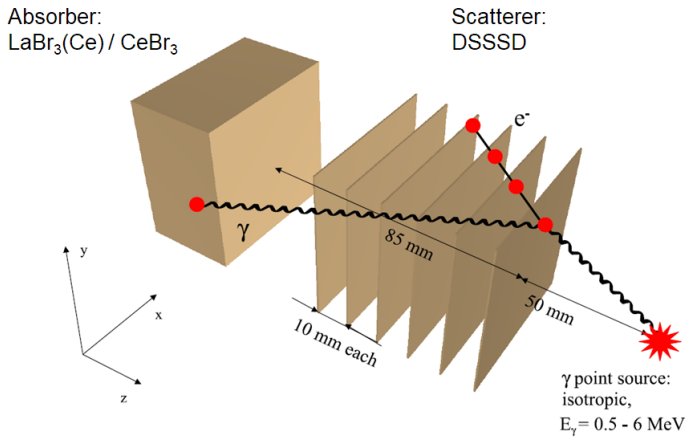

Figure 4.5: Sketch of the setup of the LMU Compton camera. It is composed of six layers of double-sided silicon strip detectors, with an active area of 50 × 50 mm^2 and a thickness of 500 μm acting as scatter component, while for the absorber component initially a $LaBr_3$(Ce) crystal, lateron also a $CeBr_3$ detector are used, both having a volume of 50.8 × 50.8 × 30 mm^3. The geometrical arrangement of the camera was adjusted as a compromise between mechanical constraints and the camera performance [121].

gamma-ray source in the energy range between 0.5 and 6 MeV, to determine the DSSSD detector thickness and the achievable angular resolution based on the spatial resolution of the absorbing crystal. In Fig. 4.7 the trend of the ARM and related spatial resolution of the whole system as a function of the gamma-ray energy and dependent on the spatial resolution of the absorber component are plotted. In the legend of the plot Δr corresponds to the assumed spatial resolution achievable in the absorber crystal, motivated by the pixel size of the readout channel, meaning the pixel size of a segmented photomultiplier that reads out the light from the scintillation crystal, whose details will be explained in more detail later in this chapter. The initial design specification goal for the spatial resolution in the monolithic scintillator is therefore to reach a value of at least 3 mm in the energy range of multi-MeV prompt photons. The assumption "3 mm resolution" implies that it already correctly defines the interaction position in 3D, while effectively this holds only for 2D. Any DOI effect can not therefore be excluded. In both spatial resolution scenarios (3 mm and 6 mm), the achievable angular resolution of the camera (whose best value reached is below 2°) is not affected by the DSSSDs thickness, since the spatial resolution of the Compton camera is directly determined by the energy and photon interaction position in the scatter and absorber detectors.

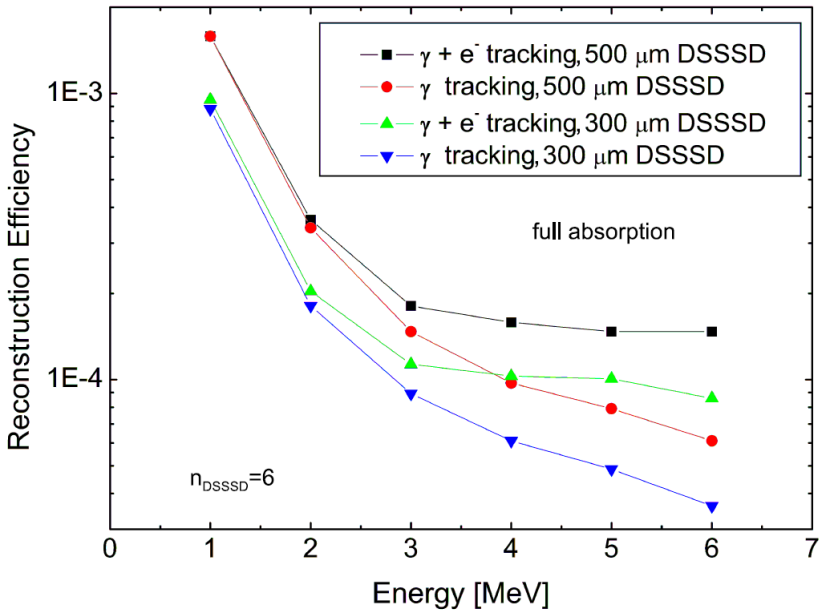

Figure 4.6: Result of a simulation study performed in [121] that quantifies the impact of the scatter detector thickness and the image reconstruction mode (γ tracking alone or with the addition of the electron tracking) on the LMU Compton camera reconstruction efficiency as a function of the incident γ-ray energy. Up to 3 MeV the DSSSDs with 500 μm thickness provide a higher efficiency compared to 300 μm thick detectors regardless of the reconstruction mode. Beyond 3 MeV, e.g. in the prompt-γ energy region, the reconstruction efficiency improves for electron and γ tracking for both DSSSD thicknesses. The maximum reconstruction efficiency of the camera at the targeted photon energy (3 - 6 MeV) was found to be about $1.5 \cdot 10^4$ with 500 μm thick DSSSDs and electron plus photon tracking.

4.3 Scatter component

4.3.1 Double-sided silicon strip detectors

According to the simulation studies performed in [121], the detectors chosen to act as multi-layer scatter component of the LMU Compton camera are a stack of six double-sided silicon strip detectors (DSSSDs). They were produced by the *Forschungsinstitut für Mikrosensorik GmbH* (CiS) [191] and can be observed in the photograph displayed in Fig. 4.8.

As the camera design has been decided in view of a small animal irradiation scenario, each of these detector layers has an active area of $50 \cdot 50$ mm^2. The thickness of one layer is 500 μm. As previously mentioned, the accuracy in the position determination in each detector component plays a very important role in the image reconstruction process: for this reason the silicon layers were decided to have a very high segmentation. Each DSSSD

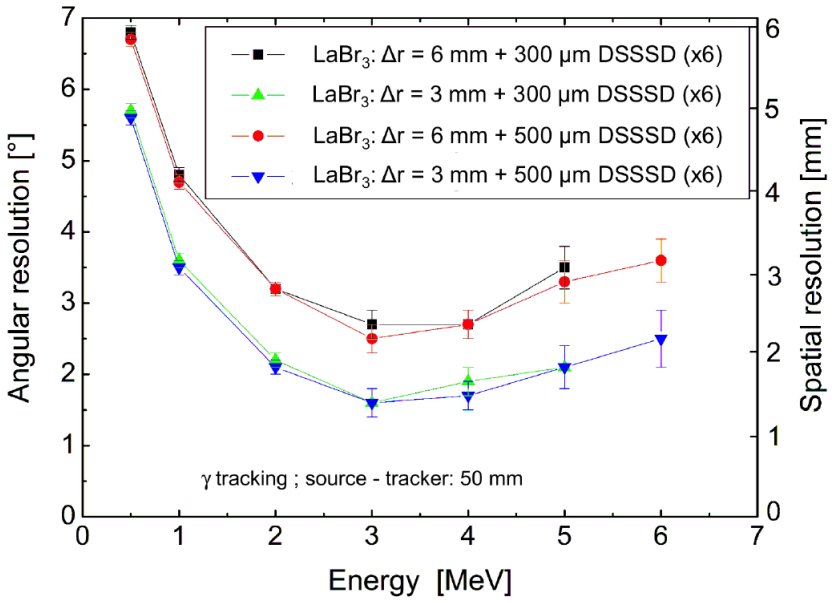

Figure 4.7: The Compton camera ARM (left coordinate) and spatial resolution (right coordinate) were evaluated as a function of the incident photon energy and based on the spatial resolution value of the absorber component, in an energy range between 0.5 and 6 MeV. The thickness of the scatter component was also varied. The spatial resolution of the absorber component was assumed to be 3 mm and 6 mm, respectively: these values were motivated by the segmentation of the multi-anode photomultiplier options considered and presented in detail in the next sections. The best spatial resolution was found to be 1 - 2 mm at the targeted prompt γ energy from 3 to 6 MeV, achieved with the $LaBr_3$(Ce) detector's spatial resolution assumed to be 3 mm [121], and the best angular resolution was found to be below 2°. These considerations hold for an assumed small-animal irradiation scenario with a distance of 50 mm between the photon source and the first scatter detector.

detector has 128 strips on each side with a pitch size of 390 μm. Moreover, these detectors were specifically requested to be built from a high resistivity wafer material, in order to keep the leakage current, and thus the electronic noise, as low as possible to be able to detect the low-energy Compton electron energy deposits: they possess a resistivity higher than 10 kΩcm, indicating a high purity of the wafer material. The leakage current in one layer was measured by the manifacturer to be less than 1 μA and this value was confirmed in the laboratory by biasing the detector with a four-channel high voltage supply module (MHV-4, Mesytec [192]), which has a current display resolution of 1 nA.

In Fig. 4.9 a photograph of one DSSSD module is shown from its p-side (a) and n-side (b). The bulk of the detector is not purely intrinsic silicon, but slightly n-doped (as the DSSSD described in Sect. 3.1.4) with a concentration of $n = 5 \cdot 10^{11} cm^{-3}$. The strips have therefore doping concentration values of $p = 7.5 \cdot 10^{14} cm^{-3}$ and $n+ = 1.0 \cdot 10^{15} cm^{-3}$, obtained by using boron and phosphor, respectively. On the n-side of the detector, where

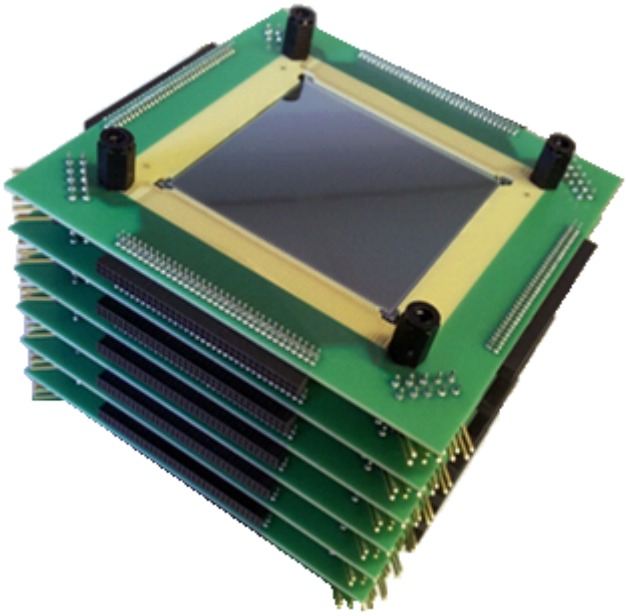

Figure 4.8: Photograph of the stacked array of six customized double-sided silicon strip (DSSSD) detectors, spaced by 10 mm and used as scatter component in the LMU Compton camera.

the bulk has been moderately doped, so called p-stops have been grown as well in order to better isolate the n-strips: these doping areas are very small and have a concentration equal to $p = 1.1 \cdot 10^{13} cm^{-3}$. The channels of the 128 p-side strips and 128 n-side strips are bonded on all four sides of the square detector in order to allow for signal read out. Therefore they are labeled on two sides (even channel numbers on one side and odd channel numbers on the other) of the detector for both p-side (Fig. 4.9(a)) and n-side strips (Fig. 4.9(b)). The choice of this arrangement was decided in order to reduce the geometrical complexity of the signal processing electronics and allow to use standard high-density multi-pin connectors. The connectors at each corner of the detector provide additional connection options that are shown more in detail in Fig. 4.10.

In Fig. 4.10 two microscopic photographs of a corner of the p-side (a) and n-side (b) of the detector are shown. The details of the different electrical bonding structures are highlighted and labeled. The outermost *contact edge* acts as a protection of the silicon wafer against dicing edge current flow, but it is usually not used because the inner guard (or so-called *bias*) rings can provide, if needed, enough protection to the wafer as there are multiple surrounding rings available. The *guard ring*(s) can also be called *bias ring*(s): depending on the side of the detector to which the bias is given, it can be either put to ground (GND) or to the same potential as the strips of the same side as additional option for biasing the detector. It can also be left floating if the biasing potential is already applied directly to the strips of the same side. When biasing via the bias ring, a technique called *punch-through effect* [171] is used (a detail of this structure is also shown in Fig.

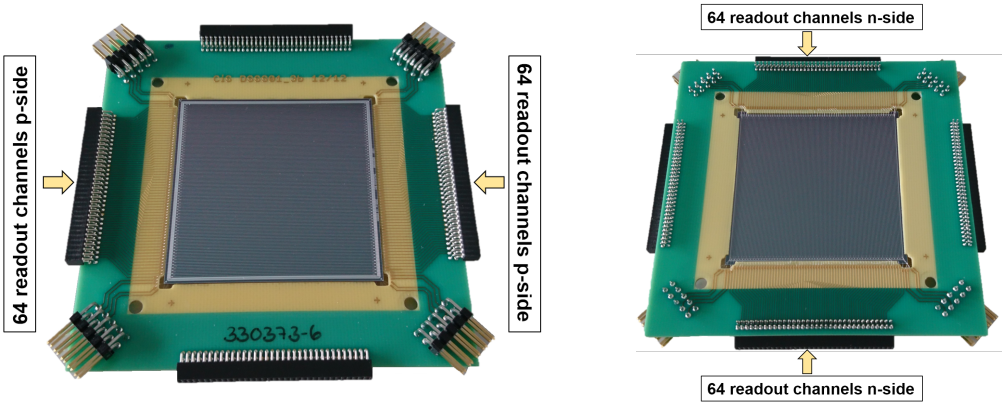

(a) (b)

Figure 4.9: Photograph of one double-sided silicon strip detector (DSSSD), used as part of the scatter component of the LMU Compton camera, seen from the (a) p-side and (b) n-side of the detector. The 128 p-strips and 128 n-strips are read out from each side of the detector, in groups of 64 channels.

4.11). This biasing technique is based on the depletion of a gap (usually < 10 μm) that is located between the ring and the strip(s) end; this then bridges the high voltage to all the strips. The signal from the *additional strip* is usually not read out, but this strip is biased to maintain a homogeneous electric field over the strip area if the biasing voltage is given via the strips. For both p- and n-side, the 64 odd strips are read out from one side and the even strips from the opposite side of the detector.

In our case, when the detector is biased directly through the strips, an AC coupler (see Chap. 5 for more details) is placed inbetween the supply voltage and the strips themselves in order to protect them, because the detector itself is DC coupled. The bias ring can also be left floating: suggestions from the manufacturer and tests performed in our laboratory brought us to the conclusion that in the two different situations in which the bias ring is left floating or is put at the same potential of the strips, the detector performance does not change significantly, since the noise induced from the dicing edge is negligibly small (conclusions from a test in the laboratory can be found in Chap. 6).

From the information shown in Fig. 4.11 in a detailed view of the implantation layout of the DSSSD as provided by the manifacturer, the internal structure of two neighboring strips can be observed. The *pad* is a passivation window created at the end of each strip in order to have a metallic contact where a wire that will carry the signal is bonded. As this passivation window is located only at the end of each strip and its area is much smaller than the whole strip area, the scattering effects on the incoming electrons due to the width of the aluminum deposited here can be neglected.

During this thesis project three other DSSSD modules with different structure and characteristics were also tested and used in some online experiments, including them in the Compton camera system as alternative or additional scattering layers, mainly to test the

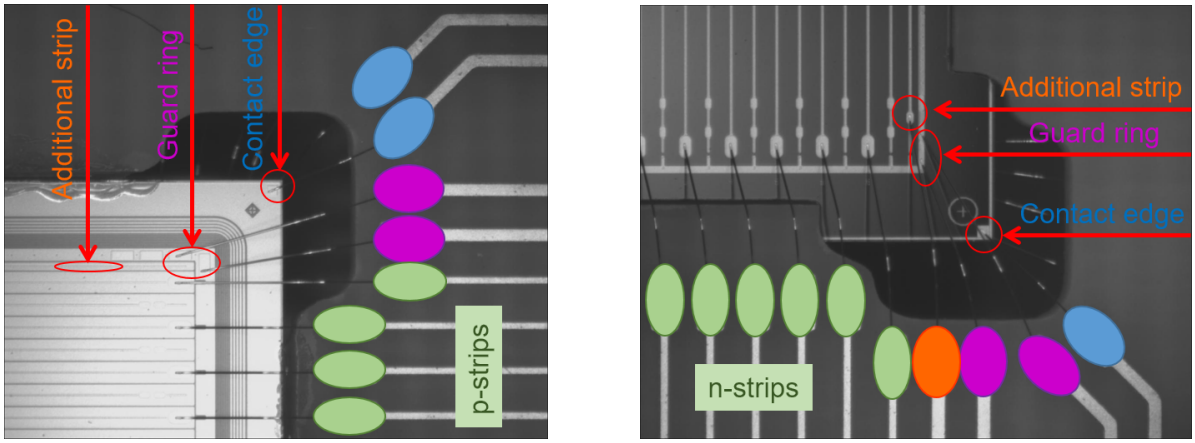

(a) (b)

Figure 4.10: Microscopic photograph of two corners of the DSSSD detector: (a) p-side and (b) n-side. The electric bondings in the corners of the detector PCB which are connected to specific structures (additional strip, guard ring, contact edge, p- or n- strips) are labeled and marked with related colors [191].

effect of the increase of single and total scatter detector thickness on the overall performance of the camera (more details about those tests will be provided in Chap. 6). Each of these additional DSSSD modules have a thickness of 1 mm, an active area of 40 × 40 mm^2 and a pitch size of 1 mm [193]. In Fig. 4.12 a photograph of the p-side (a) and n-side (b) of one of these detectors is shown. In this case the strips to be read out are 80 in total, 40 on the p-side and 40 on the n-side of the detector. All strips from one side are read out via one common connector. As the number of strips per detector side is less than the number of strips per side in the 500 μm DSSSD modules, it is possible to use the same readout electronics for both DSSSD models.

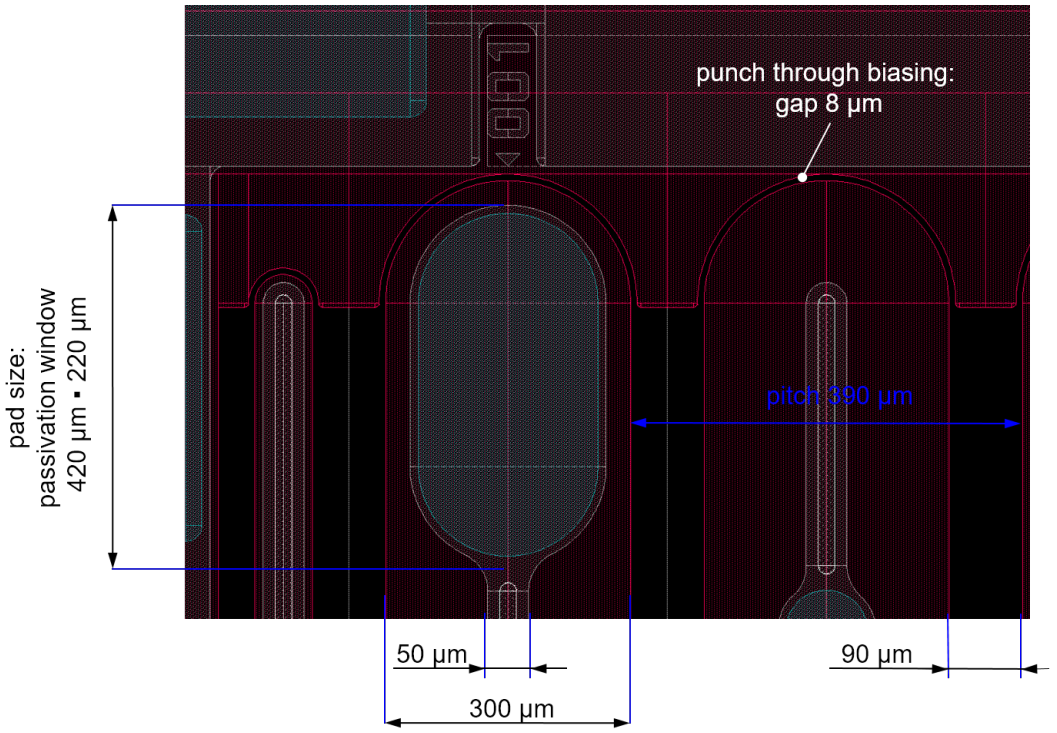

Figure 4.11: Implantation layout details of one strip of the DSSSD used in the LMU Compton camera. The pad is used to provide the metallic contact to the strip and acquire its electronic signal, the pitch size is corresponding to the width of one strip and the punch-through gap of 8 mm allows for applying an alternative method to bias the strips of the detector in the specific case of our double-sided silicon strip detectors [191].

4.4 Absorber component

This section is dedicated to the absorber component of the Compton camera. The main characteristics of the different scintillation materials being tested will be described, and the photo sensors presently in use and coupled to the scintillator crystals will be presented.

4.4.1 $LaBr_3$:Ce^{3+} scintillation crystals

The first absorber component of the LMU Compton camera prototype that has been characterized and tested is an inorganic scintillation crystal, particularly a 50.8 × 50.8 × 30 mm^3 $LaBr_3$:Ce^{3+} monolithic block, produced by Saint-Gobain Ceramics and Plastics Inc. [180] (BrilLanCe^{TM} 380 [194]). The scintillation crystal is wrapped in a reflective coating, supporting the collection of all scintillation light (a comparison with an absorptive coating scenario was carried out by [195]). The chemical composition for this material was invented about 20 years ago and since then it has received a widespread attention, as it offers excellent properties in all relevant quantities for γ-ray detection (the most important are listed in Tab. 3.1). Of specific interest for our application are the high light

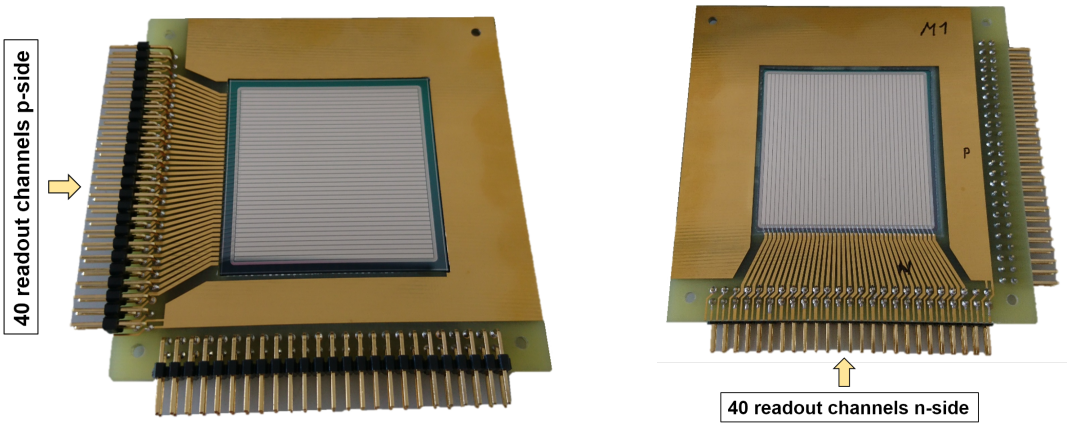

(a) (b)

Figure 4.12: Photograph of the p-side (a) and n-side (b) of the double-sided silicon strip detector from Micron [193], which has a thickness of 1 mm, an active area of $40 \cdot 40$ mm^2 and a pitch size of 1 mm.

yield of $LaBr_3$(Ce) (LY=63000 ph/MeV), its high relative energy resolution (3.5% at 662 keV) and a very fast decay time (τ=16 ns). The excellent time resolution allows for the use of the Time-of-Flight (ToF) technique for neutron-γ discrimination, and the excellent energy resolution allows for a better definition of the energy information needed for the reconstruction of the prompt-γ origin. As this scintillation crystal is used in our prototype as absorber component, the fact that its effective atomic number and density are lower compared to other scintillation materials (Z_{eff}=47 and ρ=5.29 g/cm^3, respectively) is not a drawback, because the crystal volume can be scaled accordingly to detect the photons of interest, with sufficient efficiency, while still limiting the multiple Compton-scattering probability.

However, $LaBr_3$(Ce) crystals possess also some less favorable characteristics. First their hygroscopicity should be considered: the structure of the crystal is quickly affected by humidity and for this reason the scintillator material needs to be encapsulated inside an aluminum housing which prevents water vapor from deteriorating the material. The drawback is that the layer of aluminum surrounding the material may affect the detector's performance by scattering and absorption. The other feature that should be noted is the internal radioactivity intrinsically present in a $LaBr_3$(Ce) crystal. This property has two origins: the presence of radiochemical impurities of ^{227}Ac and its α-decay daughters, and the presence of the unstable isotope ^{138}La. The contamination due to ^{227}Ac affects the spectrum for energies between 1.6 and 3 MeV: for these undesired contributions a solution can be found by a possible radiochemical purification of the material during the crystal production process [196]. In contrast, the internal radioactivity arising from the presence of ^{138}La cannot be avoided at present. The ^{138}La-induced activity dominates below 1.6 MeV [197]. ^{138}La is the only naturally occuring radioactive isotope of lanthanum, with an

abundance of 0.09 % and a half-life of $1.05 \cdot 10^{11}$ years [198]. Figure 4.13 shows the decay scheme of the ^{138}La isotope: with 66.4% it decays into ^{138}Ba by electron capture (EC) and a subsequent γ emission of 1436 keV, whereas with the remaining 33.6% the isotope undergoes a β decay that results in an excited state of ^{138}Ce and an emission of a 789 keV photon.

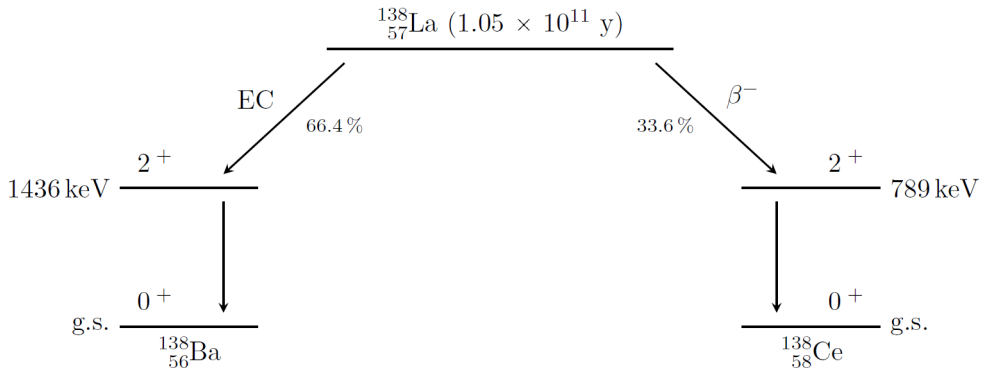

Figure 4.13: ^{138}La decay scheme

The energy spectrum showing the internal radioactivity energy distribution of the $LaBr_3$ crystal can be measured by shielding the detector with lead blocks, in order to reduce contributions from room background and cosmic radiation as much as possible, thus acquire only signals from scintillation processes due to the internal activity of the crystal. Figure 4.14 shows this γ-ray energy spectrum acquired with our $50.8 \times 50.8 \times 30$ mm^3 $LaBr_3$(Ce) crystal for 4 hours. It can be seen that in the spectral range below 1.6 MeV the main contribution is given by the radioactive decay of ^{138}La, coming from the β decay for low energies and from the EC for higher energies. The first peak structure, labeled as ^{138}*Ba K captures*, corresponds to the 35.5 keV X-ray emission caused by the refilling of the hole in the atomic K-shell of ^{138}Ba, left behind by the EC process [197]. A peak at 4.5 keV, produced in an analogous process but coming from the L-shell X-ray emission, could also be measured, but it is not shown in this spectrum because of the dominant background at low energies anf because of the related trigger threshold. The second structure observable in the spectrum accounts for the β continuum of ^{138}La, representing the 33.6% of the ^{138}La decay, with an end point of 255 keV. This contribution can also be found at higher energies, when detected in coincidence with the 789 keV γ ray, which is labeled as $^{138}La\ \gamma + \beta$ in the spectrum. The prominent photopeak that follows in the spectrum corresponds to the 1436 keV γ ray emitted in coincidence with the capture of X-rays resulting when an hole in the K and L levels of ^{138}Ba (35.5 keV and 4.5 keV, respectively), as previously mentioned, is refilled. For this reason the photopeak can be observed with an energy shift: to 1440 keV or 1472 keV, if detected together with X-rays from L or K shell, respectively. When the 1436 keV γ ray escapes the crystal, the very first two peaks, at 4.5 keV and 35.5 keV, are observable as they would not be in coincidence with the energetic γ ray. Above 1.6 MeV the peaks which originate from the β and α decay of ^{227}Ac and its daughter nuclei

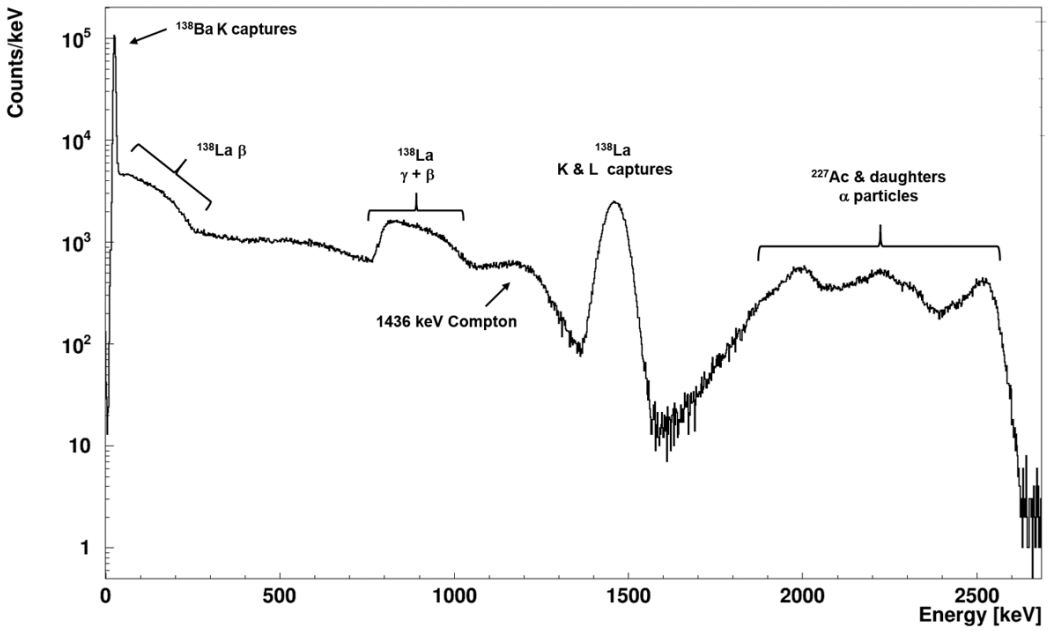

Figure 4.14: Internal radioactivity energy spectrum of a (lead-shielded) 50.8 x 50.8 x 30 mm^3 monolithic $LaBr_3$(Ce) scintillation crystal. The energy spectrum was acquired by measuring for 4 hours. The two decay modes of ^{138}La are visible, together with the contribution from the impurities of ^{227}Ac and its α-decay daughter nuclei.

are visible.

For ^{138}La the total activity has been measured to be 1.45(7) Bq/cm^3 [197]: this results in ∼150 counts/s for our 50.8 × 50.8 × 30 mm^3 crystal.

While on one hand the internal activity is an undesired feature of this scintillation crystal, on the other hand this characteristic can also be used for useful purposes. For example prominent structures, such as the photopeak at 1436 keV, can be used as a permanent online energy calibration point. Furthermore, the radiation coming from these decays can be used to mimic a homogeneous and isotropic external irradiation of the crystal, in order to define parameters that will help assessing the homogeneity of the crystal response (see more details in Chap. 6).

4.4.2 $CeBr_3$ scintillation crystals

$CeBr_3$ is a scintillation crystal that was recently developed [199, 200], after the development of the above described $LaBr_3$(Ce) crystal. Belonging to the same group of halide crystals, it has very similar properties as $LaBr_3$(Ce) [201, 202] and is therefore being evaluated as an alternative absorber material for our Compton camera prototype, as $CeBr_3$ exhibits only negligible internal radioactivity and its price is considerably lower. Its decay time is very fast (17 ns compared to the 16 ns of $LaBr_3$(Ce)), the light yield is even slightly higher (68000 ph/MeV compared to 63000 ph/MeV) and the (relative) energy resolution presents

also excellent values (around 4% at 662 keV). The scintillation light coming from $CeBr_3$ and $LaBr_3$(Ce) is emitted at the same wavelength (380 nm), meaning that the light can be guided to be read out with the same photosensors (see more details in the next section). $CeBr_3$ is also hygroscopic: the 50.8 × 50.8 × 30 mm^3 monolithic crystal from Scionix [181] came therefore already encapsulated in an aluminum housing with one side covered only with a 5 mm thick quartz light-guide window.

Neither cerium or bromine possess any naturally occuring radioactive isotopes, thus the $CeBr_3$ material per se does not contain an internal radioactivity like $LaBr_3$(Ce). However, also in $CeBr_3$ crystals minor contaminations of alpha emitting impurities from ^{227}Ac and its daughter nuclei cannot be avoided [203, 204]. Scionix offers $CeBr_3$ crystals in two different radiopurity classes: "standard" with a background rate of 0.025 counts/(s·cm^3) and "ultra-low background" with <0.001 counts/(s·cm^3) [205]. The crystal that was studied belongs to the "ultra-low background" category.

In Fig. 4.15 an energy spectrum that was acquired with the 50.8 × 50.8 × 30 mm^3 monolithic $CeBr_3$ scintillation crystal under the same conditions as for the $LaBr_3$(Ce), is presented.

The broad peak structure observable at the high-energy end of the spectrum, can again, although with reduced intensity due to radiochemical purification compared to the $LaBr_3$(Ce) case, be attributed to the α contamination in the crystal, caused by ^{227}Ac and its daughter nuclei [204].

As the internal radioactivity of the $CeBr_3$ scintillation crystal is almost negligible (the expected number of counts from the alpha contamination in the spectrum in Fig. 4.15 acquired in an hour of measurement time and in the relevant energy range from $\sim$ 1.8 - 2.4 MeV amounts to 270) and since this crystal is a cheaper option compared to $LaBr_3$(Ce), as such it is a viable alternative for the absorber component of our Compton camera prototype, as it would be able to keep comparable performance parameters.

4.4.3 Photo sensor: photomultiplier tubes

The light generated in a scintillation crystal contains the energy information of the incoming γ ray and should therefore be read out by a photo sensor. In our case we decided to use a photomultiplier tube, specifically a segmented multi-anode PMT. With the help of an algorithm that takes the pixelated 2D light amplitude distribution as input (which will be described in Chap. 6) we can therefore determine an interaction position information from the monolithic crystal that acts as absorber component of the Compton camera.

During the project presented in this thesis, three different PMTs were investigated, together with the same amount of scintillation crystals, whose characteristics were presented in the previous section. The crystals have all the same dimensions of 50.8 × 50.8 × 30 mm^3: one $CeBr_3$ and two $LaBr_3$(Ce) scintillation crystals were used.

The scintillation light from the two $LaBr_3$(Ce) crystals is collected and read out by a 256-fold segmented multi-anode PMT (H9500 Hamamatsu [206]) and a 64-fold segmented multi-anode PMT (H8500C Hamamatsu [207]), respectively. For the $CeBr_3$ crystal another type of 64-fold segmented multi-anode PMT (H12700A-10 Hamamatsu [208]) was used. All

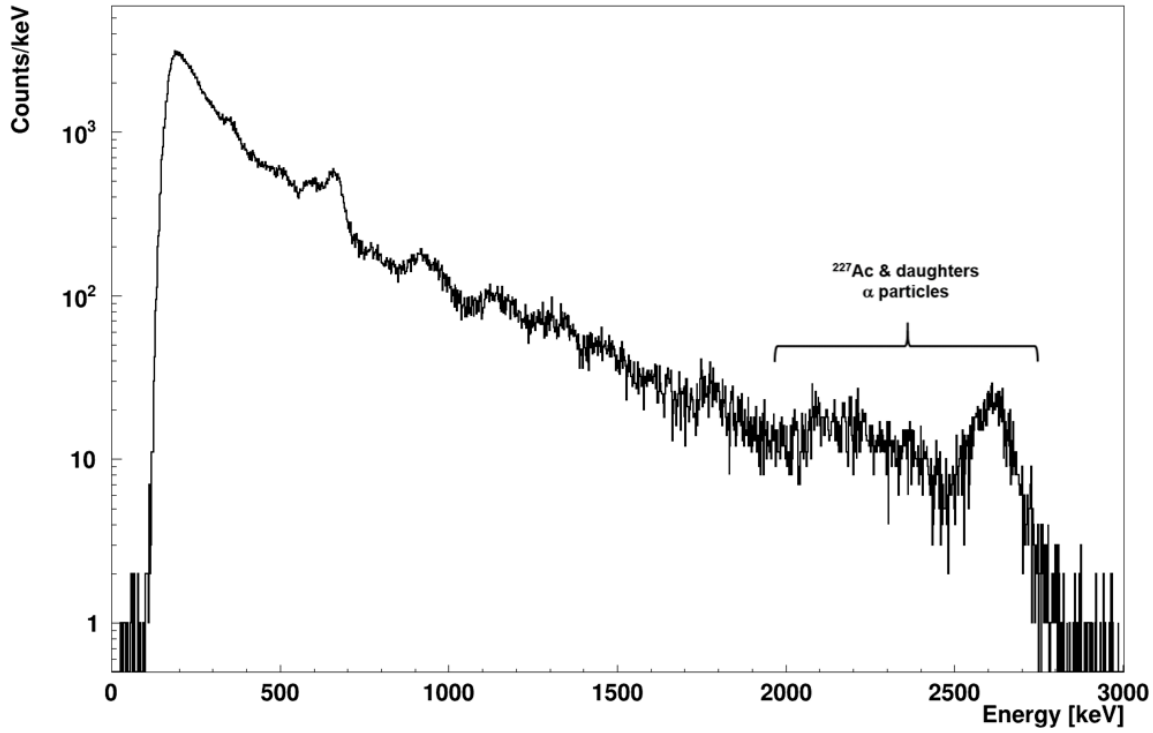

Figure 4.15: Internal activity energy spectrum of a (lead-shielded) 50.8 x 50.8 x 30 mm^3 monolithic $CeBr_3$ scintillation crystal. The energy spectrum was acquired by measuring for 1 hour. There is a small contribution coming from ^{227}Ac and its α-decay daughter nuclei impurities which can be observed at the high-energy end of the spectrum. It should be noted that most of the spectrum originates from room background and cosmic rays, since the internal activity rate is given by the manifacturer as <0.001 counts/(s·cm^3).

those PMTs also have a so-called *sum dynode* channel: here all the charge accumulated is collected at the last dynode.

The H9500 PMT [206] has 256 anode pixels (arranged in a 16 × 16 matrix) and each of them has a size of 2.8 × 2.8 mm^2 (apart from the central pixel which has a size of 3.04 × 3.04 mm^2). The outer dimensions of the PMT are 52 x 52 mm^2 and the effective area is 49 × 49 mm^2, therefore slightly smaller than the actual $LaBr_3$(Ce) crystal size: for this reason we may lose some scintillation light from the corners of the crystal in case of incomplete collection by the light-guide. The PMT can be operated with a supply voltage between (-)700 V and (-)1100 V and on the right panel of Fig. 4.16 the gain of the PMT as a function of the supply voltage is shown. On the left side of this Fig. the cathode sensitivity and the quantum efficiency as a function of the impinging photon wavelength are shown: it can be observed that the spectral response of this photomultiplier is in a wavelength range between 300 and 650 nm, with a peak wavelength at 400 nm, which is

very close to the 380 nm peak emission of the $LaBr_3$(Ce) crystal.

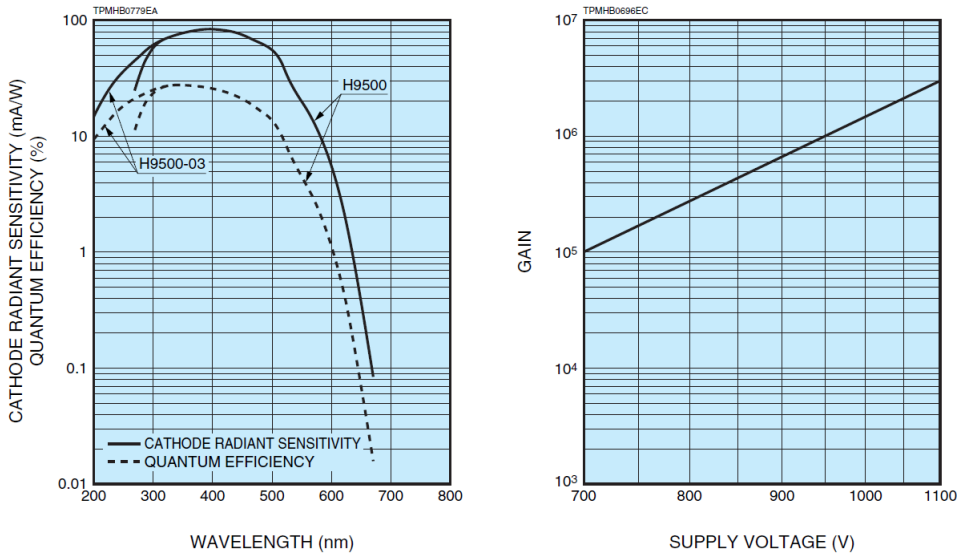

Figure 4.16: Quantum efficiency as a function of the incoming photon wavelength (left panel) and gain as a function of and supply voltage (right panel) of the H9500 PMT series from Hamamatsu [206].

The H8500C PMT [207] has 64 anode pixels (arranged in an 8 × 8 matrix) and each of them has a size of 5.8 × 5.8 mm^2. The outer dimensions of the PMT are 52 × 52 mm^2 and the effective area is 49 × 49 mm^2, therefore again slightly smaller than the actual $LaBr_3$(Ce) crystal size, like in the H9500 case. The PMT can be operated with a supply voltage between (-)700 V and (-)1100 V and on the right panel of Fig. 4.17 the gain of the PMT as a function of the supply voltage is shown. On the left side of this Fig. the cathode sensitivity and the quantum efficiency as a function of the photon wavelength are shown: it can be observed that the spectral response of this photomultiplier is also in a wavelength range between 300 and 650 nm, with a peak wavelength around 400 nm.

The H12700A-10 PMT (being the successor of the H8500 PMT in the product portfolio of Hamamatsu) has, like the H8500C, 64 anode pixels arranged in an 8 × 8 matrix, each with a size of 6 × 6 mm^2. The outer dimensions are the same as for the other two PMTs, but the effective area for this PMT is 48.5 × 48.5 mm^2 and thus slightly smaller. The range for the operational voltage is the same as for the other PMTs and the range of the spectral response is also matching with the wavelength emission of the $CeBr_3$ crystal (observable in Fig. 4.18 on the left). There are two important differences between this PMT and the H8500C: the gain is 2.33 ·10^6 for the model H8500C and 0.62 ·10^6 for type H12700A-10, at an operational voltage of -1000 V (these values were provided by the manufacturer and do not reflect the exact absolute numbers plotted in Fig. 4.17 and Fig. 4.18 since they depend on the specific PMT in use, while the trend of the values is valid for all specific PMT of one type). This is due to the fact that they have, respectively, 12 and 10 dynode stages. The second differing feature is the quantum efficiency: as it is observable in Fig. 4.17 and

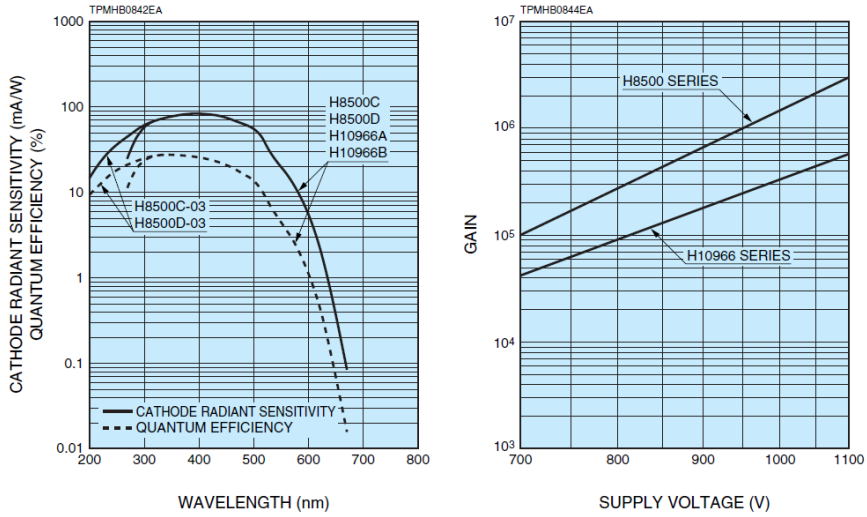

Figure 4.17: Quantum efficiency as a function of the incoming photon wavelength (left panel) and gain as a function of the supply voltage (right panel) of the H8500C PMT series from Hamamatsu [207].

4.18, H12700A-10 has a higher quantum efficiency. The operational voltage will therefore be adjusted accordingly to the signal amplitude needed for the specific readout electronics (see more details in Chap. 6 where the settings used for the different measurements are presented).

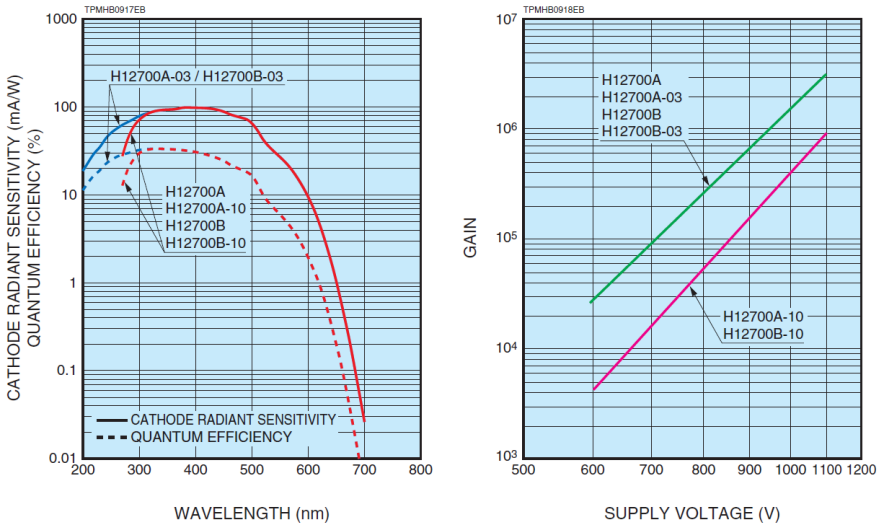

Figure 4.18: Quantum efficiency as a function of the incoming photon wavelength (left panel) and gain as a function of the supply voltage (right panel) of the H12700A-10 PMT series from Hamamatsu [208].

In Fig. 4.19 photographs of both H9500 (a) and H8500C (b) PMTs are shown, and the

different pixel sizes can be observed. For both PMTs the SHV cable for the supply voltage are also visible.

(a) (b)

Figure 4.19: Photographs of the H9500 PMT (a) [206] and H8500C PMT (b) [207] from Hamamatsu, both with their SHV cables for the supply voltage.

All of these PMTs operate on the basis of bialkali photocathodes and the window that will face the scintillation crystal is made of borosilicate glass (which has a refractive index of 1.52). In order to collect all the scintillation light from a crystal and guide it to the photomultiplier to be read out, the refractive indexes of all materials involved inbetween crystal and PMT have to match to act as an optical guide. The $LaBr_3$(Ce) coupled to the H9500 PMT was purchased already fully encapsulated and coupled from Hamamatsu (as it can be noticed from the photo in Fig. 4.20(a)): a 5 mm thick window made of quarz glass (which has a refractive index of 1.56) was inserted between the borosilicate glass window of the PMT and the $LaBr_3$(Ce) crystal.

The other $LaBr_3$(Ce) crystal and the $CeBr_3$ crystal were both separately coupled to their PMT's (H8500C and H12700A-10, respectively) in our laboratories. For this coupling we used an optical grease (BC-630 optical grease [209]) between PMT and crystal surfaces, which has an index of refraction of 1.465 and a very flat transmission of approximately 95 % for wavelengths between 280 nm and 700 nm. Figure 4.20 presents a photograph of both the $LaBr_3$(Ce) coupled to the PMT from Hamamatsu and the $LaBr_3$(Ce) crystal that was coupled in our laboratories, which from the outside looks the same as the $CeBr_3$ crystal coupled to its PMT.

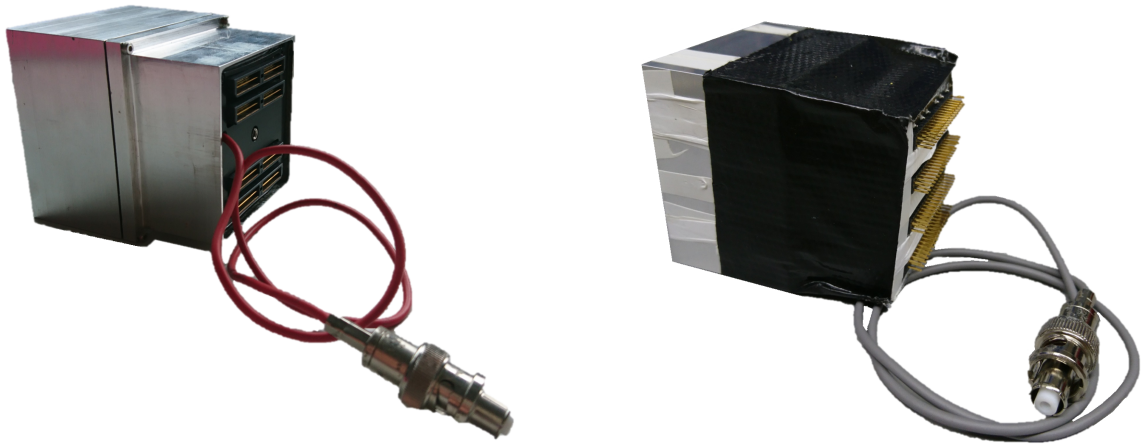

(a) (b)

Figure 4.20: Photograph of a 50.8 × 50.8 × 30 mm^3 $LaBr_3(Ce)$ monolithic scintillation crystal coupled to an (a) 256-fold segmented H9500 PMT (Hamamatsu [206]) and encapsulated into a joint housing, (b) 64-fold segmented H8500 PMT (Hamamatsu [207]) separately encapsulated and later coupled to the PMT in our laboratories.

CHAPTER 5

Signal processing and data acquisition

This chapter is dedicated to the signal processing and data acquisition system of both detector components of the Compton camera prototype we are developing in our laboratories at LMU Munich. The chapter is structured in three main sections. The first section presents the signal processing electronics for the DSSSD detectors: different options to consolidate the initial start version were tested and will be presented. In the second part of this chapter the signal processing electronics for the absorber component of the camera is presented: two solutions in use are presented, as the final aim is also to merge the data stream from the two detector components in a less complex and more user friendly way. The last section of chapter 5 is dedicated to the data acquisition system, which is based on VME in both solution implemented and tested.

5.1 Double-Sided Silicon-Strip detector readout

The Compton camera scatter component, as presented in Sect. 4.3.1, is composed of a stack of 6 layers of DSSSDs. The 128 n-strips and 128 p-strips from the two sides of each detector layer are forming a 2D grid in (x,y) dimension. These DSSSD detectors are designed to be read out from all four sides: each two opposite sides transfer the odd and even strip signals for both n- and p-side, respectively, to the dedicated signal processing electronic chain. Therefore at each of the 4 sides of each DSSSD layer the signals from 64 odd or even strips can be processed. In the following three parts of the current section, three different signal processing electronics chains are presented and discussed. These show the development and testing procedures during the course of the project, aiming to define the most suitable readout electronics system for the specifications dictated by the signal's properties of our silicon detectors. As we do not develop and produce highly integrated electronics boards in-house, this process had to take into account the availability of suitable

components on the commercial market.

5.1.1 Gassiplex ASIC chip and system

The readout system that was used as a startup configuration at the beginning of the Compton-camera project for reading out the signals from the DSSSD detectors is based on the Gassiplex ASIC chip. The front-end boards based on the Gassiplex chip were originally designed for the ring-imaging Cherenkov detector (RICH) in the High Acceptance Di-Electron Spectrometer (HADES) project [210, 211] and used also for the readout of Micromegas detectors [212]. They were kindly provided to us by the E12 group at the physics department of the Technical University of Munich.

A photo of one front-end (FE) electronic board is depicted in Fig. 5.1, together with the AC coupler, which was designed by us and is connected between the detector and the readout board. In Fig. 5.2 its electronic layout is shown.

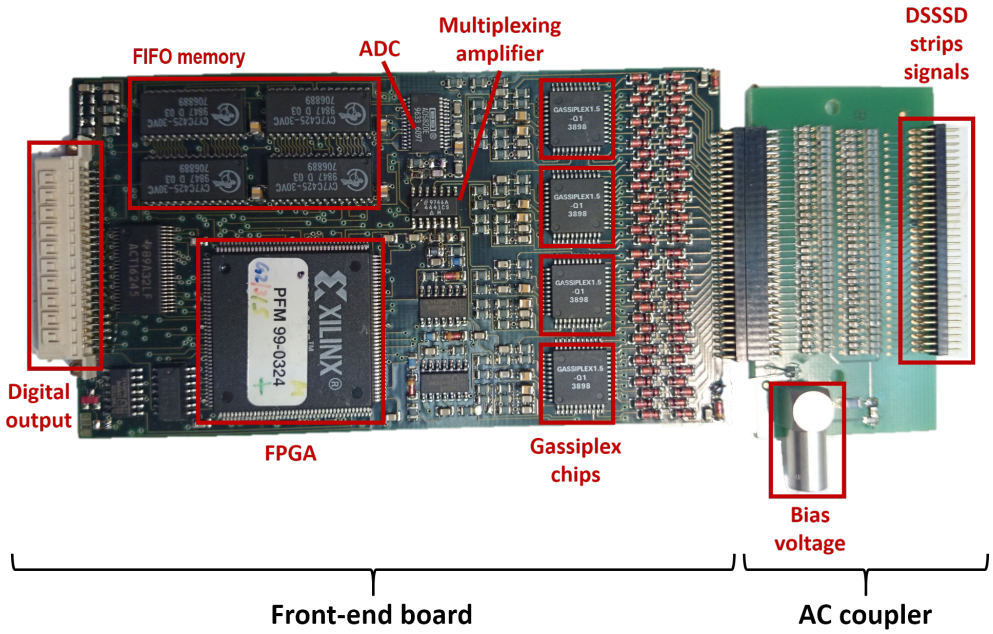

Figure 5.1: Photograph of the front-end board based on the Gassiplex chip, together with the AC coupler board. The FE board can be divided into two parts, dealing with analog and digital signals. The analog part consists of the four GASSIPLEX ASIC chips: each of them includes a charge sensitive preamplifier, shaper, track & hold stage and a multiplexer with a multiplexing amplifier that directs the analog outputs to the ADC unit. The memory, where the data are temporarily stored, is of a FIFO (First In First Out) type. The FPGA (Xilinx XC4005E) takes care of the assignments of channel number, hit address and threshold comparison.

A coupling capacitor (C = 1 nF) between the detector signal and the input of the FE

board is necessary in order to protect the circuit on the board from the detector bias voltage as well as its leakage current, which is larger than the critical level of 1 nA [213]. The AC coupler is also used to bias the detector, which in its own design is DC coupled, via the (p- or n-) strips. When a negative voltage (bias = -70 V) is applied to the p-strips, all the n-strips are grounded, and when a positive voltage (bias = +70 V) is given to the n-strips, all the p-strips are grounded. This also ensures a common grounding for the FE modules and the (n- or p-) strips of one DSSSD detector. One detector side is grounded via a 50 Ω termination connected to the strips; the AC coupler's ground potential is connected to a common grounding line and couples the FE modules' ground together with the detector ground potential. The AC coupler was initially built on a 34 × 62 × 1.6 mm^3 PCB (FR4 material [214]), having a dielectric constant of $\mu_r = 4.1$ at 11 GHz. In order to reduce the capacity of the AC coupler board, it was improved by using a 42 × 62 × 0.8 mm^3 PCB made of an available material with a lower dielectric constant, equal to 3.62 at 10 GHz (Megtron 6, Panasonic [215]).

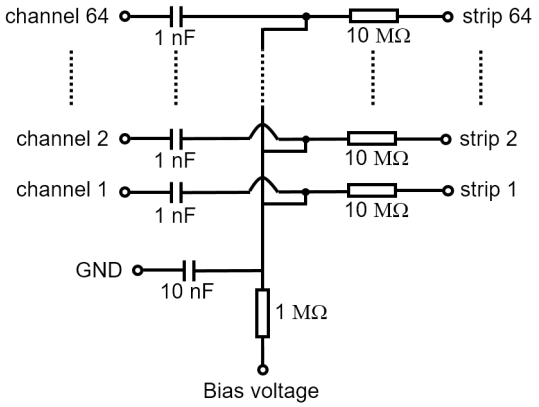

Figure 5.2: Electronical layout of the AC coupler. It has two important duties: protect the signal processing electronics from the detector leakage current and bias voltage, and allow the biasing of the detector via the (p- or n-) strips.

The front-end (FE) board contains four charge integrating Gassiplex ASIC chips (indicated in Fig. 5.1 together with all the main components on the board), each of them processing 16 channels [216]. One front-end board is therefore able to read out and digitize 64 channels, which is equal to the number of strips bonded on each of the four sides of the detector. The strips' signals are amplified and shaped in the Gassiplex ASIC chip by charge sensitive amplifiers (CSA) and shapers, respectively. The 550 ns rise time of the (semi-Gaussian) shaped signal determines the delay between the event arrival time at the absorber detector and the trigger for the DSSSD, since there is no circular buffer implemented at this stage. The analog peak height value is stored for each channel in a track and hold circuit and, for each chip, the 16 channels are multiplexed to one output. The outputs of the four Gassiplex chips are then sent to a 20 MHz 10-bit analog-to-digital converter (ADC, ADS820 [217]). In the FPGA the zero suppression is applied and the

channel number is added to each data word, generating a hit address list for all the 64 input channels of one FE board. After comparing the digitized data to a digital threshold in the FPGA, the pulse height data considered valid and their corresponding hit addresses are stored into a FIFO memory (Cypress CY7C421/5), waiting to be acquired. Thus the Gassiplex chip provides one charge value per strip and trigger, without any timing information. The latter, when operating in a Compton camera arrangement, is provided by the absorber component of the system, which is generating the trigger signal.

Since every FE board can read out 64 channels, which corresponds to the number of channels connected to each side of each DSSSD detector layer, 24 FE boards are in total needed to read out the signals from all of the six DSSSD layers. The ground potential line is guided by a flexible copper wire around the lemo connector mass of the AC couplers and the detector side which is grounded, in order to realize a common ground potential in the whole setup.

(a) (b)

Figure 5.3: Photograph of the VME Readout Controller (RC) module (a) and the Detector Trigger Unit (DTU) module (b) needed for the acquisition of the signals from the DSSSD layers using the readout electronics based on the GASSIPLEX ASIC chip system.

Figure 5.4 shows a schematic diagram of the whole setup for the six DSSSD layers based on the Gassiplex system. In order to assemble the digitized data from all the FE boards, a bus card is used: it collects data from six FE boards sequentially on each detector side, as it can be observed from the scheme. Four bus cards are therefore needed for the setup; the collected data are then sent, via a standard 0.635 mm pitch 50-pin flat ribbon cable, to a VME Readout Controller (RC) unit (a photo of this module is shown in Fig. 5.3(a)) [211]. Since these FE boards do not provide an internal trigger signal, a dedicated VME-based trigger module (Detector Trigger Unit, DTU, in Fig. 5.3(b)) is used to receive an external TTL signal, which has to be generated by the absorber detector, and return a feedback

(busy) signal while acquiring signals from the Gassiplex setup.

This arrangement allows to have the data streams from both scatter and absorber components merged and synchronized. All data are then transferred through the VME bus to the data acquisition PC using a VME-based frontend CPU (which will be described in Sect. 5.3.1 together with the data acquisition software) via an ethernet cable.

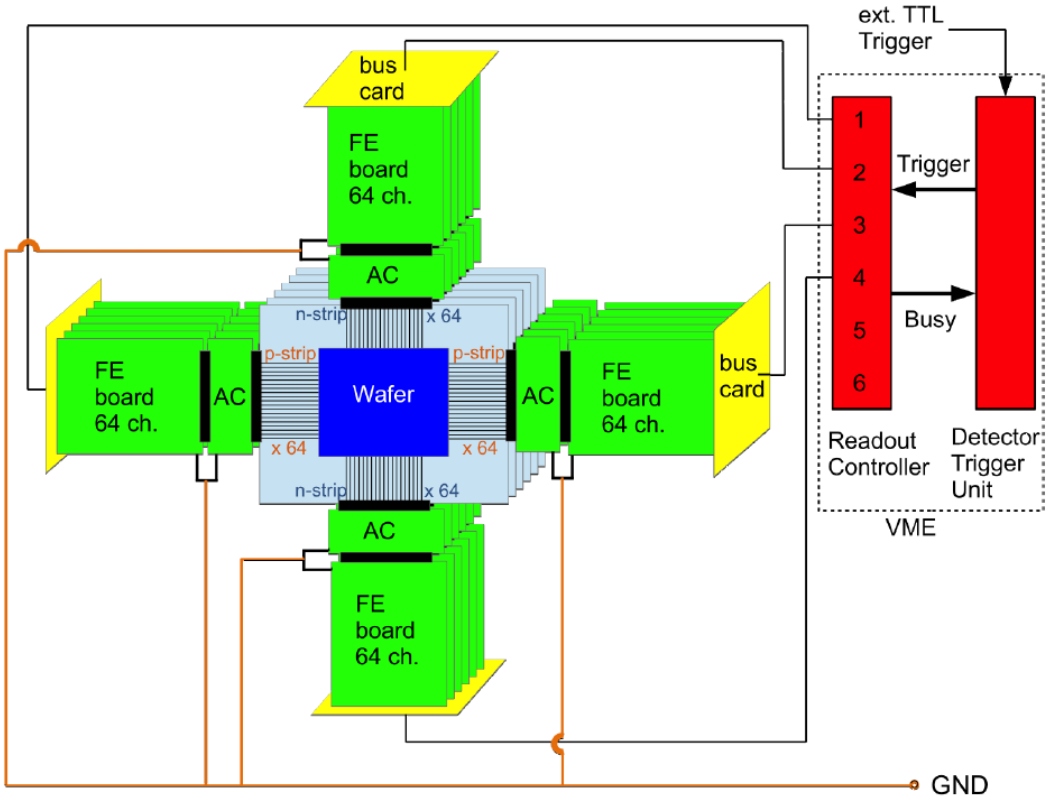

Figure 5.4: Schematical drawing for the geometrical arrangement of the six DSSSD layers with the readout electronics based on the GASSIPLEX chip. Each DSSSD layer provides 2 x 128 signal channels, which are read out using four (64 ch.) FE boards, connected to the detector via an AC coupler (see the text for more details). On each side of the whole DSSSD setup there are 6 FE boards, which are combined together using a bus card. This card collects and transfers digital data to a VME-based detector readout controller. Since the GASSIPLEX ASIC can't generate an internal trigger signal [139], a VME-based trigger unit is also needed in order to accept an external TTL trigger signal.

Drawbacks and further requirements

Since the readout system based on the Gassiplex ASIC chip was initially developed for another project in which gaseous detectors were used, it had to be adapted for our purposes. Our DSSSD detectors produce positive and negative polarity signals, on p- and n-side,

respectively, whereas the GASSIPLEX ASIC chip was designed to accept only positive polarity signals. The related modifications which were applied to the FE boards (basically a shift of the baseline for negative signal processing) can be found in a previous PhD thesis in the framework of our project [139].

The effects of these modifications should be noted: in Fig. 5.5 the output of one DSSSD module is shown (i.e. 2 x 64 signals for p- and n-side, respectively), with a bias voltage of -70 V applied to the p-side of the detector and no external radioactive source in use. The baseline of the p-strip configuration was set to 0.47 V, which translates into about 100 ADC channels (from the 10 bit overall dynamic range). For allowing the acceptance of also negative n-side signals, the baseline for this case was shifted upwards and set to 2.85 V, corresponding to about 600 ADC channels. It can therefore be noted that with these modifications the negative signal configuration allows for the acceptance of also negative signals, but at the expense of providing a smaller ADC dynamic range compared to the one for the positive signal configuration. These modifications for the n-side caused as well a reduction of the gain by a factor of 2 and an increse of the noise level by a factor of 2, which summed together made the expected energy loss of the Compton electrons appear to be buried by the noise associated with the signal processing electronics [139]. More about this topic will be discussed in Chap. 7. A new successor readout system should therefore be designed to accept both positive and negative input polarities, in order to allow for a larger ADC dynamic range for both polarities.

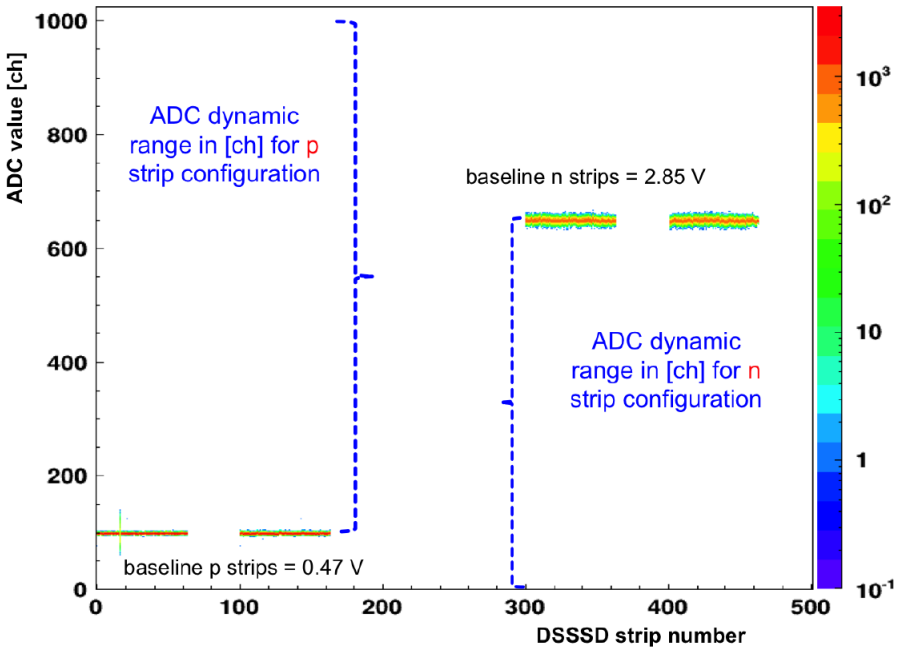

Figure 5.5: p-strip (left) and n-strip (right) data of one DSSSD module, read out with the system based on the GASSIPLEX ASIC chip, after the modifications applied in order to be able to read out both positive and negative polarity signals [139].

In order to fulfill our requirements and overcome limitations imposed by the Gassiplex system, further features of a consolidated readout system of the DSSSD detectors are highly desirable. Since the data acquired in a Compton camera setup should be coincident events between scatter and absorber detector, more logically and efficiently they should be triggered by the scatterer component of the system, providing the lower count-rate due to the lower interaction probability compared to the the absorber component. Thus a triggering capability in the readout system by the silicon layers is required. Other features are also desirable: a selectable shaping time, a larger dynamic range in the ADC component, a lower intrinsic electronic noise and a higher count rate and data throughput capability, since ultimately the concept of this setup should be able to acquire data in a real clinical scenario, in which data rates up to 1 Mcps are expected.

5.1.2 AGET ASIC chip and the GET data acquisition system

Having outlined the shortcomings of the starting version of the DSSSD signal processing electronics, a first attempt was made to cure these deficits by replacing the Gassiplex-based frontend boards by a more modern system, still using an ASIC with improved performance capabilities. The choice was made to give closer consideration to the AGET chip and its peripheral acquisition system, which appeared suitable for our purposes. The AGET (ASIC for General Electronics for TPC) ASIC chip [218] was initially developed for the readout of Time Projection Chambers used in nuclear physics experiments [219] and integrated in a readout called GET (Generic Electronics for TPCs) system [220]. The following section is dedicated to the explanation of the working principle of this readout system, to the reasons that brought us to test it as a potential replacement of the Gassiplex system and why finally our assessment resulted in the need to adopt a more suitable readout system.

The GET system has been designed to accept both signal polarities, thus matching with the signal requirements from the p- and n-side of our DSSSD detectors. Moreover, also the second main upgrade necessity in our DSSSD readout system, the triggering capability, can be provided by the GET system as it can operate either with an internal or an external trigger signal. The 12 bit ADC (instead of the 10 bit ADC of the Gassiplex ASIC system, which gets even reduced for negative signals) gives a larger dynamic range, which in this case is equal for both signal polarities. Furthermore, the amplifier shaping time can be selected in the DAQ software, from a set of different values, the intrinsic electronic noise of the system is lower than for the Gassiplex system (ENC=410 e^-rms for GET instead of ENC=600 e^-rms for Gassiplex) and there is the possibility to implement a monitor capability for the signal at different stages. However, a significant difference arises from the data transfer and communication standard utilized by the GET system, as it is based on μTCA [221] instead of the VME bus. Since the μTCA architecture was originally geared for telecommunication systems, it was designed to provide a high data throughput capability, which also makes the GET system attractive for our application. The μTCA system was introduced by PICGM (PCI Industrial Computer Manufacturers Group [222]) in 2006 and its core components are standard Advanced Mezzanine Cards (AMC [223]), which provide processing and I/O functions. So we started out from the perception that

using a μTCA-based setup in a potential upgrade of the Compton camera setup could therefore allow for a higher data rate throughput compared to the existing VME-based setup.

A complete setup of the GET system includes several μTCA-based modules, but in our case, where this system was tested by reading out an individual DSSSD module with 256 signal channels, a so-called "reduced GET system" was used and will be presented. The boards involved in the signal processing of this small test system can be operated without the need of a μTCA crate.

The first component of the (reduced) GET system is the AsAd (ASIC support & Analog-digital conversion) board, whose photograph is shown in Fig. 5.7. The AsAd board is externally powered by 3.6 V and 5 V bias voltages, delivered by a laboratory power module (ISO-TECH IPS 2303 [224]). Signals originating from the channels of the DSSSD are fed via an AC coupler board (which is shown in Fig. 5.6(a)) and one of the high density flat ribbon cables from Samtec [225] to the corresponding AGET ASIC chip located on the AsAd board, as shown in Fig. 5.7. The AC coupler board was already presented in Sect. 5.1.1 and is needed here for the same reasons as described before. The photograph in Fig. 5.6(a) shows the AC coupler and its upgraded version (b), which had to be implemented in order to add a customized external preamplifier on the same board. This was needed in order to adapt the dynamic range of the AGET chip to the low energies of interest for our DSSSD application (<500 keV). This will be explained in more detail lateron.

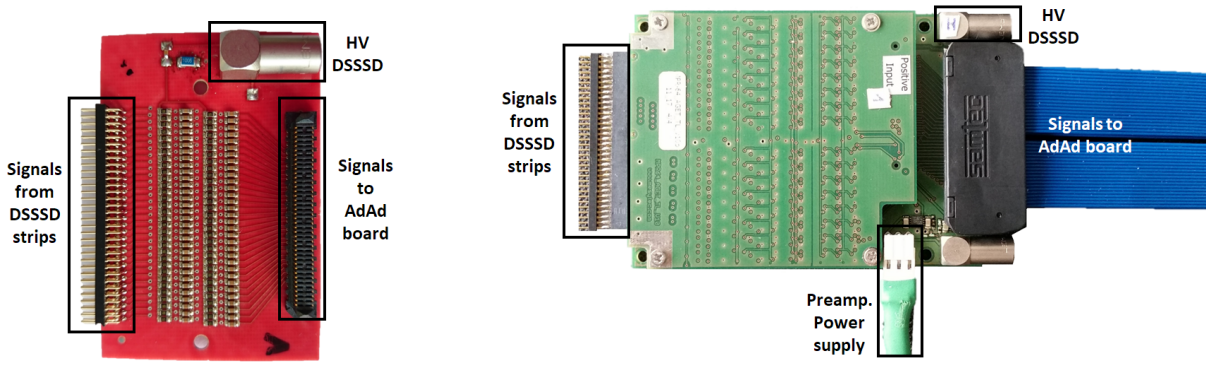

Figure 5.6: Photograph of (a) the AC coupler board which is connected to the DSSSD signal output and the AsAd board input. (b) Photograph of the board which combines both an external preamplifier and the AC coupling to be also placed between the DSSSD and the AsAd board.

Each of the four connectors to the DSSSD is connected to one of the AGET connectors on the AsAd board, since each AGET chip can handle up to 64 channels. Each chip processes also four additional fixed-pattern noise (FPN) channels, which are not connected to the input signals from the detector, thus allowing the noise of the readout electronics

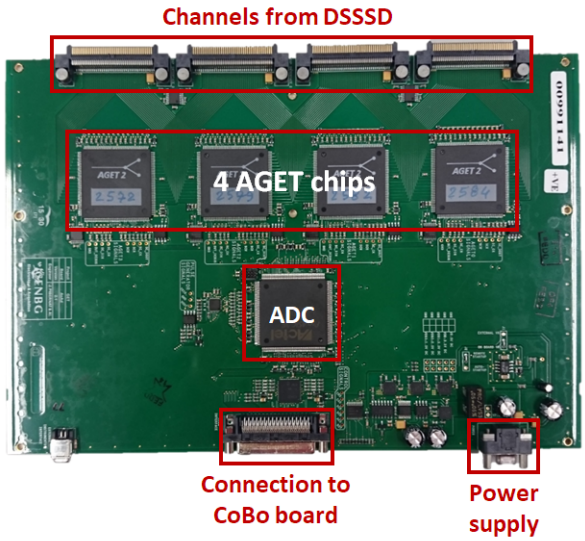

Figure 5.7: Photograph of the AsAd board [220]. The four (64 channel) AGET chips and their corresponding interface connectors, as well as the power supply connector and the CoBo interface connector, are visible. The FPGA chip is also indicated in the photograph.

(excluding detector noise) to be monitored during a measurement. For the p- and n-side of the detector, the AGET chips can be configured differently in the DAQ software in order to accept signals of different polarity. The FPGA is responsible for applying these types of configurations to each AGET chip, as requested by the user through the GET control software, called *GetController*. Through the GetController and the FPGA it is possible to change other parameter settings and to adapt the signal processing to the various signal specifications. The shaping time is selectable in a range between 50 ns and 1 μs; this makes the system flexible and adjustable to different signals, in principle originating also from different detectors than the initially motivating TPC's. The charge sensitive preamplifier (CSA) gain is adjustable in a wide range between 120 fC and 10 pC to properly select the required dynamic range. However, this leads to a minimum dynamic range of up to 20 MeV. Since this energy range is much larger than the average energy deposited in a DSSSD layer of 500 μm thickness in the Compton camera setup and a modification towards a reduced gain was not realistically achievable from the GET developers, it was decided instead to work with a customized external preamplifier, while keeping the GET system for the rest of its beneficial properties. Therefore an external preamplifier module (4 x 64 channels) was designed by Mesytec GmbH [226] (one of them is shown in Fig. 5.6(b)) and included in the GET setup. The board performing the external preamplification includes the AC coupling as well and is connected between the DSSSD detector and the high-density flat ribbon cable connecting to the AsAd board. Using the DAQ configuration software, the output signal of this external preamplifier board is programmed to be fed into the GET signal processing chain before the Sallen-Key low-pass filter (see the AGET data sheet [218] for more details on this configuration). In order to match the acceptance range in the ASIC, a DC offset is

added to the signals from the detector, which are then preamplified and result finally in a sensitivity of 500 keV dynamic range, perfectly matching with the energy range expected from the detected signals. Furthermore, the preamplification is adapted to work optimally for a subsequent 1 μs shaping time, which is the optimized value for a signal from the silicon detector. A key feature of the AGET ASIC is the on-board memory, which is based on a Switched Capacitor Array structure (SCA) and is operated as a 512 cell-depth circular buffer, in which the analog signal emerging from the shaper is continuously sampled, with a selectable frequency from 1 MHz to 100 MHz, before being stored. Another interesting feature for our purpose is given by the possibility to select different modes for the readout of the SCA channels: either all of the channels, only those channels that have fired or specific selected channels can be chosen for readout, thus helping in the acquisition rate management by reducing the amount of undesired data. It is also possible to read the SCA according to a predefined number of analog cells (1 to 512, also called buckets, all of them forming the complete signal trace after digital sampling) and fill up the circular buffer only partly for each event.

A copper plate (visible in the upper right corner of Fig. 5.9) was installed to cover the top side of the AsAd board, additionally to the protective measures always used for the DSSSD, in order to minimize the pick up of external electronic noise. The AsAd board as well as its metal cover plate are connected to the common ground of the experimental setup.

After the analog signals from the detector have been processed by the AsAd board, the digitized signals are transmitted to the rCoBo board (reduced Concentration Board) with a VHDCI cable connection, by 8 differential lines and a maximum speed of 1.2 Gbit/s. A photograph of the rCoBo board used in our setup is shown in Fig. 5.8.

In the framework of the GET system the CoBo (Concentration Board) board is responsible for issuing a time stamp, zero suppression and compression algorithms to the data, according to the user-specified GET software parameter configuration. In the full GET setup the signals from up to four AsAd boards can be transmitted to one CoBo board, whereas in our case the rCoBo is connected via an adapter board just to one AsAd board. The (r)CoBo board is responsible for the communication between the AsAd and the outside world, sending the data via ethernet connection to the computer.

The AsAd board has input ports that allow for the use of an external pulser, which can be sent via the external preamplifier board when needed. Additionally, the board also contains a built-in internal pulser, which can be beneficial for testing the basic setup of the AsAd and rCoBo boards connected to the DAQ PC before sending the actual physical signal coming from the DSSSD layer. Figure 5.9 shows a sketch of the signal flow through the different boards, in either external pulser or DSSSD signal case, before being acquired via the GetController software.

In order to test the system and its performances related to our Compton-camera application requirements, different measurement series have been performed: pedestal runs (with and without connection to the DSSSD detector), (internal and external) pulser tests and acquisition runs using a radioactive source placed in front of the DSSSD layer.

The plot in Fig. 5.10 was acquired by connecting the DSSSD module (biased with -70

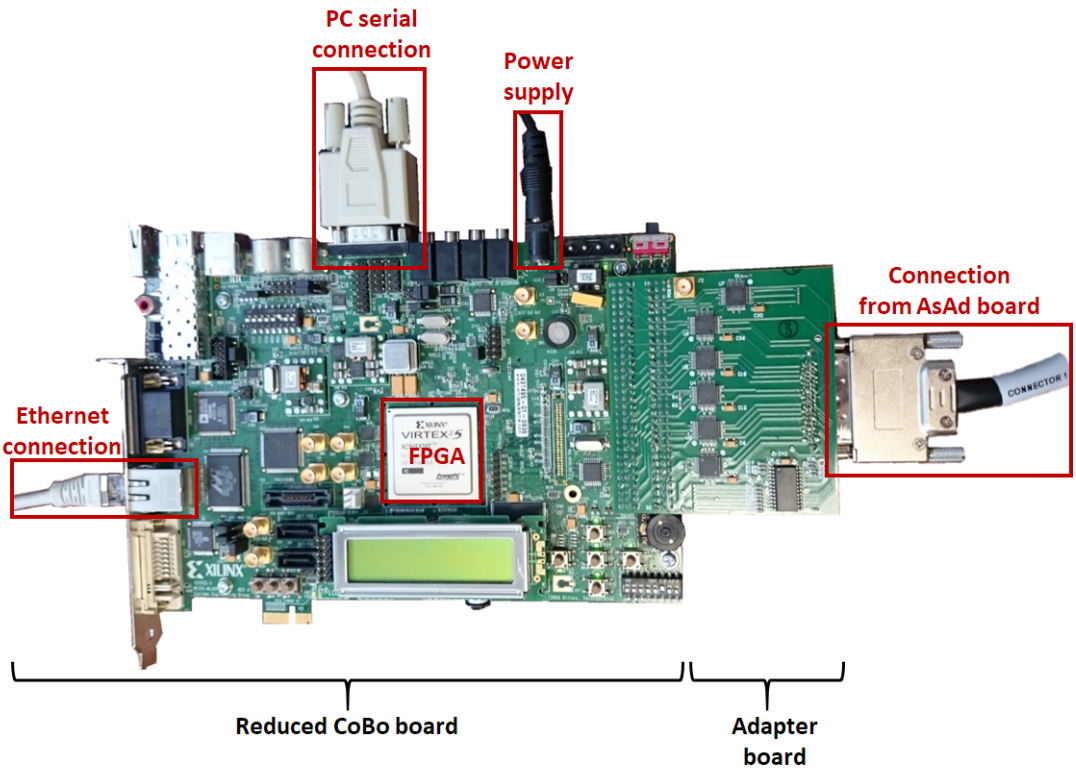

Figure 5.8: Photograph of the Reduced CoBo board together with its adapter board which connects to the AsAd board [220].

V from the p-side) to the readout electronics of the reduced GET setup without using any external source. Figure 5.10(a) shows the energy pedestal raw data, processed by all four AGET chips, whose channels are labelled in Fig. 5.10 and separated by black vertical lines. The AGET chips receiving (pedestal) signals from the p-side and n-side of the detector were configured accordingly in the GetController software. The x axes represent the DSSSD strip number (68 per chip: 64 channels + 4 FPN channels), whereas the y axes represent the ADC channel values and the colour bars on the right side refer to the intensity (number of counts for a specific ADC value in a specific AGET channel). In Fig. 5.10(a) the y axis is zoomed to visualize the distribution of the noise level in ADC channel values. By subtracting the $\sim$ 290 ADC channels as average pedestal value from the two p-side configured AGET chips and the $\sim$ 410 ADC channels from the two n-side configured AGET chips, the pedestal values are offset-corrected (Fig. 5.10(b)) and can be compared to what could be achieved with the Gassiplex readout system in terms of dynamic range (whose plot was shown in Fig. 5.5). Even though the full dynamic is reduced by $\sim$ 290 and 410 ADC channels (symbolized by the horizontal dashed lines in Fig. 5.10(b)), the usable dynamic range is still considerably larger than the one that could be obtained in the measurements using the Gassiplex chip.

Further details on the settings of these measurements can be found in two Bachelor

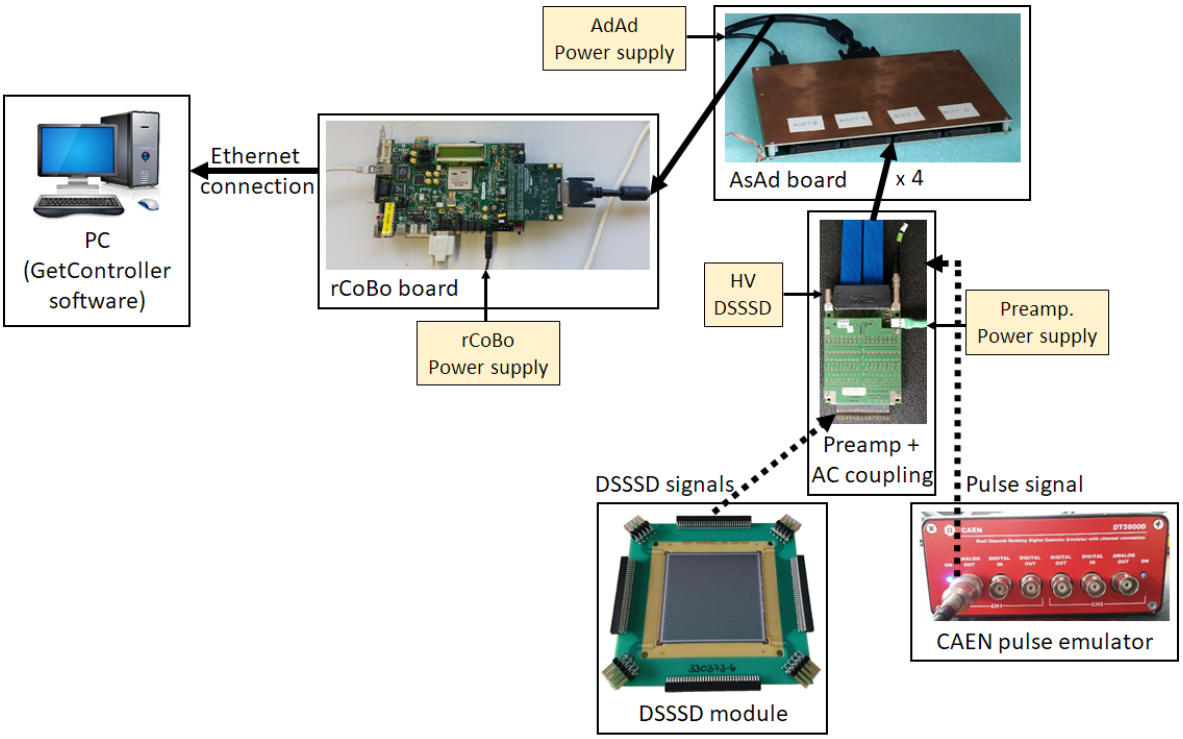

Figure 5.9: Schematic representation of the reduced GET system setup. The signals from either the DSSSD detector or an external pulse generator are fed into the AsAd board, which is connected to the rCoBo board, where the processed data end up. The data acquisition to a PC happens via an ethernet connection, using the GetController DAQ software.

theses, which were supervised within this PhD work [227, 228], together with tests of various system settings and configurations using the internal and external pulser as well. The starting point for measurements using a radioactive laboratory source was based on preparatory studies on the behaviour of the electronic noise contribution originating from the readout electronics with the attached DSSSD module. System configuration files could be defined for different measurement scenarios, containing parameters for energy thresholds, trigger and multiplicity settings. The latter correspond to the number of expected total hits among all the electronics channels of the readout system and, in combination with the other parameters, are essential in order to avoid discarding valid hit events while aiming to discard noise or background hit events.

A plot showing the result from an acquisition run performed by placing an α source in front of the DSSSD layer is depicted in Fig. 5.11. By plotting the ADC channel values of the total energy deposited in the strips of the p-side along the x axis and the same for the n-side energy deposition on the y axis, the correlation between the two detector sides is shown. The three encircled maxima correspond to the three energy peaks present in the triple-α source utilized for this measurement: 5.155 MeV from ^{239}Pu, 5.486 MeV from

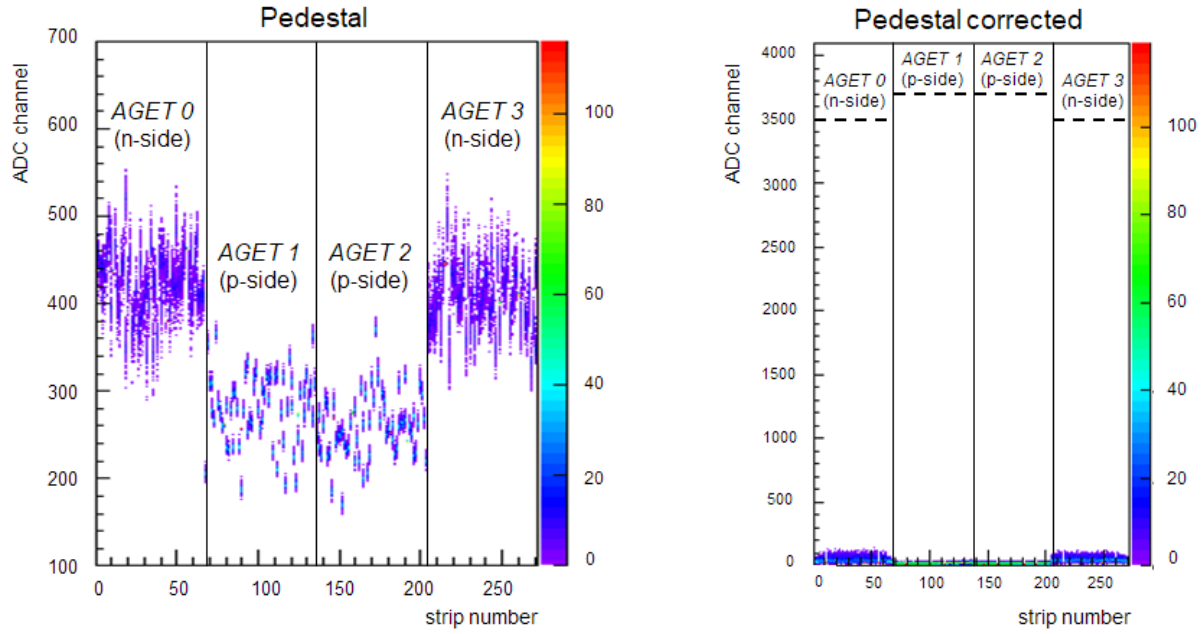

(a) (b)

Figure 5.10: Dark current background measurement of the energy pedestal value when the DSSSD detector is connected to the system. (a) Raw pedestal values and (b) pedestal values offset-corrected. In both plots the x axes represents the DSSSD strip number (68 per chip: 64 channels + 4 FPN channels), whereas the y axes represents the ADC channel values and the colour bars on the right side refers to the intensity (number of counts for a specific ADC value in a specific AGET channel). The regions of each AGET chip are separated by black vertical lines.

^{241}Am and 5.805 from ^{244}Cm, respectively.

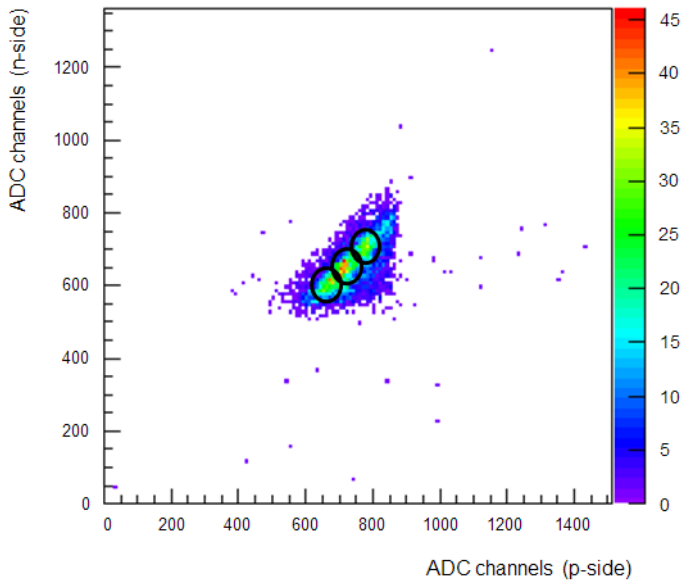

Figure 5.11: Signal correlation between p- and n-side of the DSSSD with an acquisition measurement using a radioactive triple-α source. The bias voltage was given to the p-side of the detector with a value of -70 V.

Drawbacks and further requirements

Maybe the largest deficit of the GET system from the viewpoint of our application is already embedded in its conceptual architecture and originates from the design motivation to read out Time Projection Chamber data. In these applications inherently low data rates have to be processed and acquired, thus allowing to handle intrinsic dead times of about 100 ns, imposed by the switched-capacitors architecture. However, in a clinical imaging scenario count rates of about 1 Mcps have to be processed, which seems out of reach for the GET system. Moreover, the design for low count rates also probably motivated another feature that emerged during the test campaign: in contrast to the Gassiplex chip, the AGET chip does not provide a digitizing capability. Therefore it is expected to read out the full data trace and subsequently perform an external analysis to derive the energy value from the trace data. The fact that one can in principle restrict the readout to a subset of the 512 trace "buckets" does not really improve the situation in our scenario of high counting rates. Data transfer and external analysis is still prohibitive in view of the future goal of an in-vivo beam range monitoring using the Compton-scattering data. Besides the computational efforts needed, also an enormous demand of memory and storage space would occur.

Here the GET system also turns out to be rather unflexible in the way it formats and stores primary event data: the primary data file format cannot be accessed or modified,

and it requires another conversion stage of the already gigantic data samples before the offline analysis can be started. It turned out that no access to the FPGA code in use in the GET system would be possible, so finally none of the issues identified during our tests could be remedied and as such a final decision had to be taken to abandon the AGET chip-based electronics as an alternative for the aged Gassiplex system.

5.1.3 MMR Multi-channel Readout

Following the negative outcome of the assessment of the AGET ASIC chip and its peripheral DAQ system, it was decided not to follow any longer the route of replacing the Gassiplex ASIC with a more modern ASIC successor (and its related frontend board), but rather to stay with a "conventional" solution based on individual electronics components. This was mostly based on the findings made during the market research for suitable ASIC modules that none of the existing ones would fulfill over needs to 100 %, while it would be prohibitive to start our own development in this context. Moreover, a discussion was initiated with the Munich company Mesytec GmbH which offered to develop a customized signal prosessing and DAQ solution precisely following our specifications, although based on discrete components. Under the condition that the overall geometrical requirements should not exceed those of the existing Gassiplex system, this development was started. As a further favorable consequence it turned out that the required high data rate throughput can still be achieved while keeping the existing VME bus readout, although utilizing a new and powerful VME controller from SiS (Struck Innovative Systeme, model SiS3153 [229]). Thus full hardware compatibility between the "old" and the "new" system can be achieved, keeping the investments in VME electronics also usable in the future.

Thus the MMR Multi-channel readout system [230] was developed by Mesytec GmbH [226], designed for complex detector systems according to our specifications and easy to be scaled up when large channel numbers have to be processed and read out.

The readout system is based on FE boards which perform time multiplexing, analog to digital conversion, data storage and triggered data transmission via an optical link to a VME-based central data collector module. The latter communicates via the VME-bus with a controller which sends the data to a data acquisition PC. Figure 5.12 shows a photograph of the key component of the MMR (Multiplexed Readout) system, which is the Frontend board [231]. Being based on discrete components, this makes the system more flexible than any solution where an ASIC is performing part of the signal processing. The disadvantage of lower integration density in case of discrete components is solved here by using a mezzanine concept of stacked boards, forming one FE unit. Ultimately the MMR system can be set up for 4 x 32 channels per frontend module (as visible in Fig. 5.14(a)). However, in order to stay compatible with the readout scheme of our DSSSD modules, we are using FE modules with 2 stacked boards and 2 x 32 channel processing capability. A considerable reduction of complexity is achieved by transferring all signal channels of one FE unit via one optical link to the VME crate, thus avoiding cumbersome cabling which could pick up background noise. These 64 detector signals are sent to the MMR frontend modules via 2 high density 68 pin connectors with 1.27 mm pitch. Each connector carries

4 ground lines and 64 signal channels. The analog signal processing is performed on one side of the board (upper part of the photograph in Fig. 5.12), whereas on the other side the digitization of the signals and the FPGA stage are implemented (lower part of the photograph in Fig. 5.12). The package of information obtained from the processed signals of the 64 channels is subsequently sent via an optical link to a receiver module.

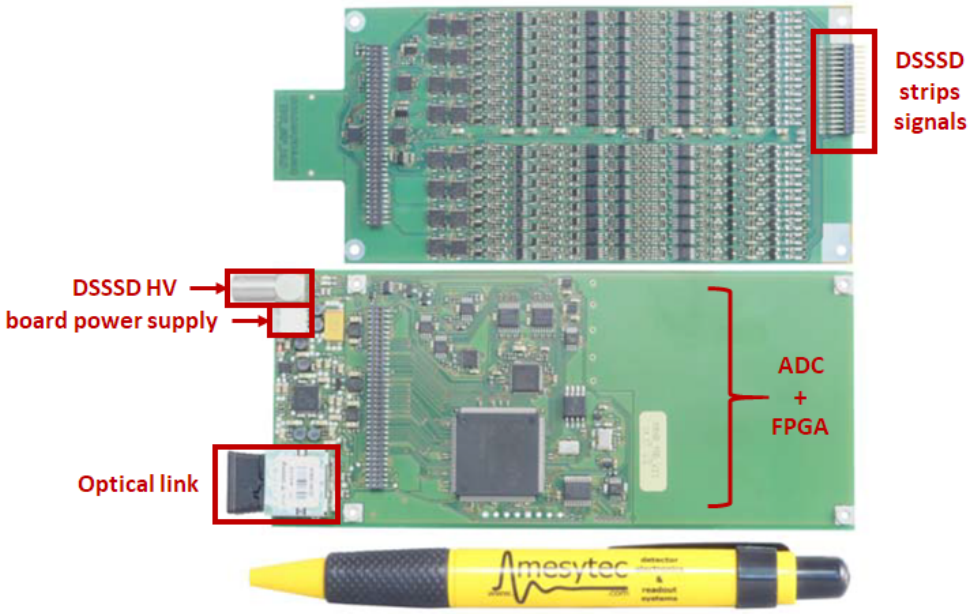

Figure 5.12: Photograph of one MMR frontend board module [231]. The connector for the optical link on one side will allow for the transmission of the data to the VME-based receiver module. The signals from the DSSSD detector are fed in on the other side of the board and the bias voltage for the detector can be applied via this module. The upper part of the photo shows the processing stages of the analog signals for 32 channels. Two of these mezzanine boards are needed to process the 64 channels of one of the four detector sides, whereas the part of the board displayed on the lower part of the photo digitizes all the 64 channels and manages the FPGA stage.

At the input of the MMR board, the signals are AC coupled in the same way as it was done using the previous readout systems. In our case the detector is biased with -70 V using the punch-through effect (introduced in Sect. 4.3.1) on the p-side of the DSSSD while grounding the n-side of the detector via the common ground of the system. Essential for our application is that the MMR board can be configured (by the manifacturer) to accept either positive or negative input signals from the detector, keeping the same electronic performances. A pulser coupling allows to apply a (internal or external) pulser and provides a check of the full chain of electronics from the signal input to the digitized data acquisition. The signal shaping time is implemented as a fixed value of 1 μs (optimized for our detectors, as it was also observed to be the optimum value during the tests performed with the GET

system). The timing signals of all the channels, coming from the discriminators, are sent to a logical OR unit and then to the digitization stage, which processes the data in 640 ns for 128 channels. The trigger is created by the first strip processed on the board that has fired, and the corresponding event will contain information from any other firing strip in the event time window (which would be set around 1 μs when running in Compton camera mode, see Chap. 6). From the DAQ software any MMR board can be set as being the trigger for the whole setup, which represents a great step forward for our application compared to the Gassiplex-based DSSSD readout, allowing us to implement flexible trigger configurations, which can be chosen according to the measurement condition. The MMR board provides a local clock, which is synchronized by the VME master receiver to a central time with a precision of about 30 ps rms. The absolute time stamping allows to buffer the data at the frontend stage without loss of timing information. The dynamic range is perfectly matching the average expected energy of the signals from the DSSSD layers, as it is implemented to be up to 500 keV.

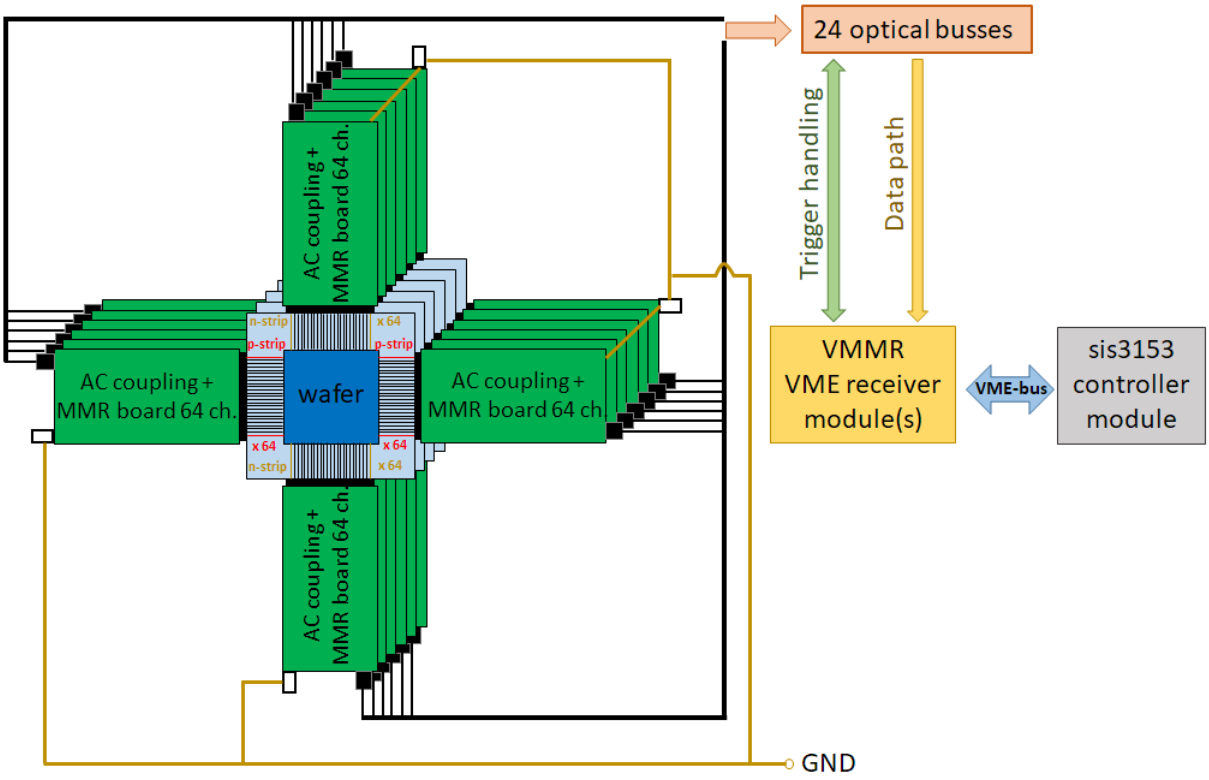

Figure 5.13: Schematical drawing for the geometrical arrangement of the DSSSD readout based on the MMR system. The MMR frontend boards are processing and reading out 64 channels each, mounted on one of the four sides of one DSSSD module. The digitized data are then sent via optical links to a VME-based module receiver, which communicates with a VME-based controller module responsible for sending the acquired data to the DAQ PC via an ethernet connection.

In Fig. 5.13 a schematical drawing of the mechanical setup for the readout system is depicted. The optical links (multi-mode optical fibers) are carrying the signals coming from the FE boards, each of them having processed 64 channels. If reading out all the DSSSD layers in our system, we need 24 optical links and two VMMR receiver modules, since each of them can accept up to 16 optical links.

The VMMR module (VME multi-readout receiver module, whose photograph is shown in Fig. 5.14(b) with the MMR board (a) connected to the optical link) is a VME module able to communicate with a VME crate control unit, which in our case is the SiS 3153 module from Struck [229], whose details, together with details about the DAQ software, will be given in Sect. 5.3.2.

The optical fiber connection (POF, plastic optical fiber) allows for a front end bus which can operate at a speed of up to 200 Mbit/s and permits to setup even complex arrangements, since up to 50 m length of the optical fiber the signal will not experience any degradation.

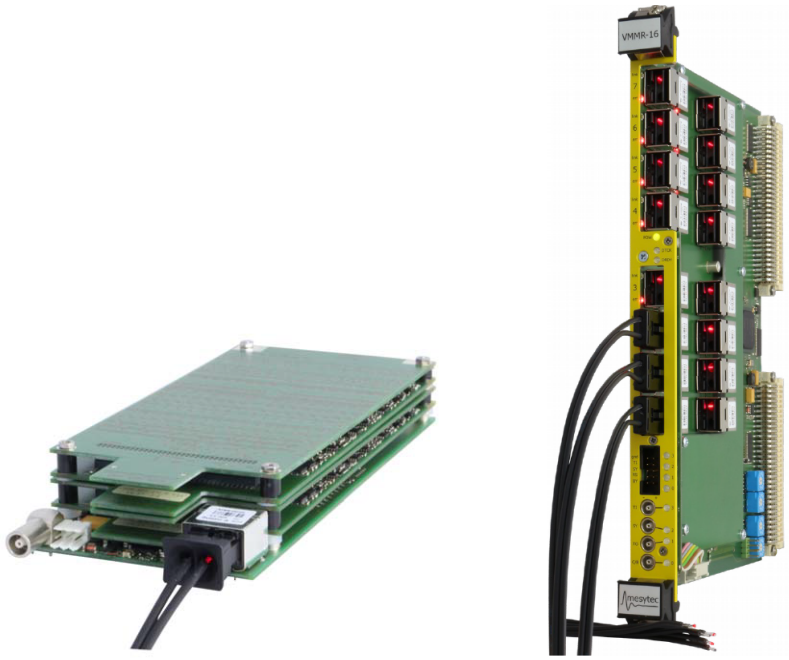

(a) (b)

Figure 5.14: Photograph of the MMR frontend board [231] (a) connected via an optical bus to the VMMR VME-based receiver module [232] (b). The frontend board version shown in (a) is able to handle 128 signal channels, while for our purposes we are using only 2 instead of 4 (32-channel) mezzanine cards to allow for 64 signal channels to be processed at each side of the DSSSD module.

As it will be presented in Sect. 5.2.2, apart from being suitable for the signals from our silicon detectors, the MMR concept can be configured to also process signals provided by the absorber component of the Compton-camera. Due to the capabilities of MMR

modules, optical links and VME controller, the system will be able also to handle data rates as expected for clinical irradiation scenarios.

5.2 Scintillator detector readout

As described in Sect. 4.4.3, all scintillation crystals used during the studies of this PhD thesis work were coupled to position sensitive multi-anode photomultipliers. This leads to a quite complex setup, in which the sum dynode signal from the PMT in addition to 256 channels (when using the H9500 PMT [206]) or 64 channels (when using either the H8500C [207] or the H12700A-10 [208] PMTs) have to be read out by an appropriate electronics chain. The following section presents the two signal processing systems that are being presently available as readout options for the absorber component of the LMU Compton camera.

5.2.1 Readout by individual spectroscopy electronics

In the "conventional" electronics setup, the readout of the signals from the absorber detector is performed by using NIM- and VME-based individual spectroscopy modules. The signals of all PMT segments (64 or 256, respectively) in addition to the sum dynode signal are directed to the inputs of the electronic modules which are part of the readout chain. Figure 5.15 shows a photograph of the first stage of the cabling between the $LaBr_3$(Ce) detector and the signal readout chain. In Fig. 5.15(a) the scintillation crystal (visible in the left part of the photograph) is encapsulated and coupled to the H9500 PMT which has 256 segments: the signals are therefore sent from the PMT connectors, via four 64-pin high-density ribbon cables [233] from Samtec [225], to four adapter boards. From the adapter boards the (256+1) signals are distributed to (256+1) individual LEMO coaxial cables. In Fig. 5.15(b) the scintillation crystal is encapsulated and coupled to a H8500C PMT with 64 segments: the signals are therefore sent from the PMT connectors to four adapter boards, in this case via four 16-pin ribbon cables [234] from Samtec [225]. From the adapter boards the (64+1) signals are distributed to (64+1) individual LEMO coaxial cables. A photograph of the cable connection for the $CeBr_3$ scintillation crystal coupled to the H12700A-10 PMT is not shown, as from outside it looks like the case displayed in Fig. 5.15(b).

The following information are conceptually identical for both PMT segmentations, as the only difference in their readout chains lie in the cabling as explained above, in the number of electronic modules in use and in the parameters to be set, which depend on the signal properties. Figure 5.16 displays a block diagram of the full readout chain for the absorber component of our Compton camera prototype.

On the right side of the diagram the number of channels and modules relevant for the two scenarios of interest is specified, i.e. for the PMT with 64 segments and the PMT with 256 segments, using violet and pink blocks, respectively. The flowchart of the readout chain drawn in Fig. 5.16 follows the same steps for the different PMT pixelations.

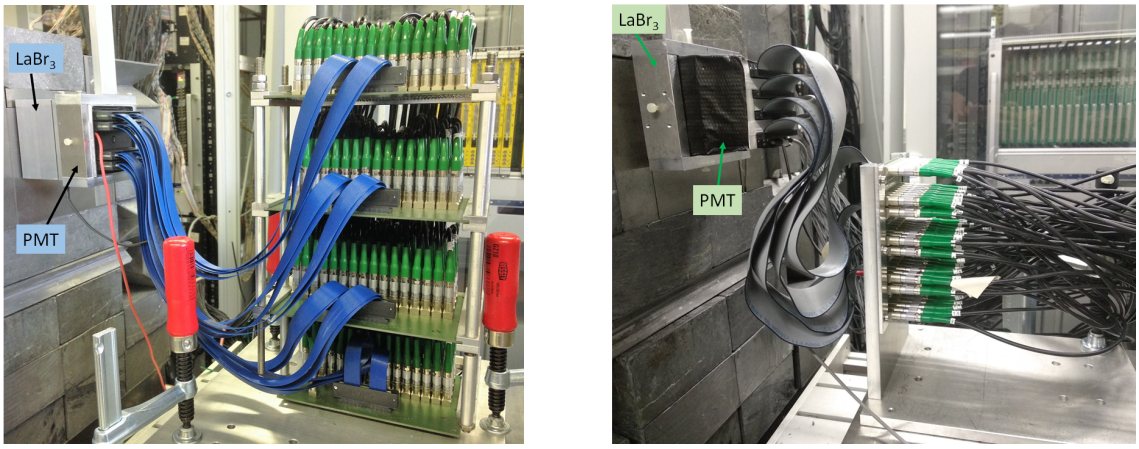

(a) (b)

Figure 5.15: Photographs of the cabling between the $LaBr_3$(Ce) scintillator and the first stage of the signal readout chain, which is the cable conversion, when the crystal is coupled to the H9500 PMT with 256 anode segments (a) and to the H8500C PMT with 64 anode segments (b). The signals are distributed to 256 (a) and 64 (b) individual LEMO coaxial cables, coming from four 64-pin high-density ribbon cables (blue cables in (a)) [233] and four 16-pin ribbon cables (grey cables in (b)) [234] from Samtec [225].

The 64 or 256 (each time plus 1 for the sum dynode signal) LEMO cables, which are the outputs of the adapter boards shown in Fig. 5.15, transfer the signals with a delay of 10 ns (given by their length) to 5 or 17 amplifier plus CFD (MCFD-16, Mesytec [235]) modules, respectively. Each of these modules is capable of processing 16 channels of the PMT segments, while the sum dynode signal is processed by a separate additional MCFD-16 module. The signals are here pre-amplified with an adjustable gain and selectable polarity (these settings are specified in Tab. 5.1) and, for each of the channels, an amplitude-independent, individually timed logic signal is created. The latter allows for a Time-of-Flight measurement of the detected signals, when registered against an external time reference, e.g. using an MTDC-32 Time-to-Digital Converter module [237] (see some details later in this chapter). By checking the signals with an oscilloscope and a differential probe, an energy threshold is set just above the electronic noise level for all the individual channels in the MCFD-16 modules: if exceeded, the logic CFD output signal is created and this will act as individual gate responsible for the charge integration time in the MQDC-32 module. The individual energy and time signals are sent to a Charge-to-Digital converter (MQDC-32, Mesytec [236]) by 13 m and 8 m long ribbon cables (34-pin $3M^{TM}$ Twisted Pair Flat Ribbon Cable, 3782 Series, 4.99 ns/m propagation delay), respectively. These two ribbon cables are combined via an MQDC-32 adapter cable (Mesytec [226]) before the connection to the MQDC-32 input. Figure 5.17 shows a photograph of the MCFD-16 module (a), the MQDC-32 module (b) and the adapter cable for the ribbon cables together with the layout of its pins (d). A photograph of the MTDC-32 module, which will be explained later in

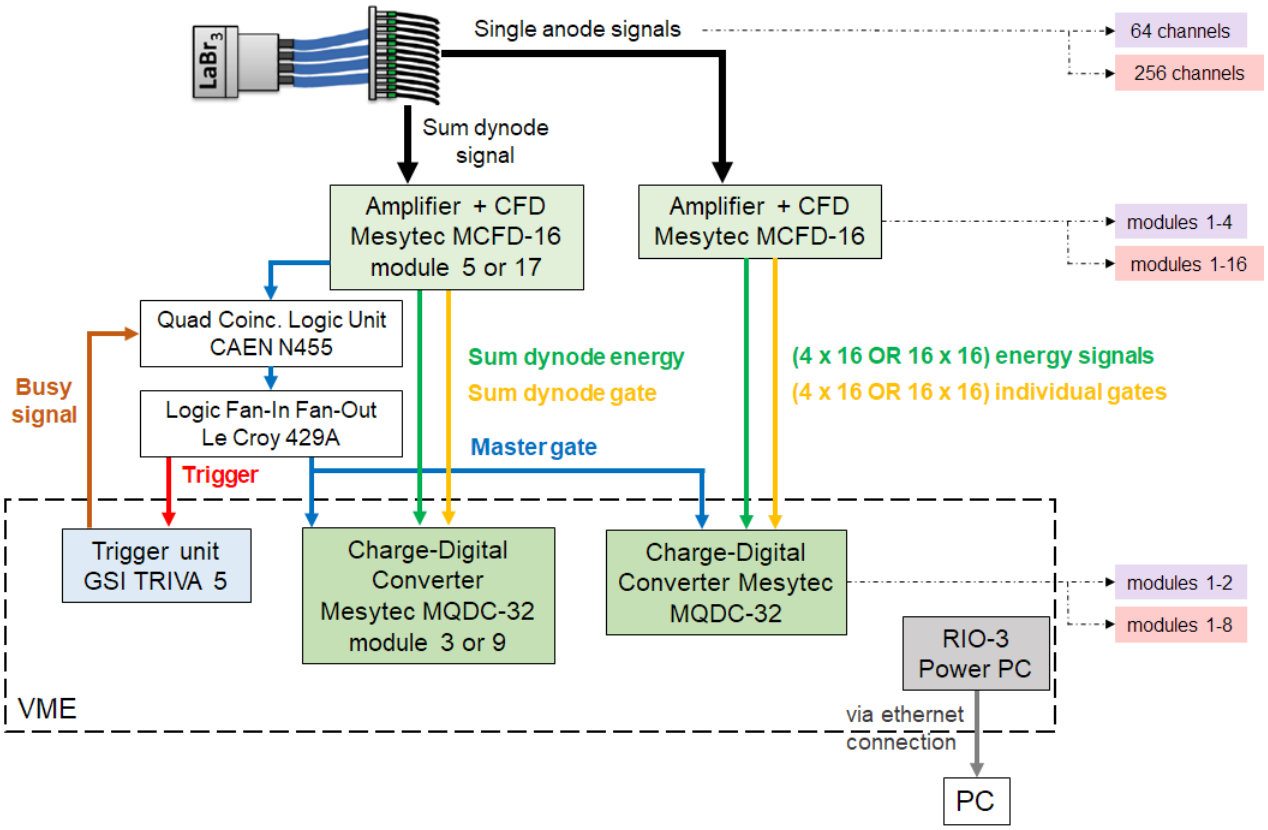

Figure 5.16: Block diagram of the readout chain for the absorber component of the Compton camera prototype. The number of PMT signals to be read out are either 64 or 256 (plus the sum dynode signal), depending on the PMT pixelation. The PMT signals and the number of modules in use are specified in violet for the H8500C and H12700A-10 PMTs and in pink for the H9500 PMT. The signals are processed by MCFD-16 [235] NIM-modules and MQDC-32 [236] VME-modules.

this section, is also shown in Fig. 5.17(c).

Each MQDC-32 module can process 32 channels divided in two input banks, and the sum dynode signal is again treated in an independent module. This means that each input bank of the MQDC-32 is responsible for all 16 signals of one MCFD-16 module, and the sum dynode signal is processed by one channel of additional MCFD-16 and MQDC-32 modules. The common logic output (labelled as OR output signal) of the MCFD-16 module responsible for processing the sum dynode signal generates the trigger signal for the DAQ system, after passing through a Quad Coincidence Logic Unit in OR operation mode (CAEN, model N455 [238]). This module accepts as common VETO input the busy signal from the trigger module (whose details will be explained in the data acquisition section 5.3.1), and is subsequently multiplying the mentioned common logic output to several copies in a Logic Fan-In Fan-Out module (Le Croy, model 429A [239]). The whole

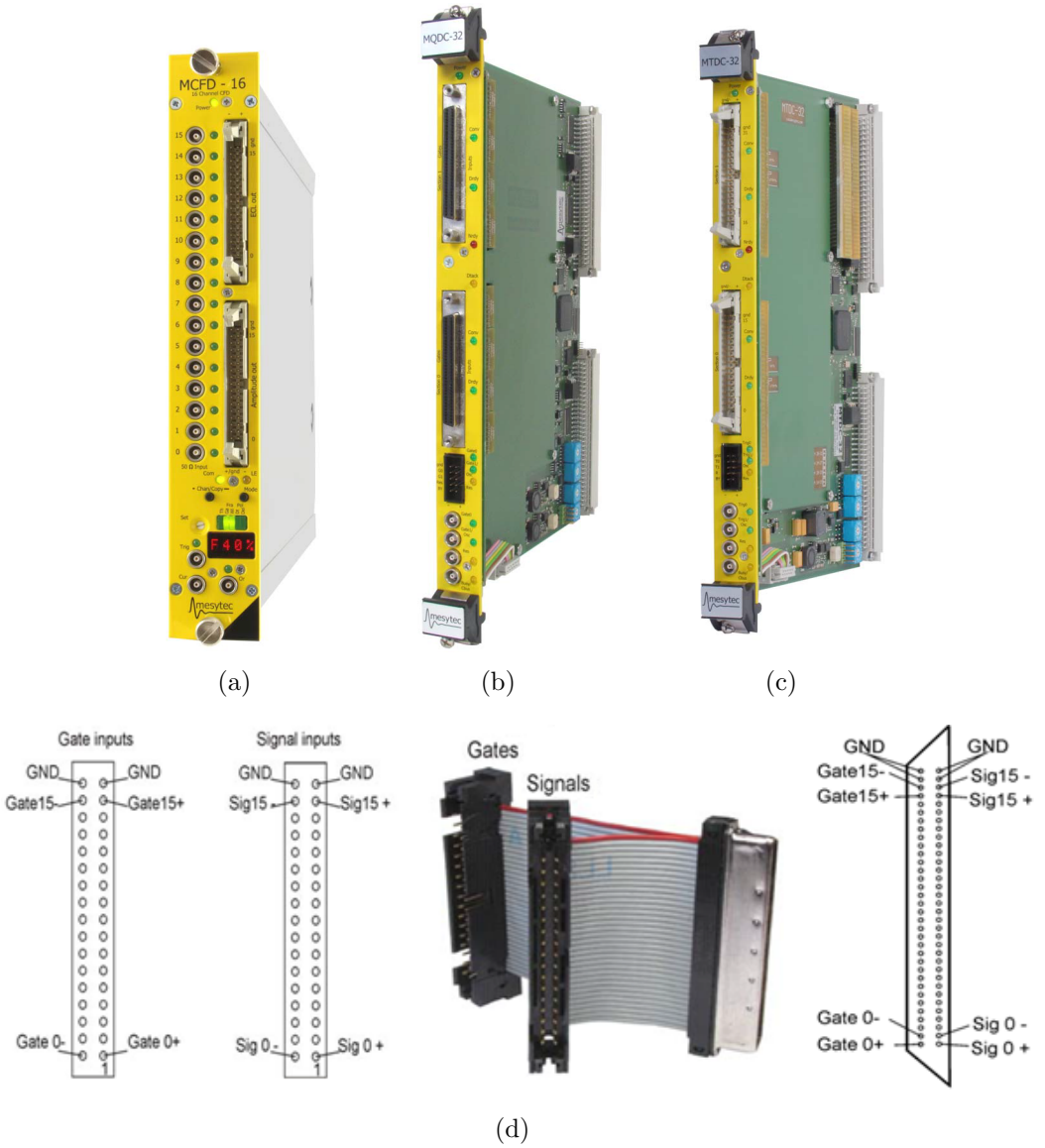

Figure 5.17: Photographs of the NIM-based MCFD module (Constant Fraction Discriminator from Mesytec [235])(a) and the VME-based MQDC (charge integrating ADC from Mesytec [236])(b) and MTDC (time digitizer from Mesytec [237])(c) modules. In (d) a photograph of the adapter cable for the ribbon cables entering the MQDC-32 modules with 16 signals and 16 individual gates from one MCFD-16 module, together with the layout of its pins, is shown.

PMT pixelation	Signal	MCFD parameters						MQDC parameters
		polarity	gain	dead time	tap	width	chip delay	sensitivity jumper
64 ch.	segments	neg.	3	300 ns	5	105 ns	5 ns	500 pC
	sum dynode	pos.	1	300 ns	5	135 ns	5 ns	1.5 nC
256 ch.	segments	neg.	10	300 ns	5	105 ns	5 ns	500 pC
	sum dynode	pos.	1	300 ns	5	135 ns	5 ns	1.5 nC

Table 5.1: Configuration parameters for the MCFD-16 modules and the MQDC-32 modules used for the processing of the 64 / 256 segments of the PMT as well as for the sum dynode output signal of the PMT (for details see text).

system is therefore triggered when the sum dynode signal is exceeding its energy threshold, defining any valid event in the absorber scintillation detector.

In order to ensure a synchronized data acquisition among all of the channels processed, this OR output is also used as the master gate of all MQDC-32 modules, whose responsibility is to start the acquisition of all events in every VME-based module. The number of required master gate signals corresponds to the number of MQDC-32 modules multiplied by two (because each module has two banks): for this reason the above mentioned Logic Fan-In Fan-Out module (LeCroy 429A [239]) is used. This module distributes the master gate signal into identical copies. These two modules introduce a small delay of a few nanoseconds to the generated gates. This is taken into account by checking if the timing requirements for the input signals to the charge integration modules are fulfilled (see later in Fig. 5.18), using an oscilloscope and a 400 MHz differential probe (Tektronix, P6246).

In Tab. 5.1 the most important setup parameters used for the MCFD-16 and MQDC-32 modules are summarized. The table shows configuration parameters for the processing of the PMT signals of each individual segment, as well as of the sum dynode, and for both PMT pixelations, 64 and 256 segments, respectively. The configuration parameters of the MCFD-16 module are set using the front panel of the module, whereas the parameters indicated for the MQDC-32 modules are changed by exchanging small chips on the VME-based module boards.

The polarity was set according to the corresponding output signal type of the PMT, either negative or positive for the individual segment signals and the sum dynode signal, respectively. The amplification factor applied in the MCFD module (gain) is chosen depending on the energy range of the γ ray impinging on the scintillation detector (which can reach up to 8 MeV for prompt-gamma measurements) in order to avoid saturation of the signal. Gain 1 (which corresponds to an input signal range of 0 ± 3.5 V) is indicated in both cases for the sum dynode output signal, but it should be noted that for the H12700A-10, which has 10 dynode stages instead of the 12 for the H8500C, the gain was in some situations set also to 3. For the PMT segments a gain of 3 (input signal range: 0 ± 0.5 V) or 10 (input signal range: 0 ± 350 mV) is indicated, for a PMT with 64 or 256 segments,

respectively: when the PMT segments are larger, the incoming light amplitude registered by each of them can be larger and the required amplification factor can be lowered.

In order to adjust the dynamic range for the sum dynode signal, laboratory calibration radioactive sources are used, which will be used as well for the energy calibration. Furthermore, when the bias high voltage for the PMT is varied around its recommended value for optimum performance (which will be discussed more in details in Chap. 6), the amplitude of the sum dynode signal will also significantly vary.

When defining the dynamic range of interest, the sensitivity and input resistance of the MQDC-32 module should also be configured by gain sensitivity jumpers that can be exchanged. As shown in Tab. 5.1, during the measurements the default value of 500 pC was kept for all PMT segments for the different PMTs that were used, whereas jumpers of 1.5 nC were chosen to digitize the sum dynode signals. For the online measurements, when the energy range of interest reaches up to 8 MeV, the latter was exchanged to 3 nC. The MCFD dead time was adjusted to be longer than the recovery time of the MQDC-32, estimated to be 250 ns. Thus, 300 ns were selected as dead time for all channels of all MCFD-16 modules. The delay is created by a standard delay chip (SIP7, impedance 100 Ω) with 5 taps (i.e. setting positions) and can be selected electronically. It is set to be the time between the fraction point and the maximum of the pulse. Since the fraction was set to 20% for all channels in all modules and since the $LaBr_3$(Ce) and $CeBr_3$ are fast scintillators, a delay of 5 ns was set for all channels in all modules. This was created by using a 5 ns delay chip and by selecting on the front panel of the MCFD-16 modules tap 5 (which is the maximum TAP selectable and allows to use the full delay of the delay chip).

The logic signal for each of the 16 channels in every MCFD-16 module (individual gate) is generated from the corresponding input energy signal and its width can be adjusted on the front panel of the NIM-based module. In case of our scintillation detectors, the width of each signal from the PMT segments was set to 105 ns to ensure the correct charge integration time for the corresponding energy signals. The width of the master gate, which corresponds to the OR output of the MCFD-16 module processing the sum dynode signal, was set to 135 ns. If required, this length can also be adjusted in a second stage. In Fig. 5.18 the analog energy signal, individual and master gates are sketched in order to show the requirements for their timing relations.

These requirements are needed for a correct operation of the MQDC-32 module. The minimum time which is mandatory between the start of the master gate and the start of the individual gate is 2 ns, while the amplified analog signal should not start earlier than 6 ns after the falling edge of the individual gate. It is very important to fulfill these requirements in order not to lose events and to ensure a correct charge integration of the energy signals, respectively.

The length of the flat ribbon cables which connect an MCFD-16 module to a MQDC-32 module was also decided accordingly to the timing requirements: 13 m and 8 m for the analog signals and individual gates, respectively. Since the timing performance of a $LaBr_3$(Ce) and a $CeBr_3$ scintillation crystals are almost the same (16 ns and 17 ns of decay time, respectively), and since they are read out using the same readout chain, the cable delay can be kept the same for both of them.

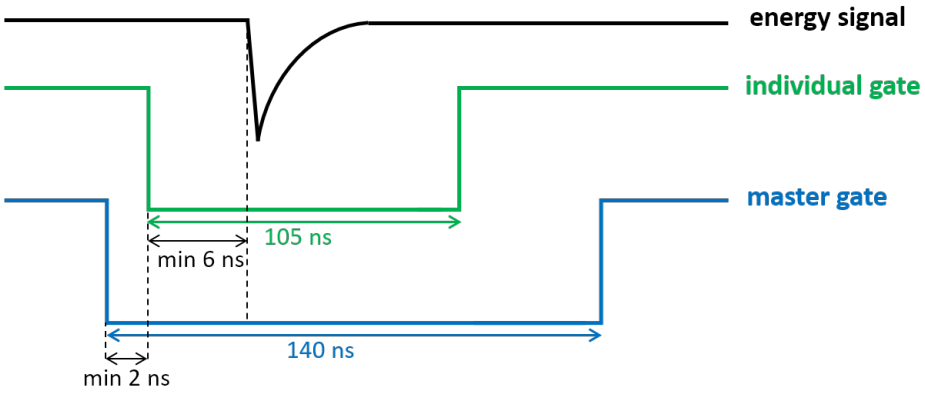

Figure 5.18: Timing requirements for the input signals of the MQDC-32 module for the integration of an input energy signal. The minimum required time between the MQDC-32 trigger signal (master gate) and the individual gate, responsible for the charge integration period, is 2 ns. The amplified energy signal should then start at least 6 ns after the start of the individual gate of the corresponding channel, in order for the charge to be integrated and acquired.

The setup described was used for the offline and online measurements described in the next chapter, when triggering and acquiring data from the absorber component of the camera as well as when acquiring data together with the scatter component. When the γ rays detected are emitted from a target being hit by an energetic ion (proton) beam, a neutron background, originating from various nuclear reactions between the particle beam and the target materials, is also produced and may affect the detection of the desired signals. Thus the excellent timing properties of the $LaBr_3$(Ce) or $CeBr_3$ absorber become crucial for the discrimination of signals coming from neutrons and γ rays, utilizing the Time-of-Flight (ToF) technique. For this purpose VME-based Time-to-Digital converter modules (MTDC-32, Mesytec [237]), already shown in Fig. 5.17(c), can be additionally installed in the Compton camera setup to process the timing signals from all PMT segments and the sum dynode signal. Some results that will be shown in the next chapter were obtained with a setup in which one channel of a MTDC-32 module was processing the sum dynode signal, as this one is most relevant for the suppression of the neutron background. In order to be correctly operated, the MTDC-32 module needs a master gate for starting the event acquisition, as it was described previously for a MQDC-32 module. The timing values that will be finally recorded in a MTDC-32 module will be determined as the timing difference between a start and stop signal, provided by the sum dynode signal of the scintillation detector and the radio frequency (RF) signal of the accelerator pulsing system, respectively.

5.2.2 MMR Multi-channel Readout

Thesignal processing and readout system described in the previous section, based on individual spectroscopic electronics modules, is perfectly fitting to the PMT signals from the absorber detector of the Compton camera and provides optimum resolution in energy and time. However, it results in a detector system which is quite complex with a number of signals to be read out amounting to more than 2000. Thus a reduction of electronic complexity and unification of the different readout schemes for scatter and absorber component appears to be highly attractive. Moreover, the rate capability offered by this conventional readout system should be improved when targeting clinical application scenarios.

Very favorably it turned out that the MMR system, which was initially developed for the readout of the DSSSD signals, could be adapted also for the PMT signals of the scintillation detectors of the Compton camera. For this purpose the MMR FE boards were adapted to accept only negative signals, as this is the polarity of the (256 or 64) single anode segments.

In order to act as input to the MMR board, the individual PMT segment signals are first sent from the PMT's connector to an adapter board, which sorts the channels in the right order to be accepted by the MMR module. Figure 5.19(a) and 5.19(b) show photographs of the adapter boards developed for the H9500 PMT and for the H8500C and H12700A-10 PMTs, respectively. The output of these boards is the same, the only difference is the input connector, as it has to match the connector type mounted on the corresponding PMT.

Figure 5.19(c) and 5.19(d) present photographs of the adapter boards mounted on all of our scintillation detectors, including the MMR board connected to one of them, respectively. The sum dynode signal is not yet included in the readout based on the MMR board, but this is part of the future implementation plans for the system. The sum dynode is therefore presently still read out with the system described in the previous section, based on MCFD-16, MQDC-32 and MTDC-32 modules. This also illustrates the flexibility of the system, being fully compatible with the standard VME readout system.

Thus the event data generated by the absorber component can therefore be also read out with the new MMR readout system and can easily be analyzed and merged with the data coming from the scatter component. The DAQ software, which is presently in use with this readout setup, was also developed by Mesytec and thus can be implemented to include further electronic VME-based modules, like MQDC-32 and MTDC-32 modules. An overview of the workflow for this system is depicted in Fig. 5.20.

5.3 Data acquisition

All signals which are processed by any of the readout systems described in the previous sections of this chapter, have to be acquired using a transmission unit which receives the data and is able to communicate with a PC, in our case via ethernet connection. Apart from the GET system, which is based on μTCA-bus communication (Sect. 5.1.2),

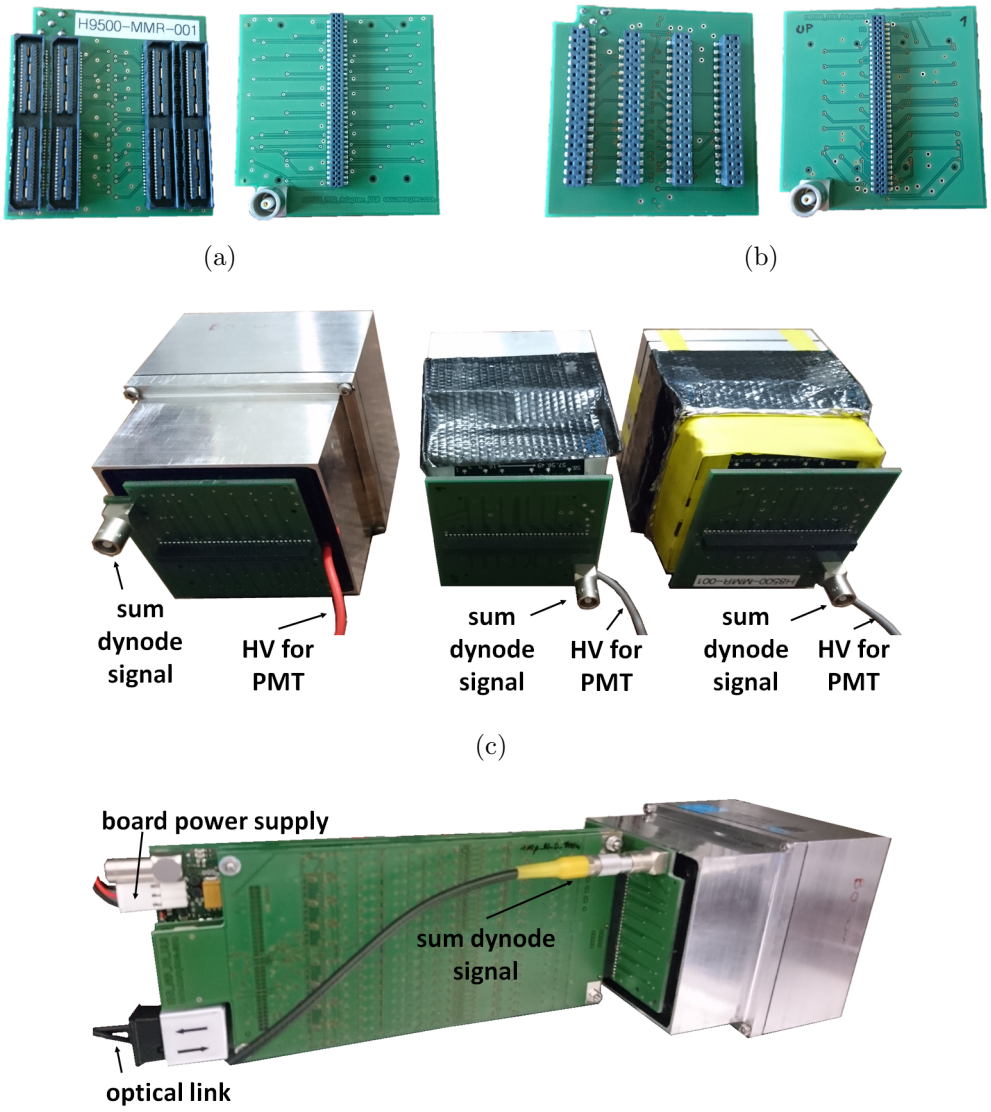

(a) (b) (c) (d)

Figure 5.19: Photographs of the adapter boards for the MMR readout of the absorber signals, designed for the (256-fold segmented) H9500 PMT (a) and for the (64-fold segmented) H8500C and H12700A-10 PMTs (b). In panel (c) the adapter boards are connected to their respective scintillation detectors and in (d) the detector is finally connected via the adapter board to the MMR frontend board.

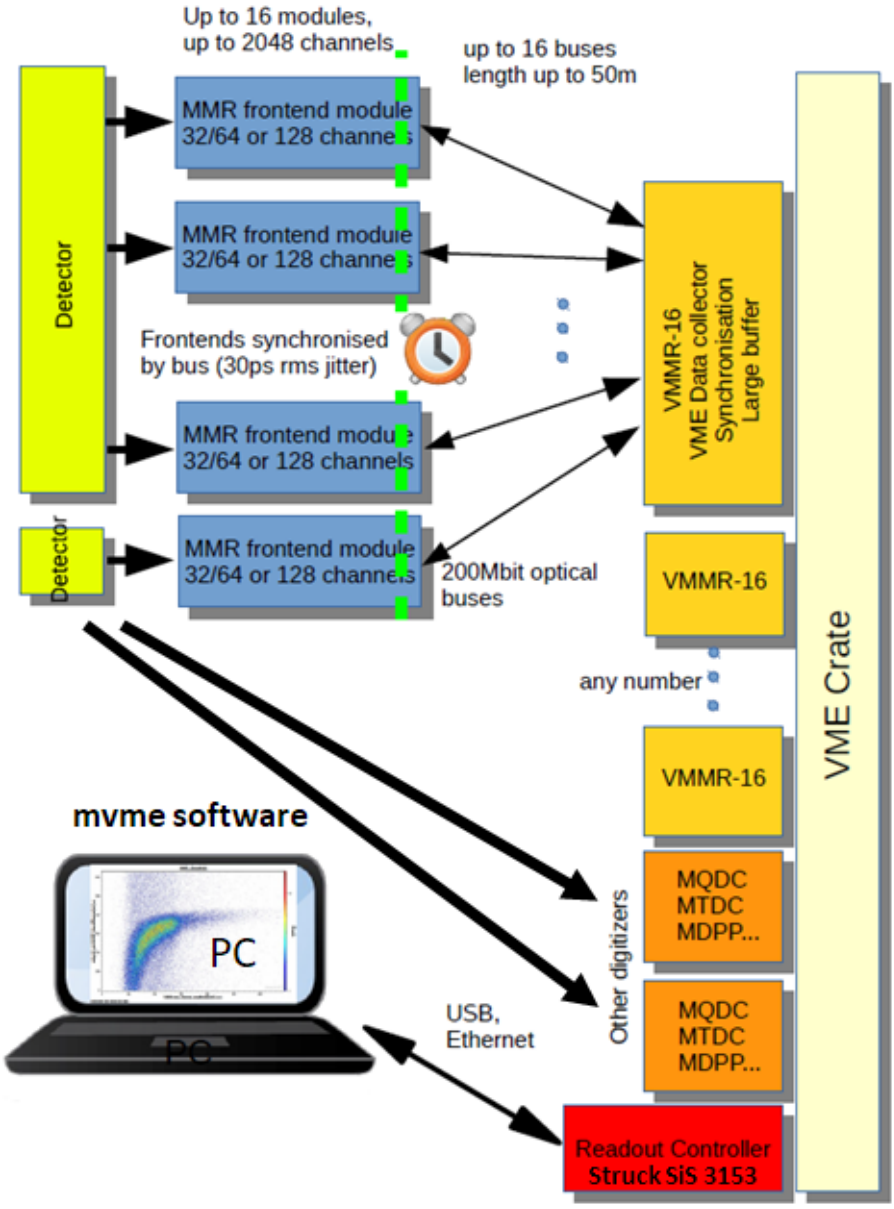

Figure 5.20: Overview of the MMR system when combined with other VME-based readout modules. The sketch of the system is taken and adapted from the data sheet of the MMR system [230].

the other described readout systems are all based on the VME bus and VME modules, designed for handling the transmission of the data to an external DAQ PC. In this section the different VME-based data transmission modules, utilized for the described electronic signal processing systems, will be described together with the corresponding software for data acquisition and analysis.

5.3.1 RIO PowerPC and Marabou DAQ software

The scintillation detector readout system consisting of individual spectroscopy electronics modules (described in Sect. 5.2.1) is triggered using the OR output from the MCFD-16 module which processes the PMT sum dynode signal. This logic NIM signal, which also acts as master gate for all VME digitizer modules involved in the setup, is converted in a NIM-ECL converter module to ECL standard and sent to the TRIVA 5 Trigger Unit [240] (shown in Fig. 5.21(b)), which accepts an ECL signal level and specifically the trigger signal in the pin 0 of the ribbon cable. The TRIVA module is responsible for handling the trigger of the system. It enables the start of an event acquisition for all the VME-based modules, communicating with them via the VME bus. The event acquisition is started only when the acquisition of the previous event is completed: this is possible due to the busy signal (which is a 300 ns long gate), sent by the TRIVA module (in pin 7 of the ribbon cable) to the Quad Coincidence Logic Unit, as it was depicted in the block diagram in Fig. 5.16. The acquisition system is then linked to the data acquisition PC through a frontend CPU (PowerPC RIO-3 from C.E.S. [241] operated in realtime with the operational system LynxOS [242], whose photograph is shown in Fig. 5.21(a)).

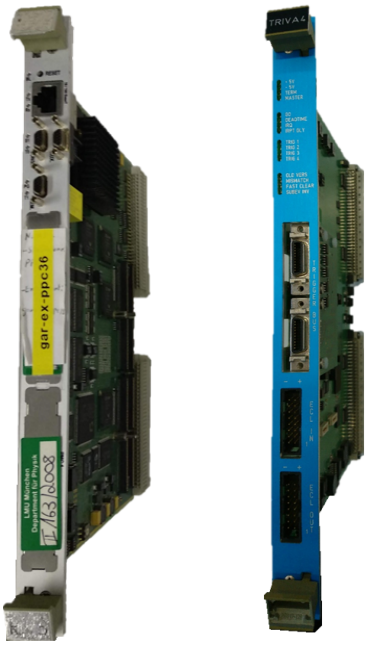

(a) (b)

Figure 5.21: Photograph of the VME-based RIO-3 PowerPC frontend CPU [241] and the TRIVA 5 Trigger Unit [240].

The data acquisition (DAQ) is controlled by the MBS (Multi Branch System) [242], and the ROOT-based Online/Offline Utility MARaBOU [243, 244]. MARaBOU consists of an MBS-based frontend, which is responsible for data readout, event building, data

transport and acquisition, and a ROOT-based [190] backend which manages the control of the measurement runs and the data analysis and histogram creation. The two parts are connected by a shared memory in the PowerPC unit.

For each experimental configuration a ROOT-based macro is modified and initialized accordingly: the macro serves to generate codes for the MBS-frontend and for the ROOT-based backend in the Linux workstation. Moreover, the ROOT-based backend allows for the implementation of either online or offline data analysis. At this stage the data are calibrated and processed, and can be selected by applying different conditions. An output file can also be produced in a suitable format to act as input for the subsequent image reconstruction process.

Figure 5.22 shows a screenshot of the DAQ control GUI "C_analyze" (on the left) and of the analysis GUI "HistPresent" (on the right). The DAQ control window is opened after having set the experimental configuration, to start a new offline or online run. When opening the analysis window, all histograms generated from raw and analyzed data are listed.

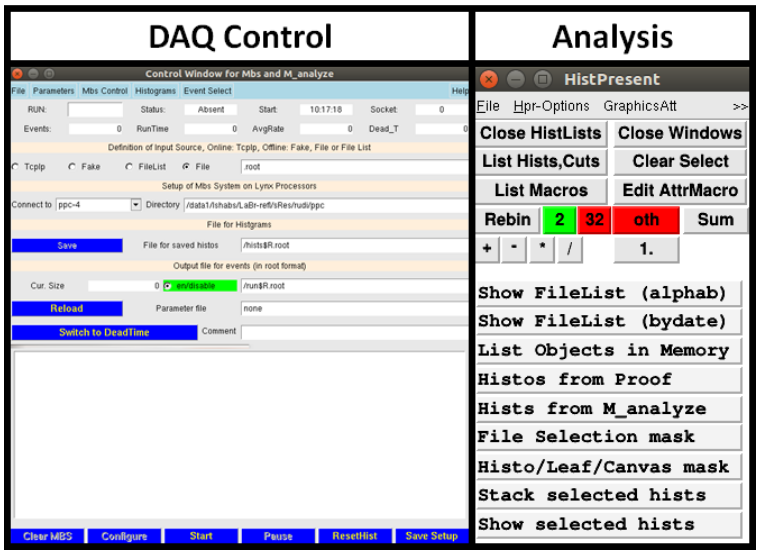

Figure 5.22: GUI overview of the Marabou utility [243]. On the left panel a screenshot of the DAQ control GUI "C_analyze" is shown, whereas on the right panel the GUI called "HistPresent" [245] is shown, which is based on the "ROOT" toolkit and enables visualization and manipulation of data acquired in various format.

The use of the RIO-3 PowerPC in combination with the Marabou software during measurements with our Compton camera prototype allowed us to acquire data with an effective event rate of about 1-2 kHz. This rate value refers to a configuration where the absorber signal is set as the trigger of the Compton camera, since the Gassiplex system used in combination with the PowerPC readout for the scatter detector does not provide a triggering capability. The achievable event rate is limited by the data transfer capability of the PowerPC and by the data packaging in the Marabou software.

5.3.2 SiS VME controller and Mesytec DAQ software

The MMR multi-channel readout system makes use of a novel VME controller module, the SiS3153 module from Struck [229]. This module communicates via the VME bus with the VMMR module receiver, packs the data and sends them via a Gbit/s ethernet connection to an external PC workstation. A photograph of the Struck module is shown in Fig. 5.23.

Figure 5.23: Photograph of the SiS3153 VME module from Struck, which in our setup is the ethernet to VME interface [229].

As explained in Sect. 5.1.3 and 5.2.2, where the signal processing for scatter and absorber detectors using the MMR multi-channel readout is described, the trigger is configured in the DAQ software and treated already in the VME receiver module (VMMR module), which acquires data received from all optical links. The SiS3153 module was programmed at Mesytec [226] in order to receive via the VME bus the data packed in the right format to be then sent to the PC.

Figure 5.24 shows an overview of the "mvme" DAQ software (from Mesytec GmbH [246]) connected to the VME data acquisition. The scripts in the VME configuration part of the software define all VME acquisition modules and settings involved: this allows the VME receiver module to accept data from these VME modules, defining which of them sends the trigger signal to the setup. Once the type of trigger is defined, the system can acquire data, which are sent through the VME receiver (VMMR module) and VME

controller (SiS3153 module) to the acquisition PC.

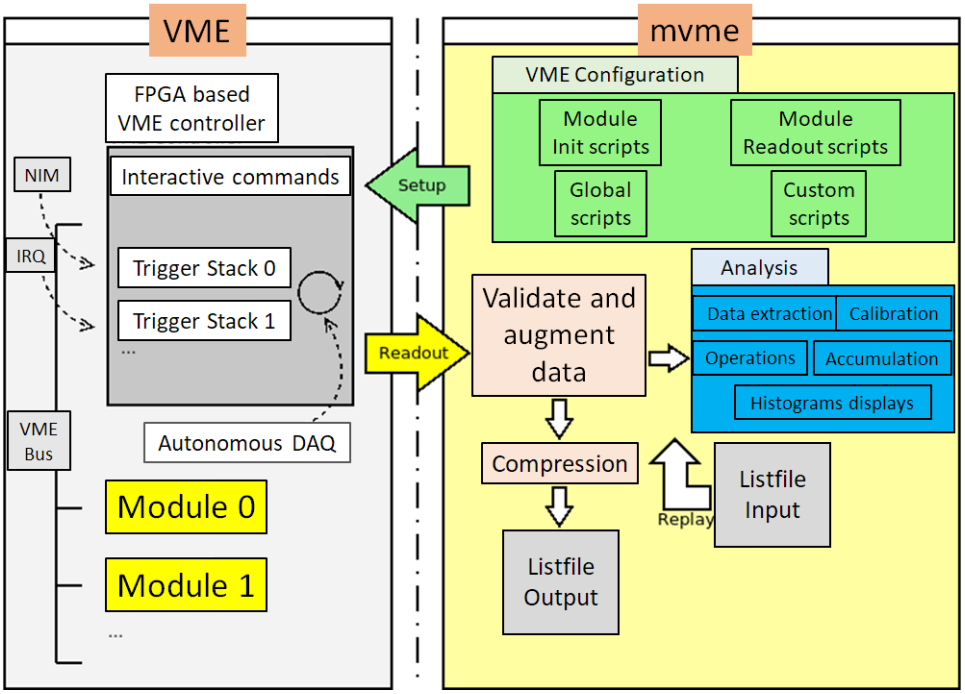

Figure 5.24: "mvme" DAQ software overview. Block diagram taken and adapted from the data sheet of the Mesytec software [246].

The SiS3153 controller module can reach a data transfer rate up to 35 MB/s for a single module, and, by using the MMR readout system, any detector component can trigger the system. The DAQ software has been programmed in python and C++ to produce a (compressed, if needed) file for each run: these files store, together with a list-mode file of the data, the configuration scripts of the VME module setup and the analysis steps implemented for this specific measurement. This allows for a structured and clear data storage and a direct offline reply of the listfile data which were produced online.

A screenshot of the GUI window of the program is depicted in Fig. 5.25. Visible in the left column are the DAQ control window (top) that controls the system and below the VME configuration window, in which the VME modules involed in the setup are implemented and initialized. On the top right a screenshot of the analysis GUI is shown: it allows for a (1D and 2D) histogramming of the readout data, either in real-time or as offline analysis. The rate monitoring of internal system rates and external rates generated from readout data (e.g. scaler modules, event counters) is also possible from this GUI. A flexible VME module data extraction is also possible at this stage, as it is also specified in the corresponding (blue) box in the sketch in Fig. 5.24. The remote control interface is controlled by a TPC (Transmission Control Protocol) connection: DAQ runs can be remotely started and stopped using the DAQ control GUI and requested status information can be checked in the log view window (bottom right of the figure), together with information about the

initialization of each VME module.

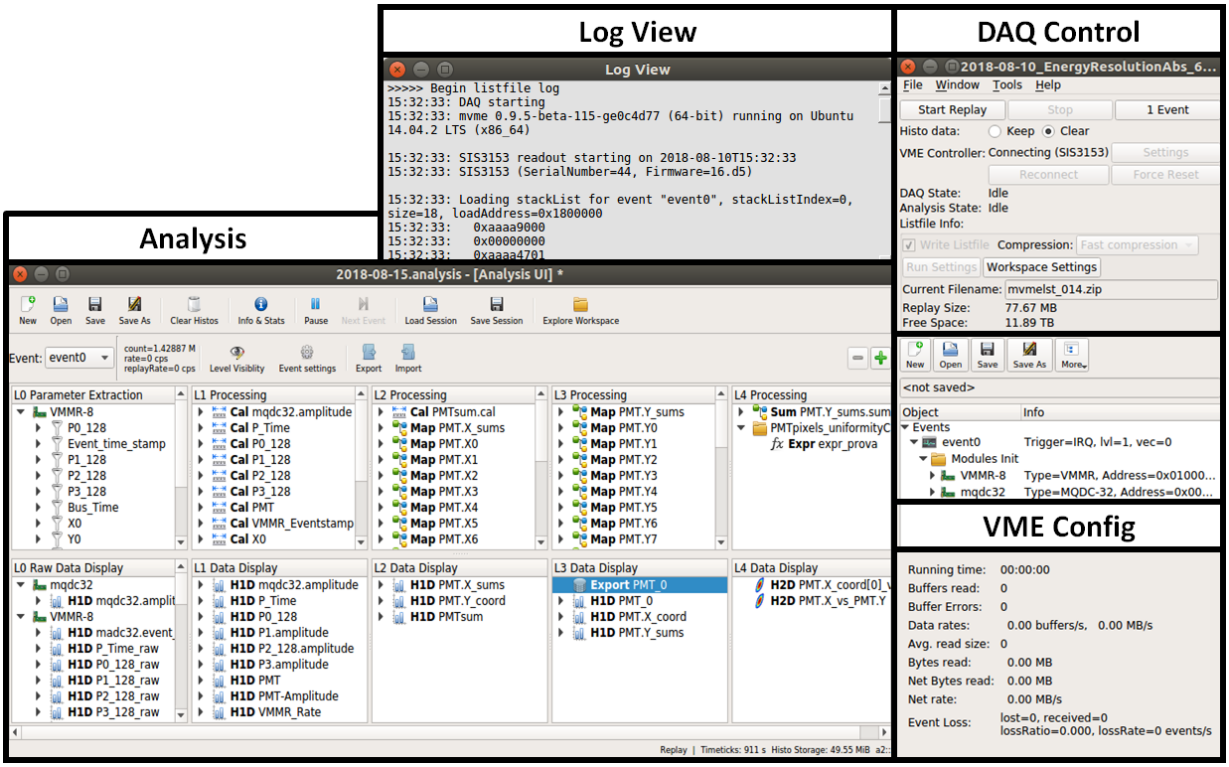

Figure 5.25: GUI overview of the "mvme" - VME data acquisition software introduced by Mesytec for operating their new signal processing and data acquisition system based on the MMR frontend modules [246]. Screenshots of the DAQ control window and VME configuration window are shown in the left panel, whereas in the right panel the GUI windows for the analysis and the log view are depicted.

In view of the desired real-time application of our prototype system, some additional analysis features are required from the mvme software in order to be able to apply online further selections on the data. For deeper analysis procedure, a root-compatibility is desired (and envisaged): this will allow the use of the same current framework for the postprocessing of the data. This step is needed in order to properly analyze and prepare the data which will be an input for the image reconstruction performed in MEGAlib.

CHAPTER 6

Components' characterization

This chapter is dedicated to the characterization of the detector components which are part of the Compton camera prototype being developed at LMU in Munich. Namely, the double-sided silicon strip detectors which form the scatter component and the monolithic scintillator, which is acting as absorber component. The structure of the detectors was described in Chap. 4, whereas their signal processing and data acquisition was described in Chap. 5. The chapter is divided into two main parts, the first one dedicated to the characterization of the DSSSD detectors and the second part dedicated to the characterization of the monolithic scintillation detector(s) based on $LaBr_3$(Ce) or $CeBr_3$ crystals.

6.1 Double Sided Silicon Strip detector

The scatter component of our Compton camera prototype is comprised of a stack of six double-sided silicon strip detectors, which were produced by CiS (Forschungsinstitut für Mikrosensorik GmbH [191]). Tests and results obtained from a characterization of these detectors will be presented here.

A detailed profile of the internal structure of a DSSSD detector (which was theoretically explained in Sect. 3.1.4) is depicted in Fig. 6.1. The bulk of the silicon detector is slightly n-doped (n=$5 \cdot 10^{11}$ cm^{-3}); p-strips and n-strips are located on the two front and back sides of the detector with doping values of p=$7.5 \cdot 10^{14}$ cm^{-3} and n=$1 \cdot 10^{15}$ cm^{-3}, respectively. In addition, so-called p-stops are located between the strips on the n-side of the detector, in order to create a field separation. A layer of SiO_2 ($\sim$ 850 μm thick) is placed on top of the silicon material in order to protect the detector, and an aluminum layer is deposited on top of the SiO_2 to create the electrical contact for the strips to be read out.

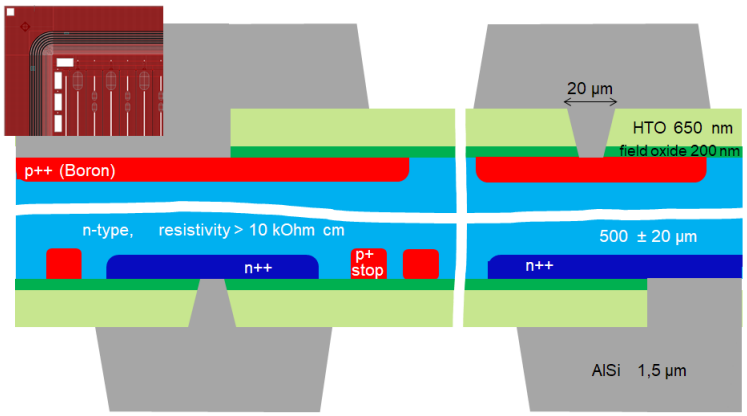

Figure 6.1: Detailed profile of the internal structure of a DSSSD detector. The bulk of the detector consists of n-type silicon, with a resistivity >10 kOhm×cm and a thickness of 500 μm. A layer of SiO_2 ($\sim$ 850 μm thick) is deposited on the strips of each side. (courtesy of R. Röder, CiS Erfurt).

The knowledge of this structure is important for a correct operation of the detector. In order to operate the DSSSD layers with correct parameters, an electrical characterization of these devices was first performed. Furthermore, given the well-known behaviour of the n-side of these detectors [139], an extensive characterization was required (see Sect. 6.1.3).

6.1.1 Electrical characterization

In order to collect all charge from the incoming signal, the depletion zone of the silicon detector should correspond to a thickness equal to the thickness of the detector (see Sect. 3.1.4 for details about that). The operational voltage which is needed in order to deplete the detector across its whole thickness can be calculated using the following formula

$$x_{depl} = x_n + x_p = \sqrt{\frac{2\varepsilon}{q}\frac{N_d + N_a}{N_d N_a}(\Phi_i + V_R)} \tag{6.1}$$

where x_n is the depleted zone in the n-side doping region, x_p on the p-side, ε is the dielectric constant of silicon, N_d and N_a are the concentrations for donor and acceptor atoms for, n-type and p-type regions respectively, Φ_i is the junction potential (see Sect. 3.1.4) and V_R is the reverse potential which is applied in order to extend the depletion region (corresponding to the operational voltage for the detector).

The structure of a double-sided silicon strip detector is quite complex and many junctions are interacting with each other. The value of $V_R \cong 100$ V which can be derived from Eq. (6.1) based on typical values for the various input quantities and considering the junction on one of the two sides of the detector, is in the correct order of magnitude, but many other field effects should be considered, i.e. the junction potential which is created on the other side of the detector and inbetween the strips on the same side. Since an extensive study on the structure and field propagation inside this kind of silicon detectors goes

beyond the scope of this thesis, an experimental test was performed in order to quantify the optimum operational voltage (V_R)to be applied to the detector (while also considering the minimum V_R of 50 V which was suggested by CiS [191]).

The DSSSD detector can be supplied from either the p-side or the n-side; when one side of the detector is biased, with either a negative or a positive voltage, the other side should be grounded. The detection process does not change within these two cases, but our DSSSD modules are normally biased from the p-side, since the junction potential on that side is higher and the stability of the depletion zone should be reached faster. An energy spectrum from a triple α source (from which the following photopeaks can be detected: ^{239}Pu (5.155 MeV), ^{241}Am (5.486 MeV), ^{244}Cm (5.805 MeV)) was acquired with one layer of DSSSD. The (negative) bias voltage V_R was applied on the p-side of the detector, whereas the n-side was put on ground (GND). The plot in Fig. 6.2 shows the peak position (in ADC channels) of the ^{239}Pu photopeak at 5.155 MeV, as a function of the operational voltage V_R. The plot saturates around -70 V, meaning that with this voltage applied between the two sides of the detector the charge generated by the impinging α particle is fully collected. Thus V_R does not need to be further increased, since an increase of the operational voltage leads as well to an increase of the leakage current.

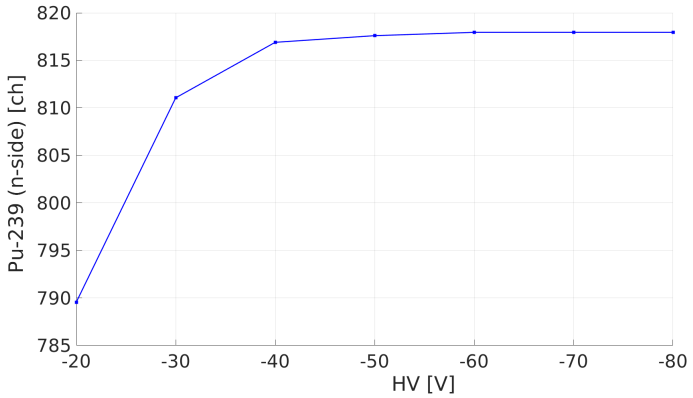

Figure 6.2: Charge collection as a function of the bias voltage. The spectrum of a triple α-source was acquired and the position of the ^{239}Pu peak (5.155 MeV, characterized in ADC channels) was monitored as a function of the bias voltage, in order to experimentally determine the minimum operational voltage which permits a full charge collection ("full depletion").

Another confirmation for the use of the correct operational voltage is the evaluation of the bulk capacitance of the detector. This was tested at the detector laboratory of CiS [191] with the use of their LCR meter. Figure 6.3 reveals a clear trend of the bulk capacitance as a function of the voltage applied: the capacitance decreases as the operational voltage increases. The minimum capacitance value is reached around -70 V, which was determined before as the correct bias voltage V_R to be used to fully deplete the detector. The measured absolute capacitance values depend on the area and on the thickness of the detector,

according to the simplified approximation as a plate capacitor which leads to:

$$C = \frac{\varepsilon_0 \cdot S}{d} \tag{6.2}$$

where S is the area of the capacitor and d is its thickness.

Furthermore, in order to be sure that the breakdown voltage (which is the maximum reverse voltage that can be applied to a p-n junction to avoid a subsequent rapid increase of the current [174]) safely exceeds the bias voltage V_R used to operate the detectors, all layers of the DSSSD were tested at CiS [191] with precise measurement devices, applying V_R between the two sides of the detector.

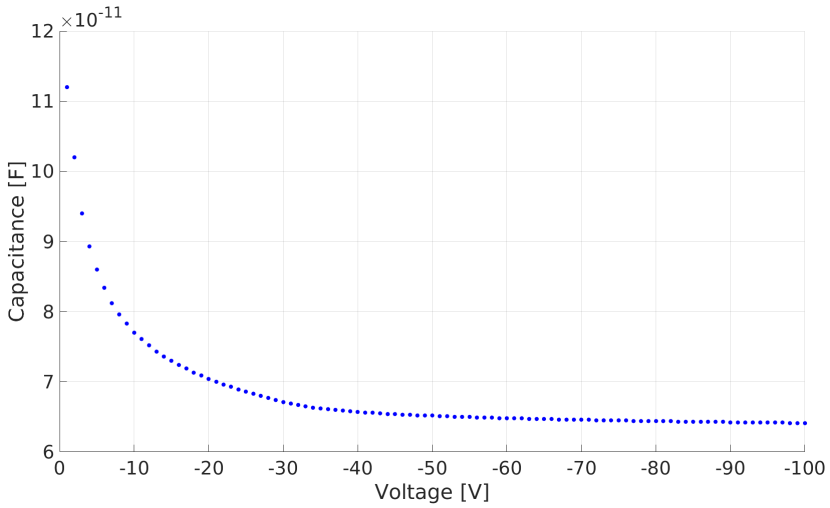

Figure 6.3: Bulk capacitance of a DSSSD layer, measured with an LCR meter.

In Fig. 6.4 the I-V curves for the DSSSD modules (a) "layer 2" and (b) "layer 7" are presented. The operational voltage was applied in a range between 0 and -400 V. The breakdown voltage is $\sim$ -300 V for layer 2 and $\sim$ -250 V for layer 7, far from the -70 V which are needed to operate the detector fully depleted. The behaviour of only these two layers is exemplified, since all other detector modules which are part of the Compton camera prototype exhibit breakdown voltages inbetween these two values.

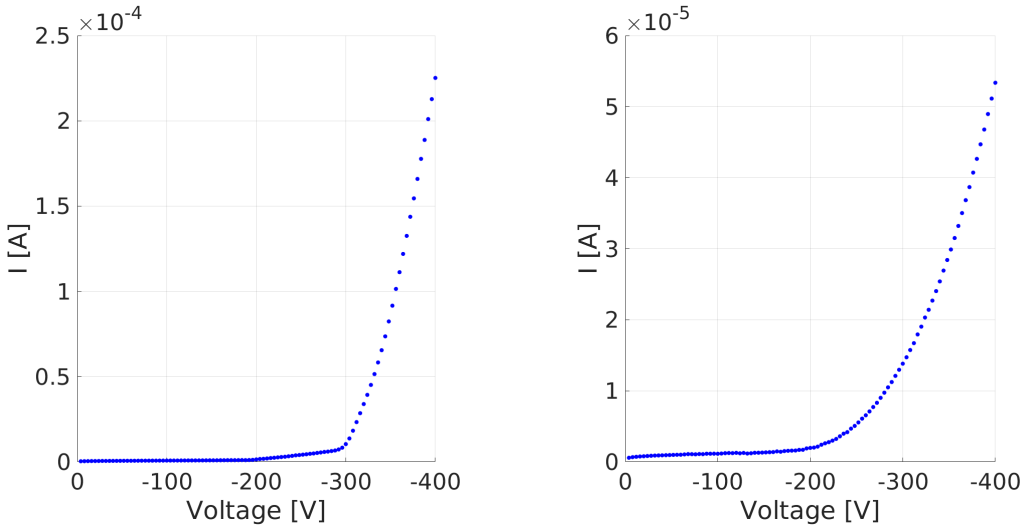

Figure 6.4: I-V relation of two prototypical layers of DSSSD, (a) "layer 2" and (b) "layer 7". The bias voltage was applied to the bias ring of the p-side, whereas the ring of the n-side was put to ground. The voltage was increased up to -400 V for both detectors and the breakdown voltage was determined.

The tests presented above have all been performed by supplying the detector with its operational voltage via the so-called *bias ring* and thus utilizing the so-called *punch-through effect*. But, as mentioned in Sect. 4.3.1, the operational voltage of the detector can also be applied just via its strips, on the p-side (negative V_R) or on the n-side (positive V_R), while grounding the strips on the other side of the detector. This allows for the creation of a homogeneous potential level on each detector side.

The leakage current is an important parameter to be monitored, since it is responsible for a considerable part of the electronic noise created in the detector. A test measurement was performed in order to evaluate the impact of using the guard ring as a bias ring on the measured leakage current. In Fig. 6.5 the leakage current, measured between the two sides of the detector, is shown as a function of the bias voltage V_R applied to the p-side of the detector. The red data points, together with the red linear fit curve, show the leakage current as it was measured when the operational voltage was applied just via the p-strips. The blue data points, together with the blue linear fit curve, show the leakage current measured when the operational voltage was applied via the bias ring, in addition to the p-strips. A slight decrease of the leakage current can be observed when using the bias ring as well. With this configuration the potential level is forced to be homogeneous and small voltage drops within this area, potentially causing an increase of the leakage current, are less probable. However, the difference cannot be considered crucial, becoming even smaller with increasing values of V_R. Therefore the operational voltage, for this detector layers, can either be given via their strips or via the bias ring located on one of the two sides, without affecting the performance of the detector.

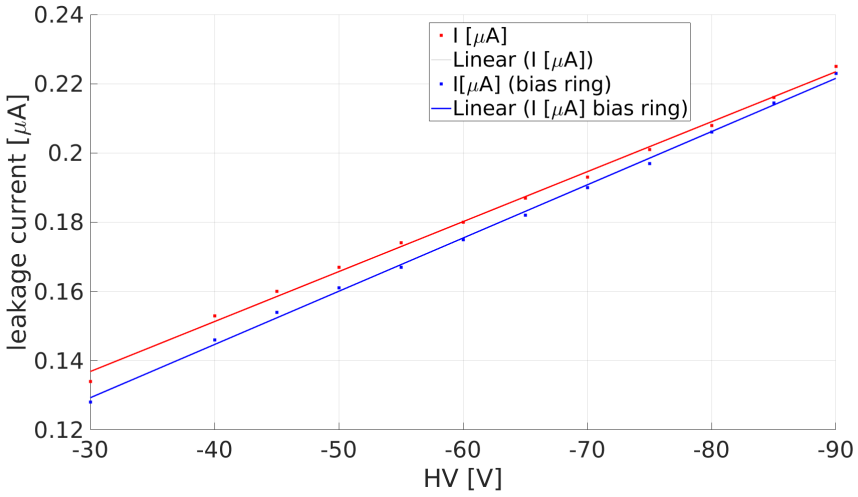

Figure 6.5: Leakage current as a function of the bias voltage. Two different scenarios are plotted: when biasing the detector via the strips or together via strips and bias ring. See the text for more details.

6.1.2 Response to radiation sources

In order to characterize the energy resolution, the detector response to offline laboratory radiation sources was studied, using the same triple α source (with an activity of ~ 5 kBq) already used before. The signal from one strip was extracted using the customized channel selection test board shown in Fig. 6.6. This board was developed in order to be able to select one or more strips whose signals could be read out together or separately, since the board provided two LEMO cable outputs. A simple setup could make use of this board in order to check its response to laboratory radiation sources. In Fig. 6.6(a) a photograph of this board is displayed, while Fig. 6.6(b) shows its circuiting layout.

The extracted signal from one strip was then processed by the signal processing chain which is schematically illustrated in Fig. 6.7. The preamplification and shaping of the signal was performed by an MSI-8 module (from Mesytec GmbH [247]). A shaping time of 1 μs was selected. This module provided an energy and a time output signal: the energy signal was sent to a peak sensing ADC module (CAEN V785 [248]), whereas the time signal was split in two copies. It was used to create the integration gate needed in the ADC unit (by using the Gate Generator module from ORTEC GG8000 [249]) and the trigger signal for the data acquisition system, through the use of a NIM-ECL converter (CAEN N638 [250]) which was sending the converted signal to a TRIVA trigger unit module (GSI TRIVA 5 [240]). The output signal of the TRIVA module was sent back to a Coincidence Logic Unit (Quad. Coinc. Logic Unit, CAEN N455 [238]) as a "busy" signal, in order to prevent pileup while acquiring subsequent events. The data acquisition was based on a PowerPC RIO-3 frontend CPU, which was described in Sect. 5.3.1.

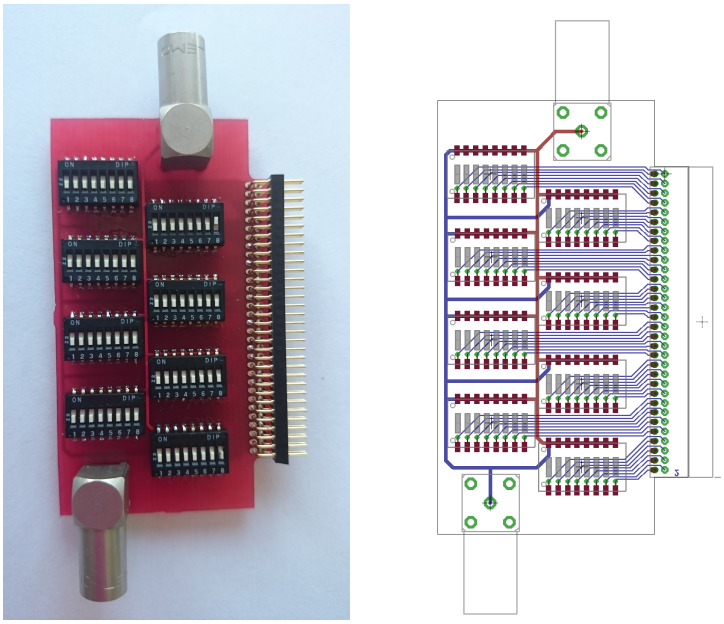

(a) (b)

Figure 6.6: Customized channel selection test board which was developed in order to select part of the DSSSD channels to be read out via the electronic signal processing chain whose block diagram is depicted in Fig. 6.7. (a) A photograph and (b) the circuiting layout of the board is shown.

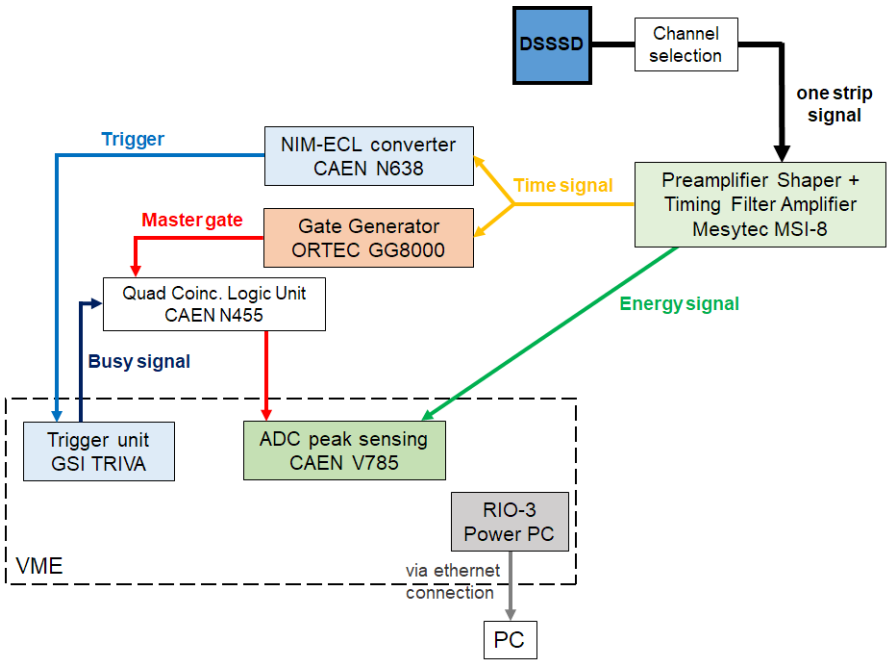

Figure 6.7: Block diagram of the readout chain used to acquire data for the test performed placing a triple α-source, with a 2 mm collimator opening in front, at $\sim$ 1 cm distance from the surface of the DSSSD detector. The tests were performed under vacuum conditions.

For this measurement the DSSSD layer was placed inside a vacuum chamber, in order to increase the rate of α particles reaching the detector surface on the other side. Furthermore, this could also ensure the proper light shielding. The radioactive source was mounted on a holder with a collimation hole of 2 mm, placed in a distance of about 1 cm from the detector surface. The detector was biased with a V_R = -70 V applied to its p-side; this side was also oriented towards the radioactive source. In Fig. 6.8 a photograph of the setup inside the vacuum chamber is shown.

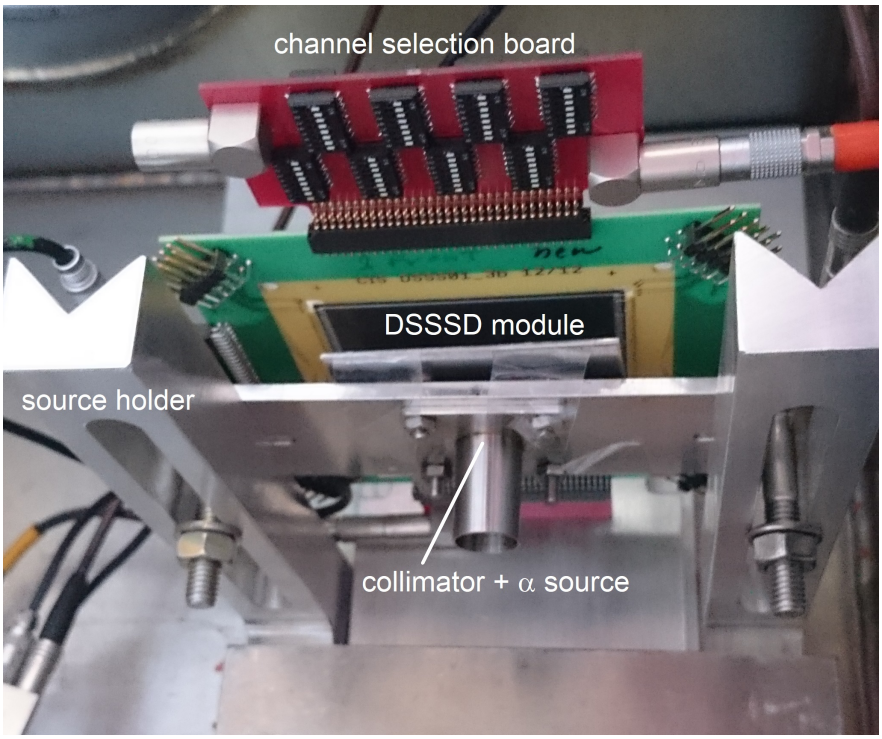

Figure 6.8: Photograph of the setup which was installed for the α-source characterization of one DSSSD layer. The source is placed at $\sim$ 1 cm distance from the DSSSD detector behind a 2 mm collimator. The setup was placed inside a vacuum chamber.

The energy spectrum obtained from this measurement is shown in Fig. 6.9. The three peaks correspond to the three transition lines of the source. The energy resolution which could be achieved is a rather modest value of $\sim$ 64 keV, being even larger for signals acquired from the n-side of the detector.

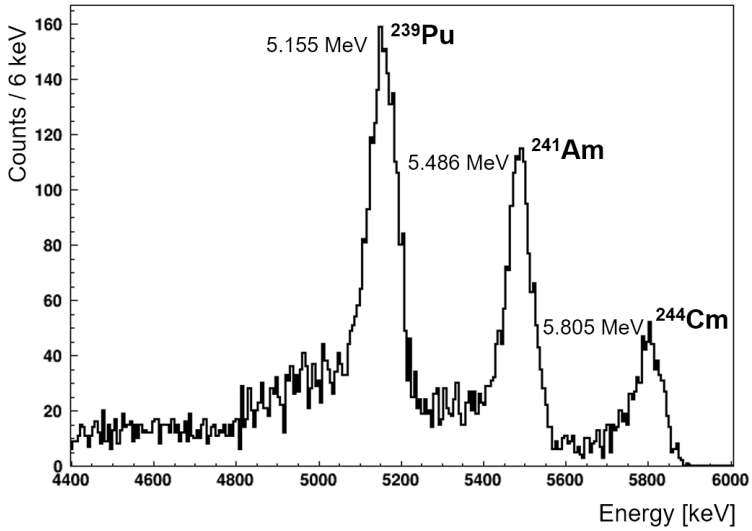

Figure 6.9: α energy spectrum acquired with one strip of the p-side of the DSSSD detector. A triple α-source (^{239}Pu (5.155 MeV), ^{241}Am (5,486 MeV), ^{244}Cm (5,805 MeV)) was used for the measurement. The calculated energy resolution ΔE in the energy range of 5 MeV was determined to $\sim$ 64 keV.

In fact a better energy resolution by about a factor of two was expected. The explanation could go in the direction of both a high interstrip capacitance, causing high electronic noise in each strip signal, or a too thick SiO_2 layer deposited on top of the detector. This layer of insulating material is protecting the sensitive part of the detector and can be considered a *dead layer*, since no signal can be produced within this thickness. If the thickness of this layer is too high, it could cause unexpected high scattering and energy loss of the impinging particles. However, this would even be more relevant when detecting electron signals, as those light particles would suffer more from these effects. In our case of α particles detection the reason of this performance could therefore predominantly lie in the values of the interstrip capacitance. Another test was performed, using the same signal processing setup and data acquisition, but sending a pulser signal (generated by a pulse generator from CAEN, DT5800D [251]) instead of acquiring signals from a radioactive source. 60 mV rectangular and narrow pulse signals (with minimum selectable rise and fall times of 8 ns) were sent to the same detector strip whose energy resolution was before characterized with an α source. The signal from the pulser was also acquired by being sent directly to the MSI-8 module. The ADC channel values of the two energy spectra obtained were calibrated using a linear calibration curve with offset and gain parameters obtained from the previously described α source test. Since also the signal processing chain was the same in all these tests, the resulting value of the peak width (FWHM) could therefore be compared: a FWHM equal to 10 keV was obtained when the detector was not connected, while when being connected the resulting FWHM was equal to 62 keV. Since the dead layer could not influence these last tests, the interstrip capacitance values seem to play an important role. Detailed evaluations, e.g. using the support of detector simulation

tools are not within the scope of this thesis, but since these preparatory characterization tests suggested a considerable influence of a noise component generated by the interstrip capacitances, the latter were measured and the outcome of these tests is presented in the next section.

6.1.3 Interstrip properties and characterization

The interstrip properties are important parameters for this kind of segmented semiconductor detectors, since they crucially contribute to the energy resolution performance and such essential for our Compton camera imaging application. Since the energy range of interest of signals detected by a DSSSD in the Compton setup does not reach high values (the energy range considered extends up to $\sim$ 500 keV), the noise and energy resolution performances are important parameters to be considered. The individual strips should be as much as possible electrically isolated from each other, in order to reduce the noise and obtain good energy resolution.

An interstrip characterization of the DSSSD layers could be performed at the laboratories of CiS [191] in Erfurt. In tests whose results are plotted in Fig. 6.10, the interstrip capacitance between one selected strip and its two neighboring ones was measured. A bias voltage of 70 V was given to the n-side or the p-side (in this case -70 V) of the detector, and the interstrip capacitances were measured between strips of the opposite detector side. Figure 6.10(a) shows the interstrip capacitance values on the p-side, whereas Fig. 6.10(b) displays the same for strips on the n-side. As expected, the p-side strips exhibit better performance, i.e. lower values of the interstrip capacitance. The interstrip capacitance was measured in different regions of the detector, showing results within the same range of values.

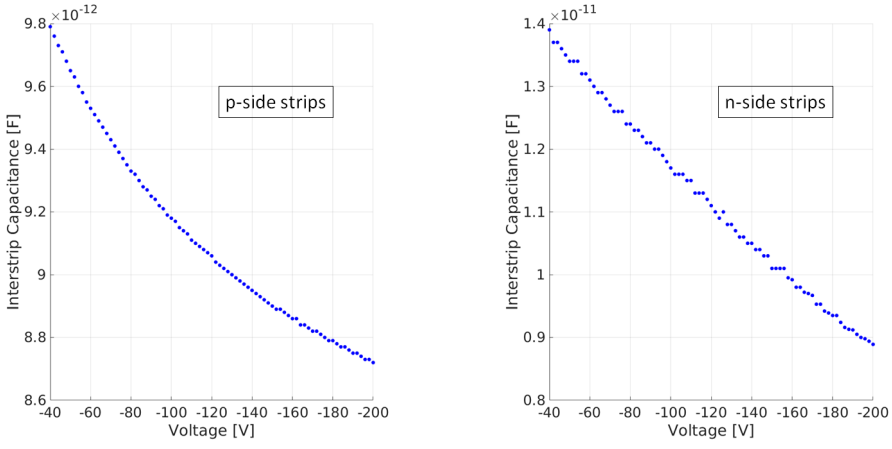

(a) (b)

Figure 6.10: Interstrip capacitance between one selected strip on (a) the p-side and (b) the n-side and its two neighboring strips. The selected strips were located in the central region of the detector.

Figure 6.11 displays values from a similar measurement where four instead of two neighboring strips were considered. The values are shown again for (a) p-strips and (b) n-strips. An obvious increase of the capacitance values acn be observed, due to the higher number of strips connected, can be observed. The same trend between the interstrip capacitance values of p-strips and n-strips is observed. All interstrip capacitance values are decreasing with an increase of the bias voltage, since the deeper the depleted zone the lower intrinsic electronic noise is present in the detector.

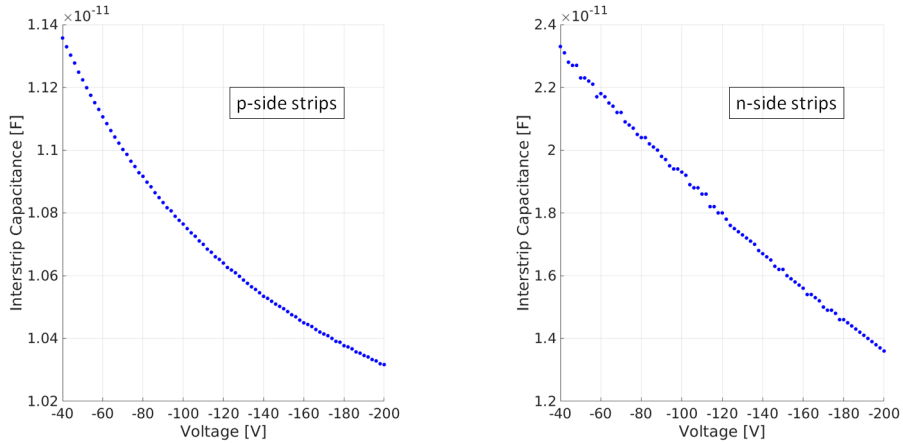

(a) (b)

Figure 6.11: Interstrip capacitance between one selected strip on (a) the p-side and (b) the n-side and four neighboring strips. The selected strips were located in the central region of the detector.

In order to characterize the electric insulation between neighboring strips, a further test was performed, aiming at obtaining interstrip resistance values for both sides of the detector.

A positive bias voltage (+150 V) was applied to the bias ring of the n-side of the detector. Simultaneously, on the p-side of the detector, a strip was connected to ground and a small voltage (from -0.3 to +0.1 V) between this strip and the two neighboring ones was applied. The plot in Fig. 6.12(a) shows the resulting I-V relation between the voltage applied and the current flowing in these p-side strips. The same test was performed for the n-side of the detector (this time applying a bias voltage for the detector equal to -150 V and a voltage between the n-strips between -1 mV and +1 mV), the resulting correlation is shown in Fig. 6.12(b).

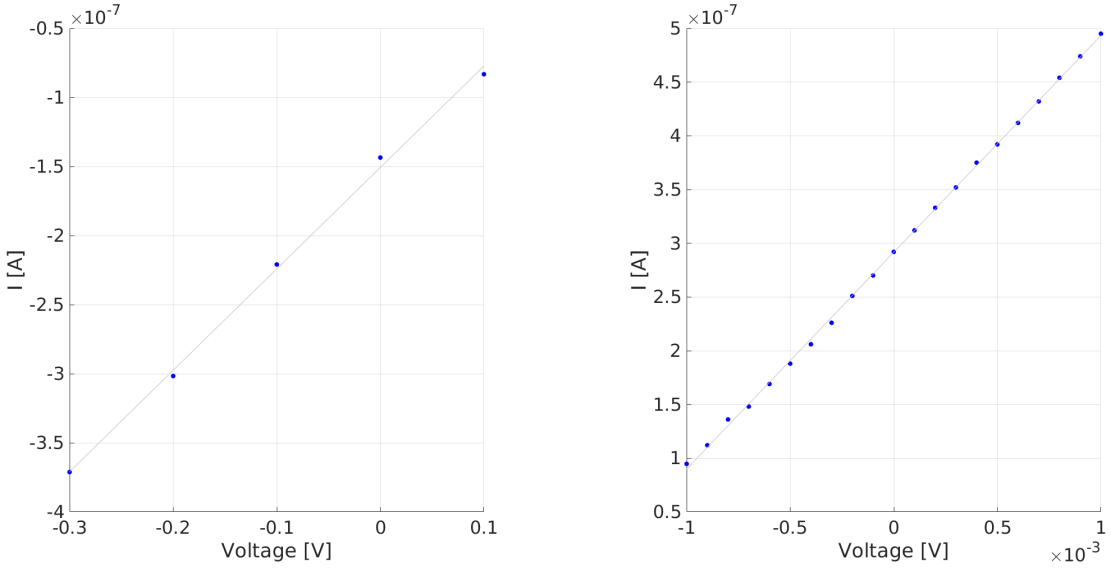

(a) (b)

Figure 6.12: I-V interstrip relation on (a) the p-side and (b) the n-side. See the text for details.

The interstrip resistance can easily be calculated from the relation $R = V/I$, obtaining a value of 1.4 MΩ for the strips on the p-side and a value of 5 kΩ for the n-strips. The values which were obtained are rather low considering that they were calculated from a fully depleted detector situation, in which values in the order of hundreds of MΩ or even few GΩ could be expected [175, 176, 252]. It will be observed that, for our application and our energy range of interest for the signals to be detected, these values will lead to noise which can severely compromise the detector performance (see Chap. 7).

6.2 $LaBr_3$(Ce) Scintillator

The absorber component of the LMU Compton camera is a monolithic scintillator crystal coupled to a segmented multi-anode PMT. It was described in Chap. 4 and its readout electronics in Chap. 5. This section is dedicated to its characterization, namely time and energy resolution. The spatial resolution characterization will be presented in Sect. 6.4 and 6.3, respectively, together with the algorithm to obtain it. First evaluation studies for a $CeBr_3$ scintillation crystal coupled to a 64-fold segmented PMT were also performed and are discussed in the last section of this chapter. This scintillation crystal is presently considered as alternative absorber material for the Compton camera, since it is a comparable but cheaper solution to the $LaBr_3$(Ce) crystal.

6.2.1 Time resolution

An evaluation of the timing performance of the $LaBr_3$(Ce) crystal coupled to the (256-fold segmented) H9500 PMT was performed in the PhD thesis work of S. Aldawood [139]. Since we are now assessing different scintillation detectors to be used as extension of the absorber component of the Compton camera prototype, the timing performance of these detectors was investigated (in the framework of T. Binder's ongoing PhD studies). The resulting values of the time resolutions are presented in this section for completeness of the presentation of relevant performance parameters of the scintillation detectors in use for the LMU Compton camera prototype. The explanation of the setup and the procedure for these measurements is not in the scope of this thesis, therefore those details can be found in the above mentioned thesis. This section presents the results obtained with two different $LaBr_3$(Ce) crystals coupled to the 256-fold segmented H9500 PMT and the 64-fold segmented H8500C PMT, respectively. A coincidence method was used: the time resolution of a reference detector was determined through the measurement of the Coincidence Resolving Time (CRT) between two simultaneously emitted γ rays from a ^{60}Co source. Two identical fast plastic detectors (Saint-Gobain, type BC-418 [253]) were coupled to fast PMTs (Photonics XP2020/Q [254]) and used as a reference. Since the signals from these two detectors were read out using the same electronics chain, the time resolution of one of them, $\Delta T_{reference}$, was extracted according to

$$\Delta T_{plastic,1} = \sqrt{\frac{(\Delta T_{plast,1+2})^2}{2}} \tag{6.3}$$

where $\Delta T_{plast,1+2}$ is the total time resolution (i.e. width of the coincident time difference peak) measured by the two identical reference detectors.

Subsequently, while keeping the same configuration for the readout electronics, one of the two reference detectors was replaced by one of the scintillation detectors under investigation. The coincidence time peaks from these measurements, for both $LaBr_3$(Ce) scintillation detector configurations, are depicted in Fig. 6.13.

By knowing the time resolution of the reference detector and the combined time resolution (ΔT_{tot}) of plastic scintillator and $LaBr_3$(Ce) scintillator, the time resolution of the

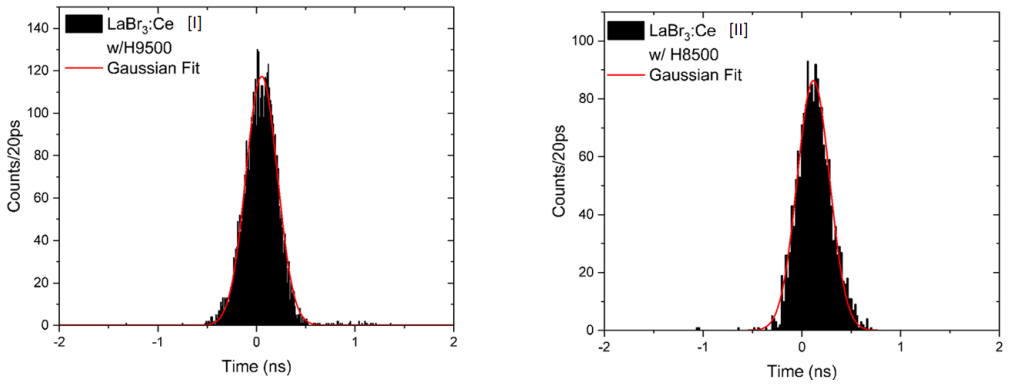

(a) (b)

Figure 6.13: Coincidence time peaks obtained from the measurements using (a) the monolithic $LaBr_3(Ce)$ crystal coupled to the 256-fold segmented H9500 PMT and (b) the monolithic $LaBr_3(Ce)$ crystal coupled to the 64-fold segmented H8500C PMT.

Scintillation detector	Time resolution [ps]
$LaBr_3(Ce)$ + H9500	250 ± 3
$LaBr_3(Ce)$ + H8500C	266 ± 3

Table 6.1: Time resolution obtained for the two different $LaBr_3(Ce)$ monolithic scintillation crystals coupled to an H9500 PMT and an H8500C PMT, respectively.

latter one can be derived using

$$\Delta T_{scintillator} = \sqrt{(\Delta T_{tot})^2 - (\Delta T_{plast,1})^2} \tag{6.4}$$

The results obtained are summarized in Tab. 6.1. The value obtained for the time resolution of the $LaBr_3(Ce)$ coupled to the (256-fold segmented) H9500 PMT was slightly improved compared to the value which was presented in [139] and was determined to be equal to 250 ± 3 ps. The same procedure was repeated for another, newly acquired $LaBr_3(Ce)$ crystal scintillator coupled to the 64-fold segmented H8500C PMT, for which a time resolution of 266 ± 3 ps was found. As expected, comparable values can be derived for the detector combinations with two different PMTs used to read out the scintillation light from the two different $LaBr_3(Ce)$ crystals with identical geometrical specifications.

6.2.2 Energy resolution

The evaluation of the energy resolution for the $LaBr_3(Ce)$ scintillation crystal coupled to the 256-fold segmented H9500 PMT was previously evaluated and can be found in [139], for an absorptive and reflective coating scenario of the crystal. During the work presented in this thesis, the energy resolution performance was extensively evaluated for the newly purchased but geometrically identical $LaBr_3(Ce)$ scintillation crystal which was coupled in

our laboratory to a 64-fold segmented PMT. This evaluation and performance comparison is essential in view of the foreseen upgrade of the Compton camera system, which envisages using scintillation crystals coupled to 64-ch. PMTs instead of the initially used 256-fold segmented PMT, in order to reduce the complexity of the readout electronics. The results presented for the energy resolution evaluation are divided in two parts: in the first one, more extensive, the "standard" signal processing and data acquisition (described in Sect. 5.2.1 and sec:RIO, respectively) was used. In the second part the energy resolution performance of the $LaBr_3$(Ce) crystal coupled to a 64-fold segmented PMT was evaluated using the readout electronics based on the MMR boards and related controller (described in Sect. 5.2.2 and 5.3.2).

Readout by individual spectroscopy electronics

The results presented in this section were achieved within a Master thesis project supervised by the author of this work [255]. The energy resolution, which was defined in Eq. (3.14), is expressed as relative quantity $\Delta E/E$ [%].

Since the results presented in this section refer to three different detector configurations, in Tab. 6.2 a list of them and their photosensor coupling configuration is shown. For each of these detectors, the results presented in this section will be divided in two main parts, corresponding to the acquired (position dependent) 2D energy resolution maps and to the energy resolution study as a function of the PMT bias voltage.

Detector configuration	Scintillation crystal	PMT
Detector 1	$LaBr_3$(Ce) I	H8500C
Detector 2	$LaBr_3$(Ce) II	H8500C
Detector 3	$LaBr_3$(Ce) I	H12700A-10

Table 6.2: Scintillation detector configurations whose energy resolution performance was studied. The numbers I and II refer to two different $LaBr_3$(Ce) scintillation crystals, which were purchased from the manufacturer requesting identical geometry and crystal properties. The detector I was also used for the spatial resolution determination which will be presented in Sect. 6.4.4.

For all detector configurations the energy resolution values were extracted from the energy spectra which were acquired from the sum dynode signal of each PMT. The signal processing readout was based on Constant Fraction Discriminator (and amplifier) modules (MCFD-16 [235], Mesytec GmbH) and Charge Integrating modules (MQDC-32, [236], Mesytec GmbH), which were in details described in Sect. 5.2.1. The DAQ system used for the measurements presented in this section was identical to the one described in Sect. 5.3.1 and is based on a PowerPC (RIO-3) frontend CPU in a VME crate and on the Marabou software [244]. The scanning system used for the collimated radioactive source will be explained in more detail in Sect. 6.3, since it is identical to the device used in the procedure for the spatial resolution determination of the monolithic scintillator.

2D energy maps Firstly, the energy resolution of "detector 1", which was also used for the spatial resolution measurements (whose results are presented in Sect. 6.4.4), was evaluated.

In order to study the position-dependent energy resolution of the detector across the front surface of the scintillator with an area of 50.8 × 50.8 mm^2, the $LaBr_3$(Ce) crystal's front surface was scanned in x and y directions with a 1 mm collimated ^{137}Cs source and a step size of 6.08 mm, which corresponds to the size of each PMT pixel. Each irradiation position was consecutively centered on an individual PMT pixel, therefore obtaining 64 irradiation positions in total.

The resulting 2D energy resolution map is depicted in Fig. 6.14. The x (top) and y (left) projections are also displayed and were derived by averaging, for each pixel row (x projection) or column (y projection), all energy resolution values contained. In general the energy resolution of a monolithic and homogeneous scintillation crystal is expected to be position independent. In fact this behaviour was observed in good approximation in the study performed for the $LaBr_3$(Ce) crystal coupled to the highly granular H9500 PMT (which can be found in [139]): the energy resolution was found, within the experimental uncertainties, to be position-independent and equal to 3.5%.

A degradation of the energy resolution can in principle be expected in the crystal corners, of significant amount if the crystal coating is absorptive (because of scintillation light absorption) or negligibly small if the crystal coating is reflective (because of light scattering) [139]. Since all detectors under investigation here are reflectively coated, only a slight degradation of the energy resolution can be expected in the corners or along the edges. However, as it can be observed from the map and projections in Fig. 6.14, the results obtained for "detector 1" show counterintuitive behaviour with a minimum value of $\Delta E/E = 3.8\%$ in a corner position, whereas the energy resolution obtained for a central position on the detector surface, amounts to around 5.3%, thus increased by about 30%.

In order to investigate if this behaviour can be traced back to the scintillation crystal or the PMT, additional measurements were carried out.

The same H8500C PMT as before was coupled to a different and newly acquired $LaBr_3$(Ce) scintillation crystal, corresponding to the "detector 2" configuration. A 2D energy resolution map was acquired under the same measurement conditions as for "detector 1". The resulting 2D energy resolution map is depicted in Fig. 6.15, together with x and y projections of the averaged values. The observed trend does not significantly differ from the one already obtained for "detector 1", with the energy resolution values being in the same range.

In order to complete the piture, a third detector system was coupled: the "detector 3" configuration makes use of the $LaBr_3$(Ce) scintillation crystal which was used for "detector 1", but now coupled to another type of 64-fold segmented PMT (H12700A-10 [208] from Hamamatsu) with different gain and quantum efficiency. The 2D energy resolution map for "detector 3" was acquired with the same method as described before and is shown in Fig. 6.16 together with its (averaged) x and y projections. The results feature the same trend as observed with the other two systems, however with slightly improved values of $\Delta E/E$.

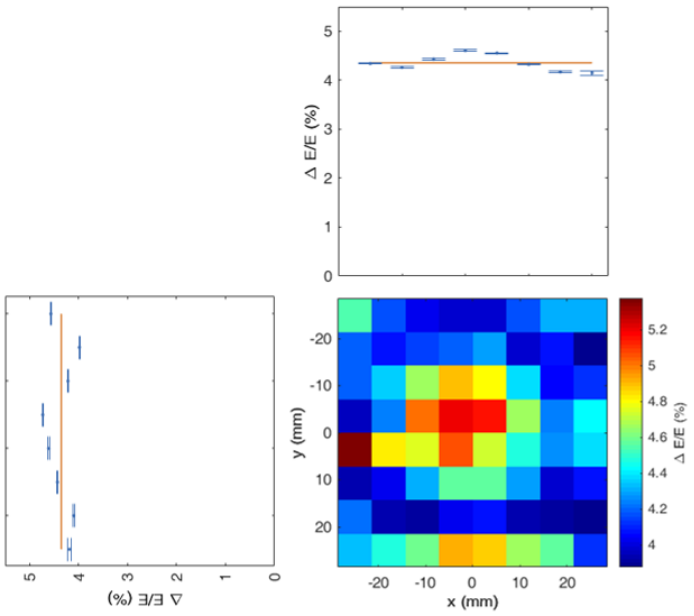

Figure 6.14: 2D energy resolution map acquired by scanning the $LaBr_3$(Ce) scintillator crystal (L_1) coupled to the H8500C PMT with a 1 mm collimated ^{137}Cs source with a step size of 6.08 mm (corresponding to the PMT pixel size) in x and y directions. The x and y projections are shown on top and left of the map, respectively. The orange solid lines denote the mean value obtained for the corresponding row or column.

To quantitatively compare the results from the three scenarios, the variances σ_x^2 and σ_y^2, respectively, for the distribution of the energy resolution values along the rows and columns of the x and y projections were calculated. They are listed in Tab. 6.3, together with the energy resolution values averaged over the whole detector area. The energy resolution which was obtained in [139] for the $LaBr_3$ scintillation crystal coupled to the H9500 PMT (here defined as "detector 4") is also listed. For all detector systems it can be therefore stated that, although the energy resolution varies with the source irradiation position, the σ_x^2 and σ_y^2 variance values which are obtained are typically less than 1% of the determined energy resolution values (which are found to be in the range between 3% and 5%). Thus the observed position dependent differences of the energy resolution can be considered as too small to be relevant for our detector assessment. From Tab. 6.3 it can also be noted that the "detector 1" configuration exhibits on average a variance value which is more than about twice as large compared to the corresponding values of "detector 2" and "detector 3". The average energy resolution obtained with the "detector 1" and "detector 2" configurations are comparable, whereas the value obtained with "detector 3" features a significant improvement.

So the trend that was first observed for "detector 1", with a slightly position dependent energy resolution that degrades from the corners to the center of the crystal independent of the coupled PMT shows up also for the other systems and cannot be attributed to either

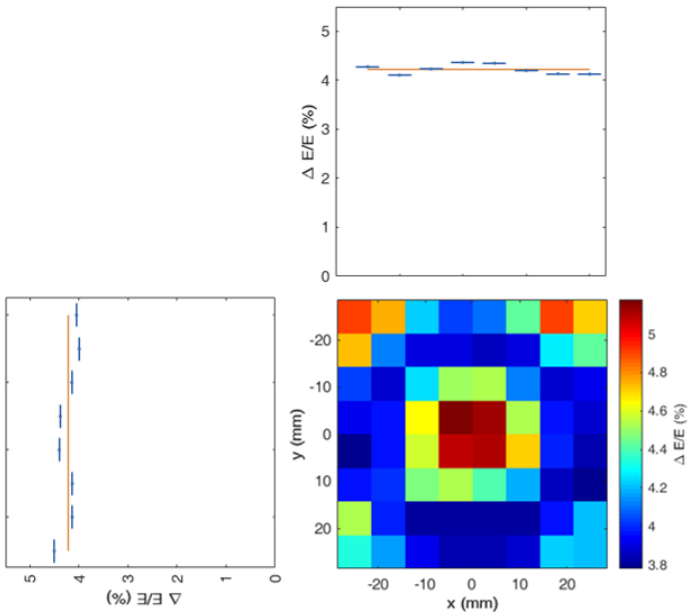

Figure 6.15: 2D energy resolution map acquired by scanning the new $LaBr_3$(Ce) scintillator crystal (L_2) coupled to the (already previously used) H8500C PMT with a 1 mm collimated ^{137}Cs source with a step size of 6.08 mm (corresponding to the PMT pixel size) in x and y directions. The averaged x and y projections are shown on top and left of the map, respectively. The orange solid lines denote the mean value obtained for the corresponding row or column.

the crystal or the PMT alone. Its origin is still an open issue.

However, it can be concluded that the better performance achieved with the "detector 3" configuration can be attributed to the different type of PMT (H12700A-10) in use. This rather recently introduced PMT model has a higher quantum efficiency compared to the predecessor, the H8500C PMT. This finding is useful in view of an envisaged upgrade of the Compton camera system, where the absorber's field of view could be expanded by adding more absorber crystals placed aside of each other, read out by the PMT model with the best performance.

Energy resolution as a function of energy and high voltage The energy resolution study for the $LaBr_3$(Ce) scintillation detectors was extended to an investigation of the energy resolution as a function of the photon source energy and PMT high voltage. The relation to the latter one was studied in order to define an optimum operational voltage for the $LaBr_3$(Ce) detector. The applied PMT bias voltages are in the range between -750 V and -1100 V, which is the maximum operational voltage suggested by the manufacturer. The performance at different high voltage settings was evaluated in steps of 50 V. Different γ-ray calibration sources were used: isotropic point sources and collimated sources. Although the energy resolution should not depend on the emission characteristics of the

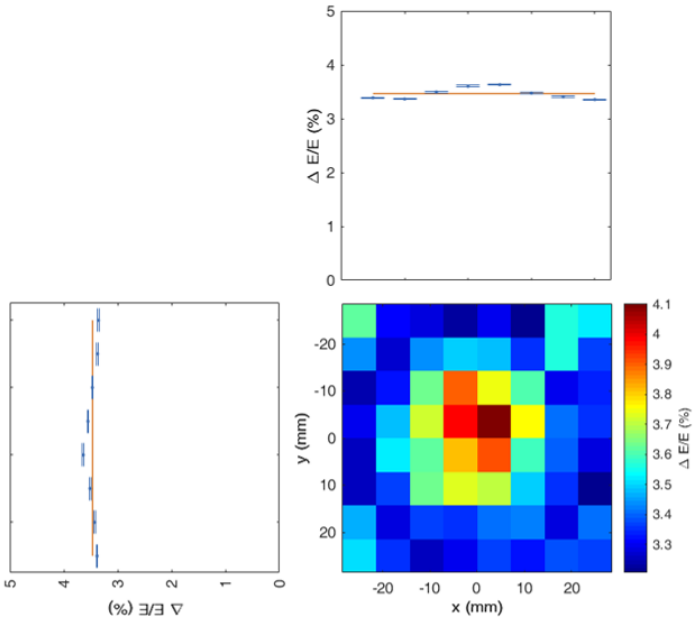

Figure 6.16: 2D energy resolution map acquired by scanning the $LaBr_3(Ce)$ scintillator crystal (L_1) coupled to the H12700A-10 PMT with a 1 mm collimated ^{137}Cs source with a step size of 6.08 mm (corresponding to the PMT pixel size) in x and y directions. The averaged x and y projections are shown on top and left of the map, respectively. The orange solid lines denote the mean value obtained for the corresponding row or column.

photon source, the previously observed slightly position-dependent energy resolution could result in slightly different results to be expected from the use of an isotropic or a collimated radioactive γ-ray source.

The radioactive γ-ray calibration sources used for this measurement series are listed in Tab. 6.4 together with their corresponding γ lines and emission characteristics (isotropic or collimated).

	^{22}Na	^{137}Cs	^{60}Co
source energy [keV]	511; 1275	662	1173; 1332
isotropic	✓	✓	✓
collimated		✓	✓

Table 6.4: Radioactive γ-ray calibration sources used for the energy resolution evaluation as a function of the high voltage applied to the PMT. The sources listed are either isotropic or collimated. For each calibration source the corresponding photopeak energies are specified.

The isotropic calibration sources were placed at a central position about 20 cm in front of the detector surface, whereas the collimated sources were subsequently positioned in front of the center of the detector surface and in front of an area of the detector surface where the best energy resolution was obtained before. Data from each measurement were

	Detector configuration	σ_x^2 [%]	σ_y^2 [%]	mean(ΔE/E) [%]
Detector 1	$LaBr_3$(Ce) I + H8500C	0.03	0.07	4.3(1)
Detector 2	$LaBr_3$(Ce) II + H8500C	0.01	0.03	4.1(1)
Detector 3	$LaBr_3$(Ce) I + H12700A-10	0.01	0.01	3.4(1)
Detector 4	$LaBr_3$(Ce) + H9500			3.5 [139]

Table 6.3: Variance σ_x^2 and σ_y^2 of the x and y projection values, respectively. The energy resolution value averaged over the whole detector area is also listed for the three detector configurations. The energy resolution value for the $LaBr_3$(Ce) + H9500 configuration ("detector 4") is also listed.

acquired for 15 minutes. The determination of the energy resolution as a function of the photon source energy was carried out for each PMT high voltage value. The trend of these values could be fitted using a fit function according to

$$\frac{\Delta E}{E} = 100 \times \frac{A + B \times E}{E} \tag{6.5}$$

where A and B are free parameters [256].

As for the 2D energy resolution map, the "detector 1" was first evaluated and its results are shown in Fig. 6.17 and 6.18.

In Fig. 6.17 the energy dependence of the energy resolution is shown for each PMT voltage applied and the values are fitted using the function described by Eq. (6.5). Panel (a) refers to the detector irradiation using isotropically emitting point sources, in panel (b) the resulting graphs are shown for collimated sources irradiating the crystal in its center and panel (c) displays the results for the irradiation scenario when the collimated sources are placed in an area of the detector where the best energy resolution was observed in the previous measurements series. In all the three plots and for all PMT voltages applied, an improvement of the energy resolution is observable with an increasing photon energy. This expected trend is related to the fact that incident γ-rays with higher energies have a larger depth of interaction inside the crystal, which leads to a higher probability of a full collection of all generated scintillation light. Specifically, for bias voltages (absolutely) lower than -1000 V the trend is almost parallel for the different voltages applied, whereas for a bias voltage of -1000 V, -1050 V or -1100 V the slope of the fitting curve becomes steeper, leading to a degradation of the energy resolution for lower photon energies and a corresponding improvement for higher energies, compared to the resolution values obtained at lower operational voltages. Furthermore, it should be noted that the more the operational voltage decreases, the more the energy resolution degrades and the fit curves are shifted to larger values. This is due to the lower electric field generated along the PMT dynode stages and therefore to a lower photoelectron detection probability. The differences which can be observed in the absolute values of the energy resolutions displayed in the sub-panels (a), (b) and (c) of both Fig. 6.17 and Fig. 6.18 can be attributed to the position-dependent differences already discussed in the context of Fig. 6.14 - 6.16.

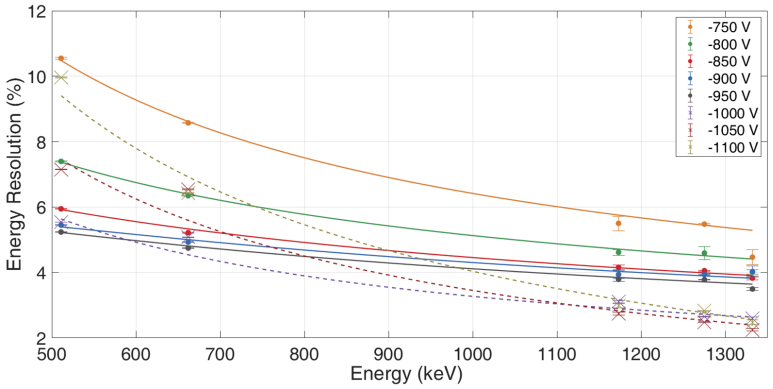

(a)

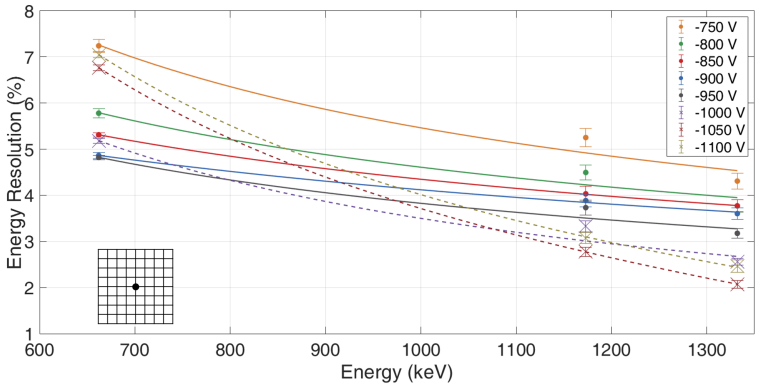

(b)

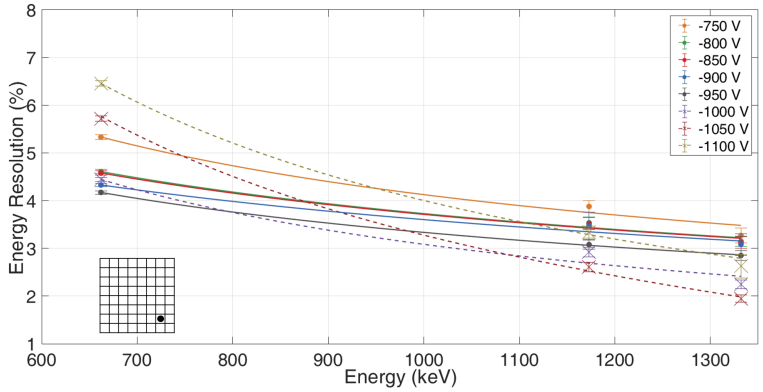

(c)

Figure 6.17: Energy dependence of the relative energy resolution calculated for the $LaBr_3(Ce)$ scintillation crystal coupled to the H8500C PMT ("detector 1"). The measurements were performed using radioactive calibration sources, specifically: (a) isotropic calibration point sources and collimated radioactive sources irradiating perpendicularly the surface of the detector in (b) the center and (c) a corner in which the best value of the energy resolution was observed before.

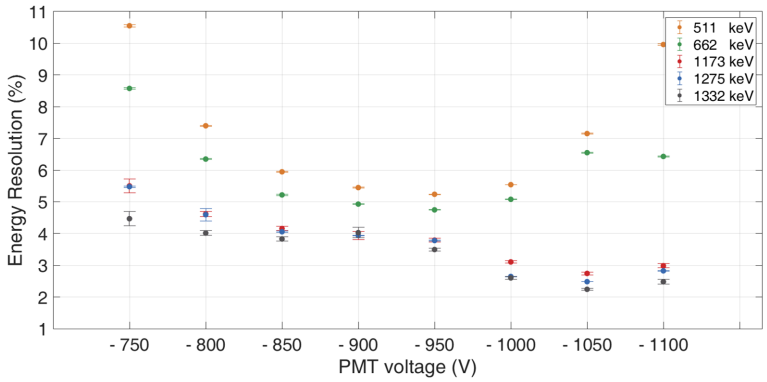

(a)

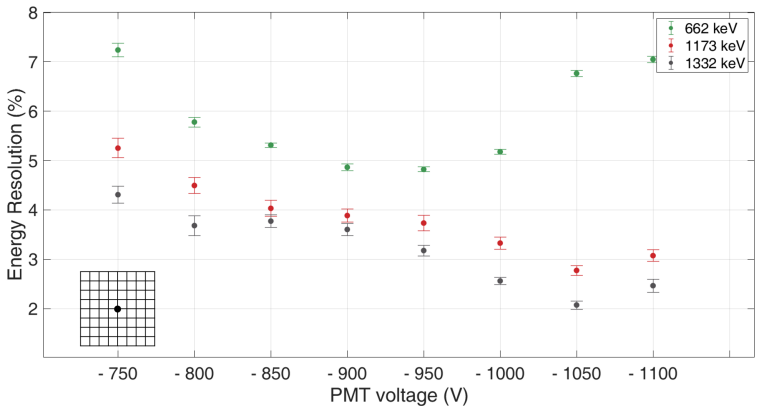

(b)

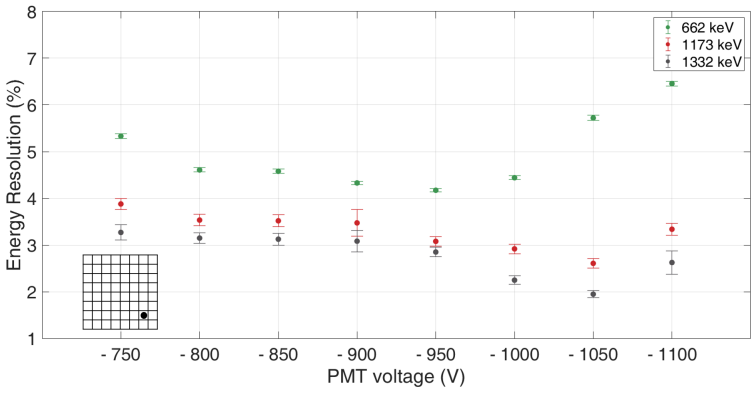

(c)

Figure 6.18: Relative energy resolution of a $LaBr_3(Ce)$ crystal coupled to a 64-channel H8500C PMT ("detector 1"), studied as a function of the PMT bias supply voltage. The measurements were performed using radioactive calibration sources, specifically: (a) isotropic calibration point sources and collimated radioactive sources irradiating perpendicularly the surface of the detector in (b) the center and (c) a corner in which the best value of the energy resolution was observed before.

As it was already derived from the 2D map in Fig. 6.14, the best energy resolution values are obtained for a setup configuration in which a collimated gamma source is placed in front of an area of the detector close to one of its corners.

In order to learn about the correlation between the applied PMT bias voltage and the energy resolution, the plots in Fig. 6.18 show the energy resolution as a function of the applied PMT voltage for different photon energies, using (a) the isotropic calibration source and (b) the collimated calibration source, both placed in the center of the detector surface and (c) in the corner where previously the best value of ΔE/E was found.

A similar trend can be observed in all plots of Fig. 6.18: the best values for lower photon energies (511 keV and 662 keV) are achieved with an operational voltage in the range between -900 V and -950 V, whereas for higher photon energies (1173 keV, 1275 keV and 1332 keV) the best values lie around -1000 V operational voltage.

The same evaluation procedure was applied also to the "detector 2" (in Fig. 6.19) and "detector 3" (in Fig. 6.20) configurations. The measurements for "detector 2" and "detector 3" were performed by placing the collimated ^{137}Cs and ^{60}Co sources in front of the "best" corner of the detector surface.

Figure 6.19 shows the energy resolution as a function of (a) the incoming photon energy and (b) the applied PMT applied high voltage. In Fig. 6.19(a) the solid lines are showing fit curves to the data points using a fit function according to Eq. (6.5) for PMT voltages between -750 V and -950 V, whereas the dashed lines refer to PMT voltages between -1000 V and -1100 V, which is the maximum high voltage value which can be applied to this PMT according to the manufacturer. In Fig. 6.19(b) the minima found for the energy resolution correspond to the same operational voltages which were determined for "detector 1": around -900 V and -950 V for incident low energy gammas and around -1000 V for the highest photopeak energies studied. Thus the results are comparable with the results obtained for the "detector 1", as already stated for the 2D energy resolution maps, since both configurations make use of the same PMT, which seems to be the decisive component concerning the performance of the detector system.

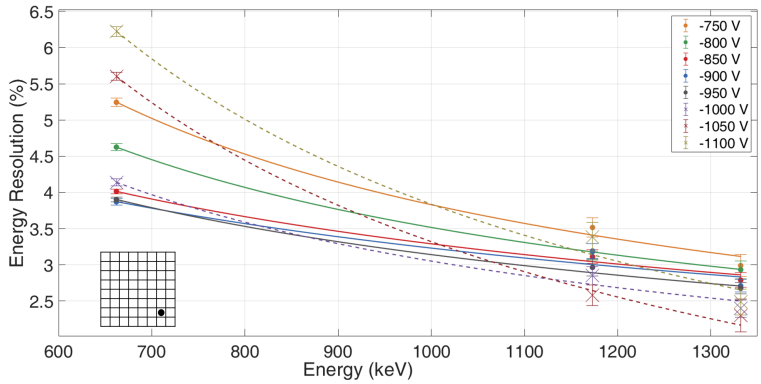

(a)

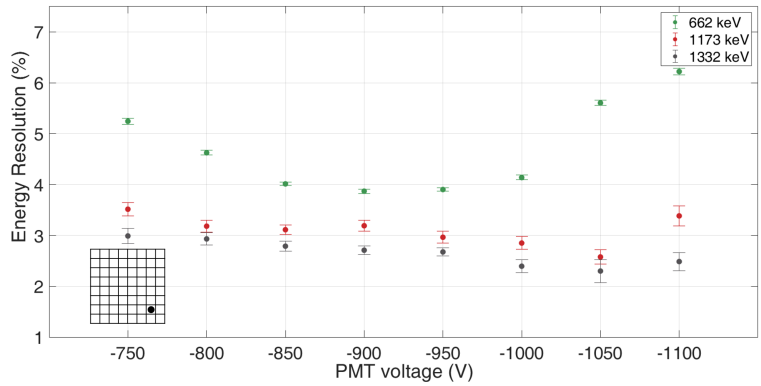

(b)

Figure 6.19: Relative energy resolution of a $LaBr_3(Ce)$ crystal as a function of (a) the photon source energy and (b) the PMT operational voltage, obtained for the "detector 2" system (i.e. coupled to an H8500C PMT).

In Fig. 6.20 the results obtained with "detector 3" are depicted for the energy resolution as a function of (a) the gamma source energy and (b) the PMT operational voltage. As for the other detector systems and for the 2D energy map already presented for this system, the high voltage ranges from -750 V to -1100 V and the photon energies range from 511 keV and 1332 keV. Although the PMT in use for this detector system is different (H12700A-10), the trends that were observed for both energy resolution dependencies are still valid. It should be noted that for this detector configuration, the energy resolution measured at higher photon energies and lower PMT bias voltage is comparable within the error bars. These slight differences in the performance can be due to the PMT properties, where the H12700A-10 PMT, compared to the H8500C, features a higher quantum efficiency and a lower gain (see Sect. 4.4.3).

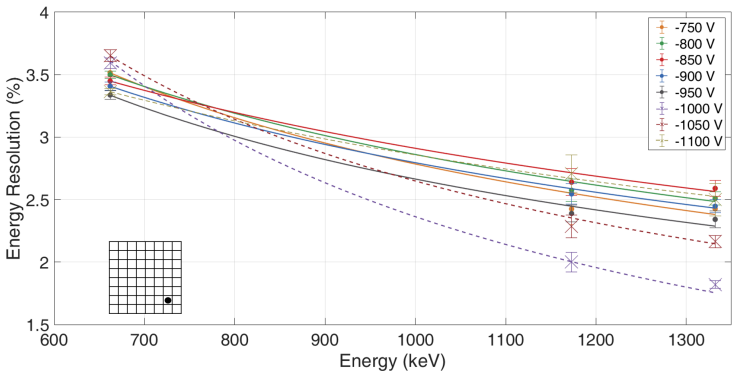

(a)

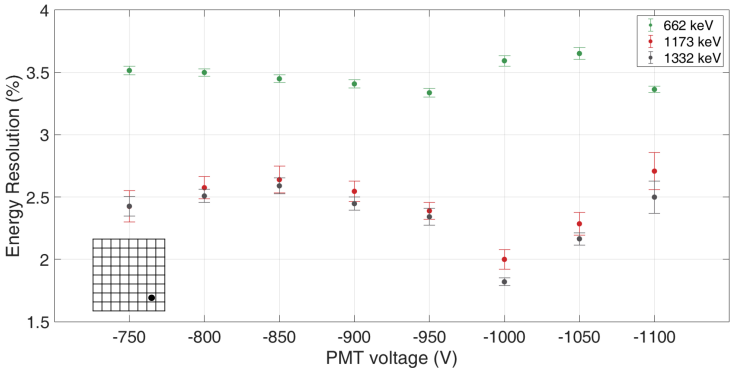

(b)

Figure 6.20: Relative energy resolution of a LaBr$_3$(Ce) crystal as a function of (a) the photon source energy and (b) the PMT operational voltage, obtained for the "detector 3" system (i.e. coupled to an H12700A-10 PMT).

Conclusions can be drawn on the overall trend of the energy resolution for each of the LaBr$_3$(Ce) detector configurations under study, where ΔE/E improves with an increasing energy of the incoming photons. This is related to the decreasing probability of scintillation light losses at higher photon energies and most important to the increasing scintillation light yield. Also the energy resolution trend as a function of the PMT operational voltage can be summarized as constantly improving with an increase of the bias voltage up to about -950 V. This effect is related to the reduced number of collected photoelectrons at lower voltages [183], which results in a decrease of the detection efficiency. For higher PMT operational voltages, an inverse trend can be observed: a possible explanation may be pointing in the direction of the emission of additional electrons caused by the stronger electric field created across the chain of PMT dynodes, which would lead to a higher dark current acquired. However, excessive PMT voltages where such effects should be unambiguously observable were not applied in our case, since the manufacturer's specifications were not exceeded and therefore only an onset of this behaviour might have been observed for the highest bias voltages applied.

MMR Multi-channel Readout

This section is dedicated to the energy resolution evaluation using the recently upgraded readout system based on the MMR boards (which was described in Sect. 5.2.2). The intention is to verify that the detector system performance can be maintained in the same range of values which were previously obtained. The energy resolution was evaluated for the $LaBr_3$(Ce) scintillation crystal (which was defined as I) in Sect. 6.2.2) coupled to either the H8500C PMT or the H12700A-10 PMT. Both of them are 64-fold segmented PMTs. It should be reminded that in this readout configuration the 64 channels from the PMT pixels are read out using the MMR board and they are set as trigger in the VMMR module. Therefore the sum dynode is not considered. The energy spectrum from which the energy resolution was calculated was obtained by summing up by software the 64 signals belonging to the same photon event. The PMT was biased with a high voltage (HV) equal to either -850 V or -900 V, which correspond to the suggested voltages when using this readout system. The detector performance was evaluated using ^{137}Cs and ^{60}Co radioactive laboratory sources. Table 6.5 summarizes the energy resolution values which were obtained.

	HV = -850 V			HV = -900 V		
Detector configuration	662 keV	1173 keV	1332 keV	662 keV	1173 keV	1332 keV
$LaBr_3$(Ce) + H8500C	4.4(1) %	3.6(1) %	3.1(1) %	4.3(1) %	3.5(1) %	2.6(1) %
$LaBr_3$(Ce) + H12700A-10	4.4(1) %	3.4(1) %	3.1(1) %	4.3(1) %	3.4(1) %	2.9(1) %

Table 6.5: Energy resolution performance for the $LaBr_3$(Ce) crystal coupled to either the H8500C PMT or the H12700A-10 PMT. The MMR Multi-channel Readout was used for these evaluation measurements.

It can be observed that the values obtained are consistent with the performance achieved with the previous readout system, although the difference between the performance of the two PMTs which was previously observed is now less significant.

6.2.3 $CeBr_3$ as alternative to the $LaBr_3$(Ce) scintillator

Studies on the energy and time resolution characterization were also performed for the $CeBr_3$ scintillation crystal, in order to assess it as a possible alternative to $LaBr_3$(Ce), since it would be a cheaper solution for the absorber component of the Compton camera prototype. The $CeBr_3$ scintillation crystal was described in Sect. 4.4.2. The characterization study presented here was performed using the identical signal processing electronics and DAQ system described in Sect. 5.2.1 and 5.3.1, respectively, and used for the characterization of the $LaBr_3$(Ce) detector.

First, a 2D energy resolution map was acquired for the $CeBr_3$ scintillation crystal coupled to the H8500C PMT (Hamamatsu [207]). A similar map was already acquired for the $CeBr_3$ coupled to the H12700A-10 PMT (Hamamatsu [208]) and position-dependent energy resolution values ranging from 3.5% to $\sim$ 6% were observed, with an overall mean value of $\sim$ 4%. These results can be found in T. Binder's Master thesis [257].

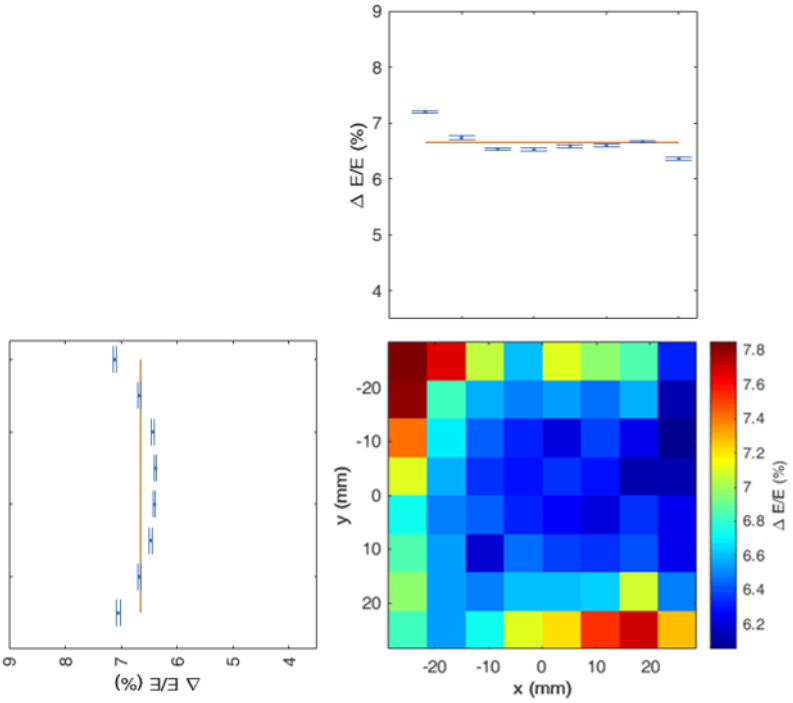

Figure 6.21: 2D energy resolution map acquired by scanning the $CeBr_3$ scintillator crystal coupled to the H8500C PMT with a 1 mm collimated ^{137}Cs source with a step size of 6.08 mm (corresponding to the PMT pixels size) in x and y directions. The averaged x and y projections are shown on top and left of the map, respectively. The averaged x and y projections are shown on top and left of the map, respectively. The orange solid lines denote the mean value obtained for the corresponding row or column.

In Fig. 6.21 the 2D energy resolution map for the $CeBr_3$ crystal coupled to the H8500C PMT is depicted, together with the averaged energy resolution values for the x and y projections (on top and at the left side of the 2D map, respectively). The map was acquired with the same procedure which was already described for the acquisition of the 2D energy resolution maps for the $LaBr_3$(Ce) scintillation detector (presented in Sect. 6.2.2). The position dependence of the energy resolution is more prominent for this detector system. However, the trend is opposite to the one which was observed for the $LaBr_3$(Ce) case: the best values for ΔE/E are found in the center of the crystal, and the energy resolution degrades towards the corners. This behaviour can be expected and attributed to scattering of scintillation light in the detector corners or absorption, mostly on the front and back sides of the crystal, since on the lateral sides a reflective coating is present. The variances

σ_x^2 and σ_y^2 calculated from the distribution of averaged values of $\Delta E/E$ in the x and y projections amount to 0.06 and 0.08 %, respectively. These values are in agreement with the ones calculated for the energy resolution study of the $LaBr_3(Ce)$ crystal, listed in Tab. 6.3.

The values for the position dependence of $\Delta E/E$ obtained from this study are consistent with those obtained with the $CeBr_3$ crystal coupled to the H12700A-10 PMT, but the absolute values obtained are higher for the $CeBr_3$ scintillation light read out by the H8500C PMT, where the averaged energy resolution amounts to $\sim$ 6.5 %. This leads to the same conclusion already drawn for the study performed for the $LaBr_3(Ce)$ scintillation crystal (in Sect. 6.2.2): the higher quantum efficiency of the H12700A-10 PMT compared to the H8500C PMT leads to a better energy resolution. This is an important findings in view of a clear preference for the H12700A-10 PMT. Thus the envisaged upgrade of the Compton camera prototype, which is foreseen in order to increase field of view of the absorber component by increasing the number of scintillation detectors, will be comprised of scintillators coupled to H12700A-10 instead of H8500C PMTs.

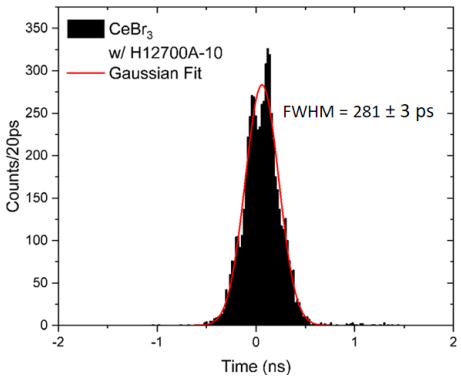

Figure 6.22: Coincidence time peak obtained from the measurements using the monolithic $CeBr_3$ scintillation crystal coupled to the 64-fold segmented H12700A-10 PMT.

For a full characterization comparison between the $LaBr_3(Ce)$ and the $CeBr_3$ scintillation crystals, the time resolution obtained in the framework of T. Binder's ongoing PhD project, is also here mentioned. The same procedure as presented in Sect. 6.2.1 for the $LaBr_3(Ce)$ detector was followed. The time resolution obtained for the $CeBr_3$ detector was determined as 281 $\pm$ 3 ps, which is within the range of expected values: comparable to the results found for $LaBr_3(Ce)$ due to the almost identical decay constants (16 ns for $LaBr_3(Ce)$, 17 ns for $CeBr_3$).

Considering the results obtained from the energy and time resolution comparison, it can be concluded that the $CeBr_3$ crystal can be considered as an attractive alternative to $LaBr_3(Ce)$ as absorber material of the Compton camera prototype. The performances are comparable, and they will be further characterized also in simulation studies. A spatial resolution study is foreseen within the PhD project of T. Binder.

6.3 Position determination in a monolithic scintillator

Since we are using a monolithic scintillator crystal, the spatial resolution does not come from a direct measurement, but it has to be instead determined via the use of a specific algorithm, whose principle and procedure is described in this section. The method based on this algorithm is used to determine the spatial resolution of the monolithic scintillator and to obtain the unknown photon interaction positions in the Compton camera absorber. Both procedures are explained in this section, together with the experimental setup and the measurements needed in order to obtain the required input data.

The studies here presented were carried out with two calibration sources, namely ^{137}Cs and ^{60}Co source, which provide photopeaks at 662 keV, 1173 keV and 1332 keV, respectively. Although the targeted photon energy range of interest for prompt-gamma imaging using the Compton camera prototype is considerably higher than these energies, an assessment can still be deduced from the spatial resolution trend as a function of the photon energy. The difficulty of further extending these studies to higher photon energies is given by the need of a highly collimated source of multi-MeV photons with good signal-to-noise ratio (S/N), in order to record the requested statistics in a reasonable amount of time.

6.3.1 The algorithm

The algorithm which was used for the spatial resolution determination and the reconstruction of the interaction positions in the monolithic scintillators is based on the *k-Nearest Neighbors* (k-NN) algorithm. This statistical method was first introduced by Fix and Hodges in 1951 [258]. Since then, many applications were based on this learning algorithm. Within the framework of our application, Maas et al. [259] initially implemented the k-NN algorithm for the reconstruction of photon interaction positions in monolithic crystal scintillator detectors. The idea of the k-NN algorithm is based on the fact that when a γ ray interacts with a scintillator material, the flash of light generated by the scintillation process in an ideal case has a spatial correlation with the primary γ-ray interaction position. At TU Delft extensive work was carried out to adapt and otimize the method for PET applications [260, 261], including proposed modifications to overcome the handicaps of extensive calibration measurements and long computational times [262]. One of the main variations introduced and explored by [262] and proven to maintain the quality of the performance is the use of only a perpendicularly incident beam of photons instead of performing the calibration at many angles of incidence. Considering the good performance obtained in these studies, we decided to adopt the same concept and adapt it to our application needs. Among the several versions of the algorithm considered by the TU Delft group, the smoothed k-Nearest Neighbors (k-NN) and the Categorical Average Patterns (CAP) algorithms were chosen and adapted for the monolithic component of the LMU Compton camera. The next sections are explaining the concept and the procedure for these algorithms, whereas in Sect. 6.4 the improvements and results obtained during the course of this PhD project are presented.

The first step needed for the application of this kind of algorithm towards the determi-

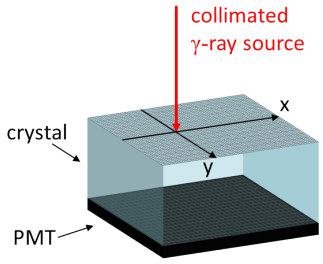

Figure 6.23: Scheme of the two-dimensional crystal scan with a perpendicularly irradiating collimated γ source, whose photons hit the detector's surface in known and defined (x,y) positions. All these irradiation positions serve to create a reference library utilized by the k-NN algorithm.

nation of the interaction position of a γ-ray in a monolithic crystal is the creation of a set of data which serves as "calibration" or response characterization data. This calibration is performed by acquiring a large set of data, the so-called *reference library*, originating from a collimated γ-ray source perpendicularly irradiating the surface of the detector, as depicted in Fig. 6.23. The detector's surface is scanned by moving the source to many regularly set and known positions.

The set of data contained in the reference library consists of measured 2D light amplitude distributions, formed by the signals from all single PMT anode segments for each event and each source position. The basic procedure of the algorithm is based on the comparison of an unknown 2D light amplitude distribution with the set of 2D light distributions contained in the reference library. The amount of data contained in the reference library is defined by the number of photopeak events acquired per position (n_{epp}) and the number of scanned positions (n_{pos}) in the (x,y) plane, chosen slightly larger than the detector surface area on a highly granular grid. Every reference light distribution from every photopeak event recorded is therefore associated with the (x,y) coordinates of the irradiation position. Thus the 2D reference light distributions contain spatial information on the position of incidence of the collimated photon beam source on the crystal's surface. Consequently the x and y coordinates of an unknown γ-ray interaction in the crystal can be determined by a comparison of this light distribution with the full set of reference light distributions.

For the studies applied to the monolithic absorber component of the LMU Compton camera, the standard version of the position reconstruction algorithm, the so-called *smoothed k-Nearest Neighbors* (k-NN) algorithm and its improved version called *Categorical Average Pattern* (CAP) algorithm were used. A workflow chart for both algorithms is shown in Fig. 6.24. For both cases, the required inputs are a 2D light amplitude distribution (from the reference library when applying the so-called *leave-one-out* method for a quantification of the spatial resolution or from an unknown event when aiming at determining its interaction position) and a reference library of 2D light amplitude distributions describing the response of the detector to impinging photons.

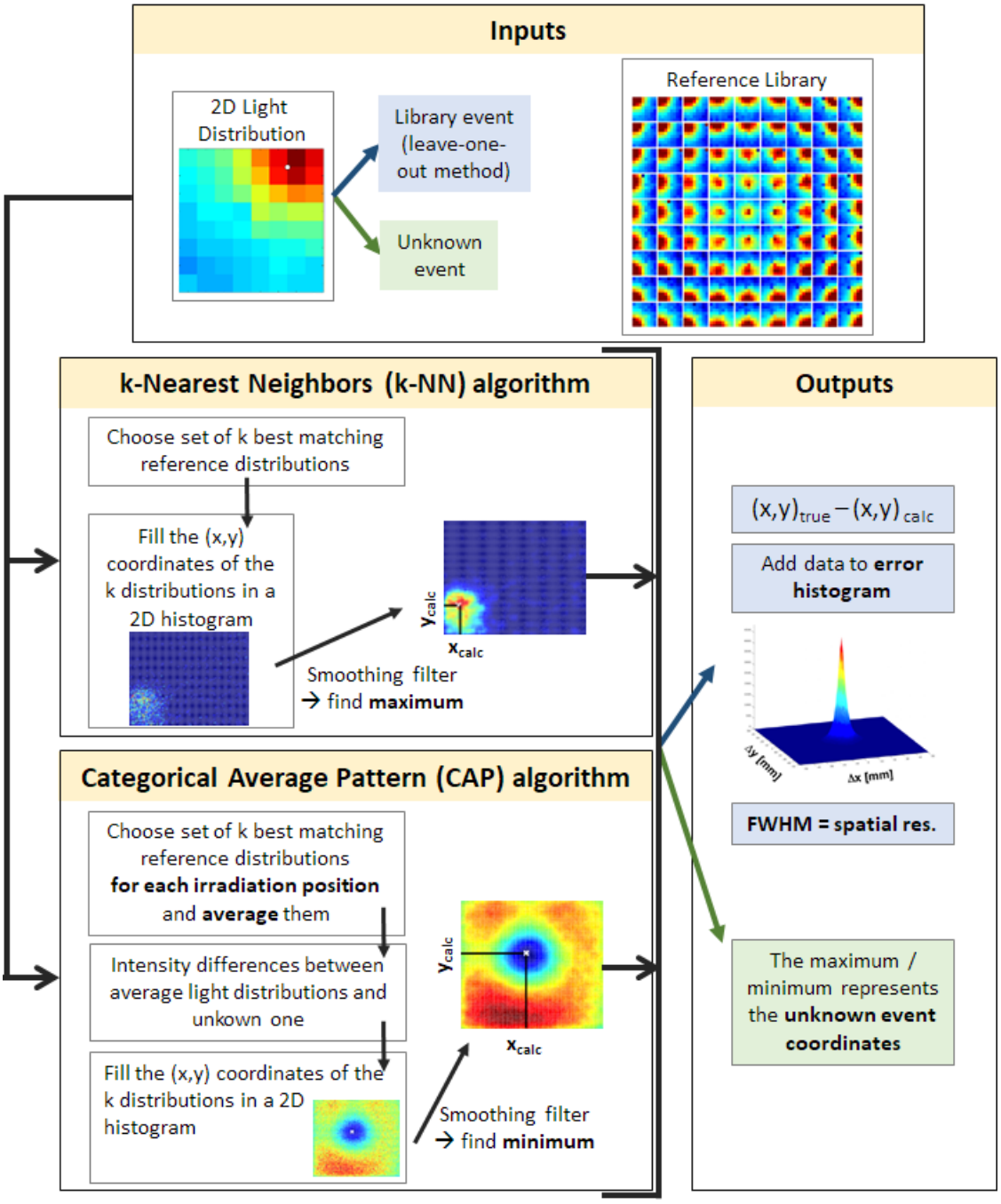

Figure 6.24: Workflow chart of the k-Nearest Neighbors (k-NN) and its improved version Categorical Average Pattern (CAP) algorithm for the determination of the interaction position of an unknown impinging γ-ray [262]. These algorithms can be used for the determination of the spatial resolution via the *leave-one-out method*, in which the unknown event is sequentially selected from the set of (known) events in the reference library, and for the determination of the interaction position from an unknown photon event in the scintillator crystal. See the text for a detailed description.

In the procedure applied for the **smoothed k-Nearest Neighbor (k-NN) algorithm** the unknown light distribution is compared to all entries of the reference library by calculating the intensity difference D_l, defined as:

$$D_l = \sqrt{\sum_{i=1}^{N}(I_{unk,i} - I_{ref(l,i)})^2}, \quad l = 1, \ldots, (n_{pos} \cdot n_{epp}) \tag{6.6}$$

where N is the total number of pixels of the segmented PMT, $I_{unk,i}$ is the intensity of the i-th pixel of the multi-anode PMT from the unknown 2D light distribution and $I_{ref(l,i)}$ is the intensity of the i-th pixel of the l-th reference 2D light distribution from the set of events in the library.

Among all reference light amplitude distributions the k closest matching 2D light distributions are chosen, according to the smallest D_l values. The parameter k is a selectable integer k≪l: its optimum value and the related study are presented in Sect. 6.4.1. The (x,y) coordinates of the k distributions are then filled in a 2D histogram. This histogram is then smoothed with a moving average filter (giving the name to the algorithm as *smoothed k-NN*), which for each pixel considers a surrounding matrix of 5 x 5 pixels and assigns to the central pixel the mean value of the surroundings. The (x,y) coordinates of the maximum intensity value of the smoothed histogram determines the (x,y) coordinates of the calculated primary interaction position inside the monolithic scintillation crystal (as it is indicated in Fig. 6.24).

The second method used for the determination of the interaction position, demonstrating even better performance (see Sect. 6.4.1), is the smoothed **Categorical Average Pattern (CAP) algorithm**. It was identified among different modifications of the standard k-NN which were tested by H. van Dam [262], who evaluated the spatial resolution achievable by different modifications of k-NN as a function of the number of photopeak events per irradiation position. Both k-NN and CAP algorithms require the same input data and return the same kind of output data (see the schematic in Fig. 6.24). The main difference between them is that in the CAP algorithm the k closest matching reference light distributions are searched within the n_{epp} reference light distributions collected independently for each irradiation position. From this subset of k references an averaged 2D light distribution is created. The difference D_l is therefore calculated between the unknown light distribution and the resulting average light distribution for each irradiation position according to:

$$D_l = \sqrt{\sum_{i=1}^{N}(I_{unk,i} - I_{ave(l,i)})^2}, \quad l = 1, \ldots, n_{pos} \tag{6.7}$$

where N is again (as in Eq. (6.6)) the total number of pixels of the photosensor, $I_{unk,i}$ is the light intensity of the i-th pixel of the unknown light distribution and $I_{ave(l,i)}$ is the intensity of the i-th pixel of the l-th average light distribution. Since an average light distribution is calculated from the k best matching distributions of a specific irradiation position, in the CAP case the total number of intensity differences D_l corresponds to the number of irradiation positions. Therefore a resulting 2D plot containing n_{pos} intensity

differences is obtained, each of them corresponding to an (x,y) pair of coordinates from the reference library irradiation positions. This plot is then smoothed with the same 5 x 5 moving average filter as used before in the context of the k-NN algorithm. In this case the (x,y) coordinates of the minimum value of the final histogram defines the (x,y) coordinates of the calculated primary interaction position inside the monolithic scintillation crystal (as shown in the bottom part of Fig. 6.24).

The leave-one-out method

As depicted in the workflow chart in Fig. 6.24, after having obtained the interaction positions calculated with either the k-NN or the CAP algorithm, the output can consist either of the spatial resolution value or the determination of previously unknown photon interaction positions in the absorber component of our Compton camera. The leave-one-out approach is the method used for determining the spatial resolution and consists, for both the k-NN and CAP algorithms, in applying the reconstruction algorithm to each one of the $n_{pos} \cdot n_{epp}$ library entries, considering them one by one as unknown events and keeping the rest of the events in the library as reference set. Once the position reconstruction has been performed and the position of the photon interaction has been calculated, projected onto the front surface of the scintillator, the differences between the x and y coordinates of the real (known from the (x,y) coordinates of the reference light distribution acting as unknown event) and calculated position is computed for each event of the reference library. These calculated ($n_{pos} \cdot n_{epp} \cdot 2$) coordinate differences (Δx, Δy) are then filled in the so-called *error histogram*.

The outcome of this procedure is a sharp peak in the 2D histogram centered at (0,0) and shown in Fig. 6.25. This specific 2D histogram was obtained with the CAP algorithm using the data from the reference library created with the collimated ^{137}Cs source for the $LaBr_3$(Ce) crystal coupled to the H8500C PMT. The peak center corresponds to those calculated interaction positions which were found to be exactly in the (x,y) position of the actual photon event considered. From this 2D histogram the full width at half maximum (FWHM) for both the x and y coordinates are determined. Their average value finally determines the spatial resolution for the specific monolithic detector under study and the specific choice of k. The whole process is executed for different values of k and the spatial resolution obtained from the algorithm applied for a specific monolithic detector is defined as the minimum value among all k-dependent averaged FWHM values. Sect. 6.4.1 presents the studies that were conducted in order to determine the optimum k values for both the k-NN and CAP algorithm.

6.3.2 The reference library

As introduced before, in order to enable applying the k-NN (or the CAP) algorithm a set of reference data characterizing the response of the scintillator to incident photon radiation, the so-called *reference library*, is needed. This library should contain a large number of events recorded at different, regularly spaced and spatially well known irradiation positions.

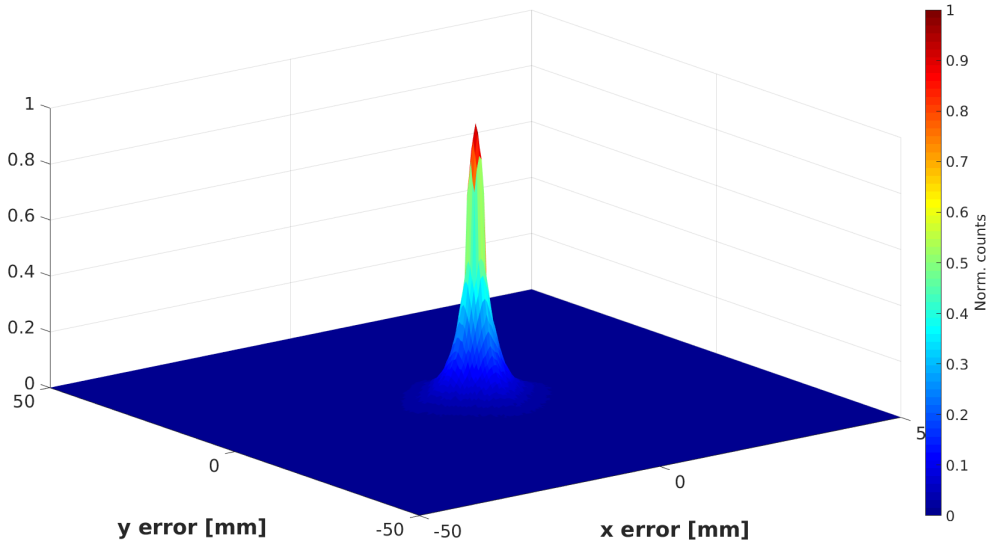

Figure 6.25: Error histogram generated from the CAP algorithm using the data from the reference library created with the collimated ^{137}Cs source for the $LaBr_3$(Ce) crystal coupled to the H8500C PMT .

It can be defined as a set of 2D light amplitude distributions $I_{(i,j)}$ such that:

$$L = \{I_{(i,j)} \quad | \quad i = 1, \ldots, n_{epp}; \quad j = 1, \ldots, n_{epp}; \quad dim[I_{(i,j)}] = 16 \times 16\} \tag{6.8}$$

for the H9500 PMT and

$$L = \{I_{(i,j)} \quad | \quad i = 1, \ldots, n_{epp}; \quad j = 1, \ldots, n_{epp}; \quad dim[I_{(i,j)}] = 8 \times 8\} \tag{6.9}$$

for the H8500C and H12700A-10 PMTs,

where n_{pos} is the number of irradiation positions on the detector surface, namely $n_{pos} = n_{pos,x} \cdot n_{pos,y}$. n_{epp} is the chosen number of photopeak events per irradiation position and $dim[I_{(i,j)}]$ is the size of the array which is recorded for each event in each irradiation position, corresponding to the PMT granularity and thus the number of pixels in each 2D light distribution. For this reason in Eq. (6.8), refering to the case of the H9500 256-fold segmented PMT, the size of $I_{(i,j)}$ is indicated to be 16×16, whereas in Eq. (6.9) it is 8×8, representing the segmentation of the H8500C and H12700A-10 PMTs.

The following part of this section is dedicated to the explanation of the preparatory analysis steps which are needed in order to acquire the data contained in the reference library. In particular, Sect. 6.3.2 and 6.3.2 are dedicated to the preparatory measurements and correction steps, followed by the description of the apparatus used for creating the data set contained in the reference library.

The correction steps

In order to obtain light amplitude distributions reliably reflecting the expected spatial correlation between the position of the collimated source and the registered maximum

of the intensity, a series of correction steps have to be applied to the raw data. This process takes into account variations between the signal properties of the PMT segments originating from the electronics readout chain, the photomultiplier and the scintillation crystal itself. The five correction steps described here are applied consecutively to the raw 2D light distributions:

1) Gain matching Each signal from all the (256 or 64 pixels) of the PMT is read out and processed independently by an individual spectroscopic readout chain. This leads to gain and offset variations within the different channels. To overcome this divergence, two pulser signals of different amplitudes (around 50 and 100 mV, which are within the energy range of interest for those signals) are injected into every LEMO PMT signal cable (using the detector emulator module DT5800 from CAEN [263]). From the acquisition of the electronic response to those pulser signals gain and offset parameters a_i and b_i are derived for each of the PMT pixels signals, using a random channel as a reference and a linear calibration curve applied to the new energy values according to:

$$E_{corrected} = a_i \cdot E_{raw} + b_i \tag{6.10}$$

2) QDC pedestal subtraction The QDC digitizer modules are composed of semiconductor components which can produce, also when the module has no input signal, a certain amount of dark current. This creates a low-amplitude signal, the so-called *pedestal peak*, which is present in the measured energy spectra in addition to the actual measured signal from the detector. However, the amplitude of this pedestal peak may differ when recorded in different channels: this requires an independent measurement in each of the electronics channels, in order to record its exact contribution. This is achieved by unplugging all input cables to the QDC modules and acquiring the data digitized in this configuration. Then the pedestal peak is fitted using a Gaussian distribution. Finally an energy threshold, which will be applied to the actual recorded detector signals, is set to a value corresponding to 3σ of the Gaussian distribution above the pedestal's centroid. An example of this process applied to the signal of an individual PMT segment channel is depicted in Fig. 6.26: (a) the pedestal peak is recorded and fitted with a Gaussian. Subsequently the energy threshold which serves to suppress the dark current contribution is set. In panel (b) this energy threshold is then subtracted from the energy spectrum of the raw data from the detector.

3) PMT non-uniformity Since segmented multi-anode PMTs are used to read out the light from the monolithic scintillation crystals, also the gain fluctuations between the PMT segments have to be taken into account. The relative correction factors that are applied refer to the values contained in a 2D non-uniformity matrix, which is provided by the manufacturer (Hamamatsu [264]). The non-uniformity maps of the PMT which were used during this thesis work are listed in App. B. This matrix is unique for each specific PMT. The values contained in the matrix for the H9500,

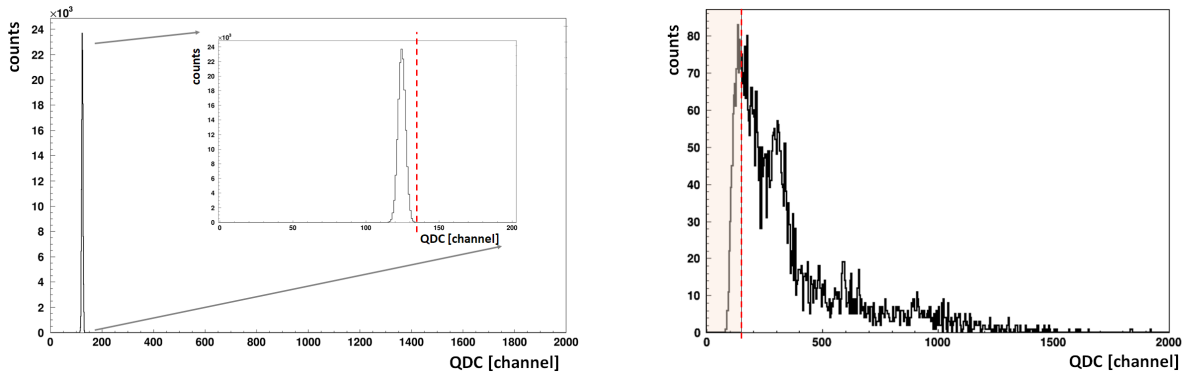

(a) (b)

Figure 6.26: Exemplary illustration of the QDC pedestal correction method for the individual PMT pixel data. The energy pedestal spectrum (a) was acquired while the signal input to the QDC module was not connected. Therefore just the dark current in the QDC module was integrated. The energy threshold (red dashed vertical line in (a)) needed to subtract the pedestal contribution from the raw energy spectrum (b) was calculated as 3σ of the Gaussian fit to the pedestal peak above the centroid of the Gaussian.

H8500C and H12700A-10 in use in this project can be found in Appendix B. Every 2D light distribution is corrected using the corresponding 2D matrix.

4) Spatial homogeneity All scintillation crystals under study during this PhD project have a reflective side surface wrapping (which is needed for an efficient light collection). Thus scattering and reflections before the final absorption of a photon in the crystal material are quite likely to happen. To take these phenomena into account, a usual way would be to illuminate the crystal with an isotropically emitting light source. However, the internal radioactivity (considerably present in the $LaBr_3$(Ce) crystal, but also noticeable in smaller amount in the $CeBr_3$ crystal) offers an alternative option to correct spatial inhomogeneity effects. The internal radioactivity can safely be assumed to be homogeneously distributed in the detector volume and to produce an isotropic emission. This step of the data correction therefore consists of shielding the detector from external background with lead blocks and measuring the internal radioactivity spectrum. The response of all different PMT segments is then used to correct the light distribution data for spatial inhomogeneities of the crystal response.

5) Energy gating This last correction step is not related to imperfections of the detector system, but it rather exploits the knowledge of the impinging radiation properties in our studies. Since the reference library is created for a specific energy, in order to maximize the amount of recorded "useful" signals from the collimated source, an energy gate is applied in the region of interest for the specific photon source energy (i.e. around the photopeak energy of the collimated source). From this process step,

a position-dependent correction matrix is derived and applied to all signals of the PMT segments.

In Fig. 6.27 the evolution of a prototypical light distribution is displayed, obtained step by step after applying the above introduced correction steps. The light distribution represents a specific irradiation position taken from the reference library which was acquired with the ^{137}Cs collimated source for the $LaBr_3$(Ce) crystal coupled to the (64-fold segmented) H8500C PMT. The white dot on each plot indicates the actual position of the collimated radioactive source with respect to the detector front surface. The consecutive improvement of the spatial correlation from one correction step to the next one is clearly visible.

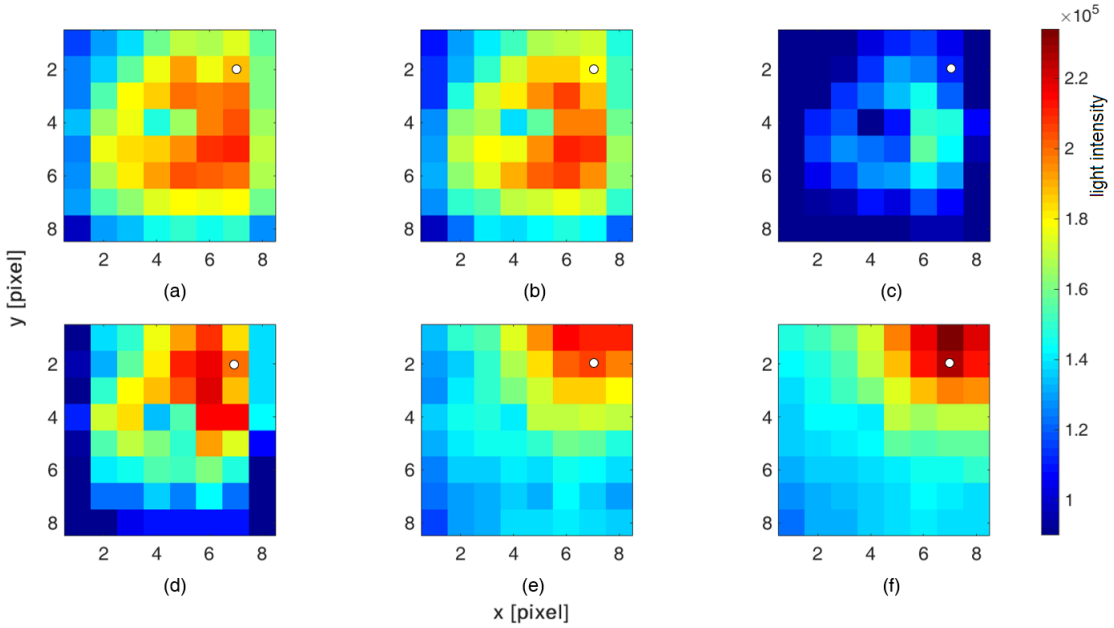

Figure 6.27: Correction steps applied to a reference light distribution from the ^{137}Cs library: (a) raw data, (b) gain matching, (c) QDC's pedestal subtraction, (d) PMT non-uniformity, (e) spatial homogeneity, (f) energy gating. The white dot on each plot indicates the actual position of the collimated radioactive source with respect to the detector front surface. See the text for details.

All correction factors described in the analysis steps discussed above -apart from the PMT non-uniformity matrix which was provided by Hamamatsu- were measured before the acquisition of any of the reference libraries. It is important to perform these correction steps just before the reference library acquisition, as the determined values have a strong dependence on the laboratory conditions, in particular on the temperature.

It should be noted that when the k-NN or CAP algorithm is used for the reconstruction of unknown interaction positions in the absorber component of a Compton camera setup, the last correction step, i.e. the gating on the photopeak energy, is not applied. This

Source activities	^{137}Cs	^{60}Co
$LaBr_3$(Ce) + H9500	82 MBq	20 MBq
$LaBr_3$(Ce) + H8500C	77.7 MBq	15.2 MBq

Table 6.6: Activities of the radioactive collimated sources (^{137}Cs and ^{60}Co) used for the acquisition of the reference libraries. The numbers are displayed for the reference libraries acquired for both $LaBr_3$(Ce) scintillation crystals characterized and coupled, respectively, to the H9500 and to the H8500C PMTs.

reflects the fact that in such a case the incident energy is unknown. Moreover, coincident data between a scatter and an absorber component intrinsically cannot contain relevant signal intensity in the photopeak region since the initial photon energy of the source is deposited in both detector components.

The experimental setup

Once the correction steps are applied, the measurement of the reference library can be carried out with the apparatus that will be described in the following section. The reference libraries were acquired using both a ^{137}Cs and a ^{60}Co collimated γ-ray source. The ^{137}Cs source emits a 662 keV γ ray, whereas the ^{60}Co source emits simultaneously a 1173 keV and a 1332 keV photon. Since the reference libraries for the $LaBr_3$(Ce) crystal coupled to the H9500 PMT and for the $LaBr_3$(Ce) crystal coupled to the H8500C PMT were acquired in different time periods during the course of this PhD project, the activities of the sources at the moment of the library acquisitions were slightly different and they are summarized in Tab. 6.6. This difference is more relevant for the ^{60}Co source with a half-life ($T_{1/2}$) of 5.27 years.

In Fig. 6.28 an illustration of the design of the radioactive source container and its related holder is shown. The latter was connected to the collimation system displayed in Fig. 6.29 for the first results presented in this thesis, and to the upgraded collimation system shown in Fig. 6.30 for almost all results discussed later. Figure 6.28 shows that the source (either ^{137}Cs or ^{60}Co) is encapsulated in an aluminum housing and then installed in a tantalum holder. The aluminum housing, with a total length of 29.5 mm, was designed such that the radioactive disc (in red) can be fixed in the center of the source holder, pointing at the collimation channel with a diameter of 2 mm. The radioactive material is placed in a distance of 20 mm from opening of the holder; this additional length was considered when calculating the total collimation length of the system.

In Fig. 6.29 a photograph of the "old" collimation system is shown, used only for the first library which was acquired during the course of this PhD work. This arrangement was used for the creation of the reference library with the collimated ^{137}Cs source for a detector configuration composed of the $LaBr_3$(Ce) scintillator and the H9500 PMT. The collimator in Fig. 6.29(a) is composed by 12 DENSIMET® slabs, which are assembled with an accuracy of 10-20 μm using precision positioning rods and which create a total collimation length of 48 mm with a collimation channel diameter of 1 mm. This solution

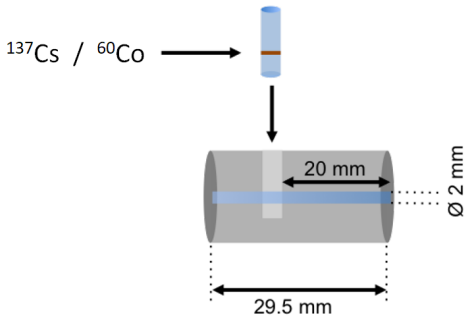

Figure 6.28: Illustration of the design of the source container and its holder for the radioactive source used for the scanning measurements. The source (red disc) is encapsulated in an aluminum housing (light blue) and then installed in a tantalum holder (grey). The aluminum housing was designed such that the radioactive disc can be fixed in the center of the source holder, pointing at the collimation channel with a diameter of 2 mm [139].

was chosen since no mechanical machining technology is available to generate a 1 mm hole precisely on axis over a length of 48 mm. DENSIMET® is a tungsten alloy (alloy of W(97%), Ni and Fe, $\rho = 18.5\ g/cm^3$) and it was produced by PLANSEE [265]. In this initial version of the scanning device the 48 mm long collimator plus the source, attached behind these 12 slabs, are mounted together on the arm of a motorized translation stage, whereas the scintillation detector is stationary (as in the arrangement in Fig. 6.29(b)). An additional shielding provided by lead blocks is surrounding the DENSIMET® collimation slabs, in order to enhance the contrast of the collimation by preventing sideways leakage of radiation.

Since the photon energies from the radioactive ^{60}Co source are about twice than the one of the ^{137}Cs source, the arrangement of the collimation system had to be adapted in order to allow for a considerably thicker collimator. In [139] the detailed calculations which led to the upgraded design of the collimation system can be found. Figure 6.30 shows the current shielding block which is used for collimating the radioactive source. In Fig. 6.30(a) a photograph (seen from the back side where the source is mounted and from the front side, respectively) of the $100 \times 100 \times 100 mm^3$ cubic block made of DENSIMET® is shown, which was produced by WHS Sondermetalle [266]. It was manufactured with a cylindrical central bore (with a diameter of 4.05 mm) in order to allow for inserting an exchangeable sintered WC tube (90% WC, 10% Co, $\rho = 14.4\ g/cm^3$). Several of those tubes, acting as the collimation channel, were produced by Hartmetall® Gesellschaft [267] with an outer diameter of 4 mm and an inner diameter of 1 mm and 0.6 mm, respectively. In Fig. 6.30(b) these collimator tubes are shown in detail, while one of them was partially retracted from the DENSIMET block to make it visible in the front side photograph of the collimator block in Fig. 6.30(a).

Due to the high density of the DENSIMET® material ($18.5\ g/cm^3$) and to the amount of additional shielding material, the source could not continue to be the movable part of the scanning system since the new collimation block would not have been able to be

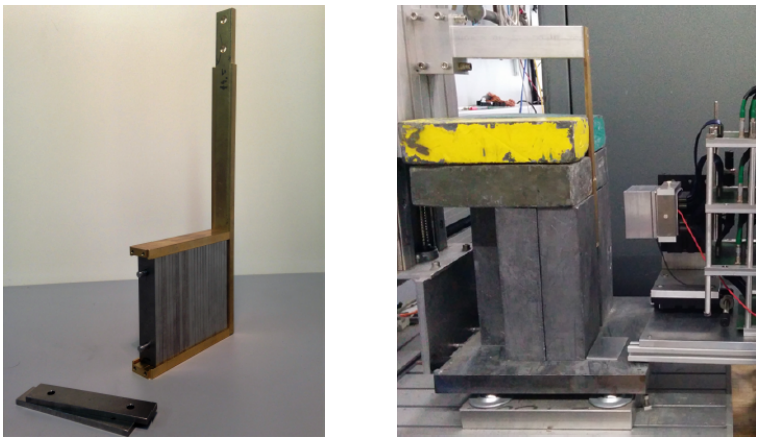

(a) (b)

Figure 6.29: Photographs of the 48 mm long collimator, which was used for the acquisition of the ^{137}Cs reference library for the $LaBr_3$(Ce) crystal coupled to the H9500 PMT. Panel (a) shows the stack of 12 DENSIMET® slabs, which were assembled together (using precise positioning rods) to create the 48 mm long collimator with an opening diameter of 1 mm. (b) Arrangement for the 2D scan of the ^{137}Cs reference library: the 48 mm long collimator plus the source are movable by hanging from a mounting arm attached to a motorized (x,y) translation stage, whereas the scintillation detector is stationary. The DENSIMET® collimator slabs are surrounded by lead blocks in order to enhance the collimation of the radiation by preventing sideways leakage of radiation.

placed on the motorized translational stage. Instead the modified arrangement for the collimation and detector scanning system is shown in Fig. 6.31. Now the collimator block, the radioactive source and the lead shielding are stationary, while the detector is hanging from an aluminum arm which is attached to the motorized (x,y) translation stage that enables precise movements in x and y direction, in close distance of $\leq$ 1 cm from the front opening of the collimator channel and oriented parallel to the collimator's front surface.

Besides the positioning of the collimated source, Fig. 6.31 shows in detail the translation stage which controls the 2D scanning along the (x,y) plane of the scintillation detector.

The horizontal part of the aluminum arm (①) is fixed with four screws to a lead-screw driven base plate attached to the vertical actuator part of a translational stage (②), which allows for the vertical shift of the arm (y direction). The lead-screw is mounted on a vertical slab, which is connected via several metallic components to the horizontal support of the PMT readout adapter boards (③). The vertical arm (which carries the detector), together with the adapter board support structure, is free to move in x direction due to a motorized horizontal rail system, supported by metal ball bearings that reduce friction during the movement (④ and ⑤). The length of the flat ribbon cables (⑥), which connect the PMT to the adapter boards, is approximately 36 cm for all monolithic detectors which were characterized and has been chosen in order to allow for unhindered movement of the detector in the needed y range. The motion of the translational stage is automatically

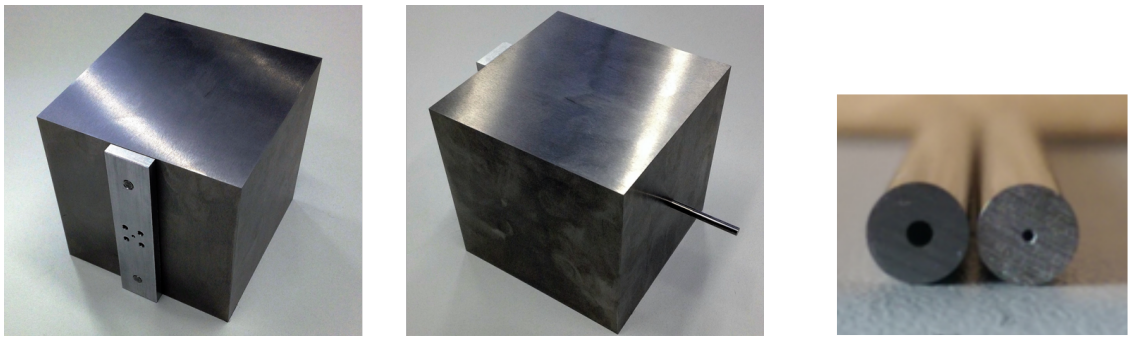

(a) (b)

Figure 6.30: (a) Photographs of the $100 \times 100 \times 100$ mm^3 shielding and collimation block made of DENSIMET® [266], with a tantalum slab attached to one side where the source holder is fixed. The block features a 4 mm diameter central bore, in which a collimation rod (b) [267] can be inserted. The two collimation rods in the photograph have a diameter of 1 mm and 0.6 mm, respectively; both of them were tested but only results obtained with the 1 mm collimator will be shown as it demonstrated better performance due to the worse signal-to-noise ratio of the 0.6 mm collimator.

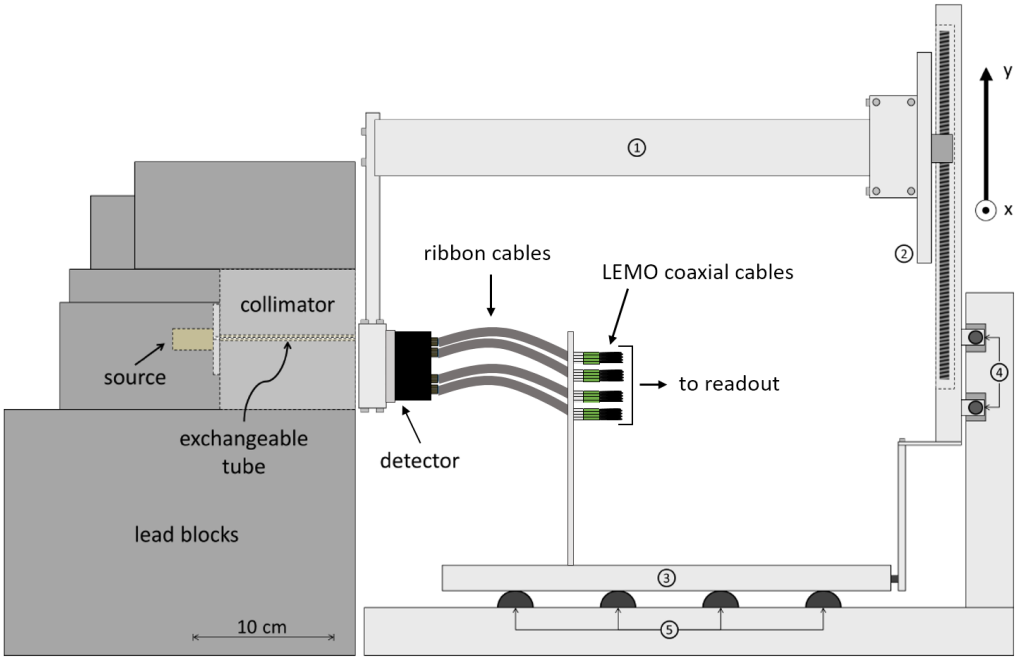

Figure 6.31: Sketch of the upgraded scanning system used for the creation of most of the 2D light amplitude reference libraries for the monolithic scintillation detector. This remote controlled motorized system allows the detector to be moved in x and y directions for scanning its front surface in front of the stationary and well-shielded collimated radioactive source.

controlled by the ROOT-based software package MARaBOU [244], which was described in Sect. 5.3.1. The motion of the detector along the x and y direction is allowing for the measurement of 2D light amplitudes in several well-defined positions in order to create the reference libraries, which are presented in this section.

The crystal edge scans

Before starting the actual measurement for the acquisition of the 2D light amplitude reference library, the (x,y) starting coordinates of the scan need to be defined. To do that, the (x,y) coordinates of the edges of the scintillation crystal, which is encapsulated in an aluminum housing, have to be determined. In order to obtain these values, the scanning system described above is used to scan the detector surface in both x and y directions with the collimated γ-ray source. The detector is positioned in front of the collimator, setting one of the two coordinates to the central plane with respect to the front surface of the detector, while the other coordinate varies from one edge of the detector to the other. For both directions, the irradiation positions are scanned with a step size of 1 mm. A gate around the photopeak energy of the source is set in the energy spectrum of the detector. The resulting intensity profiles along the two axes are utilized to localize the edges of the crystal, indicated by the increasing (rising edge) and descreasing (falling edge) number of counts registered in the photopeak region as a function of the irradiation position.

The intensity profile of the rising slope is fitted by a Fermi function according to

$$f_{Ff}(x) = \frac{A}{1 + e^{\frac{x-x_0}{B}}} + C \tag{6.11}$$

where A, B and C are fit parameters, x_0 is the origin of the x axis and x is the irradiation position under investigation.

Accordingly, the falling edge of the intensity profile is fitted by an inverse Fermi function:

$$f_{iFf}(x) = \frac{A}{1 + e^{\frac{x_0-x}{B}}} + C \tag{6.12}$$

where the parameters are the same as the ones described before in Eq. (6.11). These two fit functions are used for the rising and falling edge profiles of both x and y scans; in the latter the variable x is replaced with the respective y values. The range of the x and y scans was chosen larger than the known (from the manufacturer) actual crystal size in order to be able to resolve the step function (falling and rising edge), where the collimated photon beam enters and leaves the crystal. The two inflection points resulting from the fit functions represent the starting and ending coordinates of the crystal. The distance between these coordinates represents the measured width of the crystal (which ideally reflects the crystal dimensions known from the manufacturer).

The results from the edge scans presented here were measured using the two available collimated γ-ray sources ^{137}Cs and ^{60}Co for a collimator opening of 1 mm. They were acquired using the second monolithic $LaBr_3$(Ce) scintillator which was characterized during this PhD thesis (coupled to the H8500C PMT). The acquisition time set per irradiation

Source	Time per position [s]	
	x-scan	y-scan
^{137}Cs	760	760
^{60}Co	1080	1080

Table 6.7: Acquisition time chosen for each irradiation position during the x- and y-scans performed with collimated ^{137}Cs and ^{60}Co sources. These times were set for the edge scans performed for the $LaBr_3$(Ce) crystal coupled to the H8500C PMT.

position for each scan is listed in Tab. 6.7; for both x and y scans, a set of 65 irradiation positions was performed. The shorter time per position which was chosen for the edge scan using the ^{137}Cs source is due to the higher activity of this source (see Tab. 6.6: 77.7 MBq compared to 15.2 MBq for the ^{60}Co source).

In Fig. 6.32 the resulting intensity profiles from the edge scans in x (a) and y (b) direction performed using the ^{137}Cs source are shown. The distance between the two inflection points is equal to 49 mm and 49.4 mm, respectively. For each irradiation position data were acquired for 760 s in both x and y directions, respectively.

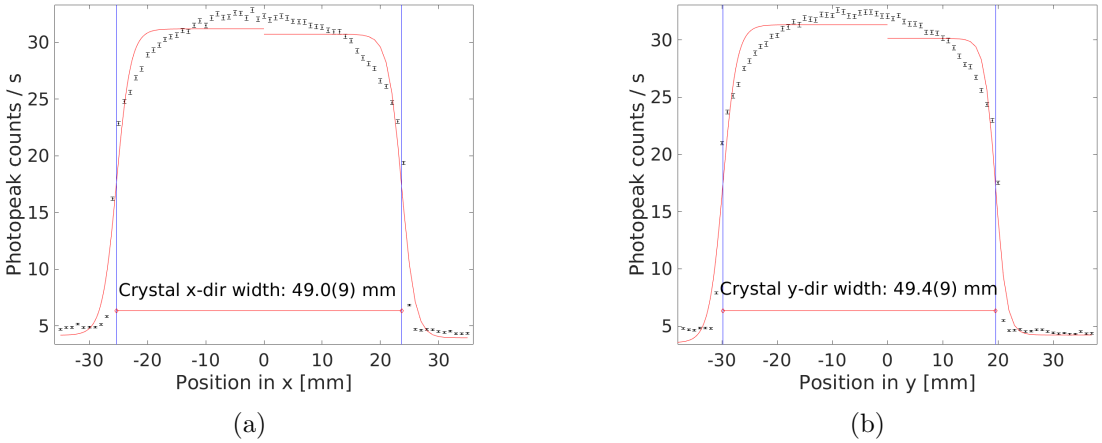

Figure 6.32: Crystal edge scan for the $LaBr_3$(Ce) scintillator coupled to the H8500C PMT, performed with a ^{137}Cs source and a 1 mm collimator in x direction (a) and y direction (b). The plots represent the intensity profile of the photopeak count rates as a function of the irradiation position. The red curves and blue vertical lines represent the fit to the profile curve using Fermi functions (see text for details).

For the edge scans carried out with the ^{60}Co source, two different energy gates have been applied to the raw data, reflecting the two photopeak energies contained in the energy spectrum, which will also correspond to the specific energies of the reference libraries created with this radioactive source. This gives the possibility to study the performance of the collimation system as a function of the photon energy under the same experimental conditions. Figure 6.33 and 6.34 present the results obtained from the edge scans performed

using the ^{60}Co source, gating on the 1173 keV photopeak and the 1332 keV photopeak, respectively. For both cases, the crystal profile was evaluated in x (a) and y (b) directions and the crystal width was calculated to be between 48.1 mm and 49.3 mm. For each irradiation position data were acquired for 1080 s in both x and y directions, respectively.

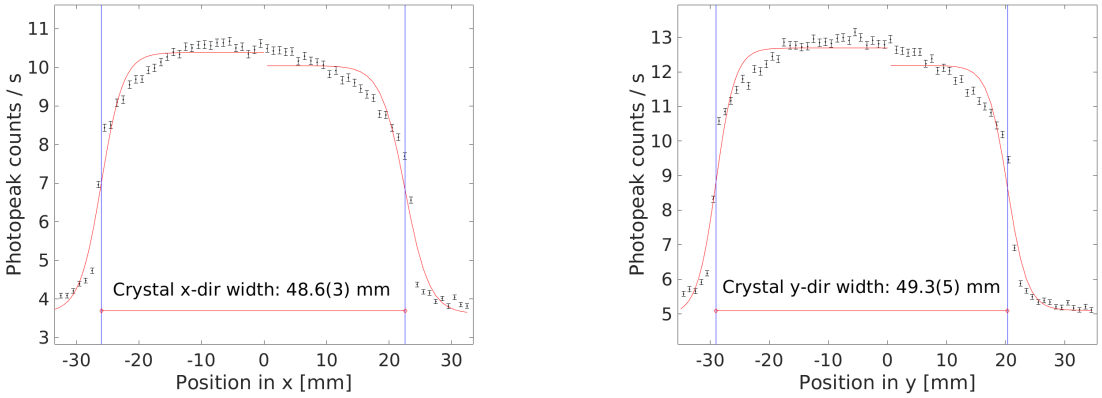

(a) (b)

Figure 6.33: Crystal edge scan for the $LaBr_3$(Ce) scintillator coupled to the H8500C PMT, performed with a ^{60}Co source and a 1 mm collimator in x direction (a) and y direction (b). The plots represent the intensity profile of the photopeak count rates for the 1173 keV photopeak of ^{60}Co, as a function of the irradiation position. The red curves and blue vertical lines represent the fit to the profile curve using Fermi functions (see text for details).

The main differences that can be noted by looking at the plots in Fig. 6.32, 6.33 and 6.34 are the absolute intensities of the detected radiation and the calculated crystal widths. The S/N ratios in the plots reflect the specific source activities, being highest for the scan performed with the ^{137}Cs source. Since the two measurements with the ^{60}Co source at 1173 keV and 1332 keV have been performed simultaneously, the difference between their S/N values is only due to the lower statistics registered in the second peak. Another detail which can be observed when comparing the two intensity profiles obtained by gating on the two ^{60}Co photopeak energies is the different background level, which is slightly higher when gating on the 1173 keV photopeak. This is mainly due to the fact that this first peak sits on top of the Compton continuum of the 1332 keV photopeak.

The values for the crystal width obtained from these measurements should also be shortly discussed: the nominal width of this crystal as provided by the manufacturer (Saint-Gobain [180]) is 50.8 mm, but the fitted widths range from 48.1 mm to 49.8 mm. Reasons for this difference can be attributed to the fit quality, the rounded shape of the count-rate profile and the slightly smaller dimensions of the coupled PMT (49 × 49 mm^2), which is reading out the scintillation light. The outcome of the fit depends on the S/N value, on the choice of the parameter settings of the fitting function and on the profile shape. The time per irradiation position was chosen accordingly in order to obtain a S/N

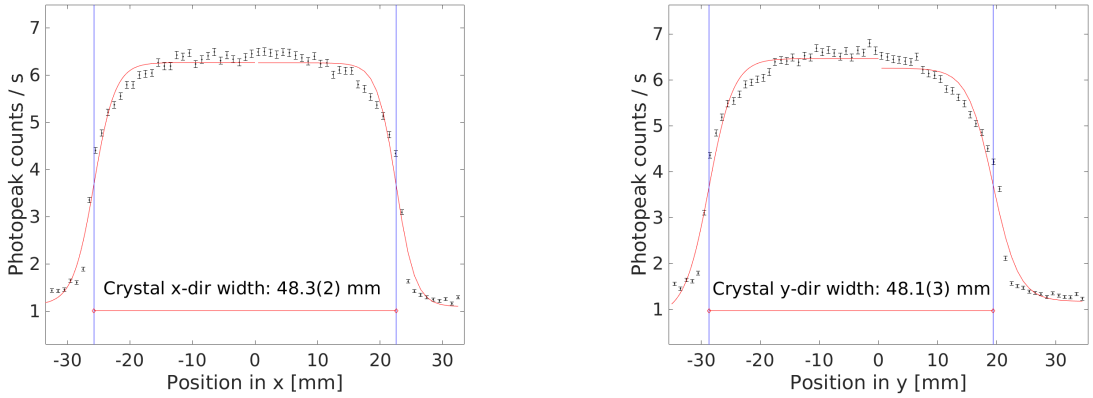

(a) (b)

Figure 6.34: Crystal edge scan for the $LaBr_3(Ce)$ scintillator coupled to the H8500C PMT, performed with a ^{60}Co source and a 1 mm collimator in x direction (a) and y direction (b). The plots represent the intensity profile of the photopeak count rates for the 1332 keV photopeak of ^{60}Co, as a function of the irradiation position. The red curves and blue vertical lines represent the fit to the profile curve using Fermi functions (see text for details).

ratio that allows for resolving the crystal profile. The three Fermi function parameters A, B and C were set in order to provide the best fit of the edges and the background. The symmetrical shape of the Fermi functions and the asymmetrical shape of the edge slopes with respect to their inflection points can also contribute to the reduction of the calculated crystal width compared to its nominal value. The main cause of the slopes' asymmetry is the rounded shape of the scan profile, which is strongly correlated to edge effects in the light detection. But since the main goal of these measurements and fits was the determination of the crystal edge positions in order to precisely start and perform the 2D scan of the reference libraries, the mentioned effects, acting in symmetric way on both detector sides, are not significantly affecting the outcome of the procedure.

2D light amplitude reference libraries

Since in a previous study [268] it was observed that using the 0.6 mm diameter of the collimator channel is prohibited by the resulting drastic reduction of the S/N ratio, all reference libraries which were acquired and are presented in the work of this thesis made use of the 1 mm collimation opening. The step size was always set to 0.5 mm and the detector surface was scanned over an area of $51 \times 51 mm^2$. In this section the 2D light amplitude distribution of the photoevents will be shown for reference libraries acquired with ^{137}Cs and ^{60}Co sources and for a $LaBr_3(Ce)$ scintillation crystal coupled to either the H9500 or the H8500C multi-anode PMT.

Figure 6.35 shows a (16×16) subset of the reference libraries which were acquired for

the $LaBr_3$(Ce) crystal coupled to the H9500 PMT [269], (a) with a ^{137}Cs and (b) with a ^{60}Co collimated source.

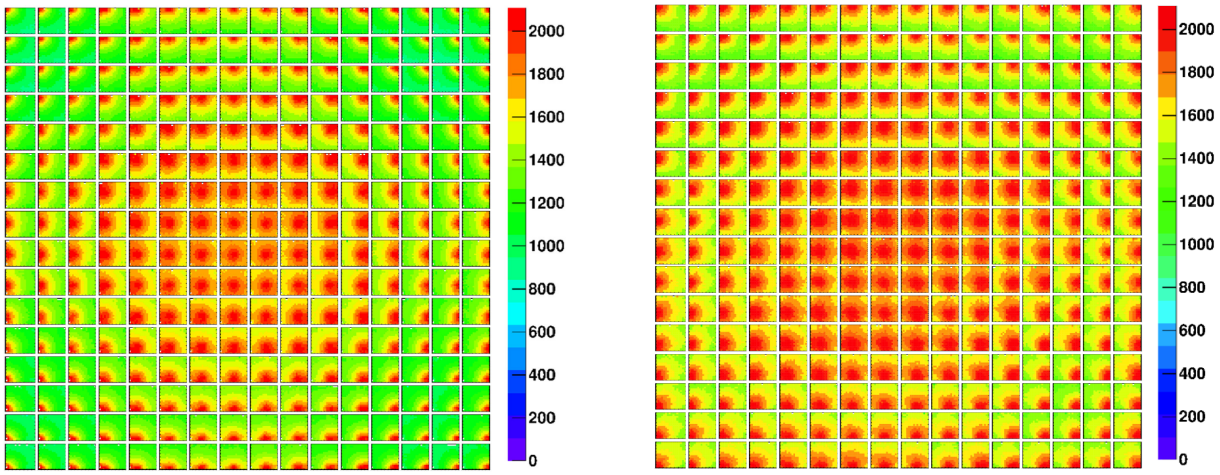

(a) (b)

Figure 6.35: 2D light amplitude reference libraries, obtained with ^{137}Cs and ^{60}Co collimated photon sources and measured with a $LaBr_3$(Ce) crystal coupled to a (256-fold segmented) H9500 PMT. Subsets of 16 x 16 irradiation positions (3 mm step size in x and y) are shown, using (a) the ^{137}Cs and (b) the ^{60}Co source (with a gate on the 1332 keV photopeak). They were measured with a 1 mm collimator opening.

The 16 × 16 subset which is shown in Fig. 6.35 has been extracted by selecting only those source irradiation positions which were located in front of one of the 16 × 16 PMT pixels. The 2D light amplitude distributions displayed in Fig. 6.35(a) were gated around the 662 keV, the photopeak energy of ^{137}Cs, while the data shown in Fig. 6.35(b) were gated on the second photopeak energy of the ^{60}Co source at 1332 keV.

It should be noted that amongst the photopeak events recorded in the reference library, a number of events were recorded with a zero amplitude in one or more PMT segment signals, some of them already lacking any valid amplitude even before the pedestal correction (which was presented in Sect. 6.3.2). The reason for the appearance of these unexpected zeros could not be traced back to any clear origin (in [268] the results from this study can be found), however, the percentage of these events is small compared to the amount of data contained in a reference library. In Tab. 6.8 the percentage of zeros recorded in the reference libraries presented in Fig. 6.35 is listed.

Source	# blank pixels	Blank pixels / all entries [%]
^{137}Cs	$\sim 6 \times 10^6$	0.6
^{60}Co	$\sim 1.5 \times 10^6$	0.15

Table 6.8: Total number and fraction of "blank pixels" contained in the reference libraries obtained with ^{137}Cs and ^{60}Co collimated sources and acquired for a $LaBr_3$(Ce) crystal coupled to a H9500 PMT.

Figure 6.36 shows the 2D light amplitude distribution in a subset of 8 irradiation positions, for the reference libraries acquired for the $LaBr_3$ crystal coupled to the H8500C PMT. Also for this case the subset of irradiation positions shown in the plots were selected for those positions where the source was positioned directly in front of the center of the 8 × 8 PMT pixels.

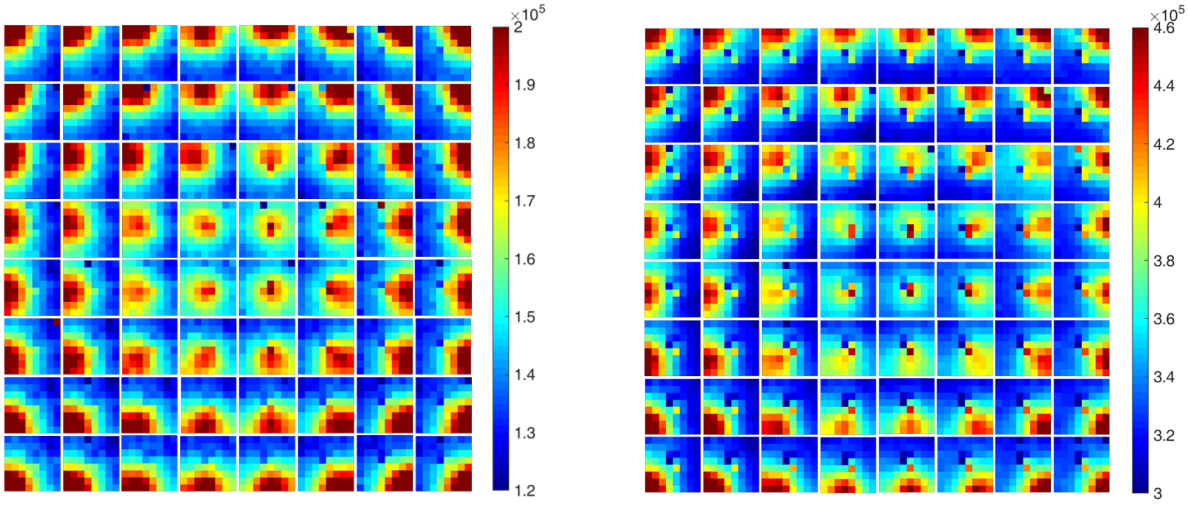

(a) (b)

Figure 6.36: 2D light amplitude reference libraries measured using ^{137}Cs and ^{60}Co collimated sources and a $LaBr_3$(Ce) crystal coupled to the (64-fold segmented) H8500C PMT. Subsets of 8 x 8 irradiation positions (6 mm step size in x and y) are shown, using (a) the ^{137}Cs and (b) the ^{60}Co source (with a gate on the 1332 keV photopeak). They were measured with a 1 mm collimator opening.

As for Fig. 6.35, in Fig. 6.36(a) the 2D light amplitude corresponds to the acquisition of a reference library using the collimated ^{137}Cs source with an energy gate applied around its photopeak energy (662 keV), whereas Fig. 6.36(b) was obtained from the ^{60}Co-based reference library where an energy gate was applied around its photopeak at 1332 keV.

The number of events found to contain pixels with an amplitude equal to zero (which are called "blank pixels" and which will be discussed in Sect. 6.4.2 together with a correction scheme), for the reference libraries acquired for the $LaBr_3$(Ce) crystal coupled to the H8500C PMT, are listed in Tab. 6.9.

Source	# blank pixels	Blank pixels / all entries [%]
^{137}Cs	$\sim 8 \times 10^5$	0.210
^{60}Co	$\sim 2 \times 10^4$	0.005

Table 6.9: Total number and fraction of "blank pixels" contained in the reference libraries measured with ^{137}Cs and ^{60}Co collimated sources and acquired for a $LaBr_3$(Ce) crystal coupled to the H8500C PMT.

When acquiring a reference library, the DAQ system is synchronized with the step motor controller, which sends commands to the moving stage. For each irradiation position an ASCII file is generated: it contains the amplitude values recorded for all PMT pixels in all events acquired in that specific irradiation position. These files are then converted to a specific format (either MATLAB, or to a binary file for the improved analysis procedure which will be discussed in Sect. 6.4.5), in order to be packed in structured arrays which then serve as input to the position reconstruction algorithm (whose core script is written in C++).

A detail worthwhile to be mentioned is the coordinate system. It is essential to take note of the orientation of the coordinate system during the library acquisition. When running the k-NN algorithm for the reconstruction of the interaction positions of unknown photon events, the (x,y) coordinates of those events will be obviously reconstructed based on the coordinate system of the reference library, and should then be converted into (x,y) coordinates based on the coordinate system of the specific measurement from where the unknown events originated. The coordinate system of the reference libraries depends on the orientation between the monolithic crystal and the radioactive source as well as their relative movements when scanning the detector surface. Figure 6.37 shows a sketch of the coordinate system orientation for all reference libraries which were created and analyzed. Figure 6.37(a) refers to the ^{137}Cs library measured for the $LaBr_3$(Ce) crystal coupled to the H9500 PMT, which is differently oriented compared to the coordinate system in Fig. 6.37(b), which corresponds to the ^{60}Co library of the same detector and both ^{137}Cs and ^{60}Co libraries for the $LaBr_3$(Ce) coupled to the H8500C PMT. This difference is due to the fact that for the first case mentioned, the collimated source was moving while hanging from the arm of the translation stage, whereas for the other library cases the situation was opposite and the detector was moving while the source was fixed.

6.4 Spatial resolution of a monolithic $LaBr_3$(Ce) scintillator

This section is dedicated to the determination of the spatial resolution obtained for the monolithic absorber detectors under study. The underlying procedure was described in Sect. 6.3, in particular Sect. 6.3.1 was dedicated to the explanation of the "leave-one-out method".

For the $LaBr_3$(Ce) scintillation crystal coupled to the H9500 PMT, which was tested

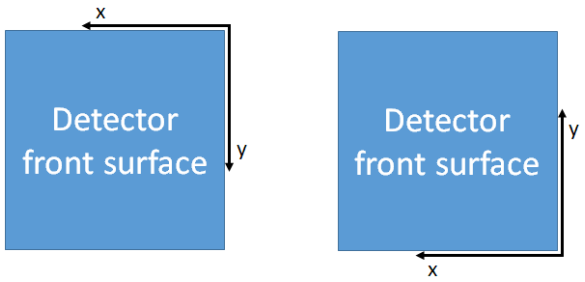

(a) (b)

Figure 6.37: Coordinate system of the reference library data from the detector front surface view, derived from the 2D scanning procedure. (a) Coordinate system of the library created with the collimated ^{137}Cs source for the $LaBr_3$(Ce) crystal coupled to the H9500 PMT, which was performed still with the old collimation system, where the source was hanging from an arm of the translation stage. (b) Coordinate system of the library created for the same detector with the collimated ^{60}Co source and for the libraries with both radioactive sources for the $LaBr_3$(Ce) crystal coupled to the H8500C PMT, which were performed with the new collimation system, where the source position was fixed and the detector was moving.

first, improved results (compared to previous results discussed in [139]) will be presented here. With the data acquired for these libraries, alternative results were also evaluated by artificially creating a 64-ch. segmentation from the actual 256-fold segmented PMT via software manipulation by summing up each four and averaging neighbouring PMT pixels. This second step is rather important in view of the desired reduction of the number of electronics channels and therefore of the complexity of the system. After having coupled a second $LaBr_3$(Ce) monolithic crystal to the 64-fold segmented PMT (H8500C, Hamamatsu [207]), its characterization was performed. In Sect. 6.2 energy and time resolution was presented, in the current section the spatial resolution will be addressed. Its obtained spatial resolution was compared to the results obtained with the $LaBr_3$(Ce) operated with a 256-fold segmented PMT, indicating a similar or even slightly improved performance for a 64-fold segmented PMT. These results are important as a basis for future upgrades of the Compton camera prototype: the plan is to include more than one absorber detector while reducing the complexity of the system by coupling each of these scintillation crystals to a 64-fold segmented PMT (or maybe a SiPM array with the same pixelation in the future).

6.4.1 Parameter optimization

The key parameters to be defined in the described procedure for obtaining the spatial resolution of a monolithic scintillator, are n_{epp} (number of acquired photopeak events per irradiation position) and k (number of nearest best matching neighbors, which is different for the standard k-NN or the CAP algorithms). Studies utilizing a scan grid step size of either 0.5 mm or 1 mm were also conducted, rendering, as expected, best results for the

finest grid step size.

Systematic studies on the spatial resolution as a function of n_{epp} and k were performed using the data acquired with the $LaBr_3(Ce)$ crystal coupled to the H9500 PMT, forming the basis for following evaluations in different configurations. Details on these studies can be found in the Master thesis of A. Miani [269], supervised by the author of this work. Since the data shown in this work all refer to the same detector configuration, the 64-fold segmentation was obtained by offline software manipulation, summing up and averaging each four adjacent channels, thus reducing the original 256-fold segmentation artificially to a 64 segmentation. This procedure is schematically shown in Fig. 6.38.

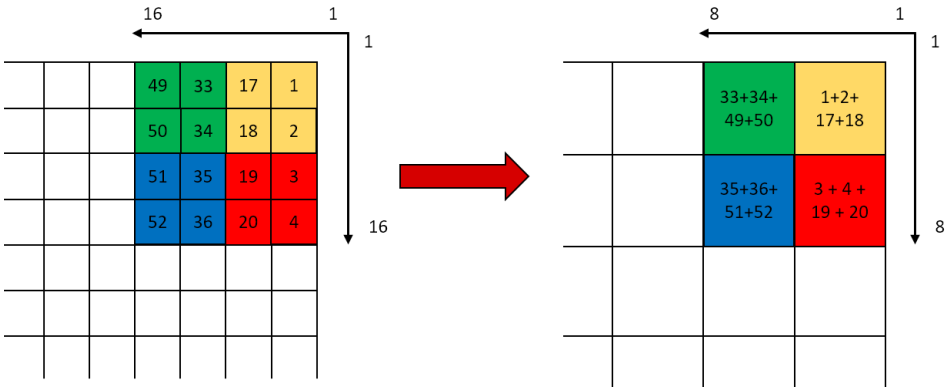

Figure 6.38: Sketch of the procedure applied in order to create 64-fold segmented 2D light amplitude distribution from the originally acquired 256-fold segmented PMT data.

The spatial resolution was determined using the "leave-one-out method" for different k values and n_{epp} event numbers per irradiation position. The number of k nearest neighbors could be varied within a certain range, for the k-NN and CAP algorithms, respectively. For the smoothed k-NN algorithm the parameter k in this study ranges from 3 to 4000, since the k closest matching reference light distributions are chosen from the complete reference set (which corresponds to $n_{pos} \times n_{epp}$ entries, i.e. around $\sim 10^6$ light distributions), :

$$k_{k-NN} = \{3, 5, 10, 20, 30, 40, 50, 70, 100, 200, 300, 400, 500, 700, 1000, 1200, 1500, 2000, 3000, 4000\} \tag{6.13}$$

where

$$k_{max}(k - NN) \ll n_{pos} \times n_{epp} \tag{6.14}$$

In contrast, the CAP algorithm looks for the k best values among the available events per irradiation position (n_{epp}), therefore considering a k parameter which is chosen in the following range

$$k_{CAP} = \{5, 10, 12, 14, 15, 25, 30, 40, 50\} \tag{6.15}$$

where

$$k_{max}(CAP) \ll n_{epp} \tag{6.16}$$

The parameter n_{epp} was investigated by creating individual reference libraries with lower numbers of n_{epp} than the one actually recorded during the measurement. Different values of n_{epp} were selected from the total number of collected events:

$$n_{epp} = 75, 100, 150, 200, 300, 400 \tag{6.17}$$

It should be noted that for the spatial resolution study of the $LaBr_3(Ce)$ crystal coupled to the H8500C PMT, whose results will be presented in Sect. 6.4.4, the ^{137}Cs and ^{60}Co reference libraries were acquired for $n_{epp} = 600$, thus allowing to extend the study to an even higher number of recorded events per position, showing a further improvement of the spatial resolution obtained for higher numbers of n_{epp}.

For the scope of this thesis, only the final results obtained from the data of the $LaBr_3(Ce)$ crystal coupled to the H9500 PMT are presented in this section.

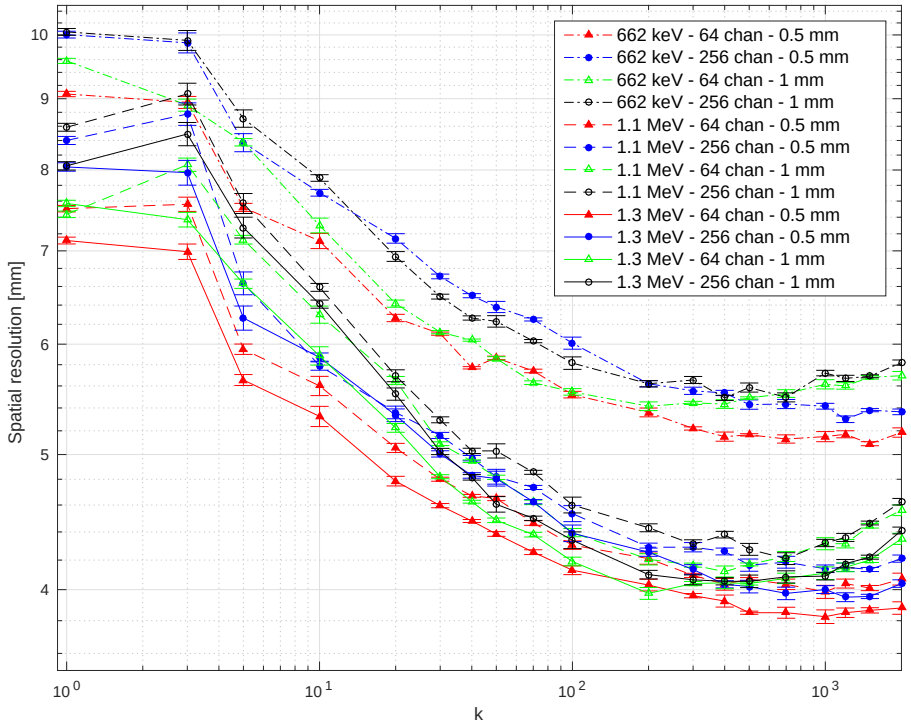

Figure 6.39: Spatial resolution of the $LaBr_3(Ce)$ crystal coupled to the H9500 PMT as a function of k (number of nearest neighbors), determined by using the k-NN algorithm for $n_{epp} = 400$ [269]. Different photon energies, PMT granularities and scan pitch sizes are distinguished by their line style, marker shape and style, respectively. Both PMT granularities refer to the H9500 PMT, where the 64-fold segmentation was created by summing up and averaging via software manipulation each four adjacent PMT pixels.

Figure 6.39 shows the values of spatial resolution obtained using the k-NN algorithm

with data recorded with the $LaBr_3$(Ce) scintillator coupled to the H9500 PMT at ^{137}Cs and ^{60}Co energies, using up to 400 reference events per position. The complete set of data enables an evaluation for all combinations of parameters (PMT granularity, pitch size and photon energy): first of all an improvement of the spatial resolution with an increasing incident photon energy is visible: this trend is probably connected to the higher statistics generated by the higher photon energy. The result that should be pointed out is the minimum of the spatial resolution observable for each set of data (photon energy and pitch size) at a value of k ≈ 1000. The best spatial resolution values are reached for a scan pitch size of 0.5 mm. From a comparison of the results from the two PMT granularities, the spatial resolutions obtained are either similar within their error bars or even better for the 64-channel case (this parameter will be further discussed in the next sections).

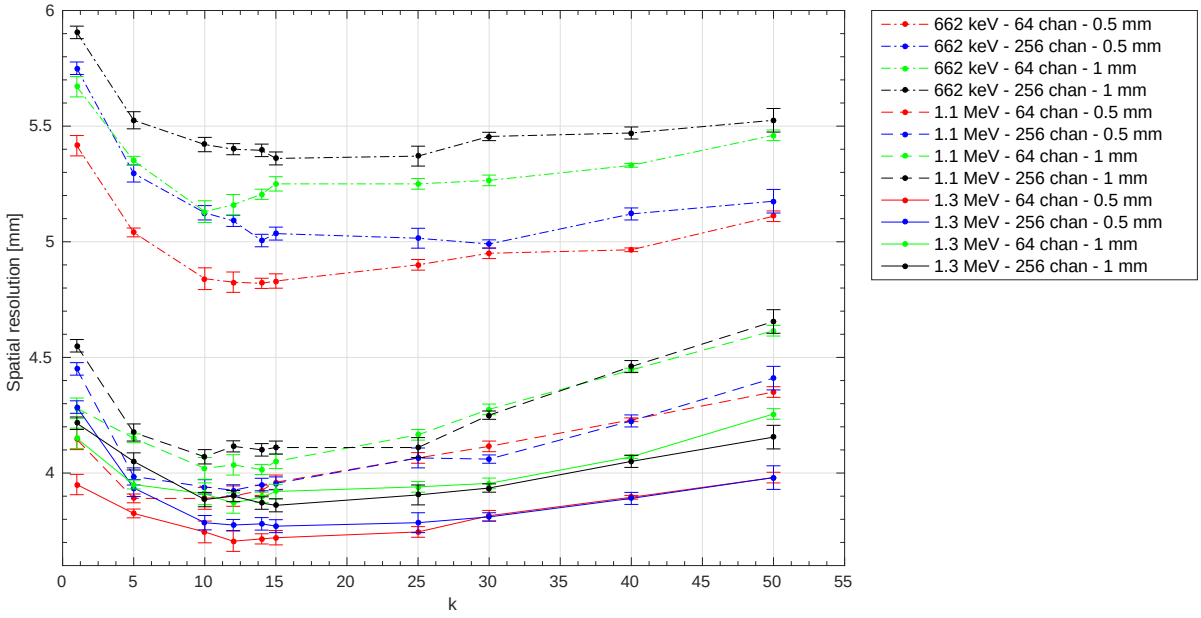

Figure 6.40: Spatial resolution of the $LaBr_3$(Ce) crystal coupled to the H9500 PMT as a function of k (number of nearest neighbors) which was achieved using the CAP algorithm, using $n_{epp} = 400$ [269]. Different photon energies, PMT granularities and scan pitch sizes are distinguished by their line style, marker shape and style, respectively. Both PMT granularities refer to the H9500 PMT, and the 64-channel segmentation is created by summing up and averaging via software manipulation each four adjacent PMT pixels.

In Fig. 6.40 the same comparisons presented in Fig. 6.39 for the k-NN algorithm are shown for the CAP algorithm. The results that are shown in this plot have been achieved using 400 photopeak events per irradiation position and the same combination of parameters can be assessed (photon energy, PMT granularity and scan pitch size). A general feature is the minimum which is found at an optimum value of $k_{CAP} \approx 12$. With

a higher number of k_{CAP} chosen, the spatial resolution degrades: the explanation could go in the direction of an over-sampling of the reference events. As in the k-NN case, there is an evident and even more pronounced separation between data acquired with the ^{137}Cs or ^{60}Co calibration source, still showing an improvement of the spatial resolution for a higher photon energy. The same conclusion as for the k-NN case can be given for the pitch size: better results are obtained from a 0.5 mm scanning pitch size. The 64-channel segmentation as well shows comparable or even slightly better results at ^{60}Co and ^{137}Cs energies, respectively.

From this systematic study the following optimum values can therefore be concluded: $k_{k-NN} \approx 1000$, $k_{CAP} = 12$, pitch size = 0.5 mm, $n_{epp} = 400$. Between the two algorithm variations the CAP shows better performances. These parameters will be taken into account for the spatial resolution evaluation of the other absorber detector which was studied, the $LaBr_3$(Ce) crystal coupled to the H8500C PMT. The PMT granularity and the achieved spatial resolution will be further discussed in Sect. 6.4.4 and 6.4.3, respectively, after having introduced in Sect. 6.4.2 a method that led to a systematic improvement.

Uncertainties determination

The error bars applied when determining the spatial resolution value are based on statistical uncertainties and are derived from sub-samples of the whole acquired reference library.

From the number of events per position n_{epp} of the full library (which is equal to 400 for the library of the $LaBr_3$(Ce) crystal coupled to the H9500 PMT and 600 for the library of the $LaBr_3$(Ce) crystal coupled to the H8500C PMT, as it will be shown in Sect. 6.4.4), sub-libraries each containing 100 events per position are created. The order of assembling these events in groups of 100 does not have an influence on the outcome, but for simplicity the groups were selected in ascending order of the photon events in the library. The "leave-one-out method" was then applied to each sub-library, using the reconstruction algorithm (k-NN or CAP) which was used for the evaluation of the complete reference library. The spatial resolution was determined for each of the k values considered; the standard deviation which can be derived from the distribution of the results from the sub-libraries is assigned to the full library results as the experimental uncertainty of the spatial resolution.

This method was applied for all libraries and for both reconstruction algorithms. The uncertainties of the spatial resolution for different values of n_{epp}, namely for values larger than 100, were extrapolated from the one obtained with $n_{epp} = 100$ using

$$\sigma(k, n_{epp}) = \sigma(k, 100) \times \sqrt{\frac{100}{n_{epp}}} \tag{6.18}$$

Figure 6.41 shows an example of the implementation of this method using the CAP algorithm applied to the data from the ^{60}Co library (gated on the 1332 keV photopeak energy) for the $LaBr_3$(Ce) crystal coupled to the H9500 PMT. Values are shown for both PMT granularities considered (256 and 64 channels) and for the different library subsets (indicated by the indices from 1 to 4).

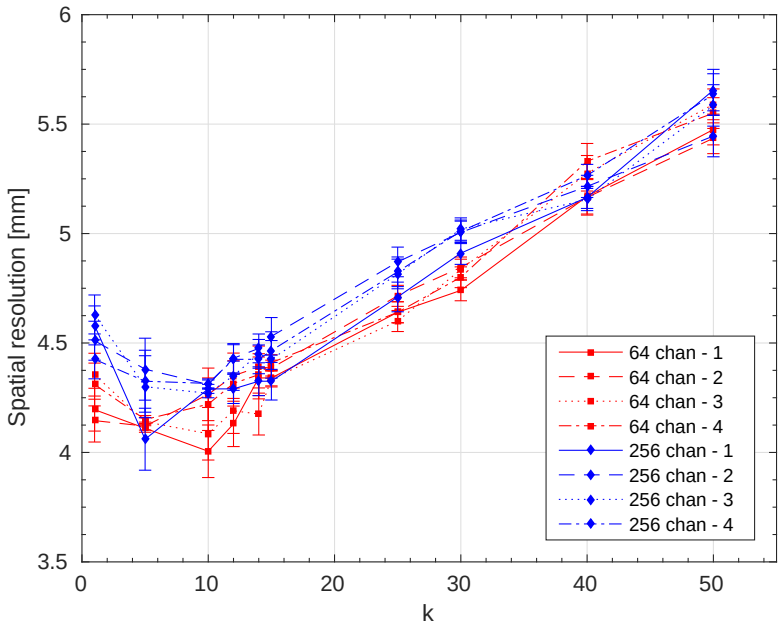

Figure 6.41: Experimental uncertainties for the spatial resolution of a $LaBr_3$(Ce) crystal coupled to a 256-fold segmented PMT and calculated from the distribution of spatial resolution values obtained from subgroups of the full reference library. In the plot the spatial resolution is shown as a function of k_{CAP} for subgroups with n_{epp}=100. Data are extracted from the ^{60}Co reference library (gated on the 1332 keV photopeak energy), which was acquired with the $LaBr_3$(Ce) scintillator coupled to the H9500 PMT. The index from 1 to 4 indicates the library subsets the data were derived from.

6.4.2 CGDR algorithm

When presenting the concept of the 2D light amplitude reference library (Sect. 6.3.2), the effect of the so-called "blank pixels" was introduced for the libraries acquired with the $LaBr_3$(Ce) crystal coupled to the H9500 PMT (Tab. 6.8) and H8500C PMT (Tab. 6.9), respectively. Although in both cases this percentage is not particularly large, it nevertheless should be taken into account when addressing the determination of the spatial resolution, where even such small numbers of erroneous pixels values can blur the achievable result.

Since the source of the unphysical "blank pixels" could not be traced to a specific hardware component, a software solution was developed in order to reconstruct, as much as possible close to a realistic situation, the contents of the "blank pixels" in any of the measured light distributions. The first solution which was tested is based on an averaging method, whose conceptual sketch is depicted in Fig. 6.42 and which was used to obtain the results shown in Sect. 6.4.1. Each "blank pixel" was substituted with an amplitude obtained from the average of the up to 8 neighboring amplitudes from the same photon event.

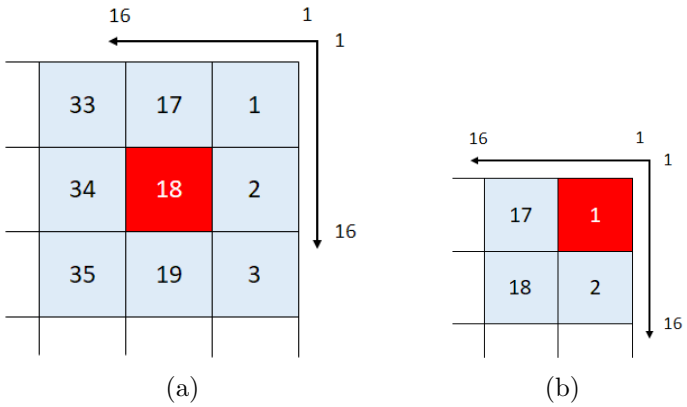

Figure 6.42: Sketch explaining the concept of the averaging method which was initially used to perform the correction of the blank pixels by substituting them with an amplitude obtained by averaging the amplitudes of the neighboring 8 pixels (or 3 if the blank pixel is located in a corner of the crystal) for the same event. The red pixel indicates the "blank pixel", whose light amplitude should be substituted.

As a first approximation, this software solution gave satisfactory results (Fig. 6.39 and 6.40). Nevertheless, in order to determine the most realistic replacement value for any blank pixel, this should be independent of the source irradiation position and the pixel position. A study of the light amplitude distribution of all 400 events per irradiation position was performed, and a new zero-replacement method was developed.

The idea behind this *Categorical Gaussian Distributed Replacement algorithm* (CGDR) is to identify first the position of blank pixels in a given reference library and then generate the distribution of all complementary non-zero values of a specific blank pixel position amongst the ensemble of 400 measured events per irradiation position. The empiric distribution was parametrized using a Gaussian fit. After normalization, performed to generate a probability distribution, a random amplitude was selected in the range between the standard deviation values -3σ and +3σ of the Gaussian distribution. This amplitude was then used to replace the blank pixel value belonging to the same irradiation position. A flowchart of the procedure is shown in Fig. 6.43. An essential step in order to apply this algorithm is the need to confirm that the distribution of the light amplitudes from the recorded events in the various irradiation positions follows a Gaussian distribution; this is shown in the next plots for the two detectors under study.

Figure 6.44 and 6.4.3 show an example of light distributions extracted from the ^{137}Cs reference library which was acquired, respectively, with the $LaBr_3(Ce)$ coupled to the H9500 PMT and the $LaBr_3(Ce)$ coupled to the H8500C PMT. In panel (a) the distribution of (400-1) pixel amplitudes is depicted, measured for a randomly chosen irradiation position and for a (randomly chosen) specific pixel. Panel (b) shows the resulting Gaussian distribution of the values replacing the "blank pixels" as obtained from the CGDR algorithm for this specific reference library.

The quality of the CGDR replacement algorithm is proven by the Gaussian distribution

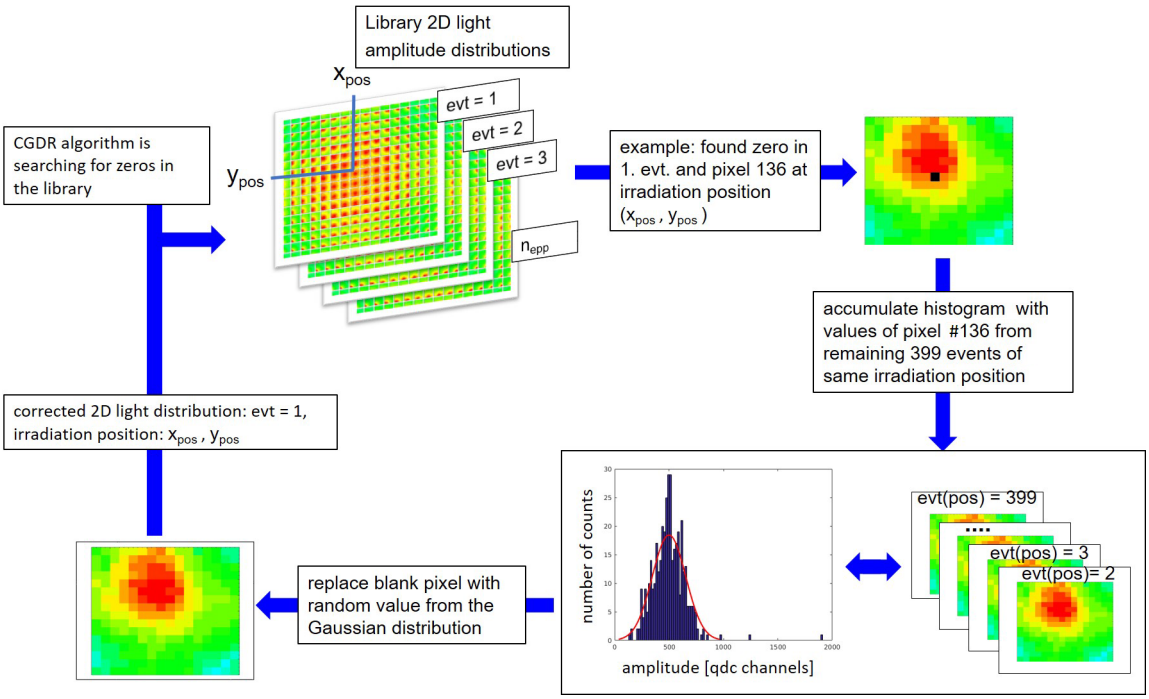

Figure 6.43: Flowchart of the Categorical Gaussian Distributed Replacement (CGDR) algorithm. See text for details.

of the blank pixel replacement values for both detector cases.

6.4.3 (Improved) results using a 256-fold segmented PMT

In this section the improved spatial resolution values are presented (compared to the ones presented in Sect. 6.4.1), resulting from applying the CGDR algorithm to the data obtained from the $LaBr_3$(Ce) crystal coupled to the H9500 PMT.

In Fig. 6.46 the spatial resolution is depicted as a function of the photon energy, comparing the results from the two blank-pixel replacement algorithms (averaging method and CGDR algorithm). The best performance achievable with the CGDR algorithm is clearly visible: for both PMT granularities evaluated (256 and 64 channels) the spatial resolution improves when the "blank pixels" are substituted using the CGDR algorithm (solid lines in the plot). The results were analyzed by using both the k-NN and CAP smoothed algorithms for the reconstruction of the interaction positions in the monolithic absorber. As expected the better performance is provided by the CAP algorithm.

In Tab. 6.10 the spatial resolution values improved by applying the CGDR algorithm are summarized, using the optimum values obtained for the parameters of the CAP algorithm as determined earlier ($n_{epp} = 400$, $k_{CAP} = 12$). Spatial resolution values obtained for both PMT granularities considered (256 channels directly from measured values, 64 channels obtained through a sum of each four adjacent PMT pixel performed by software) are listed. These values will be later used to parametrize the spatial resolution in simulation

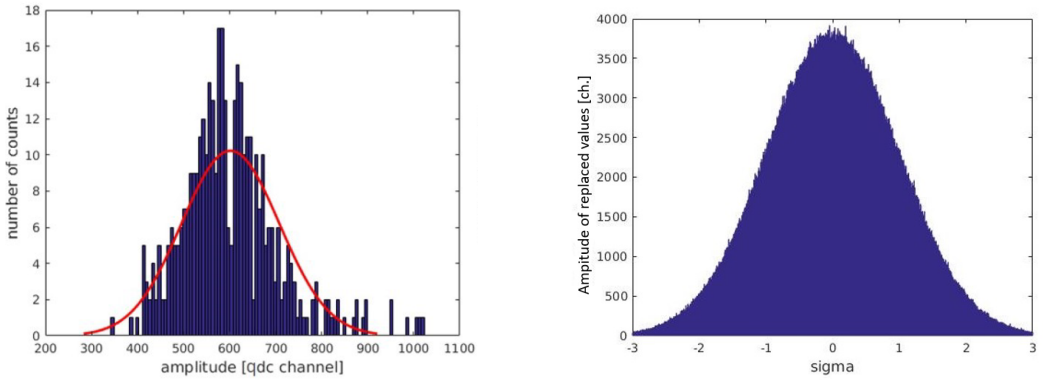

(a) (b)

Figure 6.44: From the data acquired with the $LaBr_3(Ce)$ crystal coupled to the H9500 PMT using the collimated ^{137}Cs source: (a) distribution of (400-1) light amplitudes measured for a randomly chosen irradiation position and for a specific pixel and (b) resulting Gaussian distribution of the pixel values replacing the "blank pixels" as determined via the CGDR algorithm.

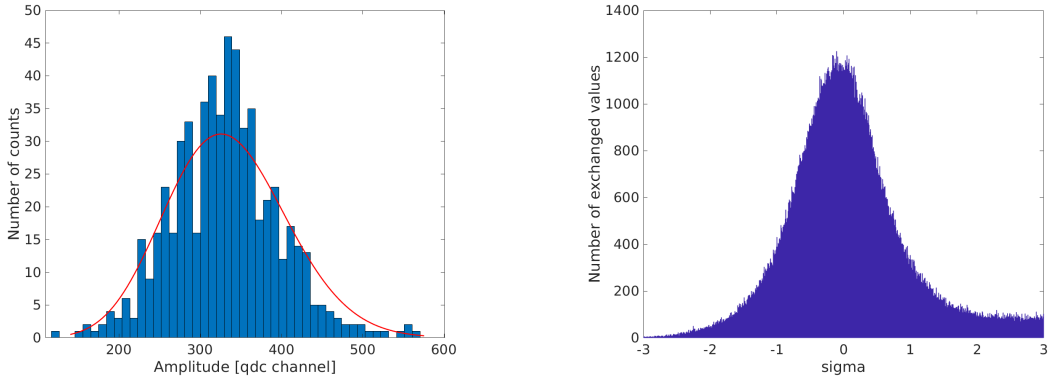

(a) (b)

Figure 6.45: From the data acquired with the $LaBr_3(Ce)$ crystal coupled to the H8500C PMT using the collimated ^{137}Cs source: (a) distribution of (400-1) light amplitudes measured for a randomly chosen irradiation position and for a specific pixel and (b) resulting Gaussian distribution of the pixel values replacing the "blank pixels" as determined via the CGDR algorithm.

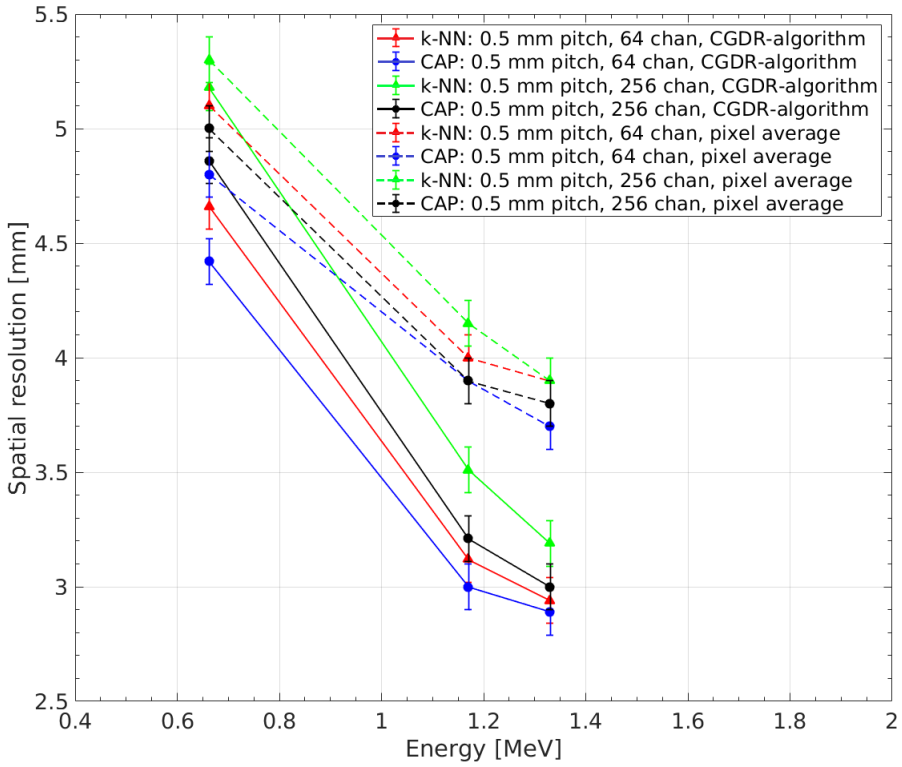

Figure 6.46: Comparison between the spatial resolution as a function of the photon energy obtained for the $LaBr_3$(Ce) scintillation crystal coupled to the H9500 PMT. Data were corrected using the CGDR algorithm (solid lines) and the averaging method (dashed lines). The data were evaluated using both the k-NN and the CAP algorithm. These results allow to compare two PMT granularities: 256 and 64 PMT segments, the latter obtained by a software summation of each four adjacent PMT hardware segments [270].

studies of an alternative Compton camera setup that includes the $LaBr_3$(Ce) scintillator coupled to the H9500 PMT as absorber component (see an example in Chap. 8).

# channels	Spatial resolution [mm]		
	662 keV	1173 keV	1332 keV
256	4.7(1)	3.2(1)	3.0(1)
64 (calc.)	4.2(1)	3.0(1)	2.9(1)

Table 6.10: Optimized spatial resolution obtained with the CAP algorithm for a $LaBr_3$(Ce) scintillation crystal coupled to the 256-fold segmented H9500 PMT, shown for different PMT granularities considered, 256 and 64 channels, respectively, the latter created by software. The values are specified for the three photon energies available from the collimated photon sources.

6.4.4 Results using a 64-fold segmented PMT

This section is dedicated to the spatial resolution results obtained from the reference libraries created with the (newly purchased) $LaBr_3(Ce)$ crystal coupled to the H8500C PMT. Both ^{137}Cs and ^{60}Co libraries for this detector were acquired with the 1 mm collimation opening for the radioactive source and a scanning pitch size of 0.5 mm.

As the scintillation crystal is different, the spatial resolution as a function of the k parameter was checked again. Figure 6.47 shows the spatial resolution dependence on k_{CAP}, for data reconstructed using the CAP smoothed algorithm. Results for different photon energies are depicted, showing the same trend which was already observed when reconstructing the spatial resolution for the detector previously studied and presented in the previous sections. The spatial resolution exhibits always better values when the photon energy increases and the optimum value for k_{CAP} was confirmed to be 12.

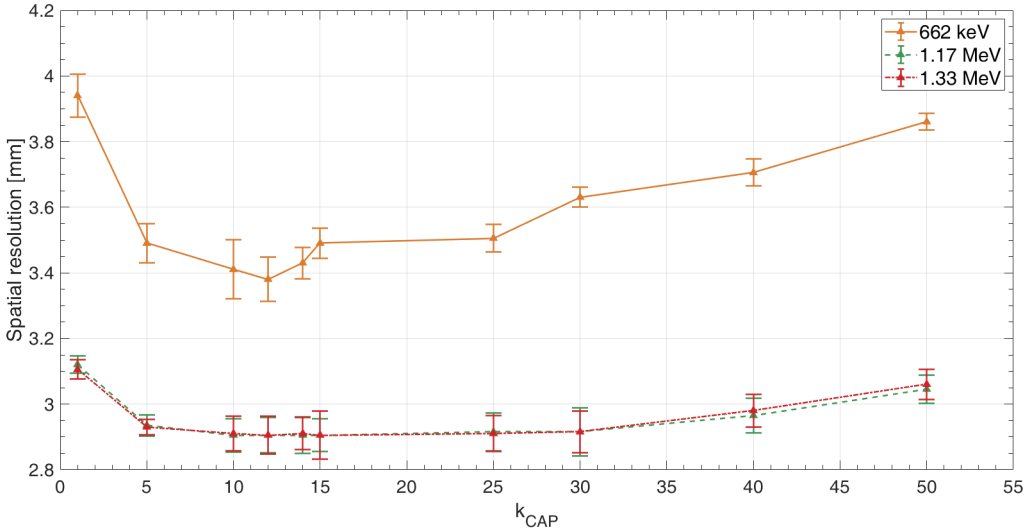

Figure 6.47: Spatial resolution as a function of the k value achieved with the k-NN smoothed algorithm, for $n_{epp} = 400$. Different photon energies are distinguished by the line style and colour. Data were acquired using a $LaBr_3(Ce)$ crystal coupled to the H8500C PMT.

The experimental uncertainties assigned to the spatial resolution results are calculated as described in Sect. 6.4.1. Like the example in Fig. 6.41 which was shown for a ^{60}Co reference library measured with the 256-fold segmented PMT coupled to a $LaBr_3(Ce)$ crystal, in Fig. 6.48 an example is depicted for the determination of uncertainties from sub-groups of the library generated using the $LaBr_3(Ce)$ crystal coupled to the H8500C PMT.

Even though better performance was demonstrated with the CAP algorithm, for comparison the spatial resolution of this detector was also evaluated using the k-NN algorithm.

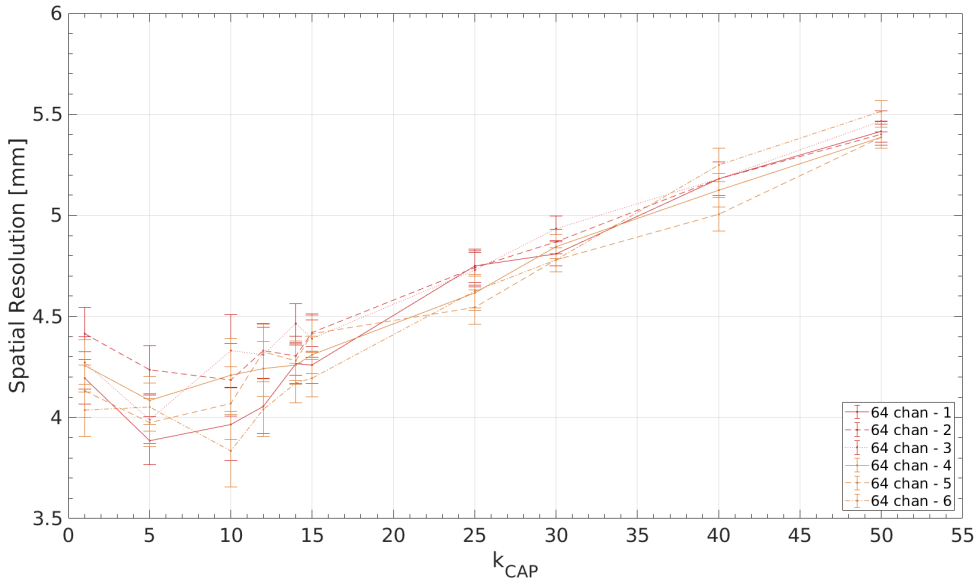

Figure 6.48: Example for the data basis leading to the determination of the experimental uncertainties for the detector's spatial resolution, calculated from the distribution of spatial resolution values obtained from subgroups of the reference library. In the plot the spatial resolution as a function of k_{CAP} is shown for library subgroups with n_{epp}=100. Data are extracted from the ^{137}Cs reference library which was acquired with the $LaBr_3$(Ce) crystal coupled to the H8500C PMT.

In Fig. 6.49 the obtained results are shown as a function of the k_{k-NN} parameter. k_{k-NN} = 1000 is confirmed to be the optimum parameter value.

As it can be concluded from Tab. 6.11, the CAP algorithm again demonstrates to provide slightly improved performance for the reconstruction of the interaction position of photon events and consequently improved spatial resolution results. For the spatial resolution determination of the $LaBr_3$(Ce) crystal coupled to the H8500C PMT, values of 3.4(1) mm and 2.9(1) mm are achieved using the CAP smoothed algorithm for the ^{137}Cs and ^{60}Co photon energies (both 1.17 MeV and 1.33 MeV photopeak energies give the same result), respectively. These optimized spatial resolution values can be used as input parameters for the generation of simulated data (see an example of their usage in Chap. 8).

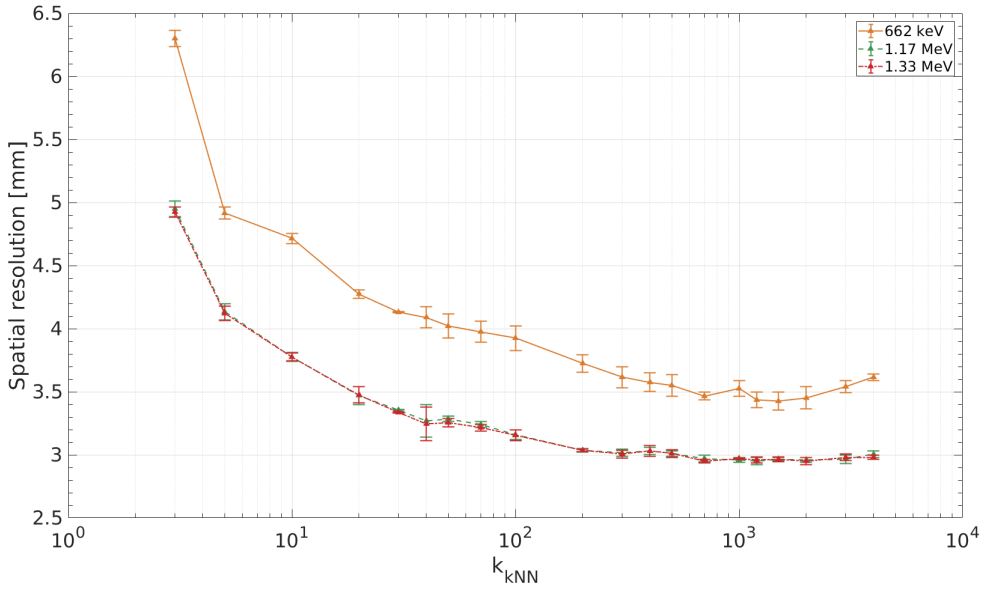

Figure 6.49: Spatial resolution as a function of the k value achieved with the CAP smoothed algorithm, for $n_{epp} = 400$. Different photon energies are distinguished by the line style and colour. Data were acquired using the $LaBr_3$(Ce) crystal coupled to the H8500C PMT.

Reconstruction algorithm	Spatial resolution [mm]		
	662 keV	1173 keV	1332 keV
k-NN (smoothed)	3.5(1)	3.0(1)	3.0(1)
CAP (smoothed)	3.4(1)	2.9(1)	2.9(1)

Table 6.11: Spatial resolution obtained with the $LaBr_3$(Ce) crystal coupled to the H8500C PMT. Results were achieved using both algorithms, k-NN and CAP. Values obtained at different photon energies are listed.

After confirming the optimum k value for (either type of) the reconstruction algorithm, and confirming as well the best performance achievable using the CAP algorithm, the spatial resolution dependence on the n_{epp} value could be evaluated for the $LaBr_3$ (plus H8500C PMT) data as well. Since the libraries for the $LaBr_3$(Ce) crystal coupled to the H8500C PMT were acquired by collecting $n_{epp} = 600$ events per irradiation position, a systematic study over increasing n_{epp} values could be carried out. The values used for this analysis range from 75 to 600 events per position, and for all of them the spatial resolution was determined using the CAP algorithm with $k_{CAP} = 12$. Depending on the n_{epp} value selected, the optimum value of k_{CAP} can slightly vary. However, since this variation is only marginal, for consistency all results are shown for a k_{CAP} value of 12.

This study was performed in order to determine the minimum value of n_{epp} required in order to still obtain the best achievable value of the spatial resolution for a given detector configuration. The more the n_{epp} value could be reduced, the less computational effort is

required when running the position reconstruction algorithm and the less time is needed to acquire the complete reference library. Figure 6.50 shows such a dependence: spatial resolution values obtained with a PMT granularity of 64 channels (acquired with a direct measurement using the H8500C PMT (solid lines) and summed by software from the experimental values acquired using the (256-fold segmented) H9500 PMT (dashed lines)) are included in the plot as a function of the number of events selected per irradiation position. The curves are shown for the three photon energies accessible with the reference libraries: 662 keV, 1173 keV and 1332 keV, respectively.

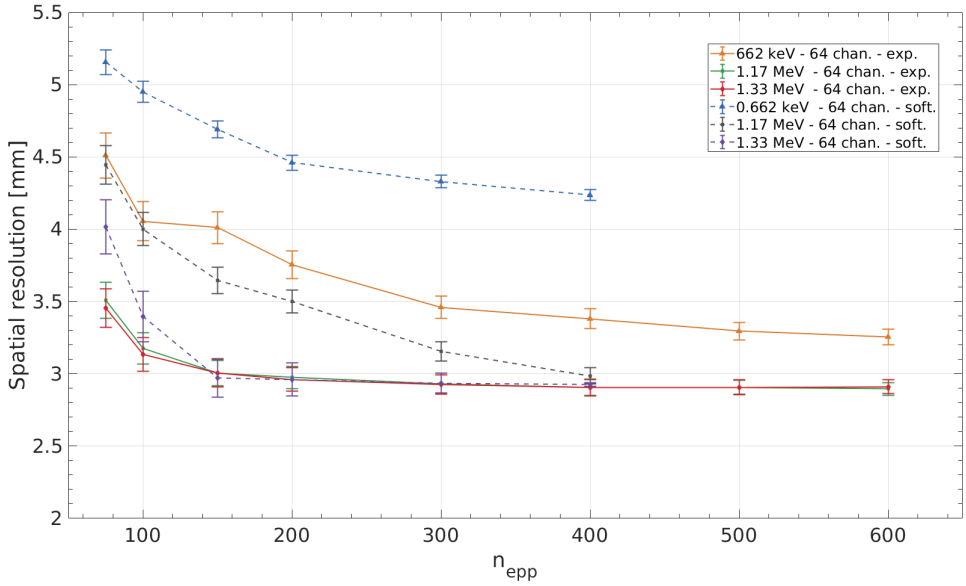

Figure 6.50: Spatial resolution at different photon energies as a function of n_{epp}. Results are plotted for a PMT granularity of 64 channels, from data acquired using the 64-fold segmented H8500C PMT (solid line) and the 256-fold segmented H9500 PMT (dashed line). From the latter the amplitudes from the segments were summed up by software in order to create a 64-channel pixelation. The optimum value of $k_{CAP} = 12$ was chosen for each data set.

As it can be observed from the plot, the spatial resolution tends to improve with a higher number of events per irradiation position used for the position reconstruction algorithm: this effect can be correlated with the correspondingly higher statistics contained in the library. Nevertheless, an onset of saturation of this curve is observed for n_{epp} values larger than about 300 for the ^{137}Cs case and even more pronounced already beyond 200 events for the ^{60}Co case: within the experimental uncertainties, no significant improvement of the spatial resolution is observed beyond those values. The energy-dependent difference between the number of events recorded per position at which this saturation occurs may be due to the fact that for lower photon energies there is a higher probability of scattering in the detector, leading to a larger spread of the light.

The overall best spatial resolution found for the $LaBr_3(Ce)$ detector whose results are presented in the current section is 2.9(1) mm measured at 1.17 MeV and 1.33 MeV, using a reference library containing 400 events per position. As it can be seen from Fig. 6.50, these results are in agreement or even better than the ones previously obtained with the same PMT granularity (realized by software, see Fig. 6.38), and displayed in Fig. 6.51 with dashed lines.

These results represent a big step forward towards the envisaged direction for future upgrades of the Compton camera prototype: this will permit the reduction of the readout complexity of the system while still maintaining its performance.

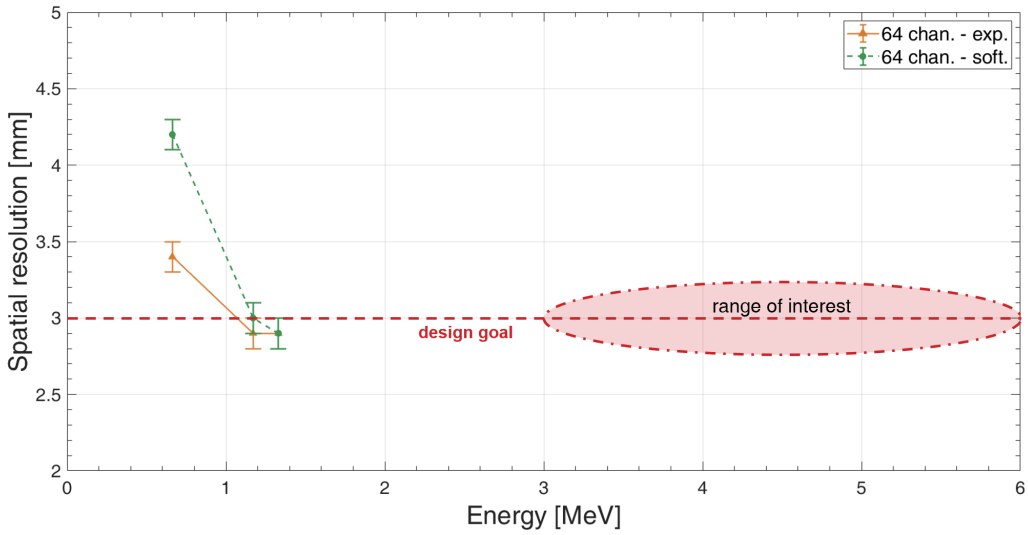

Figure 6.51: Spatial resolution as a function of the photon energy. The results from the data set with a PMT granularity of 64 channels, obtained experimentally using the H8500C PMT (orange solid line) or by software summation of four adjacent channels from the H9500 PMT (green dashed line) are shown. All data originate from reference libraries which were acquired with a 1 mm collimator, a 0.5 mm scan pich size and the optimum value of k_{CAP} = 12, for n_{epp} = 400. The horizontal red dashed line denotes the design goal of 3 mm from the initial simulation studies performed for the Compton camera prototype design. The elliptical area indicates the energy range which is of interest in prompt-γ imaging for hadron therapy.

Finally, Fig. 6.51 shows the best spatial resolution obtained for both detectors under study as a function of the incident photon energy. For these results the following parameters were chosen: a PMT granularity of 64 channels, 1 mm collimation opening, 0.5 mm scan pitch size. The CAP algorithm was used with n_{epp} = 400 and k_{CAP} = 12. As observed before, the spatial resolution improves with an increasing photon energy, reaching a value of 2.9(1) mm, which is the same, within the uncertainties, for both ^{60}Co energy peaks and

for both detector scenarios considered. The first observation can be commented by the fact that the two ^{60}Co photon energies are rather close to each other, making considerable difference of the spatial resolution rather unlikely. Concerning the second observation, the difference between the results from the two PMT scenarios may be smaller at higher energies because of the light yield, generating more statistics at higher energies. The light statistics can also be a reason for the improved spatial resolution values obtained when coupling the $LaBr_3$(Ce) crystal to a 64-fold segmented PMT rather than a 256-fold segmented PMT, whose pixels size are, respectively, 6 mm and 3 mm.

The horizontal red dashed line which is drawn in Fig. 6.51 indicates the design goal which, from simulations previously performed (see Fig. 4.7), corresponds to a spatial resolution of the whole Compton camera of 2° [121]. This goal was already achieved at 1.3 MeV photon energy with the improved results coming from the data acquired with the $LaBr_3$(Ce) crystal coupled to the H9500 PMT (see Sect. 6.4.3), when introducing the CGDR algorithm and artificially creating by software a 64-channel PMT granularity.

With the $LaBr_3$(Ce) scintillation crystal read out by a 64-fold segmented PMT (H8500C from Hamamatsu), this goal was achieved for both photopeaks energies from the ^{60}Co source (1.17 MeV and 1.33 MeV). Although higher photon energies cannot presently be tested, the trend of the spatial resolution suggests an improvement, or at least similar values achievable within their uncertainties, with a further increasing photon energy. The creation of a reference library requires a highly collimated γ source, having a S/N ratio which would allow for the measurement of the library in a reasonable time. Since offline photon calibration sources do not exist at energies within the energy range of interest for γ imaging in hadron therapy, this collimated beam has to be created accelerator-based large scale facilities. This measurement may become possible at the upcoming γ-beam facility of the Extreme Light Infrastructure-Nuclear Physics (ELI-NP) facility at Bucharest [271], which will become operational in almost two years.

6.4.5 Algorithm optimization

The photon interaction position reconstruction algorithm extensively described in the previous sections gives satisfactory results in terms of achievable spatial resolution for monolithic scintillator crystals. However, the time required to perform the reconstruction of the interaction positions with the k-NN algorithm is quite extensive: a speed optimization of the algorithm is needed in view of the time requirements of a possible future application of the Compton camera prototype in real-time. The most time consuming part of the process pursued for the spatial resolution determination (or the reconstruction of unknown photon interaction positions), based on the k-NN method, is the event-wise comparison with the extensive reference library. Reference libraries are composed of

$$n_{pos} \times n_{epp} \tag{6.19}$$

events which, in order to determine the (x,y) coordinates of the calculated interaction position, have to be compared to each other. This creates a number of mandatory comparisons of the order of 10^{10}. Furthermore, it should be considered that each event consists of a 2D light amplitude distribution, whose size depends on the PMT segmentation: this corresponds to 256 or 64 channels, which are arranged in a 16×16 or 8×8 matrix.

Considering the amount of data contained in a reference library, performing this huge amount of comparisons to determine the spatial resolution requires a considerable amount of memory (of the order of 10^2 GB). The processes are therefore sent to run on a multi-node cluster, which can provide a significantly higher memory than a single computer station. The process has to be split into different jobs (normally chosen to be around 100): considering the most ideal situation in which those would run all at the same time, the calculation of the (x,y) coordinates of all interaction positions which has to be compared during the execution of the "leave-one-out" method takes around 6 hours for a reference library acquired with a 64-fold PMT and around 18 hours for a reference library acquired with a 256-channel PMT. For both cases this time refers to a library containing 400 events per position. This corresponds to a time of ~ 2 s per irradiation position for the first case and ~ 6 s per position for the second case.

The time (and memory) consuming process is thus the weak point of the algorithm. Effort is being put in this direction in order to find a solution which works in the direction of the desired real-time application of the Compton camera prototype.

As a first step, an integrated software platform was developed, whose schematical workflow procedure can be found on the right side of Fig. 6.52. On the left side of the prototypical error histogram, the standard procedure is schematically shown. In the standard procedure, most of the memory required is due to the fact that all data have to be converted into MATLAB format, which takes care of the preprocessing of the data and then sends them to the (C++ - based) core of the algorithm which performs the event-wise comparison. The postprocessing of the data and the creation of the error histogram from which the spatial resolution is derived are again handled by MATLAB.

After having demonstrated that a minimum amount of events per position (> 300) is necessary in order to maintain the same spatial resolution performance, the integrated

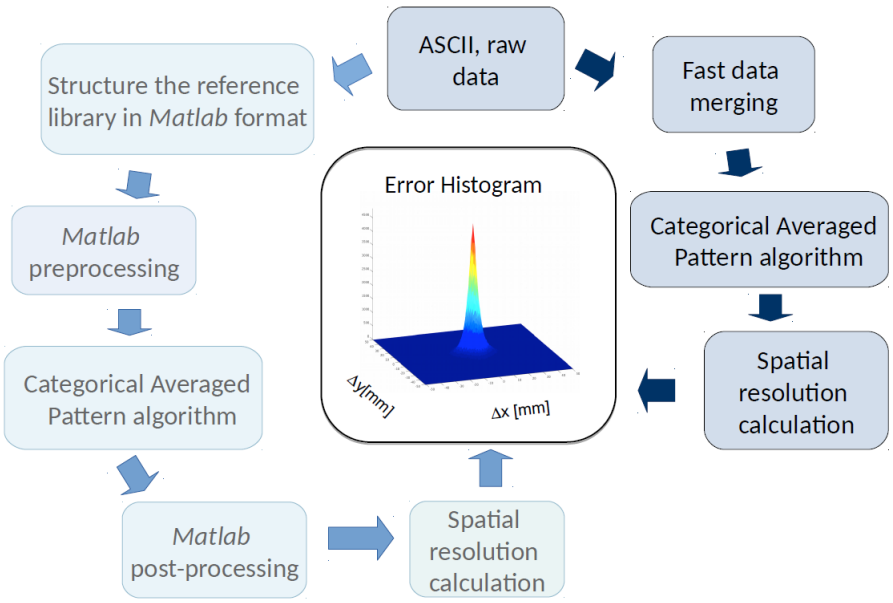

Figure 6.52: Scheme of the standard procedure which was used when running the k-NN algorithm (left, boxes in light blue) and the procedure used within the new platform which was implemented (right, boxes in darker blue) [272].

software platform mentioned above was developed with the idea of reducing processing time and memory consumption by the reconstruction algorithm. The main change which was applied is the data format, which, instead of being adapted for MATLAB, were converted to binary files from the initially acquired ASCII files. This enabled a drastic reduction of the memory requirement by about two orders of magnitude (from 10^2 GB to 1 GB), therefore allowing to run the reconstruction process without the need of high performance computers (HPCcluster) and to pursue a more automatic procedure. However, no significant change in the run time of the algorithm could be obtained.

In the meanwhile the structure of the data was carefully analyzed and there appear new perspectives to use, for example, *Deep learning* or *Artificial Neural Network* methods, which are already in use for similar applications [273]. The largest reference library, which was acquired for the $LaBr_3(Ce)$ crystal coupled to the H8500C PMT and which contains 600 events per position, will be used for first attempts in this direction, since a large fraction of the available data are needed for the training part of such networks. First steps in this direction are being performed, but are not part of this PhD thesis.

CHAPTER 7

Online Compton camera characterization using the new readout system

The detection of multi-MeV prompt γ rays is the key objective when using a Compton camera detector arrangement for ion beam range verification (see Sect. 1.3.3). This chapter presents a characterization of the LMU Compton camera, which was performed at the MLL Tandem accelerator (Maier-Leibnitz-Laboratorium, Garching [274]) with a 20 MeV proton beam and a 20 MeV pulsed deuteron beam. In both scenarios the beam was hitting either a water or a PMMA target, in order to induce the production of prompt-γ radiation by nuclear reactions between the beam and the target. The aim is to present a characterization of the detector components of the Compton camera prototype at the high photon energy range of interest (between 3 and 6 MeV) using the new signal processing and readout system. The initial goal was to obtain energy and position information from both components in order to perform the image reconstruction of the prompt-γ initial source position as well. However, as it will be reminded, the validation tests with the new signal processing modules revealed a previously hidden issue with the implantation profile of the silicon detectors that on one hand perspectively clearly pointed to the need of implementing a considerably revised version of the double-sided strip detectors, while as an immediate workaround forced to come up with an improvised arrangement of scatter detectors as will be shown in the following chapter. Therefore the goal of the online measurements was reduced to assessing the performance of the new electronics, rather than already providing data for photon source image reconstruction, which could not reasonably be performed with the improvised scatter detector arrangement and which will be subject of the continuation of the project upon the availability of a new generation of silicon detectors.

7.1 Mechanical setup

Since the DSSSD layers had to be enclosed inside a light tight metallic box, all detectors were mounted inside a Faraday cage with specific relative distances that reflects the Compton camera specifications defined by the simulation studies in [121]. As the power consumption of the frontend electronics causes a considerable temperature rise inside the box, a system which controls the temperature is required. In Fig. 7.1 the photographs of the (a) initial and (b) newly upgraded design of the Compton camera Faraday cage are shown. The initial box was made of copper-cladded PCB material and, in order to avoid a constant increase of the temperature inside the box, a ventilation fan unit was installed (see ⑥ in Fig. 7.1(a)), while the temperature was remotely controlled using thermal sensors (PT-104 from Picotech [275]). However, during online measurements the temperature could still easily reach values around 30° [139]. Since the ambient temperature directly correlates to the dark current flowing in the silicon detectors (by the relation which was shown in Eq. (3.9)), a new solution was designed (the mechanical layout can be found in App. C) and implemented. Figure 7.1(b) shows the newly designed Faraday cage for the Compton camera prototype, which was used during the online measurements at the Tandem accelerator presented in this chapter. Aluminum plates with a thickness of 8 mm were used instead of copper-plated PCB material (with a thickness of 2 mm) of the previous copper box.

As it can be seen from the photograph in Fig. 7.1(b), the new cage is composed of six aluminum plates screwed to a supporting frame from standard profile bars. The entrance window ④ was again made of a standard aluminum foil with a thickness of 15 μm, and the active compressor cooling device (from Fuhrmeister GmbH, [276]) was mounted on one side of the cage.

Figure 7.2 shows (a) the temperature registered by the two temperature sensors mounted inside the cage, the first one in the front part close to the DSSSD modules (sensor 1) and the other in the back part close to the absorber detector (sensor 2). The temperature and dark current values were registered during the first 40 minutes of operation of the camera fully mounted with its frontend readout system. The trend shows a decrease of the dark current by about a factor of two every 7°C of the decreasing temperature, with an end temperature value selected via the active cooling device. It can be seen from Fig. 7.2(a) that the temperature change in the Faraday cage occurs in a similar way in the front as in the back part of the cage, thus avoiding unfavorable temperature gradients inside the detector housing. When the ion beam is sent to the target, the detectors are collecting signal charge from the incident photons (generated by nuclear reactions between the ion beam and the water or PMMA target), and thus the DSSSDs' dark current may increase by a factor of 2. However, the trend as a function of the temperature is maintained.

Although conscious of the limitations imposed by the DSSSD modules, the noise level acquired from the p- and the n-side of the scatter layers was evaluated with the new readout system based on the MMR frontend boards. The result was not satisfactory with regard to the n-side performance: the FWHM of the noise peak was, at operational voltage, 4 keV on the p-side and almost 70 keV on the n-side (the difference was even larger than the

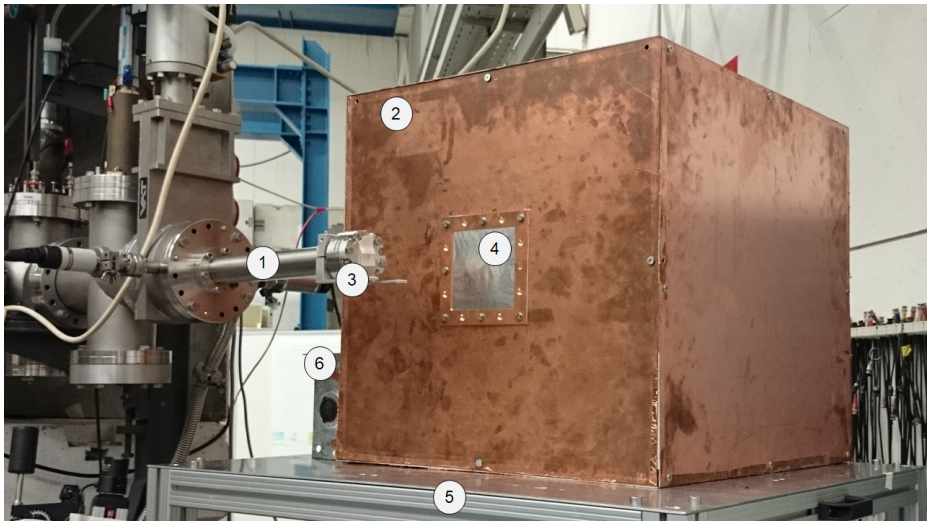

(a)

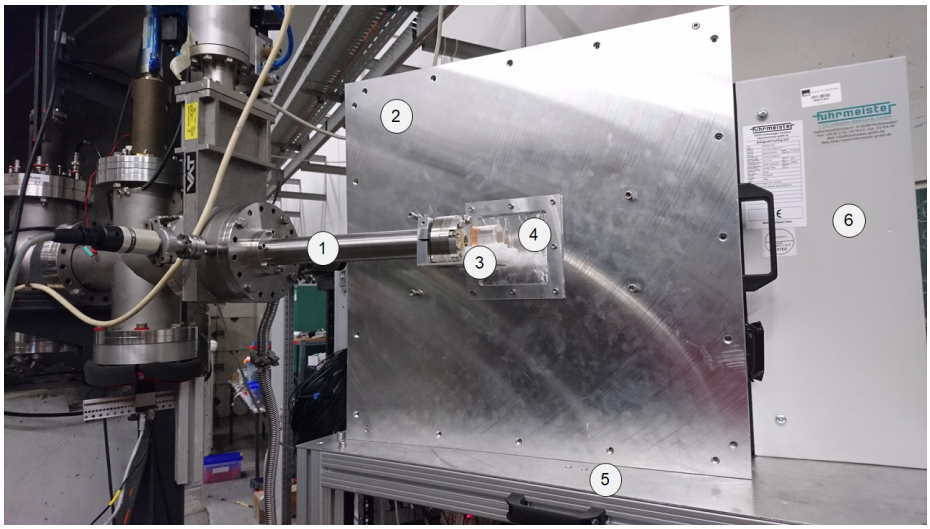

(b)

Figure 7.1: Photographs of the Compton camera prototype inside a (light tight) Faraday cage and mounted at a beamline of the Maier-Leibnitz-Laboratorium (MLL) in Garching during beam times at the local Tandem accelerator. Two generations of the Faraday cage ② are shown in (a) the initial and (b) the upgraded new design. The whole camera setup is supported by a movable and height-adjustable support stand ⑤. The beam line ① is parallel to the aluminum entrance window ④ of the cage, which separates the (water or PMMA) target ③ and the detectors mounted inside the cage. In the new design the initially used ventilation fan unit ⑥ (a) was replaced by an active compressor-based cooling device ⑥ (b).

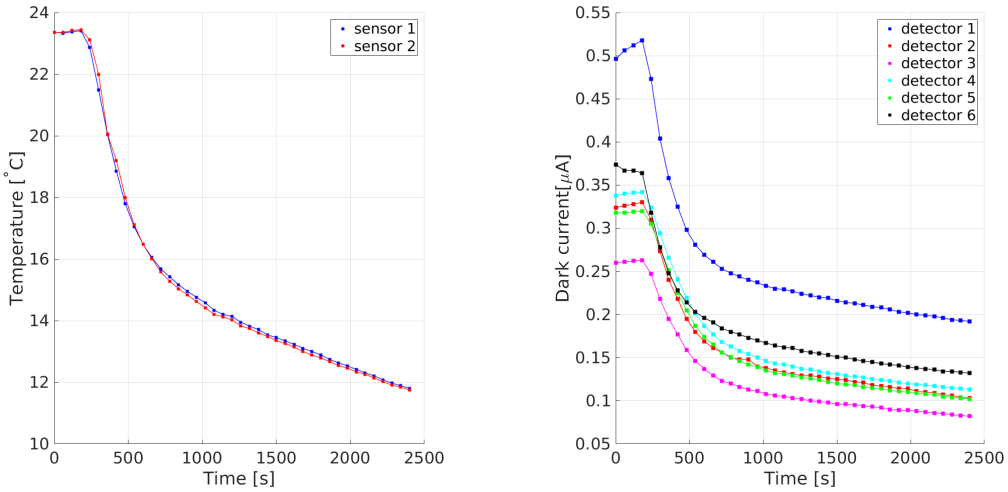

(a) (b)

Figure 7.2: Plots showing (a) the temperature registered in the Compton camera cage by the two thermal sensors placed inside (sensor 1 in the front part and sensor 2 in the back part) and (b) the related dark current in all six DSSSD modules, in the time frame of the first 40 minutes after the device starts to cool down the cage volume.

one observed with the initial Gassiplex-based readout system [139], since the new MMR modules allowed to reach an even lower noise level on the p-side of the detector). This led to the final conclusion that even with the upgraded readout system, adapted to positive and negative signals, the limitations imposed by the low interstrip resistance on the DSSSD n-side prevents the acquisition of low-energy signals emerging from Compton-scattered recoil electrons signals from the n-side of the scatter detectors. Thus a temporary and improvised workaround had to be used in the online measurements to be able to assess the rate capability and trigger performance of the new electronics.

In Fig. 7.3 the detectors arrangement used during the online measurements performed at the Tandem accelerator is depicted. The detectors were mounted inside the Compton camera Faraday cage which was described above.

This solution had to be chosen as an improvised solution due to the already discussed n-side deficits of the present 0.5 mm DSSSD modules. While this inhomogeneous improvised setup foreseeably prevented an attempt of tracking and image reconstruction, it nevertheless allowed for a validation of the fully upgraded new readout system at the prompt-γ ray energies of interest. In Fig. 7.3, seen from the position of the target, two (1 mm thick) DSSSD modules were mounted (1,2), 10 mm apart from each other and 50 mm from the target. These detectors had an active area of 40×40 mm^2 and a pitch size of 1 mm, which provides a total of 40 strips per side from each detector. They were placed as first scatter layers behind the target in order to increase the probability of generating events in Compton coincidence between the absorber and the subsequent "standard" DSSSD layers with

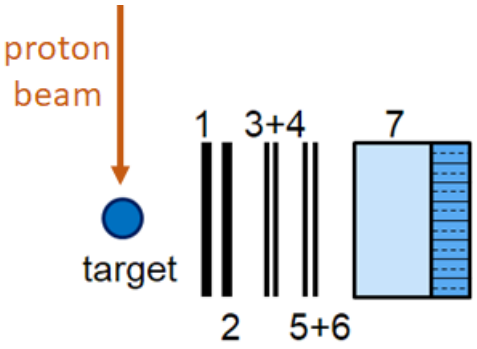

Figure 7.3: Detector arrangement used for the online measurements performed at the Garching Tandem accelerator. From the target perspective, two standard DSSSD modules with a thickness of 1 mm (1,2 from Micron [193]) were placed, followed by 4 layers of DSSSD with a thickness of 0.5 mm (3+4, 5+6 from CiS [191], both pairs rotated by 90 degrees against each other). The absorber (7) completed the camera setup at the end. See text for more details.

a thickness of 0.5 mm. While these detectors have a smaller field of view and a different pitch size than the "standard" Compton camera modules, and as such prevent a consistent tracking analysis, they were nevertheless useful for a validation of the upgraded system, as it will be shown later. The 0.5 mm thick DSSSD detectors, which are indicated as no. 3,4,5,6 in Fig. 7.3, were placed behind the two 1 mm detectors. Trying to overcome the problem with the n-side noise level, they were placed in two pairs of detectors (3+4, 5+6), where the second detector of each pair was rotated by 90° with respect to the first one: the idea was to read out only the "good" p-strip signals and obtain the interaction position by considering one pair of DSSSD modules as one detector unit. Furthermore, the two detectors were placed facing each other with the same (p- or n-) side, in order to avoid the creation of an electric field in-between them. The mechanically feasible distances between these DSSSD modules did not correspond to the desired ones from the previous simulation studies (see Sect. 4.2): the DSSSD modules within the same detector pair had a relative distance of 11 mm, while the two detector pairs were spaced with a relative distance of 15 mm to the other detector pair and to the preceding 1 mm thick detector. The distance between the DSSSD layer facing the absorber component and the absorber itself could be maintained to 35 mm as required by the camera design.

7.2 Rate performance

With the introduction of the powerful VME-based SiS3153 controller (Struck Innovative Systeme, [229]) and the new mvme DAQ software (see Sect. 5.3.2), the data acquisition rate could be substantially improved.

Table 7.1 and 7.2 show data rates which could be achieved with the "old" and "new"

readout and data acquisition systems during online measurements at the MLL Tandem accelerator in Garching. Additionally, the data acquisition with the MMR readout system could for the first time be performed by selecting the scatter component as trigger for the camera system, thus allowing for a drastically higher ratio of events registered in Compton coincidence. Data were acquired by detecting γ-rays generated from the nuclear interactions between a 20 MeV proton beam and a water or PMMA target. The proton beam current was varied and the data rates achieved by using the two readout systems are compared.

In Tab. 7.1 data rates achieved with the Marabou data acquisition system and the DSSSD signals processed by the Gassiplex-based frontend boards are shown for prototypically selected proton beam currents. The trigger could be set only on the absorber

Beam current	Free rate [Hz]	Accepted rate [Hz]	Trigger
500 pA	$\sim$ 1.5 k	1 k	absorber
1.5 nA	$\sim$ 15 k	1.1 k	absorber

Table 7.1: Data acquisition rates for different beam currents. The signal processing for the DSSSD detectors was based on the Gassiplex readout system and the data acquisition was based on the VME-based RIO-3 PPC controlled by the Marabou DAQ software.

component, whose trigger signals besides predominantly consisting of non-scattered primary photon also include the ones originating from the $LaBr_3$(Ce) internal radioactivity, leading to a considerable part of the recorded events not being in coincidence with the scatter detector layers. Furthermore, it can be observed that the dead time related to this acquisition mode is considerably large, since in all cases a maximum data rate in the order of 1 kHz could not be exceeded. In Table 7.2 data rates obtained from online

Beam current	Free rate [Hz]	Accepted rate [Hz]	Trigger	Data rate [MB/s]
200 pA	$\sim$ 5 k	$\sim$ 5 k	scatterers	0.5
300 pA	$\sim$ 6 k	$\sim$ 6 k	scatterers	0.6
400 pA	$\sim$ 9 k	$\sim$ 9 k	scatterers	1.2
2 nA	$\sim$ 50 k	$\sim$ 38 k	scatterers	8

Table 7.2: Data acquisition rates for different beam currents. The signal processing for the DSSSD detectors was performed with the MMR boards and the data acquisition was based on the VME SiS3153 operated via the mvme DAQ software.

measurements using the upgraded readout and data acquisition system are listed. Two main improvements can be highlighted: the trigger derived from the scatter component of the camera system allowed to avoid the acquisition of those events which were related to the internal radioactivity of the absorber component. Furthermore, as the scattering layers provide a total of $\sim$ 1.5% scattering probability, the system trigger derived from these events allowed to drastically increase the number of events in coincidence with the absorber component. Due to the SiS3153 VME controller, which provides in its present

configuration a data transfer capability of up to 35 MB/s, the reachable data acquisition rate could also be improved by one order of magnitude. This, together with the scatterer's triggering capability, allowed for an overall data quality improvement by up to three orders of magnitude.

7.3 Energy deposition in the scatterer layers

Figure 7.4 shows the front view of the mechanical setup for the DSSSD layers and their signal processing electronics, which were mounted inside the aluminum Faraday cage during the online measurements. The Compton camera cage was placed on a movable and height-adjustable support stand in order to fix the height of the entrance window, which corresponds to the detectors area, to the height of the target (water or PMMA) hit by the beam (175 cm).

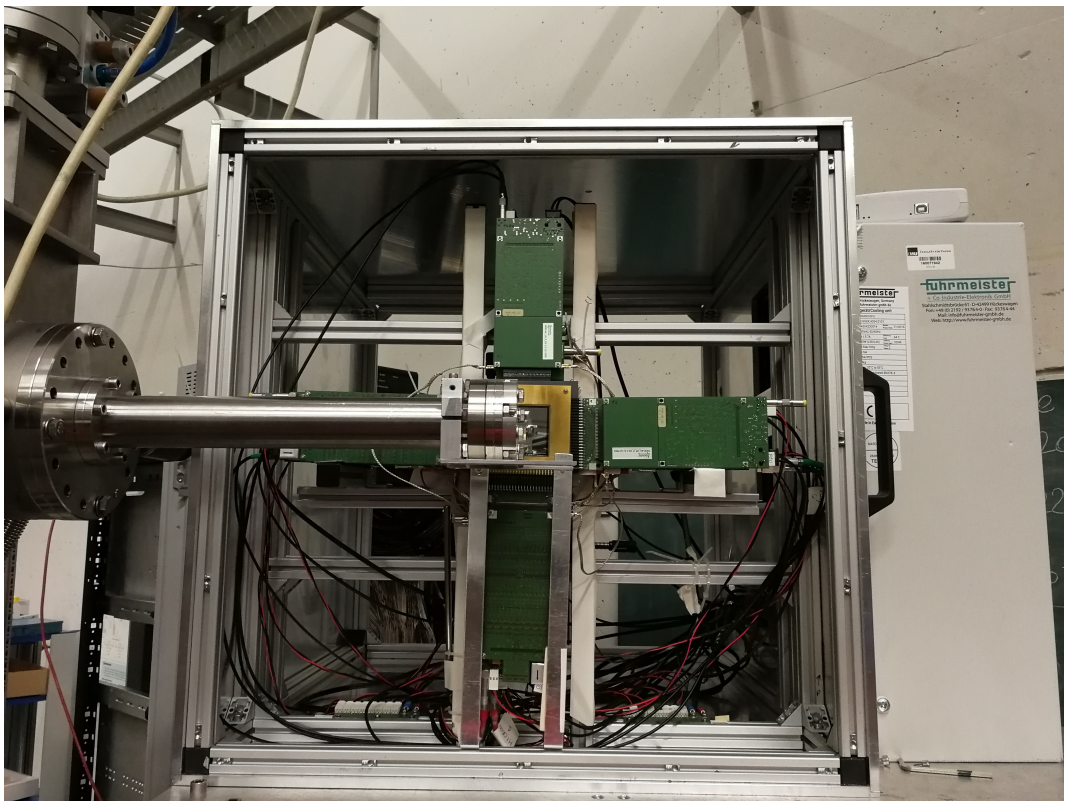

Figure 7.4: Mechanical setup of the DSSSD modules whose signals were preocessed by the MMR frontend boards during online measurements at the MLL Tandem accelerator in Garching. In the front the beamline extension with the end flange carrying the Kapton exit window is visible.

In order to validate the use of the readout electronics based on the MMR frontend boards for the signals from the DSSSD detectors, a 20 MeV proton beam was used. A

simulation study for the Compton camera was performed in [185]: from prompt γ-rays generated by nuclear reactions between a proton beam and a water target an energy deposition in the scatterer layers can be expected as it is depicted in Fig. 7.5(a). The impinging photons are generating, via their interactions with the DSSSD layers, Compton scattered electrons, which are then releasing their energy in the silicon detectors.

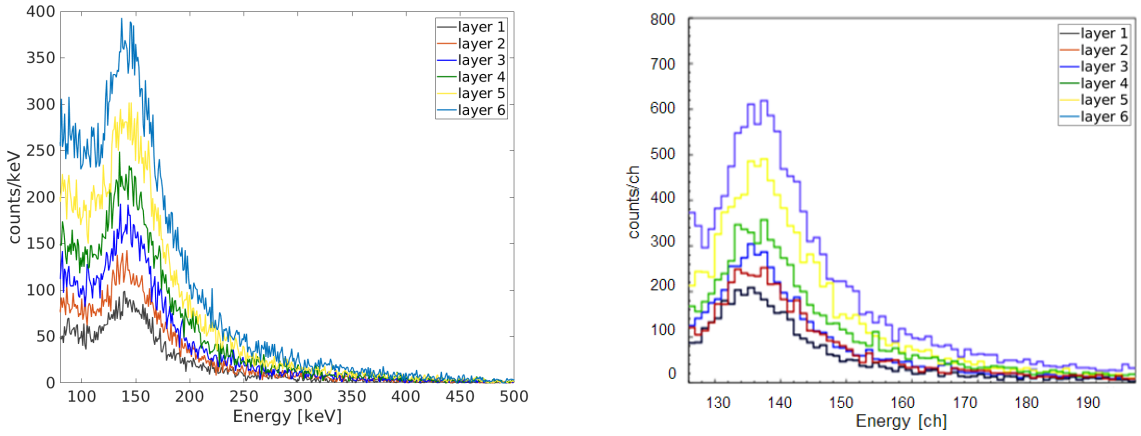

(a) (b)

Figure 7.5: Energy deposition from Compton-scattered electrons in the scatterer layers. Data in (a) were simulated from a scenario in which a proton beam was hitting a water target and the prompt γ-rays generated by nuclear reactions between beam and target were detected by the Compton camera [185]. Data in (b) were acquired experimentally from the p-side strips of the DSSSD layers at the OncoRay facility in Dresden [99] with a 160 MeV proton beam hitting a water target. The detector numbering starts from the target side.

From the energy spectra it can be observed that the energy deposition is concentrated around a value of $\sim$ 140 keV and the intensity of recorded signals is increasing across the stack of scattering layers in ascending order towards the absorber component of the camera (which in this scenario is triggering the data acquisition). These results were already compared to experimental data: in Fig. 7.5(b) the energy deposition layers in all six DSSSD scatterers is depicted. The signals recorded were generated by prompt γ-rays which were produced by a 160 MeV proton beam hitting a water target.

Since the energy resolution which can be obtained with the DSSSD detectors does not allow for a reliable energy calibration at the low electron energies of interest (the energy resolution could be evaluated at high energies, using a triple α-source, see Sect. 6.1.2), the energy deposition acquired experimentally in the DSSSD layers was quantified based on the simulation data [185] and is thus shown here expressed in ADC channels.

In order to validate the new readout electronics based on the MMR frontend boards, measurements were performed by detecting the prompt γ-rays generated by the nuclear interactions between a 20 MeV proton and deuteron beam (with a selected beam current of 0.2 nA) and a water target. The generated prompt gammas cover the same energy

range of the photons which were generated in the measurement using a clinical proton beam energy as shown in Fig. 7.5(b) and the energy deposition in the scatter layers is thus expected to reflect the same energy range. Since the energy spectra displayed in Fig. 7.6 and 7.7 were acquired in a measurement where the detectors were arranged as in the setup sketched in Fig. 7.3 (and not according to the "standard" Compton camera arrangement as underlying the data shown in Fig. 7.5(a) and the experimental data in 7.5(b)), only spectra from strips prototypically selected in the center area of the detectors are shown in Fig. 7.6 and 7.7, with the aim of proving a validation of the new readout electronics for n- and p-side strips of the DSSSD detectors.

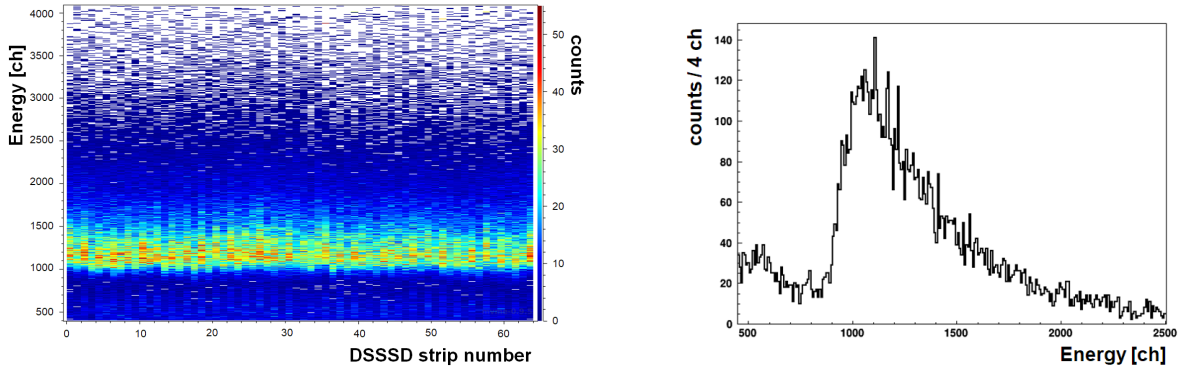

(a) (b)

Figure 7.6: Energy deposition in the p-side strips of the 0.5 mm thick DSSSD detector. (a) Combined view showing the energy deposition of all the 64 p-strips processed by one MMR board and (b) energy spectra of one prototypically selected p-strip located in the central area of the detector.

Figure 7.6(b) shows the energy deposition on a strip on the p-side of one of the 0.5 mm thick DSSSD modules from CiS (layer 6 from the setup in Fig. 7.3); the strips on the n-side of the same detector were not read out for the reasons previously explained. Figure 7.7(c) and (e) show the energy spectra of prototypically chosen strips on the p-side and n-side of layer 2 (which has a thickness of 1 mm) from the setup in Fig. 7.3, respectively. The related 2D combined energy plots are also shown in Fig. 7.7(b) and (d), demonstrating a consistent energy deposition in all the strips of the 1 mm DSSSD detector, on the p- and n-side, respectively. As a further proof, in Fig. 7.7(a) is depicted a 2D correlation plot between the energy recorded on the p- and on the n-side of the 1 mm thick detector, thus showing events in coincidence between p- and n-strips. The MMR frontend boards could therefore be successfully validated for the readout of both positive and negative signals from a DSSSD detector.

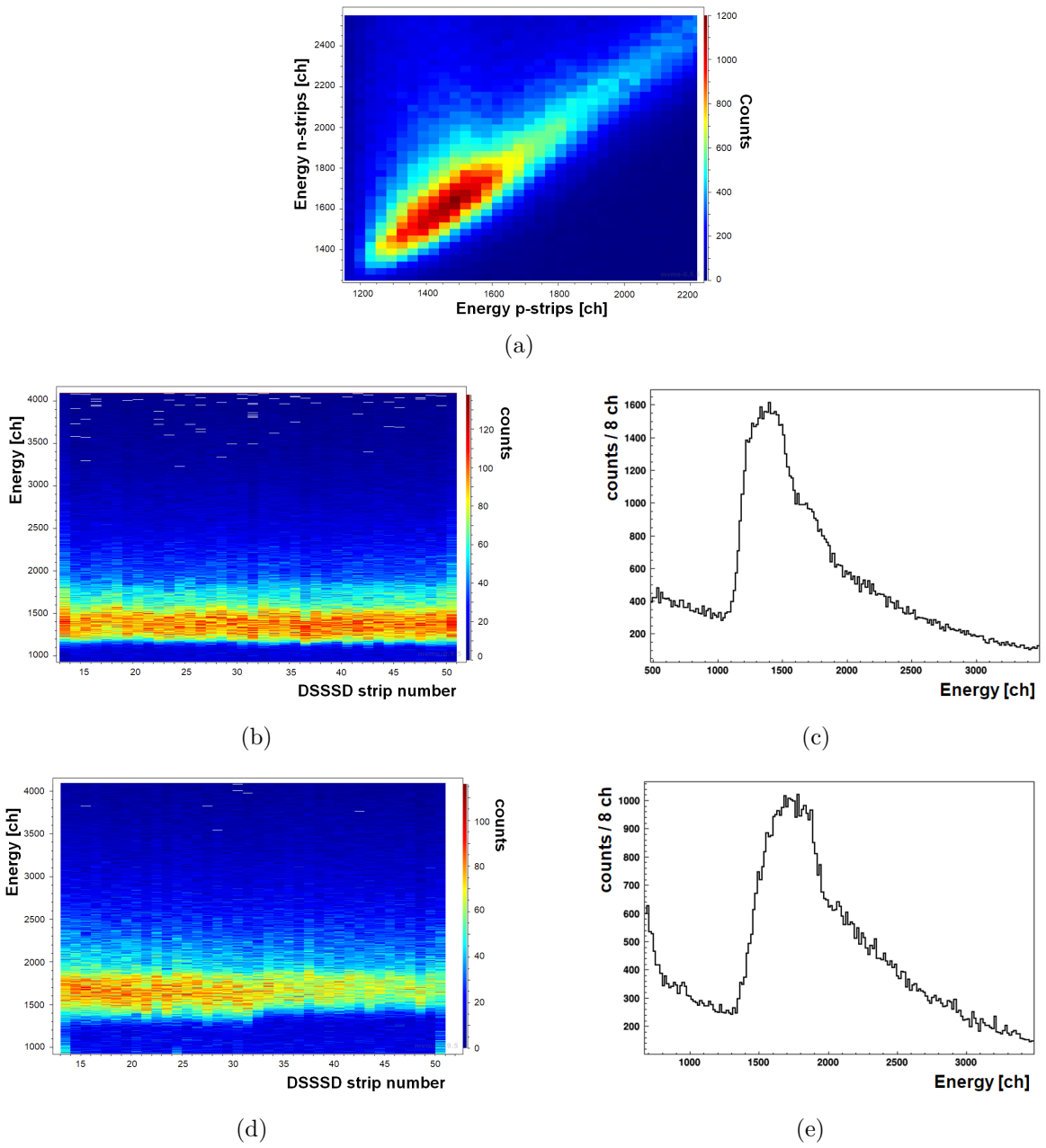

Figure 7.7: Energy deposition in the 1 mm thick DSSSD detector. (a) 2D correlation plot between the energy recorded on the p- and n-side of the 1 mm thick detector which shows the coincidence between p- and n-strips. (b) Combined view of all the p-strip signals and (c) energy spectrum of a prototypically selected p-strip from the central region of the detector area. (d) and (e) refer to the same information as in (a) and (b), but for the n-side of the detector. The data were acquired during a measurement with a 20 MeV pulsed deuteron beam.

7.4 Scintillator performance at high energies

This section is dedicated to the performance validation of the MMR readout system, here in the version adapted to the PMT signals of the absorber component. As they are (besides the spatial information) the two essential sources of information in a Compton camera system, energy and time responses were evaluated during online measurements at the high prompt γ-ray energies of interest.

7.4.1 Energy information

In order to validate the new signal processing and data acquisition system for the readout of PMT signals as well, firstly the energy information recorded by the absorber component at the high energies of interest was evaluated. The detected prompt γ-rays were generated from the irradiation of a small cylindrical water target (4 cm diameter, 3.5 cm height) and a small PMMA target ($2.5 \times 2 \times 1$ cm^3) with a 20 MeV proton beam (and a beam current at the last cup of 0.2 nA) at the MLL Tandem accelerator in Garching. Since the MMR board is processing the 64 signal channels from the individual pixels of the multi-anode PMT, in order to obtain information on the total energy deposited in the detector and analyse its energy spectra, a gain matching correction step was applied together with the PMT non-uniformity map adjustment of the pixels signals. The 64 signals were then summed up. In the H8500C PMT and H12700A-10 PMT cases the signals processed correspond to the 64-fold pixelation of the PMT, while in the H9500 PMT case each adjacent four of the initial 256-channels from the PMT segmentation were summed up through the use of an adapter board (see Sect. 5.2.2).

In order to permit the acquisition of signals in the prompt-gamma energy range of interest, the operational high voltage (HV) of each PMT was adjusted during the online measurements with the 20 MeV proton beam. Since the signals from the PMT increase their amplitude with increasing HV applied (within a defined range of values, which in this case is between -750 V and -1100 V), the HV was selected in order to acquire signals from impinging photons with an energy ranging up to ~ 8 MeV. Table 7.3 summarizes the operational HV values, which were chosen for the three studied PMTs for their operation at prompt γ-ray energies.

Detector	operational HV
$LaBr_3$(Ce) + H9500	-860 V
$LaBr_3$(Ce) + H8500C	-780 V
$CeBr_3$ + H12700A-10	-900 V

Table 7.3: Operational high voltage applied to the different scintillation detectors. The HV was optimized for the acquisition of photons in the range of high energies of interest.

The energy spectra obtained from the detection of prompt gammas generated by nuclear reactions between the 20 MeV proton beam and (a) a water or (b) a PMMA target are

depicted in Fig. 7.8(a), (b) and Fig. 7.8(c), (d) for the $LaBr_3$(Ce) and the $CeBr_3$ detectors, respectively. The energy spectra are shown in the energy range from 3 MeV to 7 MeV, as this is the range of interest for the detection of prompt γ-rays.

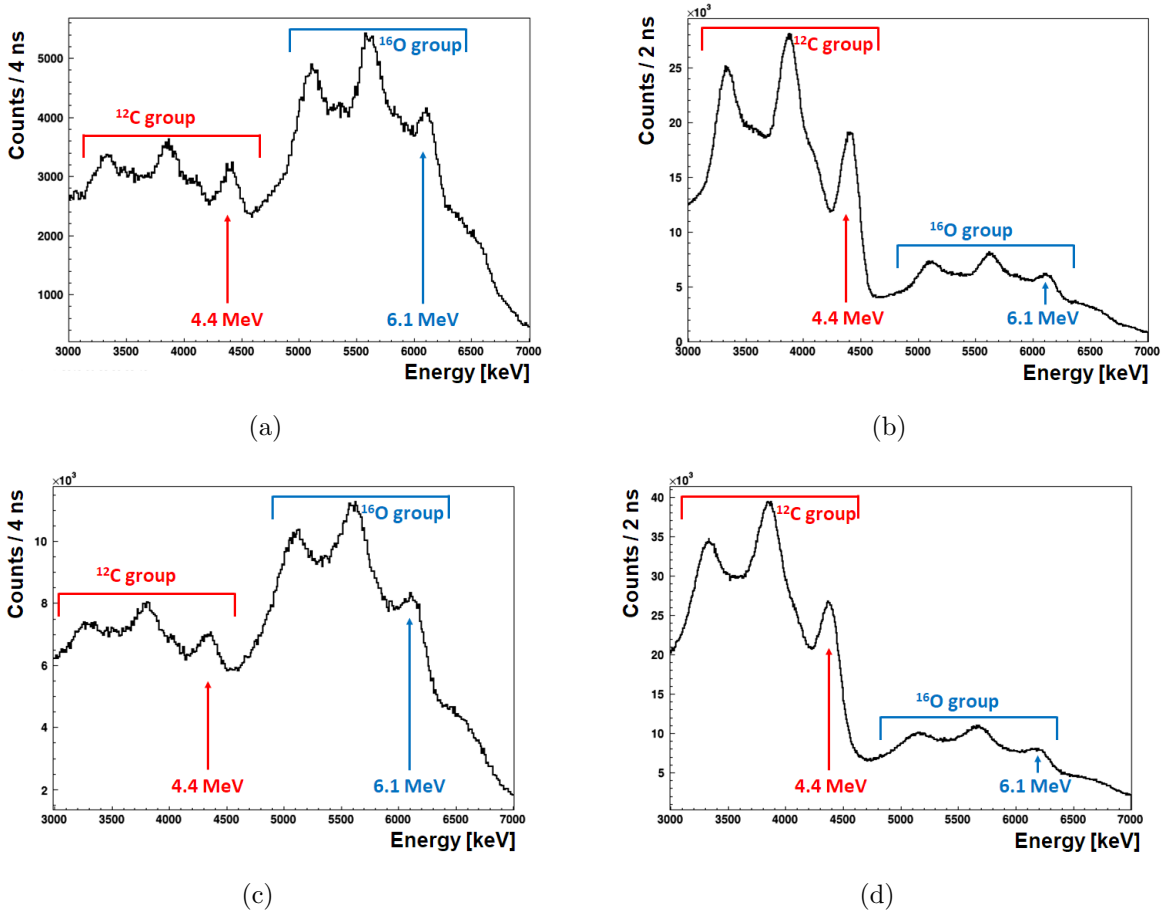

Figure 7.8: Energy spectra at high energies for the $LaBr_3$(Ce) crystal read out by the H8500C PMT. The photons registered were generated by the interaction of a 20 MeV proton beam with a (a) water target and (b) PMMA target. The spectra of the $CeBr_3$ crystal read out by the H12700A-10 PMT are shown as well, for registered photons generated from the interaction of a 20 MeV proton beam with a (c) water target and (d) PMMA target.

The gamma-rays coming from the carbon and oxygen group are visible in all the energy spectra presented in Fig. 7.8, in an amount which relates to the phantom composition, since the production intensity of prompt γ-rays from particular excited nuclei strongly depends on their initial concentration in the irradiated target material. For the scenario in which the proton beam was irradiating a water target, the (high-energy) component of the prompt γ ray spectrum is dominated by the 6.129 MeV transition (plus its single- and double-escape peaks) emitted from the ground-state de-excitation of the 3^- state of $^{16}O^*$. In this target scenario, the 4.4 MeV photons from excited ^{12}C nuclei are only

generated after a fragmentation reaction of ^{16}O. Due to the higher concentration of carbon in PMMA rather than in water, the main component in this scenario is the 4.439 MeV peak, emitted during the de-excitation of the $^{12}C^{*}$ from inelastic (p,pγ) collisions. Together with the 4.439 MeV peak, the single- and double-peaks are also present in the spectra. The energy resolution performance which were obtained from these measurements at high photon energies revealed a consistent trend from the $LaBr_3$(Ce) detector to the $CeBr_3$ detector values. The degradation in energy resolution was in the order of $\sim$ 1%, thus maintaining the trend already observed at lower energies from laboratory sources (see Sect. 6.2.2). This is a further confirmation of the possibility of replacement of the $LaBr_3$(Ce) scintillation material with the more cost-effective $CeBr_3$ crystal.

7.4.2 Timing information

The evaluation of the timing performance of the absorber, which is the fastest component of the Compton camera prototype, is essential in order to allow for a γ-neutron discrimination, which can enable a reduction of the background. The Time-to-Digital converter module (MTDC-32, Mesytec [237]), previously tested with the "old" readout system [139], was included in the new readout system and related DAQ software. The performance was evaluated with both the $LaBr_3$(Ce) and the $CeBr_3$ scintillation detectors.

In order to validate the timing performance of the absorber detector with the upgraded readout system, online measurements were performed at the MLL Tandem accelerator in Garching, using a 20 MeV pulsed deuteron beam. The beam current was set to 0.2 nA as in the previous measurements presented in this chapter. The deuteron beam pulse period was selected to be 1.6 μs, while the width of every pulse was tuned to be 2.5 ns, thus short enough to allow for a γ-neutron discrimination. The radio frequency (RF) signal of the accelerator pulsing system was used as Common Stop signal for the timing measurement, while the start signal was derived from the PMT sum dynode of the $LaBr_3$(Ce) scintillator. The time interval between the start and stop signals was digitized by the MTDC-32 module with a resolution of 31.3 ps per channel. This allowed on one side for a sufficient time resolution and on the other side for the coverage of a 4 μs wide range, which could accommodate for a full time time-of-flight cycle of the 1.6 μs pulsed beam. Since the evaluation was performed for the absorber component of the camera, the trigger of the system was set to the signals from the 64 PMT single pixels which were processed by the MMR frontend board and collected by the VMMR receiver.

The experimental setups used during the time-of-flight measurements are illustrated in Fig. 7.9: the detector was placed (a) under 90° with respect to the deuteron beam path at a distance of 21 cm from the irradiated water phantom and (b) under 30° with respect to the deuteron beam path at a distance of 200 cm from the irradiated water phantom. Data were acquired in both scenarios in order to observe the different neutrons component as a function of their travelling distance.

Time-of-flight spectra measured in different scenarios and with different scintillation detectors are shown in Fig. 7.10. Panel (a) and (b) refer to the scenario depicted in Fig. 7.9(b), in which the detector was placed relatively close to the target and thus to the beam

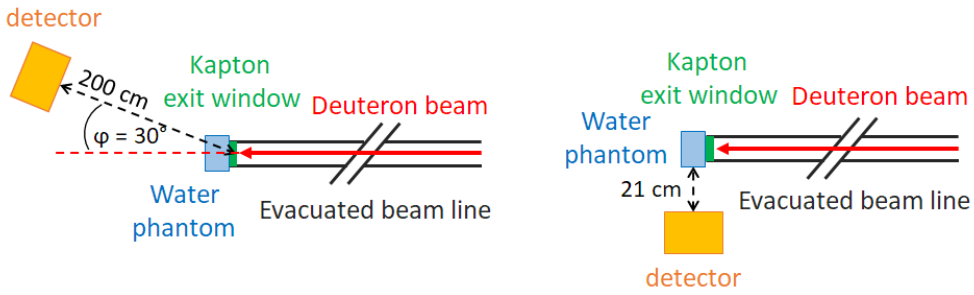

Figure 7.9: Illustrative sketch of the experimental setup at the MLL Tandem accelerator used during the time-of-flight measurement, aimed to validate the use of the Time-to-Digital converter module integrated in the new signal processing and data acquisition system. The $LaBr_3$(Ce) (or $CeBr_3$) scintillator was placed (a) under 30° with respect to the beam line and 200 cm far from the water phantom, (b) under 90° with respect to the beam line and 20 cm far from the water phantom. The water phantom was mounted directly in front of the beam exit window, made of a 30 μm Kapton foil, through which the deuteron beam left the vacuum.

line exit window. The time spectra were acquired with (a) the $LaBr_3$(Ce) coupled to the H9500 PMT and with (b) the $CeBr_3$ coupled to the H12700A-10 PMT and accumulated for 30 and 10 minutes, respectively. The shape of the prompt peak reflects the pulse structure of the deuteron beam, whose width of 2.5 ns is also reflected in the spectra in Fig. 7.9. The tail which can be observed in the falling edge region of the peak relates to the neutron component, which in this scenario does not present a strong separation from the prompt peak, since the travelling distance for the neutrons was only 21 cm. The plots are shown in logarithmic scale in order to highlight the neutron background component which can be subtracted with the use of the timing information.

Panel (c) and (d) in Fig. 7.10 show time spectra for the scenario whose sketch was depicted in Fig. 7.9: the detector was placed at 30° with respect to the deuteron beam path, at 200 cm from the water target from which the prompt gammas are emitted. The time spectra in this scenario were acquired for the $LaBr_3$(Ce) scintillation crystal coupled to (c) the H9500 PMT and and (d) the H8500C PMT, and accumulated for 20 and 30 minutes, respectively. Given the longer distance between the detector and the water target, the tail on the falling edge region is in this case more composite, since the "big" tail due to the delayed neutrons is now preceded by a smaller tail which can be caused by delayed photons having a certain transit time. Furthermore, it can be observed that the neutron component has a time-of-flight peaking at about 5 ns for the scenario sketched in Fig. 7.9(b) and at about 50 ns for the scenario in Fig. 7.9(a). This nicely reflects the flight time of the fastest neutrons with the full beam velocity, recoiling from an inelastic proton collision. This can be verified with the following formula [277]:

$$\beta = 0.04635 \cdot \sqrt{\frac{E[MeV]}{A}} \tag{7.1}$$

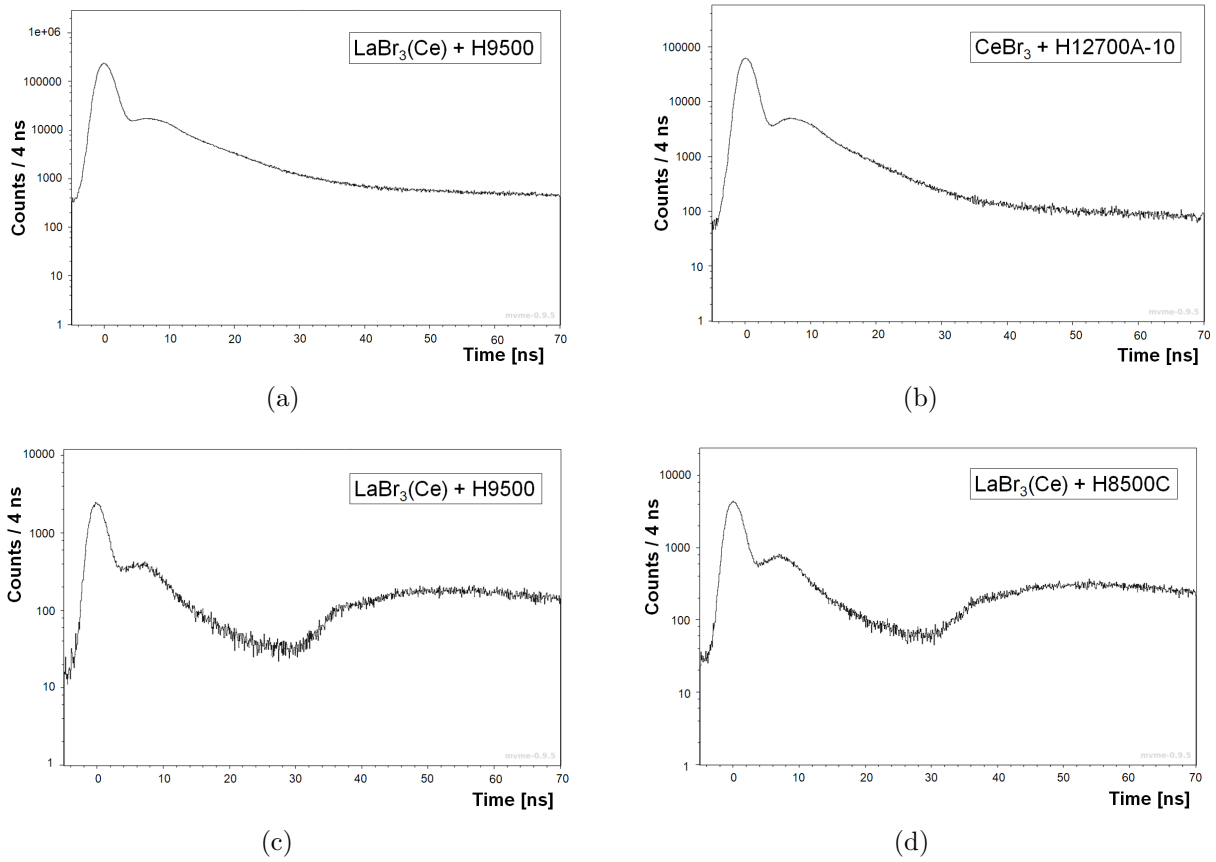

Figure 7.10: Time-of-flight spectra measured with a 20 MeV pulsed deuteron beam, using a $LaBr_3$(Ce) and a $CeBr_3$ scintillators. Panel (a) and (b) indicate the case in which the $LaBr_3$ coupled to the H9500 PMT and the $CeBr_3$ coupled to the H12700A-10 PMT, respectively, were placed close to the beam line, like depicted in Fig. 7.9(b). Panel (c) and (d) refer to the case in which the $LaBr_3$(Ce) scintillation crystal, coupled to the H9500 PMT and H8500C PMT, respectively, was placed 200 cm from the water phantom at an angle of 30° (like in Fig. 7.9(a)).

where $\beta = \frac{v}{c}$ represents the particle velocity in units of speed of light c, E is the particle beam energy, while A represents the mass number of the particle (2 for deuterons). The parameter β amounts to 0.145 for E = 20 MeV, which then results in a velocity of 4.35 cm/ns. Considering the 21 cm and 200 cm distances chosen between the detector and the beam exit, the time required by the fastest neutrons to reach the detector is, respectively, 5 ns and 46 ns, in agreement with the measured values.

In order to evaluate its physical consistency, the correlation of the acquired time spectra with the energy signals registered in the detector and obtained from the software summation of the signals from the PMT pixels (processed by the MMR board), a prototypically selected scenario is shown in Fig. 7.11. The measured time-of-flight spectrum in correlation with the energy signals registered is shown for the $LaBr_3$(Ce) scintillation crystal coupled to the H9500 PMT, placed at 21 cm from the beam exit window (scenario as in Fig. 7.9(b)).

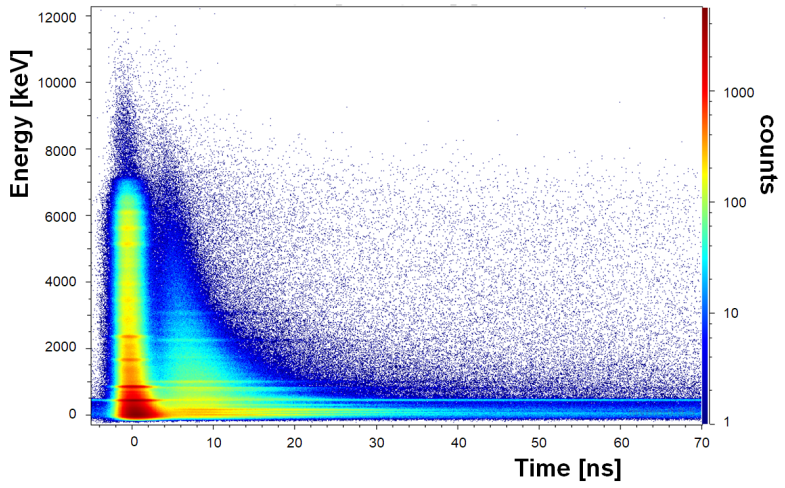

Figure 7.11: Correlation plot between the time-of-flight and energy signals registered in the $LaBr_3$(Ce) scintillation crystal coupled to the H9500 PMT. The measurement refer to a configuration like in Fig. 7.9(b) in which a 20 MeV pulsed deuteron beam was hitting a water target.

In the low-energy region, e.g. below 600 keV, the separation of fast and slow components is blurred mainly due to the contribution of the continuously emitted 511 keV γ rays and their corresponding Compton continuum. This originates during the annihilation process of the short-lived isotopes, such as ^{15}O ($t_{1/2}$ = 2.04 min) and ^{11}C ($t_{1/2} = 20.39 min$) which happens online. In the high-energy region, which is the one of interest in prompt γ-ray imaging, the separation between fast and slow components is definitely more sharply defined. This allows for obtaining a "cleaner" situation when performing γ-neutron discrimination, which was demonstrated to be achievable with both $LaBr_3$(Ce) and $CeBr_3$ as absorber detectors of the LMU Compton camera, making use of the upgraded readout system.

7.5 Discussion

The online characterization of the Compton camera, with the use of the new signal processing and data acquisition system, was presented in this chapter. The energy and time performance for the absorber component of the camera was validated at the multi-MeV energies of interest for the prompt gammas. The upgraded readout system for the scatter component of the camera was demonstrated to successfully process signals from the DSSSD detectors with both polarities. This improvement step allowed for the first time to trigger on the signals from the scatter component, thus improving by about three orders of magnitude the ratio of events in coincidence between the camera components. Although the Compton imaging performance could not be evaluated by tracking the scatter position due to the restrictions imposed by the implantation profiles of the DSSSD components, the Compton camera system was demonstrated to provide good performance at the high-energy range of interest and thus be ready for a full operation as soon as a revised version of DSSSD detectors will be available.

CHAPTER 8

An alternative scatterer component for the Compton camera system

In this chapter an alternative Compton camera setup, based on γ tracking, will be introduced. The system has been evaluated within the framework of the International Open Laboratory (IOL) collaboration with the group of Dr. Taiga Yamaya from the National Institute of Radiological Sciences at the National Institutes for Quantum and Radiological Science and Technology (QST-NIRS), Chiba, Japan [278]. The study for the alternative Compton camera setup is presented, with first laboratory tests including an analysis for the photon source image reconstruction and a benchmarking simulation study.

8.1 The detector components

The detector used as scatter component of the evaluated camera was provided by the group from QST-NIRS and consists of a segmented array of 22×22 individual GAGG ($Gd_3Al_2Ga_3O_{12}$(Ce)) scintillation crystals (each 0.9×0.9×6 mm^3) coupled, using an RTV sheet (Shin-Etsu Chemical., KE420 [279]) as light guide, to an MPPC SiPM array (Hamamatsu S13361-3050AE-08, total area 25.8×25.8 mm^2, 8×8 channels, 3584 pixel/ch., pixel pitch = 50 μm [140]). Whereas for the Compton camera prototype being developed at LMU in Munich the idea is to use several layers of scatter detectors in order to make use of the e$^-$-tracking capability, for the setup presented in this chapter we opted for one single layer acting as scatter component for a prompt-gamma imaging based on γ-tracking. However, in order to realize a sufficiently large scattering probability and record enough data in Compton scattering coincidence mode, the scatter layer of this setup is thicker compared to the DSSSD layers presented in the previous chapters. For comparison, their chosen thicknesses, their atomic numbers, densities and mass attenuation coefficients are summarized in Tab. 8.1. The listed mass attenuation coefficient values for silicon [148] and GAGG [280] are considered at 662 keV, since this is the energy of the radioactive source

which was used as a first test with the setup described in this chapter.

	total thickness scatt. material	atomic number (Z)	density [g/cm^3]	mass attenuation coeff. [cm^2/g]
silicon	3 mm	14	2.33	2.78 $\times 10^{-2}$
GAGG	6 mm	54.4	6.63	8 $\times 10^{-2}$

Table 8.1: Comparison between scattering component materials used in the two Compton camera arrangements studied in this thesis, silicon and GAGG, respectively. The chosen thickness of the detectors, the (effective) atomic number, the density and the mass attenuation coefficient of the corresponding scattering materials are listed.

The scattering probability at 662 keV for the scatter detector composed of pixelated GAGG crystals can be calculated to be $\sim$ 27%, compared to $\sim$ 5% corresponding to the stack of silicon detectors belonging to the LMU Compton camera prototype. The higher scattering probability is needed, since the events that can be used for a correct image reconstruction have to deposit all of the initial photon source energy in both of the two Compton camera components in order to allow for kinematically correct γ-tracking with optimum efficiency.

In Fig. 8.1 a sketch (a) and a photograph (b) of the array of GAGG crystals read out by an MPPC SiPM array is depicted. The sketch shows the structure of the detector:

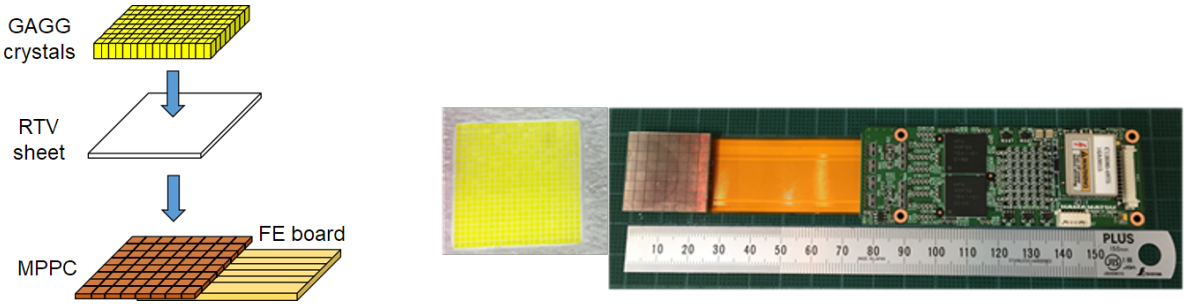

(a) (b)

Figure 8.1: Sketch of the structure of the detector used as scatterer component (a): the array of 22 $\times$ 22 GAGG crystals is read out by an MPPC SiPM array [140] with an RTV sheet placed inbetween for light guidance. (b) Photograph of the array of GAGG crystals (left) read out by the MPPC array which is shown separately in the right-hand part, connected to its frontend readout board developed by Hamamatsu [264].

the array of 22 $\times$ 22 GAGG crystals (top) is read out by an MPPC SiPM array [140] (bottom) with an RTV sheet placed inbetween for light guidance, matching the maximum emission wavelength of around 520 nm of the GAGG scintillation crystals. The RTV sheet thickness was 0.1 mm in our first measurement campaign (whose results are presented in Sect. 8.5.1) and was then optimized (to achieve better energy resolution performance and avoid saturation of the MPPC pixels), in a work conducted by S. Takyu [281], to

a thickness of 2 mm, which was used during our second measurement campaign (whose results are presented in Sect. 8.5.2).

The photograph of the detector structure in Fig. 8.1(b) shows the array of GAGG crystals and the MPPC array connected to its readout frontend board. Each GAGG crystal has a dimension of $0.9 \times 0.9 \times 6$ mm^3 and is separated from the neighboring crystals by a thin ($\sim$ 1 mm) teflon layer. The signal processing of the GAGG array was performed with customized electronics (developed by Hamamatsu [264]), providing 4 output signals derived by a resistor network and an additional sum signal. This enables an Anger logic calculation for the x and y coordinates:

$$X = \frac{-(A+C)+(B+D)}{A+B+C+D} \quad ; \quad Y = \frac{-(A+B)+(C+D)}{A+B+C+D} \tag{8.1}$$

where A, B, C and D are the four output signals, which are arranged in the formula accordingly to the coordinate system considered. In particular, the formulae shown in Eq. (8.1) refer to the output signal location and coordinate system, which are sketched in Fig. 8.2 as they were used in the experimental campaigns.

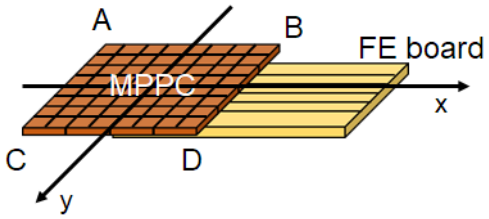

Figure 8.2: Sketch of the output signals (A, B, C and D for the Anger logic calculation) location and (x,y) coordinate system as it was considered during the experiments presented here.

The detector used as absorber component was extensively described, together with its readout system and its characterization, in the previous chapters, since it is identical to the absorber component of the Compton camera prototype being developed at LMU. It consists of a monolithic $LaBr_3$(Ce) scintillation crystal read out by a segmented multi-anode photomultiplier (PMT). For the studies presented in the current chapter, two options of PMT were used: a 256-fold segmented multi-anode PMT (H9500 Hamamatsu [206]) and a 64-fold segmented multi-anode PMT (H8500C Hamamatsu [207]). The monolithic scintillation material was chosen for this evaluation study because of its excellent energy, time and spatial resolution, which were demonstrated at LMU [195, 282, 283] and are partly presented in Chap. 6.

Figure 8.3(a) shows a sketch of the structure of the monolithic $LaBr_3$(Ce) scintillator coupled to a (256- or 64-fold segmented multi-anode) PMT; an optical grease (BC-630 [209]) was placed inbetween the two components in order to create a proper light guide (more details about this coupling can be found in Sect. 4.4.3). In Fig. 8.3(b) a photograph of the $LaBr_3$(Ce) crystal coupled (by the manufacturer) to the H9500 PMT is depicted,

whereas Fig. 8.3(c) shows a photograph of a similar $LaBr_3(Ce)$ crystal which was coupled in our laboratory to a H8500C PMT.

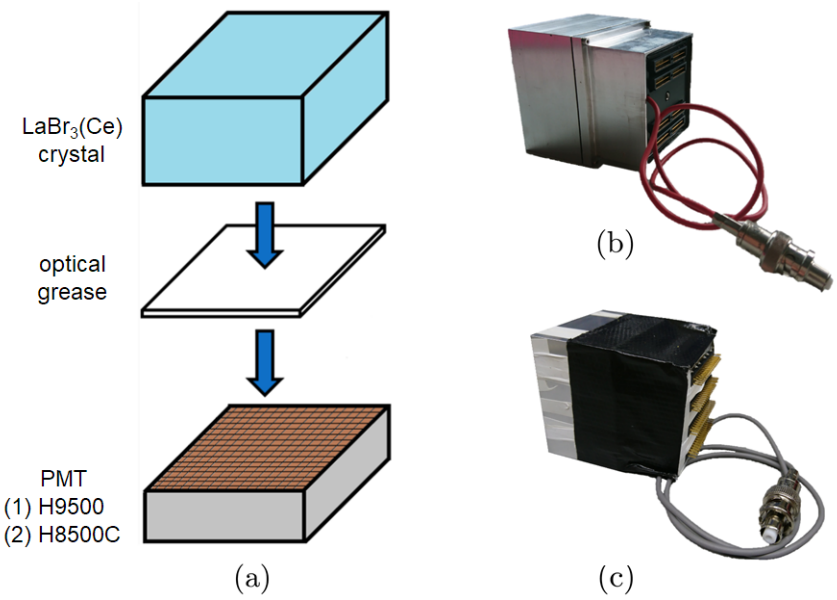

Figure 8.3: (a) Sketch of the structure of the detector used as absorber component: a monolithic $LaBr_3(Ce)$ scintillation crystal is coupled to a (b) 256- or (c) 64-fold segmented PMT with a thin layer (<1 mm) of optical grease placed inbetween as light guide coupling. Photographs of the monolithic $LaBr_3(Ce)$ scintillation crystal coupled to the (b) 256-fold segmented H9500 PMT [206] and to the (c) 64-fold segmented H8500C PMT [207].

The photon interaction positions in the monolithic absorber were determined using the k-Nearest-Neighbors (kNN) algorithm, and in particular its improved Categorical Average Pattern (CAP) version, which proved to achieve better performance (see the spatial resolution results obtained for both detector configurations used in this setup in Sect. 6.4.3 and 6.4.4). Details about the k-NN and CAP algorithms and the related procedure to characterize those monolithic scintillation detectors in view of determining unknown photon interaction positions are described in Sect. 6.3.

8.2 Setup and geometry

The functional principle of a Compton camera system was explained in Sect. 1.3.3.2 and 4.1. The Compton camera arrangement chosen for this evaluation study focuses on γ tracking primarily intended for use with low-energy primary photons ($E_\gamma < 1.5MeV$). Therefore the two detector components which have been described in the previous section, were chosen. In particular, Fig. 8.4 shows a sketch of the irradiation geometry used for the experiments that will be described in the following.

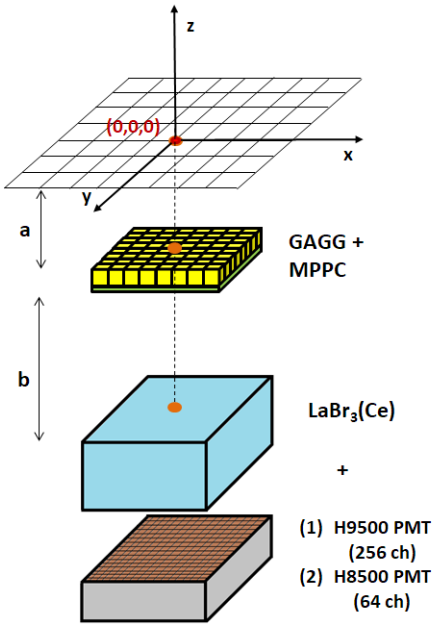

Figure 8.4: Sketch of the Compton camera setup: the GAGG and $LaBr_3(Ce)$ detectors were placed in a relative distance of b (50 mm or 200 mm). The ^{137}Cs source was placed in a distance of a (equal to 45 mm) from the scatterer component in three different positions on the (x,y,z) plane: (0,0,0), (-8,-8,0), (-16,-16,0) [mm] in the coordinate system of the setup as introduced here.

On the first level (top) a radioactive calibration source is placed. Below the scatterer component is mounted, while the absorber component is placed at the bottom level. The coordinate system is defined for the whole setup and is sketched in the figure: the origin at (0,0,0) mm is located in the center of the (x,y) plane of the photon source level, which is as well the center of all components located below. The distance along the z axis between the source and the scatterer level is defined as a in Fig. 8.4 and it was fixed during all measurements and for all simulation geometries (for both measurements campaigns) to 45 mm. The variable b defines the relative distance between the z coordinate of the front face of the scatter and the absorber components: values of 50 mm and 200 mm were investigated. In order to evaluate the performance of the camera system with respect to photon interaction position shifts, the radioactive source was placed at different positions on the (x,y) plane: during the first measurement campaign it was placed at (0,0) mm, (-8,-8) mm and (-16,-16) mm, whereas during the second measurement campaign (0,0) mm, (2,2) mm, (4,4) mm and (8,8) mm were chosen. Two radioactive calibration sources were used: a ^{137}Cs source, providings a photopeak energy of 662 keV, and a ^{60}Co source with two transitions at 1173 keV and 1332 keV. In the first measurement campaign only the configuration of the $LaBr_3(Ce)$ scintillator coupled to the 256-fold segmented PMT was studied using the ^{137}Cs source. In the second measurement campaign the study was extended to both configurations, including the use of the $LaBr_3(Ce)$ crystal coupled to

the 64-fold segmented PMT as absorber component of the Compton camera system. The response of the system was first studied at 662 keV, then further extended by using also the radioactive ^{60}Co source. The higher photon energies allow for an evaluation of the camera's imaging capabilities, in particular in the 'γ-PET' imaging mode, where in addition to the 511 keV annihilation photons, a third prompt photon is emitted in an energy range of typically 1-1.5 MeV.

8.3 Signal processing and data acquisition

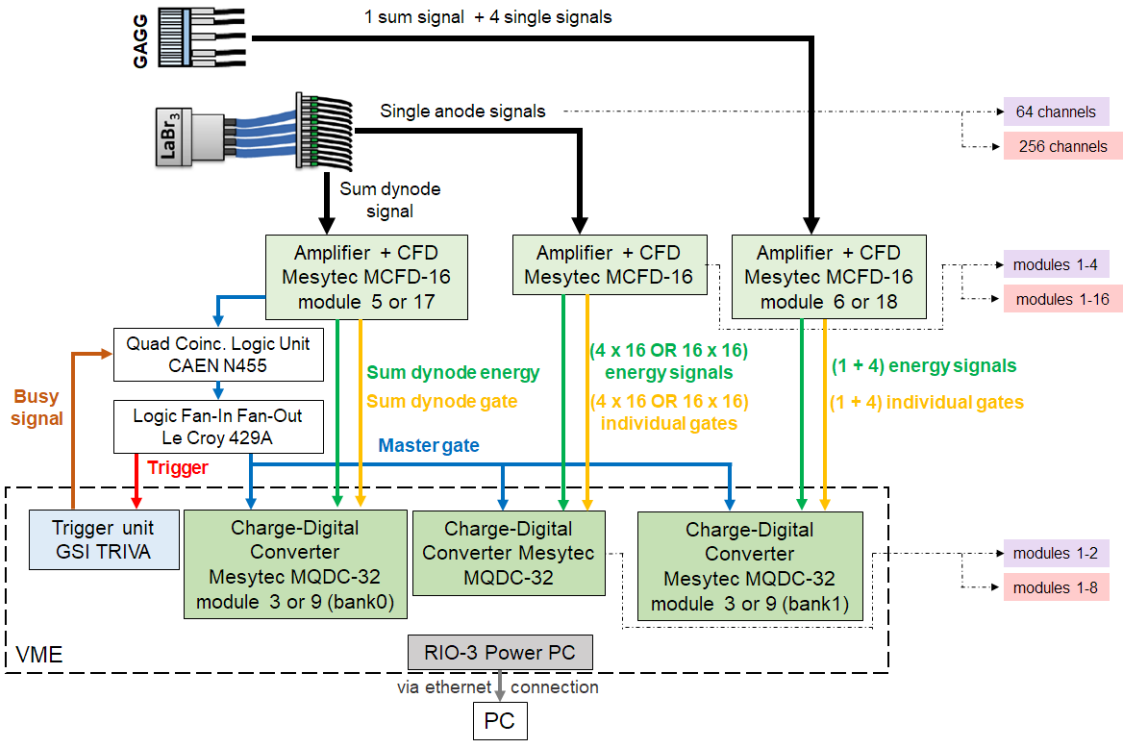

Figure 8.5: Block diagram of the readout chain for the Compton camera system composed of the pixelated GAGG-array and the $LaBr_3$(Ce) detector. The GAGG array provides a sum signal and 4 additional signals, which are used for the extraction of the interaction position by an Anger-logic calculation. The number of signals from the $LaBr_3$(Ce) detector is either 64 or 256, depending on the PMT granularity in use, plus the sum dynode signal. The PMT signals and the number of modules in use are specified in violet for the H8500C PMT and in pink for the H9500 PMT. The sum dynode signal from the absorber detector is creating the trigger for the whole system and all signals are processed by MCFD-16 [235] NIM modules and MQDC-32 [236] VME modules.

The signal processing used for the absorber component during these measurement campaigns was based on individual spectroscopy (NIM- and VME- based) electronics modules,

whose working principle was already described in Sect. 5.2.1. For the scatter component a customized frontend board (from Hamamatsu [264]) was responsible for creating four output signals derived by a resistor network plus an additional sum signal and for performing a preamplification of each signal. These signals were then sent to similar MCFD and MQDC signal processing modules (from Mesytec GmbH [226]) as they were used for the monolithic scintillator.

In Fig. 8.5 a block diagram of the signal processing and data acquisition system for the Compton camera detector arrangement composed of the pixelated GAGG crystals (read out by an MPPC array) and the monolithic $LaBr_3$(Ce) scintillation crystal (read out by a (256- or 64-fold) segmented PMT) is depicted. The four signals from the GAGG detector, which are used for the determination of the photon interaction position by an Anger-logic calculation, its sum signal, the 256 individual segment signals of the absorber detector (or 64, depending on the PMT) and the corresponding sum dynode signal, are sent to Constant-Fraction Discriminator modules (MCFD-16 from Mesytec [235]), which are individually processing the different signal channels. The 16 individual energy and time output signals of each MCFD-16 module are sent to (one bank of a 32-channel) Charge-to-Digital converter (MQDC-32, Mesytec [236]) by 13 m and 8 m long ribbon cables, respectively (see more details in Sect. 5.2.1). The signal processing and data acquisition scheme for all channels of this system are conceptually identical for the two Compton camera configurations under study with either 256 or 64 PMT segments to be processed. The readout chains for the H9500 PMT (256 channels) and H8500C PMT (64 channels) only differ in the number of electronics modules used, the related parameters settings and the cabling for the PMT signals. On the right side of the block diagram in Fig. 8.5 the number of channels and modules relevant for the two scenarios of interest is specified, i.e. for the PMT with 64 segments (H8500C) and the PMT with 256 segments (H9500), using violet and pink blocks, respectively. The flowchart of the readout chain follows the same steps for the different PMT pixelations as it was extensively described in Sect. 5.2.1 for the signal processing of the absorber detector of the LMU Compton camera prototype. The hardware trigger for the camera system was created from the fast common "OR" output generated by the MCFD-16 module that processed the PMT sum dynode signal of the absorber component. Later, during the offline analysis coincident data between absorber and scatterer were selected. The trigger signal was then sent to a Quad Coincidence Logic Unit in OR operation mode (CAEN, model N455 [238]), which accepted the busy signal from the trigger module (TRIVA 5, details on that were given in Sect. 5.3.1) as common VETO input. The length of this gate, in order to accomodate the signals from both detector components belonging to the same photon-induced event, was adjusted to be around 1 μs. Several copies of this NIM signal were created by using a Logic Fan-In Fan-Out module (Le Croy, model 429A [239]), in order to send the same signal as master gate to all of the VME modules involved in the data acquisition. Thus data were acquired when the sum dynode signal of the PMT exceeded its energy threshold, thus defining the trigger condition. The DAQ system was based on a PowerPC (RIO-3) frontend CPU in a VME crate and on the Marabou software [244], whose detailed description can be found in Sect. 5.3.1.

Detector signals	MCFD parameters						MQDC parameters
	polarity	gain	dead time	tap	width	chip delay	sensitivity jumper
(256) segments from H9500	neg.	10	300 ns	5	105 ns	5 ns	500 pC
sum dynode from H9500	pos.	1	300 ns	5	135 ns	5 ns	1.5 nC
(64) segments from H8500C	neg.	3	300 ns	5	105 ns	5 ns	500 pC
sum dynode from H8500C	pos.	1	300 ns	5	135 ns	5 ns	1.5 nC
(4) single signals from GAGG	neg.	3	300 ns	4	106 ns	75 ns	3 nC
sum signal from GAGG	neg.	3	300 ns	4	106 ns	75 ns	3 nC

Table 8.2: Configuration parameters for the MCFD-16 and MQDC-32 modules used for processing the 64 or 256 PMT segments, the sum dynode output signal of the PMT and the (4 plus 1) signals from the GAGG detector array (for details see text).

In Tab. 8.2 the parameter settings used for the MCFD-16 and MQDC-32 modules when processing the various detectors and camera arrangements are listed. The energy thresholds for the signals from both detectors were set in the MCFD-16 modules via the selection switch on the front panel. These thresholds, namely "7" for the $LaBr_3$(Ce) sum dynode signal (corresponding to ~ 7 mV), "15" for the $LaBr_3$(Ce) signals from the segments (corresponding to ~ 1.5 mV for the H9500 and ~ 4.5 mV for the H8500C PMT segments) and "13" for the GAGG signals (corresponding to ~ 4 mV), were chosen above the noise level. All parameters are selected according to the respective signals characteristics: the polarity is set to negative for all PMT segments and GAGG signals, only the sum dynode signals from the segmented PMTs are positive. The amplifier gain is selected depending on the typical amplitude of the input signal, taking into account that together with the charge-sensitivity jumper chosen for the MQDC-32 module (which defines the total amount of charge that can be integrated) the signal amplitude will fit in the available dynamic range. It should be noted that the gain values chosen for the PMT segment signals are different for the H9500 and H8500C PMT, since the segment amplitudes of the 64-channel PMT are higher due to the larger light collection and therefore need only a lower amplifier gain. The dead time in the MCFD-16 modules can be adjusted to be longer than the recovery time of the MQDC-32 modules, estimated to be 250 ns; thus, a value of 300 ns was selected as dead time for all MCFD-16 modules. The "width" parameter defines the width of the timing output of the MCFD-16 modules and it is selected according to the length of a signal from a photon event, in order to be able to gate along its full duration and to integrate the full

charge that belongs to a certain event. The delay chip is programmable (SIP7, impedance 100 Ω) and is located on the MCFD-16 module. Together with the *tap* parameter, it defines the delay for the Constant Fraction Discriminator. The delay is configurable via a front panel switch in 5 tap steps up to a maximum value which is set by the chip delay connected inside the module. This value has to be set as the time between the fraction point and the maximum of the pulse. The fraction was set to 20 % for all channels in all MCFD-16 modules; since the GAGG detector is slower (92 ns decay time [182]) compared to the $LaBr_3$(Ce) detector, delay chips of 75 ns and 5 ns were chosen, respectively. Tap values of, respectively, 5 and 4 were set, creating an effective delay for the CFD of 5 ns for the signals from the $LaBr_3$(Ce) detector and 60 ns for the signals from the GAGG detector.

8.4 Simulated and experimental data

In order to perform a source image reconstruction, energy and position information are needed from both camera detector components. These data have to be provided as input for the MEGAlib software toolkit [186], which is based on the List-Mode Maximum-Likelihood Expectation-Maximization (LM-ML-EM) algorithm. This toolkit (whose description was given in Sect. 4.2) was used for the source image reconstruction of the experimental data presented in this chapter, and for the simulated data which were produced for benchmarking the results. Since the simulation and image reconstruction work is beyond the scope of this thesis, only the main input parameters will be presented together with the results as comparison to the experimental data, which in turn will be presented in detail. More details about the simulated data and image reconstruction work in the context of this evaluation study can be found in the PhD thesis of I. Valencia [185].

In this section the parameters chosen for the production of simulated data and important for the comparison with the experimental data are presented, together with the inputs needed in order to obtain position and energy information from both simulated and experimental data.

Simulated data

In order to benchmark the experimental data, simulated data with properties as close as possible to the ones of the actual detectors in use were produced. More details about this part of the evaluation study can be found in [185], together with details about the geometry used in the MEGAlib toolkit. Here the energy and spatial resolution values are presented, which are needed as inputs in the MEGAlib toolkit in order to produce realistic simulated data from both detector components. These (energy dependent) values are listed in Tab. 8.3 and 8.4, for the scatter and absorber component used in these measurement campaigns, respectively.

In Tab. 8.3 the energy and spatial resolution values of the pixelated GAGG detector used as scatter component are specified for the analysis of the first and second measurement campaign, since an upgrade of its structure was introduced between the two measurement

		scatter component	
		1^{st} meas. campaign	2^{nd} meas. campaign
Energy resolution	662 keV	11 %	9.1 %
	1173 keV	8 %	6.9 %
	1332 keV	7.5 %	6.4 %
Spatial resolution	662 keV	1 mm	1 mm
	1173 keV	1 mm	1 mm
	1332 keV	1 mm	1 mm

Table 8.3: Energy and spatial resolution values used to simulate data for the scatter component of the 2-layer Compton camera with pixelated scatterer.

		absorber component	
		$LaBr_3$(Ce) +H9500	$LaBr_3$(Ce) +H8500C
Energy resolution	662 keV	3.5 %	3.8 %
	1173 keV	2.2 %	3.2 %
	1332 keV	2.1 %	2.7 %
Spatial resolution	662 keV	4.7 mm	3.4 mm
	1173 keV	3.2 mm	2.9 mm
	1332 keV	3.0 mm	2.9 mm

Table 8.4: Energy and spatial resolution values used to simulate data for the absorber component of the 2-layer Compton camera with pixelated scatterer.

campaigns. Specifically, as described in Sect. 8.1, the RTV light-guide sheet between the pixelated GAGG crystals and the MPPC array had a thickness of 0.1 mm in the first measurement campaign and 2 mm in the second. This upgrade allowed for improving the energy resolution achievable with this detector, as it can be seen in Tab. 8.3. The spatial resolution remains constant, also as a function of the photon energy, since it corresponds to the crystal pixelation.

In Tab. 8.4 the energy and spatial resolution of the monolithic $LaBr_3$(Ce) detector used as scatter component are specified for both scenarios of the $LaBr_3$(Ce) scintillation crystal being coupled either to the H9500 PMT (with 256 segments) or to the H8500C PMT (with 64 segments), respectively. The spatial resolution was determined by the extensive studies performed for both detector configurations which can be found in Sect. 6.3.

For both detector components the energy resolution values listed in Tab. 8.3 and 8.4 represent the optimum values obtained from experimental data (at NIRS [281] for the scatter component and at LMU for the absorber component). They were used as input for the MEGAlib software in order to realistically describe the detector properties as prerequisite to perform the source image reconstruction from simulated data.

Experimental data

The energy and position information from both detectors and for each of the recorded Compton events, i.e. acquired as coincidence between the two camera components, were extracted and used to reconstruct the 2D image of the initial source position. Since a depth-of-interaction (DOI) correction capability for these detectors was not available, the positions registered in the two detector components necessarily lie on the (x,y) middle plane of the detectors.

In particular, in order to obtain the interaction positions in the monolithic absorber, the data from the single PMT pixels of the $LaBr_3$(Ce) crystal were compared to a reference library (described in Sect. 6.3.2) using the CAP algorithm, whose procedure is described in Sect. 6.3.1. A specific 2D light amplitude library was used as a reference for each specific detector ($LaBr_3$(Ce) coupled to H9500 or to H8500C) and each specific photon energy (662 keV, 1173 keV and 1332 keV).

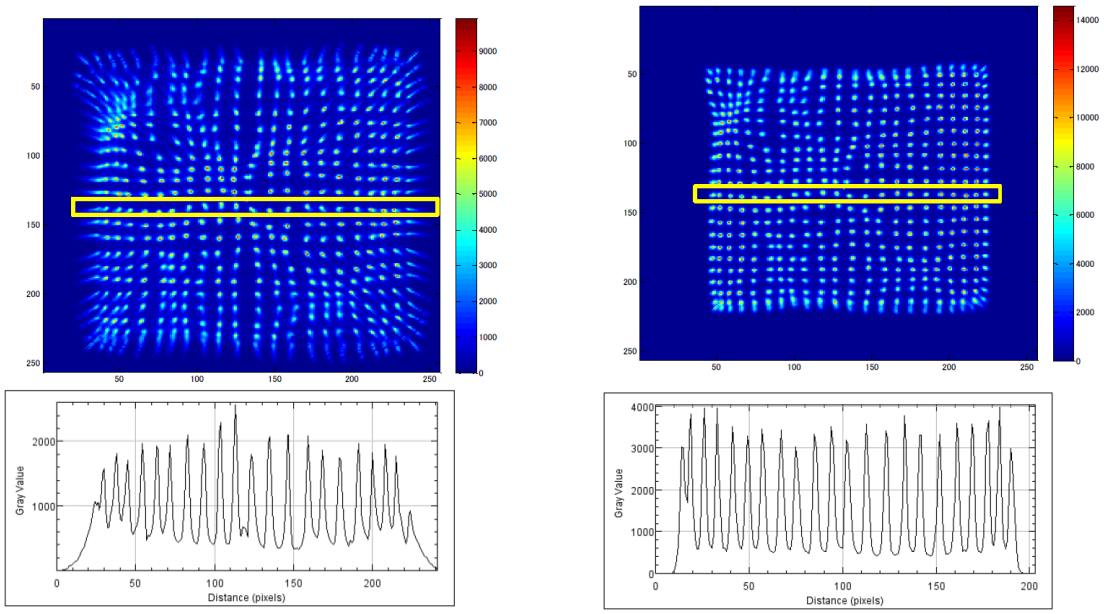

(a) (b)

Figure 8.6: Look-up table (LUT) map and x-axis projection of the pixel positions for the pixel row specified by the yellow rectangle. The LUT map is shown for the GAGG array having (a) a 0.1 mm thick RTV light-guide sheet and (b) a 2 mm RTV sheet. Both maps were obtained using a ^{22}Na point source [281].

For the scatter component consisting of pixelated GAGG crystals, the four acquired signals allowed for calculating interaction points using an Anger-logic calculation (as indicated in Eq. (8.1)), which were then compared to a LUT (look-up table) map to derive the precise x and y coordinates (which in this case correspond to a specific crystal within the GAGG array). The LUT map was obtained with a specific calibration run in which a

radioactive calibration source was placed in front of the scatter detector, which provided the trigger of the camera system. An example of a LUT map, obtained using a ^{22}Na calibration source, is depicted in Fig. 8.6 [281]. It was obtained for the GAGG detector structure having a 0.1 mm thick RTV light-guide sheet (Fig. 8.6(a), used during the first measurement campaign), while panel (b) of Fig. 8.6 displays the map for the GAGG crystals coupled via a 2 mm thick RTV sheet (used during the second measurement campaign). The improvement obtained with this upgrade is clearly visible, in particular concerning the individual pixels position resolution, where the lower part of the figure shows projections on the x axis defined by the yellow rectangle for both LUT maps. By increasing the RTV sheet thickness from 0.1 mm to 2 mm the energy resolution of this detector could be improved and a saturation of the MPPC pixels was avoided. The latter has to be taken into account due to the high light yield of the GAGG crystals of 50000-56000 photons/MeV together with the rather small pixel size (pixel pitch = 50μm).

For both measurement campaigns, as a first evaluation study, the energy information of the scatter detector was derived from the energy information of the absorber, since it provides higher precision. The relation $E_{scatt} = E_{photopeak} - E_{abs}$ could be applied, because all events used for the image reconstruction were acquired in coincidence between the two detector components and the effect of possible Compton-losses in the absorber was considered negligible.

8.4.1 Selection of data (Compton data)

In order to perform the image reconstruction of the photon source located in different positions on the (x,y) plane, the acquired raw data were processed in different steps which are summarized in the following list.

1. **2D energy plot** For each measurement a 2D plot was created, showing the total energy deposited in the absorber component on the x axis and the total energy deposited in the scatter component on the y axis. Examples of such plots will be shown in the results part of Sect. 8.5.1 and 8.5.2. This plot contains a number of events equal to the total number of triggered events in a specific measurement.

2. **Events in coincidence** In the 2D energy plot, a 2D window cut is applied on events around the photopeak energy of the source with a width adjusted to the energy resolution of the triggering detector. Thus clear and valid coincidences between the two detector components are selected, removing random coincidences generated by electronic noise and background photons. Examples of this 2D condition will be shown in the results part (Sect. 8.5.1 and 8.5.2).

3. **Creation of ASCII files** Under the filtering condition created in the previous step, an ASCII file is created for each detector component: it contains the energy amplitude values registered in each electronics channel for each event. In this step it is imperative to maintain the same event ordering in every signal channel of each detector component.

4. **Reconstruction of the interaction positions** The ASCII files created in the previous step are used as inputs for the algorithms which serve to reconstruct the photon interaction positions in the two detector components, namely:

   (a) **GAGG detector:** The Anger-logic calculation, described in Sect. 8.1, is applied using the four output signals, resulting in the (x,y) coordinates of the primary interaction positions in the scatter array. The z coordinate of the interaction positions is always fixed to be located in the center plane of the detector (considering the 6 mm thickness of the GAGG crystals).

   (b) **$LaBr_3$(Ce) detector:** The CAP algorithm is applied as it was extensively described in Sect. 6.3.1, and using as inputs the amplitudes registered in the PMT pixels for each event. From this analysis step the (x,y) coordinates of the photon interaction positions are derived. The z coordinate of the interaction positions is always fixed to be located in the center plane of the detector (considering the 30 mm thickness of the $LaBr_3$(Ce) crystal).

5. **Removal of unphysical scattering angles** From the validated set of coincident events, those events exhibiting unphysical scattering angles were discarded. Using the kinematical relation

$$cos\theta = 1 - m_e c^2 \Big(\frac{1}{E_{abs}} - \frac{1}{E_{abs} + E_{scatt}} \Big) \tag{8.2}$$

   where E_{abs} and E_{scatt} represent the energies deposited in the absorber and scatter components, respectively, θ is the Compton scattering angle of the incident gamma ray and m_e is the electron mass, the following selection condition was applied:

$$0 < m_e c^2 \Big(\frac{1}{E_{abs}} - \frac{1}{E_{abs} + E_{scatt}} \Big) < 1 \tag{8.3}$$

6. **ASCII file creation for MEGAlib** From the events fulfilling the conditions listed in the previous steps, an input ASCII file for the MEGAlib software toolkit was created: it contains, for each identified and validated Compton scattering event, the position and energy information from each of the two detector components.

8.5 Compton image reconstruction

This section presents the results obtained in the study on the imaging capabilities of the two-layer Compton camera system. The section is divided in two main parts, which correspond to the two measurement campaigns.

8.5.1 First measurement campaign

In the first measurement campaign the two-layer Compton camera was investigated by using the GAGG detector as scatterer and the $LaBr_3$(Ce) scintillation crystal coupled to

the H9500 PMT as absorber. A radioactive ^{137}Cs source with an activity of 233.6 kBq was used. The geometry for these measurements was depicted in Fig. 8.4 and explained in Sect. 8.2. The results presented in this section refer to a configuration in which the distance between the source and the scatter detector front surface was set to 45 mm, whereas the distance along the z axis between the scatterer and the absorber, was set to 200 mm. These results were presented at the IEEE NSS-MIC conference in 2017 [283].

Figure 8.7 shows the 2D energy plot comprised of the total energy deposited in the scatter and absorber detectors as input. The area encircled by the grey rhomboid defines the coincidence window which was described in Sect. 8.4.1 and applied in order to extract only coincident events following a Compton scattering interaction.

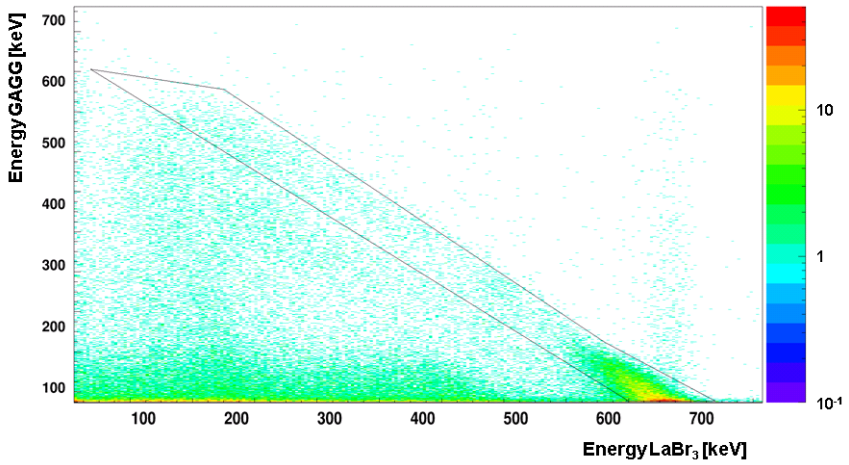

Figure 8.7: 2D energy plot between the total energy registered in the Compton camera absorber component on the x axis (which also creates the trigger for the data acquisition) and in the scatter component, as represented by the y axis. Events in Compton-scattering coincidence are located within the area encircled by the grey rhomboid.

The 2D plot in Fig. 8.7 contains data from a 4 hours measurement where the ^{137}Cs source was placed in a central position at (0,0,0) mm and the two detector components had a relative distance of 200 mm. The data set that could be extracted from the graphical coincidence cut while also fulfilling the conditions listed in Sect. 8.4.1 contained about $20{\times}10^4$ events.

In Fig. 8.8 reconstructed 2D images of the ^{137}Cs gamma source are shown, from simulated (left column) and experimental data (right column), for the source placed at (0,0,0) mm (first row), (-8,-8,0) mm (second row) and (-16,-16,0) mm (third row), respectively. The white cross-hair lines indicate the actual (x,y) source coordinates. In order to realize the same conditions for the comparison between experiment and simulation, the number of simulated events that were used to reconstruct the photon source image was kept identical to the number of events available from the experimental runs ($\sim 2 \cdot 10^4$ events for all source positions).

Each of the reconstructed images was fitted using a 2D Gaussian function in order

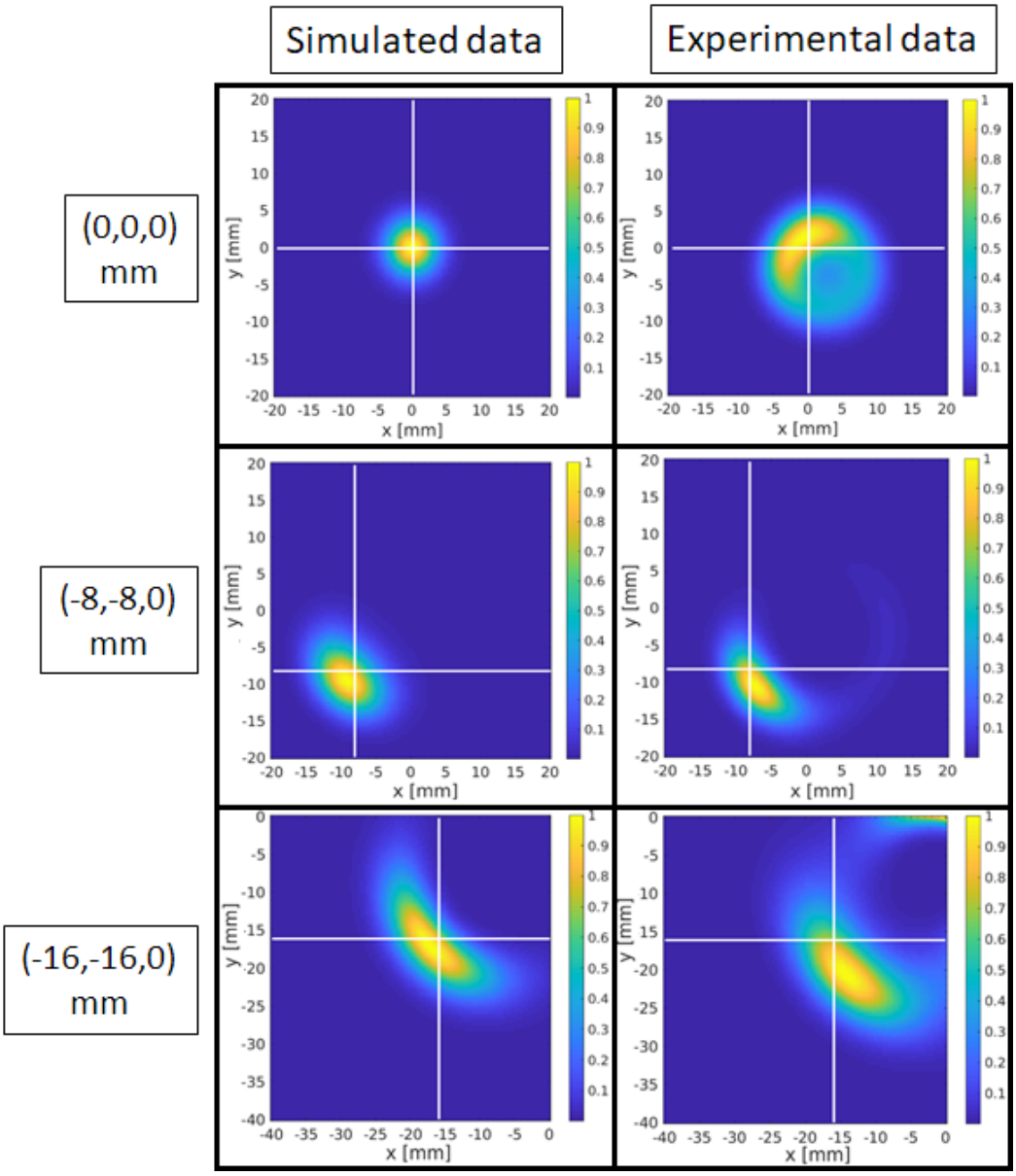

Figure 8.8: Reconstructed ^{137}Cs source position images from simulated data (left column) and experimental data (right column) for the (0,0,0) mm [283] (first row), (-8,-8,0) mm (second row) and (-16,-16,0) mm (third row) source positions, respectively. The relative distance between scatter and absorber detector was 200 mm.

to obtain the calculated (x,y) centroid source position, from which the actual (x,y) source position was subtracted, resulting in Δx and Δy values of the deviation in both dimensions. From the 2D Gaussian fit also the standard deviations σ_x and σ_y of the centroid position were also derived, in order to quantify the accuracy of the imaging capabilities of this Compton camera setup. In Tab. 8.5 these values are listed, for each source position realized

Source position	Parameter	Simulated data [mm]; °	Experimental data [mm]; °
(0,0,0) mm	x	0.17	-0.34
	y	0.20	0.76
	σ_x	2.6	4.8
	σ_y	3.7	7.2
	ARM	6.0	13.2
(-8,-8,0) mm	x	-8.84	-7.76
	y	-8.84	-8.82
	σ_x	3.4	2.5
	σ_y	4.7	4.5
(-16,-16,0) mm	x	-16.70	-15.68
	y	-16.52	-22.95
	σ_x	6.9	4.2
	σ_y	3.9	7.0

Table 8.5: Parameters derived from the 2D Gaussian fit of the reconstructed photon source position images. They refer to the geometrical arrangement described and an actual source position at (0,0,0) mm, (-8,-8,0) mm and (-16,-16,0) mm, respectively. For each source position the deviations Δx, Δy between the image centroid coordinates of simulated / experimental data and the actual source position and the standard deviations of the centroid coordinates σ_x and σ_y are listed. For the central source position also the obtained angular resolution measurement (ARM) value is listed.

in this geometrical arrangement and for images from both simulated and experimental data. For the source located at (0,0,0) mm, also the ARM (angular resolution measurement, which was defined in Sect. 4.1) is listed.

Submillimeter accuracy could be achieved in the reconstruction of the (x,y) coordinates for the (0,0,0) mm and (-8,-8,0) mm source positions. For the most eccentric source position at (-16,-16,0) mm a considerably larger deviation was observed for the y coordinate: this may be due to the fact that this position is already located beyond the (x,y) area covered by the GAGG detector with an area of 22×22 mm^2. Therefore in the second measurement campaign (whose results are presented in the next section) the source positions were chosen closer to the origin of the coordinate system.

The ARM value is prototypically shown only for the source placed in the central position, since it is affected mostly by the fixed relative distance between the detector components, rather than by the source position. For the source placed at (0,0,0) mm, a relative distance from the source to the scatterer of 45 mm and a relative distance between the two camera layers of 200 mm, the simulated data show an ARM value of 6.0°, whereas for the image reconstruction from experimental data this value amounts to a twice as large ARM = 13.2 °.

8.5.2 Second measurement campaign

In the second measurement campaign the study was extended by reading out the scintillator light of the monolithic $LaBr_3$(Ce) crystal with either the 256-fold segmented PMT (H9500 PMT) or the 64-fold segmented PMT (H8500C PMT). Furthermore, the Compton camera detector arrangement was investigated at different relative distances and at different impinging photon energies. The results presented in this section will focus on the geometry which makes use of the 64-fold segmented H8500C PMT to read out the scintillation light from the $LaBr_3$(Ce) crystal, since this PMT was proven to maintain, and even slightly improve, the spatial resolution performance achievable with the 256-fold segmented H9500 PMT (see Sect. 6.4.4). Results from one set of data that uses the H9500 PMT to read out the light from the scintillator are presented here for comparison with the results from the first measurement campaign. Images of the source position reconstruction are presented for a ^{137}Cs and a ^{60}Co radioactive source, which provide photon energies of, respectively, 662 keV, 1173 keV and 1332 keV. The images were reconstructed using the MEGAlib software toolkit, which is based on the LM-ML-EM algorithm. A number of 30 iterations was used, for reconstructing the image [185]. These results will be presented at the 2018 IEEE NSS-MIC conference.

In Fig. 8.9 reconstructed ^{137}Cs source position images are depicted, obtained from data acquired from a detector configuration with a 256-fold segmented multi-anode PMT. The fitted x and y projections of the images are also depicted, prototypically presented for this set of data. The relative distance between scatter and absorber component was 200 mm and the distance on the z axis between the source and the scatterer was kept as 45 mm. The geometrical and detector arrangement is therefore the same as the one which was set up in the first measurement campaign and thus the results can directly be compared. The decision to place the ^{137}Cs source in lateral positions not exceeding the side borders of both detectors was based on the results of the first measurement campaign. Thus the experimental results, which are prototypically presented in Fig. 8.9, refer to source positions on the (x,y) plane located at (2,2) mm, (4,4) mm and (8,8) mm.

Table 8.6 lists the (x,y) coordinates and σ values obtained from a 2D Gaussian fit of the images of Fig. 8.9, clearly improved from the results presented from the previous measurement campaign. The statistical errors from the fitting related to the (x,y) and (σ_x, σ_y) calculation are almost three orders of magnitude smaller than the actual values, and can thus be considered negligible. A 2 mm shift can be clearly resolved thanks also to reduced σ_x and σ_y values compared to the values for (8,8,0) mm source position listed in Tab. 8.5. A more detailed simulation comparison for these data can be found in [185].

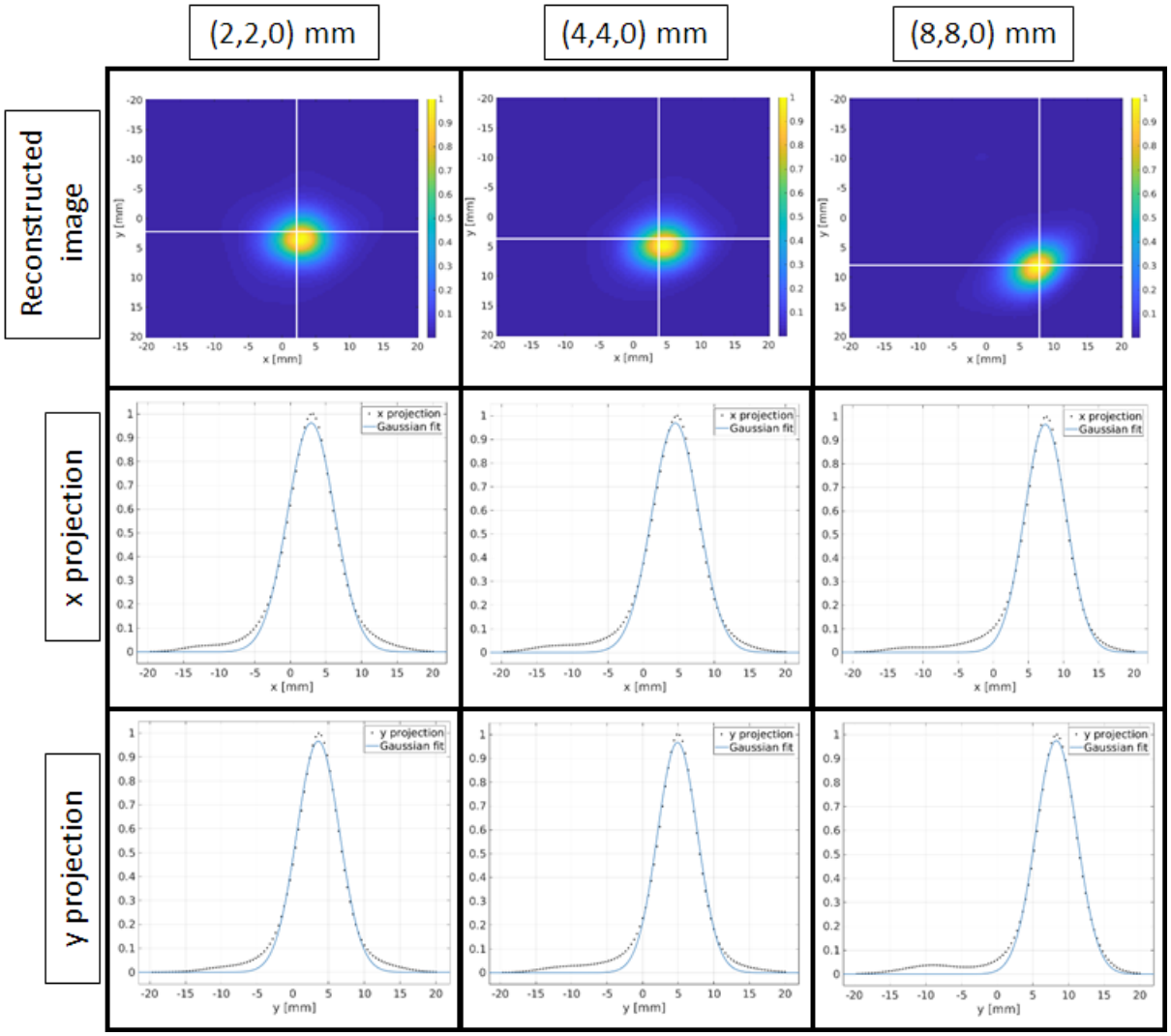

Figure 8.9: Reconstructed ^{137}Cs source position images (first row) from experimental data for the following source positions (on different columns): (a) (2,2,0) mm, (b) (4,4,0) mm, (c) (8,8,0) mm according to the coordinate system introduced in Fig. 8.4 and indicated by the white cross hair. The second and third row are the fitted x and y projections of the reconstructed images. The $LaBr_3$(Ce) absorber crystal was coupled to the H9500 PMT. The relative distance between scatterer and absorber was 200 mm, whereas the distance between source and scatter component was 45 mm.

From this comparison, since the position information constituted the most significant difference between simulated and experimental data, in addition to the upgraded composition of the GAGG array (see in Sect. 8.4), a change was also introduced in the procedure followed to retrieve the (x,y) positions in the monolithic absorber. The last correction step of the photopeak energy gate (see Sect. 6.3.2) applied to the absorber data obtained during the procedure for the spatial resolution evaluation of 2D detector scan data could

Source position	x [mm]	y [mm]	σ_x [mm]	σ_y [mm]
(2,2,0) mm	2.90	3.57	2.9	3.9
(4,4,0) mm	4.58	4.90	2.9	3.7
(8,8,0) mm	7.62	8.19	2.6	3.6

Table 8.6: (x,y) coordinates and σ values derived from the 2D Gaussian fit of the photon source position images reconstructed from experimental data. They refer to the geometrical arrangement in which scatterer and absorber had a relative distance of 200 mm and a ^{137}Cs source was placed at a distance of 45 mm far from the scatterer, in positions of (2,2,0) mm, (4,4,0) mm and (8,8,0) mm, according to the coordinate system of Fig. 8.4. The $LaBr_3$(Ce) crystal was coupled to the H9500 PMT.

be avoided. Data are acquired from a Compton setup where the events which are selected are in coincidence between the two detectors (see Sect. 8.4.1) and thus inherently are not part of the photopeak. Thus it was decided to not apply the photopeak energy gating condition to the data. Figure 8.10 shows the improvement which could be achieved: the reconstructed interaction positions in the absorber are shown for (a) data from the first measurement campaign which included the energy gate as last correction step applied to the data and (b) data from the second measurement campaign, where this last correction step was not applied. Both data sets were acquired in a Compton camera arrangement using the $LaBr_3$(Ce) scintillator coupled to the H9500 PMT as absorber and in which the relative distances between scatterer and absorber and source (^{137}Cs) and scatterer were, respectively, 200 mm and 45 mm. The plots show the front surface area of the absorber detector in the coordinate system chosen for the Compton camera setup.

It is clearly visible that the reconstructed photon interaction positions are distributed more homogeneously in Fig. 8.10(b) and therefore more in agreement with simulated data [185]. Since the unphysically spatially localized reconstructed interaction positions shown in Fig. 8.10(a) could distort the Compton angles, this finding could provide an explanation of the banana-like shape visible for the reconstructed images in Fig. 8.8, not present any more in the reconstructed images in Fig. 8.9.

This change of the procedure performed when preparing the absorber data to be reconstructed with the CAP algorithm was applied to all data acquired in different geometrical configurations. The results presented from here on refer to a detector configuration in which the monolithic $LaBr_3$(Ce) absorber was coupled to the 64-fold segmented H8500C PMT and to a geometrical configuration in which the relative distances between scatterer and absorber and source and scatterer, respectively, were 50 mm and 45 mm. This configuration was chosen in order to study also the performance of the system for an arrangement which could be suitable for prompt-γ imaging techniques (whereas the relative distance between scatterer and absorber equal to 200 mm give better performance for PET applications).

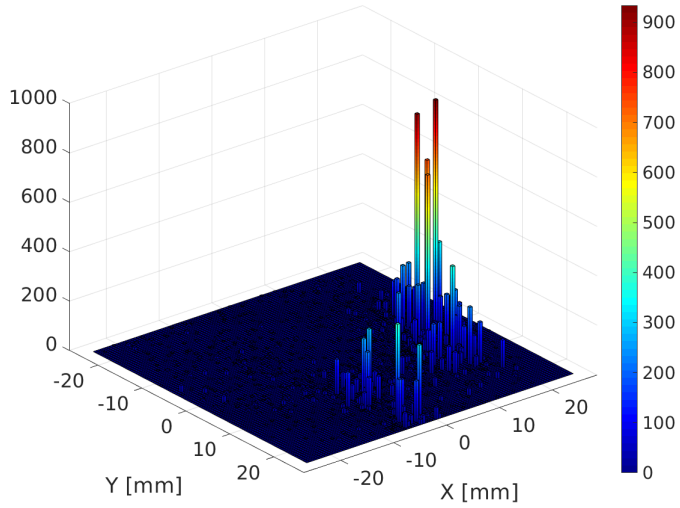

(a)

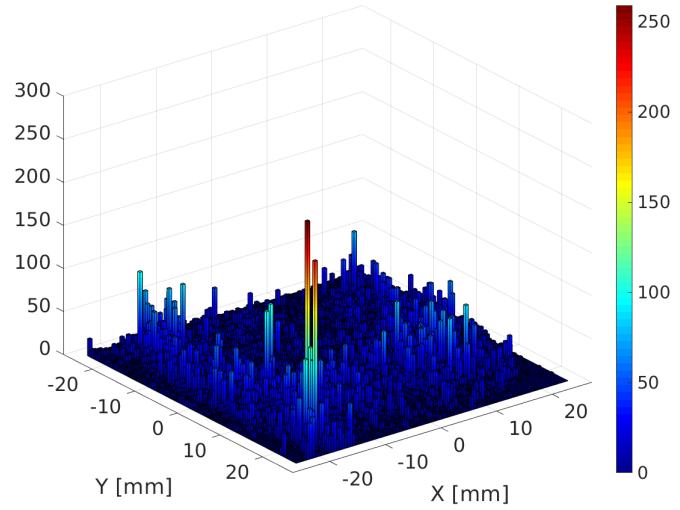

(b)

Figure 8.10: Reconstructed photon interaction positions in the monolithic $LaBr_3(Ce)$ scintillator crystal used as absorber component of the Compton camera setup. The plots refer to (a) interaction positions reconstructed including all correction steps explained in Sect. 6.3.2 and (b) all correction steps except the energy gate on the photopeak previously applied as last correction step. See the text for more details.

Figure 8.11 shows a 2D energy plot between the total energy deposited in the absorber component (on the x axis) and in the scatter component (on the y axis) for a measurement with a ^{137}Cs source. The coincidence window that was selected for the extraction of the

data to be analyzed, which contains events in Compton-scattering coincidence, is indicated by the grey polygon. The width of the polygon corresponds, within uncertainties due to the cut definition, to the energy resolution of the absorber component of the camera (which is triggering the system). The data were acquired for 4 hours and, from the total number of $\sim 16 \times 10^6$ triggered events, around 17×10^4 events could be extracted after noise subtraction and after the definition of the coincidence window.

By following the steps explained in Sect. 8.4.1, the data were given as an input to the MEGAlib software toolkit and reconstructed images of the source position could be obtained. In Fig. 8.12 the reconstructed images are presented for simulated data (left column) and experimental data (right column) for the source positions at (0,0,0) mm, (2,2,0) mm, (4,4,0) mm and (8,8,0) mm (shown in different rows).

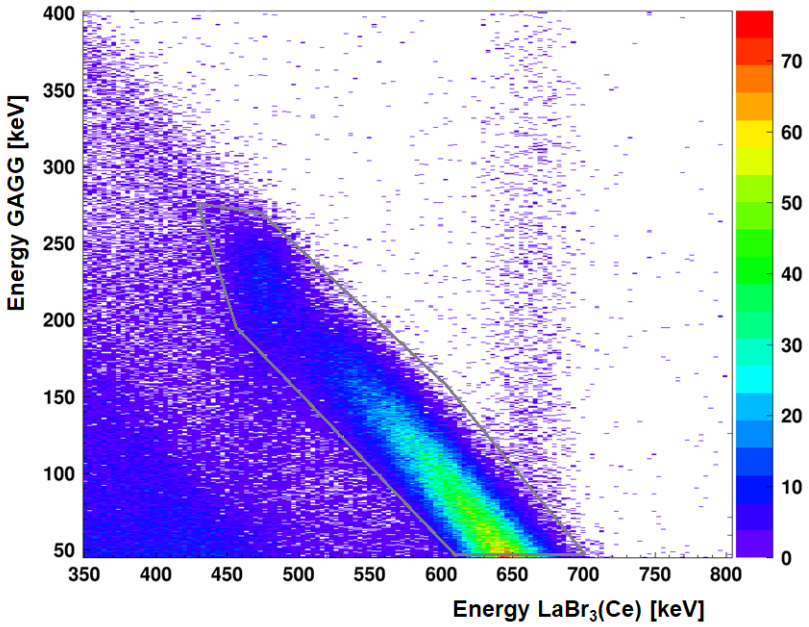

Figure 8.11: 2D energy plot between the total energy registered in the Compton camera absorber component on the x axis (which also creates the trigger for the data acquisition) and in the scatter component, as represented by the y axis. Events in Compton-scattering coincidence are located within the area encircled by the grey polygon. It refers to the geometrical arrangement in which scatterer and absorber had a relative distance of 50 mm and a ^{137}Cs source was placed in a distance of 45 mm from the scatterer at the (0,0,0) mm position.

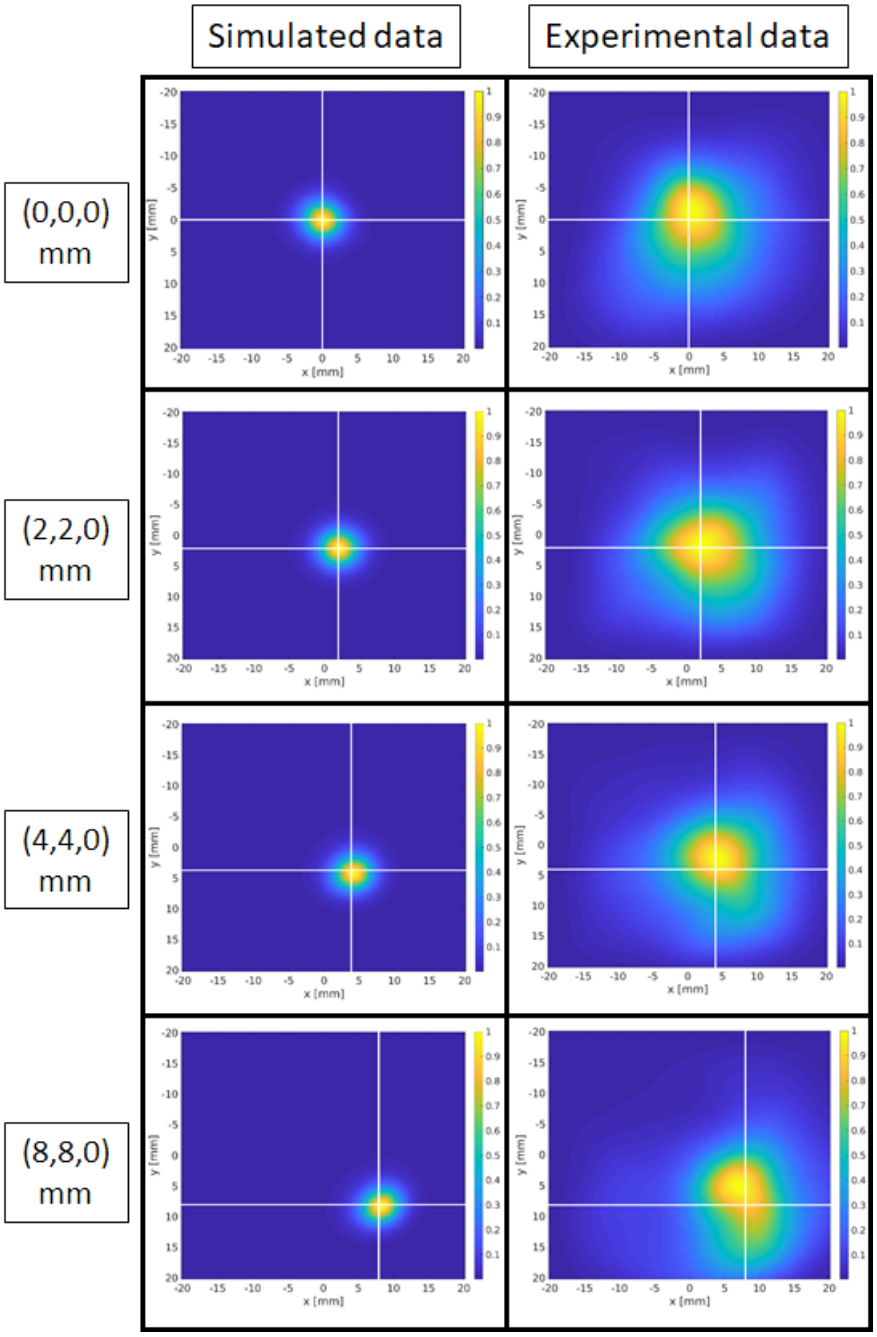

Figure 8.12: Reconstructed ^{137}Cs source position from simulated data (left column) and experimental data (right column). The images refer to a geometrical arrangement in which scatterer and absorber had a relative distance of 50 mm and a ^{137}Cs source was placed in a distance of 45 mm from the scatterer at positions located at (0,0,0) mm, (2,2,0) mm, (4,4,0) mm and (8,8,0) mm according to the coordinate system introduced in Fig. 8.4 and indicated by the white cross hairs.

The ARM was determined to be around 8° for all images obtained from simulated data and about twice this amount for all images from experimental data. Even though there is room for improvement for what concerns the precision, the accuracy which was achieved is quite satisfactory: a shift of 2 mm could clearly be observed. The (x,y) coordinates and σ_x and σ_y values which were derived from a 2D Gaussian fit of the reconstructed images in Fig. 8.12 are listed in Tab. 8.7. The statistical errors from the fitting related to the (x,y) and (σ_x, σ_y) calculation are almost three orders of magnitude smaller than the actual values, and can thus be considered negligible.

Source position	Data	x [mm]	y [mm]	σ_x [mm]	σ_y [mm]
(0,0,0) mm	Simulated	0.25	0.19	1.9	2.8
	Experimental	0.92	1.03	5.3	9.6
(2,2,0) mm	Simulated	2.31	2.27	1.9	2.9
	Experimental	3.53	2.77	6.2	9.5
(4,4,0) mm	Simulated	4.37	4.32	1.9	2.9
	Experimental	5.16	3.36	5.3	9.6
(8,8,0) mm	Simulated	8.33	8.37	1.9	2.9
	Experimental	7.99	7.96	5.0	10.8

Table 8.7: (x,y) coordinates and σ values derived from the 2D Gaussian fit of the photon source position images reconstructed from simulated and experimental data. They refer to the geometrical arrangement in which scatterer and absorber had a relative distance of 50 mm and a ^{137}Cs source was placed at 45 mm far from the scatterer, at (0,0,0) mm, (2,2,0) mm, (4,4,0) mm and (8,8,0) mm. The $LaBr_3$(Ce) crystal was coupled to the 64-fold segmented H8500C PMT.

Figure 8.13 shows a 2D energy plot between the total energy deposited in the absorber component (on the x axis) and in the scatter component (on the y axis) for a measurement with a ^{60}Co source. The selected coincidence windows are indicated by the grey polygons. Even if the two photon transitions are quite close in the energy spectrum, they had to be selected separately since the absorber data were reconstructed with two different reference libraries. The data were acquired for 6 hours and, from a total of $\sim 9 \times 10^6$ triggered events, around 23 $\times 10^3$ and 15 $\times 10^3$ events could be extracted for the 1773 keV and 1332 keV ^{60}Co lines, respectively.

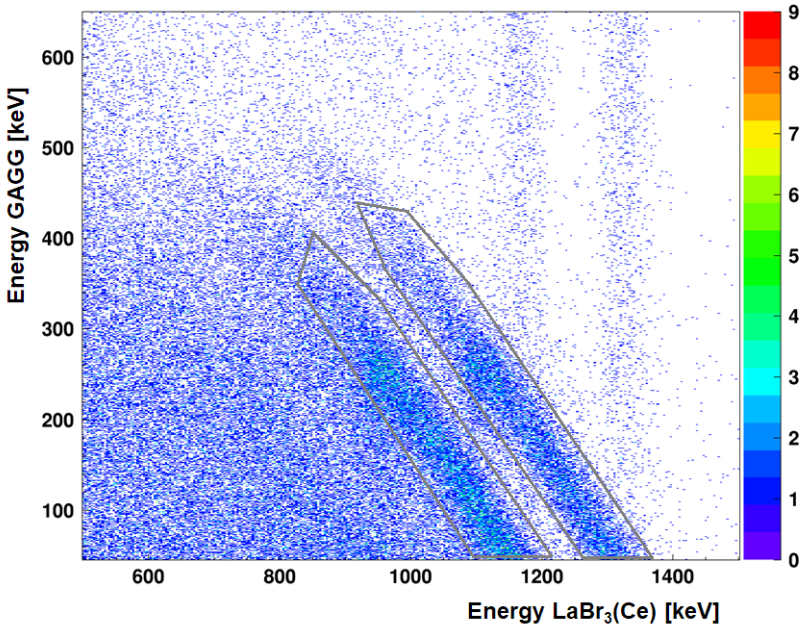

Figure 8.13: 2D energy plot between the total energy registered in the Compton camera absorber component on the x axis (which also creates the trigger for the data acquisition) and in the scatter component, as represented by the y axis. Events in Compton-scattering coincidence are located within the area encircled by the two grey polygons. The measurement scenario refers to the geometrical arrangement in which scatterer and absorber had a relative distance of 50 mm and a ^{60}Co source was placed at a distance of 45 mm far from the scatterer located at the (0,0,0) mm position.

The corresponding reconstructed images are depicted in Fig. 8.14: from simulated data (left column) and experimental data (right column) and for source positions located at (0,0,0) mm, (2,2,0) mm, (4,4,0) mm and (8,8,0) mm, which are shown in different rows and indicated by the white cross hairs. The good quality of the reconstructed point source positions in Fig. 8.14 in turn is a direct indicator on the quality of the photon interaction position reconstruction in the monolithic absorber crystal.

The ARM was found to be around 6° for all images obtained from simulated data and again about twice this amount for all images from experimental data, reflecting an expected

Source position	Data	x [mm]	y [mm]	σ_x [mm]	σ_y [mm]
(0,0,0) mm	Simulated	0.24	0.20	1.8	2.5
	Experimental	-0.44	1.76	5.5	2.3
(2,2,0) mm	Simulated	2.22	2.16	1.7	2.5
	Experimental	1.80	3.29	3.1	5.2
(4,4,0) mm	Simulated	4.24	4.19	1.7	2.5
	Experimental	3.46	5.68	5.9	3.3
(8,8,0) mm	Simulated	8.10	8.22	1.7	2.5
	Experimental	6.74	8.96	6.1	3.3

Table 8.8: (x,y) coordinates and σ values derived from the 2D Gaussian fit of the photon source position images reconstructed from simulated and experimental data. They refer to the geometrical arrangement in which scatterer and absorber had a relative distance of 50 mm and a ^{60}Co source was placed in a distance of 45 mm from the scatterer at positions located at (0,0,0) mm, (2,2,0) mm, (4,4,0) mm and (8,8,0) mm. The $LaBr_3$(Ce) crystal was coupled to the 64-fold segmented H8500C PMT.

improvement with respect to the results using a ^{137}Cs source because of the higher initial photon energy and the corresponding better spatial resolution of the absorber component. The smaller ARM leads to smaller σ values, which were determined from the 2D Gaussian fit and which are listed in Tab. 8.8 together with the (x,y) coordinates calculated from the fit. This provides again a good accuracy, since the 2 mm shift could nicely be observed. The statistical errors from the fitting related to the (x,y) and (σ_x, σ_y) calculation are again almost three orders of magnitude smaller than the actual values, and can thus be considered negligible.

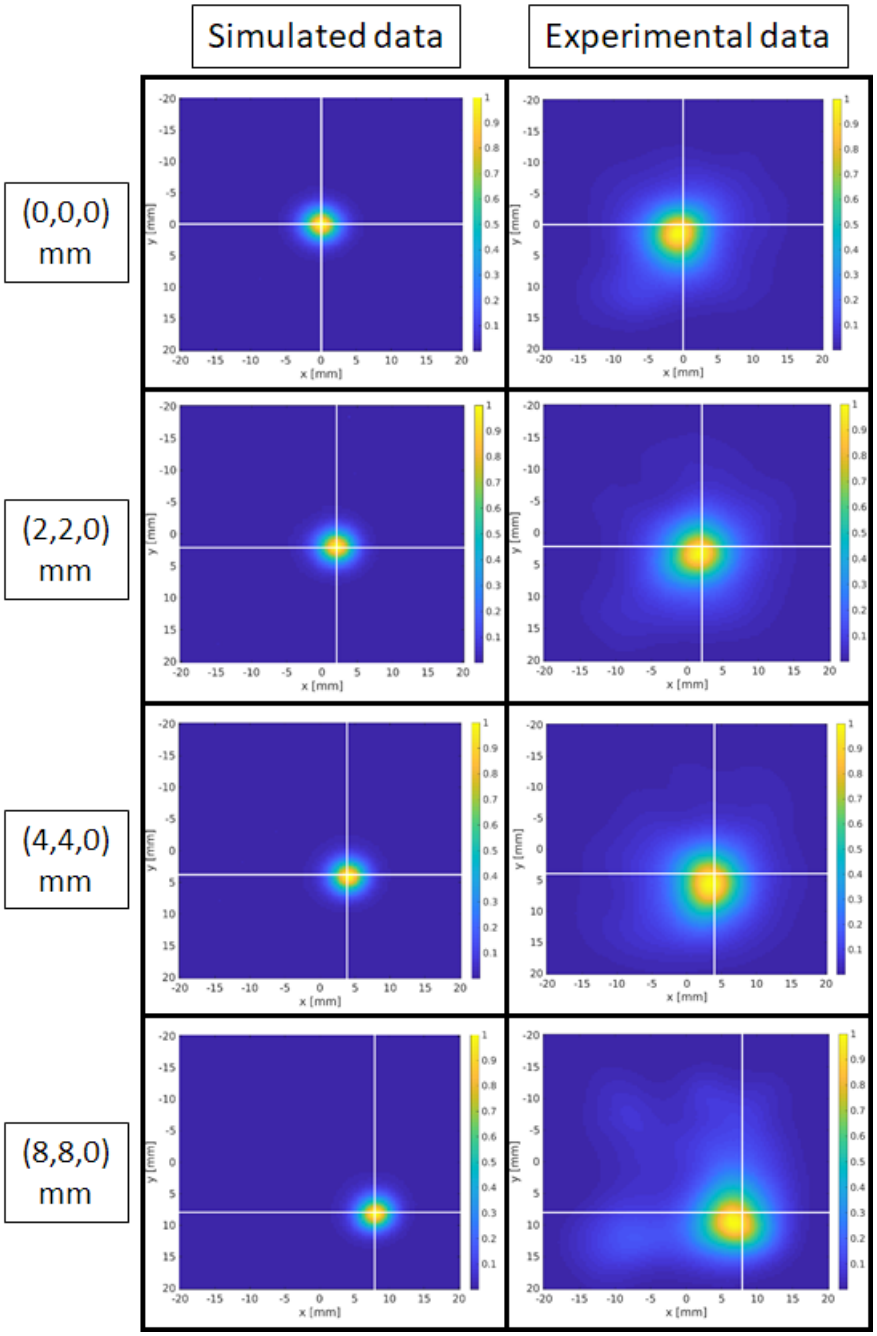

Figure 8.14: Reconstructed photon source positions from simulated data (left column) and experimental data (right column). The images refer to a geometrical arrangement in which scatterer and absorber had a relative distance of 50 mm and a ^{60}Co source was placed in a distance of 45 mm from the scatterer at positions located at (0,0,0) mm, (2,2,0) mm, (4,4,0) mm and (8,8,0) mm, relative to the coordinate system introduced in Fig. 8.4 and indicated by the white cross hairs.

Furthermore, the newly purchased and implemented signal processing and data acquisition system (described in Sect. 5.2.2 and 5.3.2) was tested with this setup as well. Even though this readout system could also allow for a trigger setting on the scatterer component, for a direct comparison with the firstly used readout system, the trigger on Compton events was derived from the absorber and not the scatterer component. Figure 8.15 shows the 2D energy plot between the energy in the absorber (x axis) and in the scatter component (y axis), in which a clear correlation between the two can be observed on a diagonal axis. This measurement corresponds to the geometrical arrangement in which scatterer and absorber had a relative distance of 50 mm and a ^{137}Cs source was placed in a distance of 45 mm far from the scatterer at the (0,0,0) mm position, as for the data which were shown in Fig. 8.11.

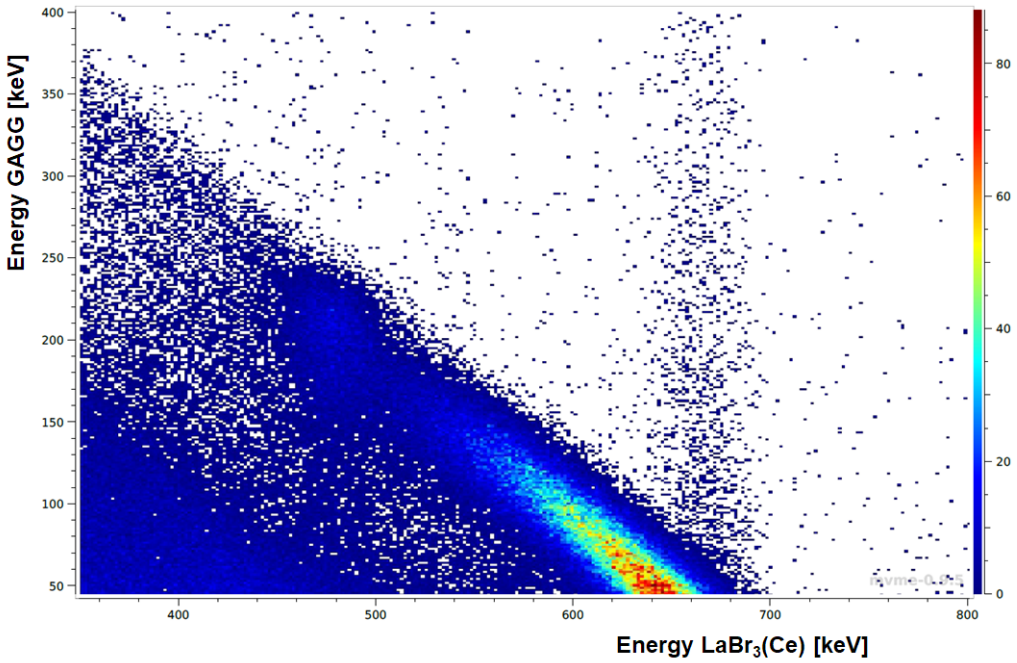

Figure 8.15: 2D energy plot between the total energy registered in the Compton camera absorber component on the x axis (which also creates the trigger for the data acquisition) and in the scatter component, as represented by the y axis. Events in Compton-scattering coincidence are clearly visible on a diagonal axis. It refers to the geometrical arrangement in which scatterer and absorber had a relative distance of 50 mm and a ^{137}Cs source was placed in a distance of 45 mm far from the scatterer at the (0,0,0) mm position. Data were acquired with the newly purchased signal processing and data acquisition system from Mesytec [230].

A couple of differences underlying the data sets presented in Fig. 8.11 (and Fig. 8.13) should be pointed out as further potential improvements:

- The signals of the absorber component were processed and acquired using the new

MMR frontend board [231], which is much more compact than the "old" scintillator readoutbased on the MCFD-16 [235] and MQDC-32 [236] modules. The total energy deposited in the absorber, which can be found on the x axis of Fig. 8.15, was obtained from a software sum of the PMT pixels processed by the MMR board and not from the PMT sum dynode output as shown in Fig. 8.11, and still the 2D energy plot shows a clear Compton correlation between the two detectors, which can be defined on the diagonal axis of the plot.

- With the use of the new data acquisition system the acquisition rate can be improved. The change in the case presented here is not too impressive, since with the limited activities of laboratory radioactive sources the dead time in either of the two systems is not so high, but the new electronics could already be observed to acquire the same amount of data in half of the measurement time.

8.6 Discussion

The evaluation study presented in this chapter led to a proof-of-principle of the functionality of the Compton camera setup which was presented. Different geometrical configurations were tested and led to sub-millimeter accuracy, with improving performance at higher photon energies. The spatial resolution achieved with this Compton camera setup is ~ 2 mm for shifts of point sources. With these achievements as a basis, further systematic studies should be perfomed and further improvements with this setup should be evaluated. The system should be tested online and at different γ energies. Depending on the geometrical arrangement selected, further studies could go in the direction of an application for prompt-γ or γ-PET [284] imaging techniques.

CHAPTER 9

Conclusions and future perspectives

This chapter is intended to conclude this thesis with a discussion on the contents and achievements pursued during the work presented in the previous chapters, in view of the next steps envisaged for the project. The current status of the LMU Compton camera is reviewed, from the detectors' performance optimization to the data acquisition system upgrade, both characterized offline and online in order to delineate the conditions for a Compton imaging scenario. The satisfactory results obtained with the alternative Compton camera setup with a mono-layer scatter component are also summarized. On the basis of the conclusions which can be drawn from the studies conducted in this thesis, future perspective for Compton imaging applicabilities are discussed and delineated, together with next steps which can be defined within the project.

9.1 Conclusions

Thanks to the characteristic Bragg peak, which gives a well-localized depth-dose deposition of ion beams in tissues at the end of their stopping range, hadron therapy is continuously gaining interest over the conventional photon-based radiation therapy as a cancer treatment modality. However, unavoidable uncertainties in the determination of the ion beam range force to add safety margins around the target volume and, in order to reduce adverse effects to the adjacent healthy tissues, there is a need to ensure that the maximum dose deposition is released in the targeted volume. A precise and preferably online ion beam range verification is thus a mandatory prerequisite to guarantee the success of the treatment. Several research groups are evaluating different techniques for a real-time beam range monitoring. These diverse experimental approaches aim to provide precise information on the Bragg peak position: the approach object of this thesis is based on the detection of prompt-γ rays emitted along the ion beam path, which originate from nuclear interac-

tions with the patients' tissues. Therefore, the main objective of this thesis was to develop and upgrade an (ultimately) online imaging system prototype based on a Compton camera detector arrangement towards the needs of a clinical application. A Compton camera detector prototype was characterized, consolidated and commissioned with both a multi-layer and a mono-layer scatter component. The Compton imaging of the second design is based on γ-tracking, while the first design allows to track the Compton electrons as well. The electron-tracking capability motivated the LMU Compton camera design [121], which consists of a stack of six layers of double-sided silicon strip detectors (DSSSD, each $50 \times 50 \times 0.5$ mm^3 with 128 strips on each side having a pitch size of 0.39 mm) acting as scatter (tracker) component, while the absorber component is formed by a monolithic $LaBr_3$(Ce) scintillator coupled to a segmented position-sensitive multi-anode photomultiplier tube (PMT). The PMT segments are processed individually, using spectroscopy electronics: the energy and time signals are digitized in a VME-based charge-to-digital converter and time-to-digital converter, respectively. In order to reduce part of the system complexity, the initially applied 256-fold segmented PMT (H9500, Hamamatsu) was replaced by a 64-fold segmented PMT (H8500C, Hamamatsu). With this scenario, the spatial resolution was determined using the Categorical Average Pattern (CAP) improved version of the k-Nearest Neighbors (k-NN) algorithm, which consists of comparing each 2D light amplitude representing a specific photon interaction position to photopeak events contained in a previously acquired 2D light amplitude reference library. The spatial resolution performance was evaluated using the so-called "leave-one-out" method and introducing the Categorical Gaussian Distributed Replacement algorithm (CGDR), which takes care of substituting the non-physical "blank pixels" permitting an improvement of the results from all PMT configurations. A similar or even superior performance for the lower PMT granularity scenario was demonstrated. A sub-3mm spatial resolution was experimentally achieved, thus reaching the design specifications defined in [121], which were already reached by creating a 64-channels PMT granularity, obtained by software summation from the data experimentally acquired with the 256-fold segmented PMT. The spatial resolution was determined at different photon energies, corresponding to the available collimated radioactive sources which were used to create the reference libraries: at ^{137}Cs energy a value of 3.4(1) mm was obtained, while at 1173 keV and 1332 keV ^{60}Co photopeaks the spatial resolution was improved to a value of 2.9(1) mm, thus maintaining the same trend as a function of the photon energy as the one already observed for the monolithic $LaBr_3$(Ce) coupled to a 256-fold segmented PMT. The same CAP algorithm was also adopted to extract the interaction positions of unknown Compton-scattered photons in the monolithic absorber when used in a Compton setup arrangement. Thus the reconstruction time is an essential feature in view of an envisaged (ultimately) real-time application: the present situation together with ideas to improve the speed of this process will be later discussed. Furthermore, the characterization of the spatial resolution performance in typical prompt-gamma rays energy ranges is needed: the availability of a related 2D light amplitude reference library is required, calling for the availability of a highly collimated photon beam of specific energies between 3 and 6 MeV, as discussed later.

The DSSSD modules, whose signals were previously processed by the Gassiplex ASIC-

based electronics, were during the work of this thesis extensively characterized in order to determine the limitations which were found to be partially imposed by their internal structure. The energy resolution could be determined at 5 MeV using a triple α-source (^{239}Pu, ^{241}Am, ^{244}Cm) revealing a full-width-at-half-maximum (FWHM) of 74 keV and pointing to the dead layer as the first property to be improved. The interstrip resistance values, obtained from measurements on the p- and n-side of the detectors, revealed a poor n-strip separation (~ 5 kΩ), which caused a high noise level, initially attributed to the first-generation electronics based on the Gassiplex chip, which did not allow for a separation of the low energy signals from the noise level on the n-side signals. This calls for an upgrade of the DSSSD detectors, which is examined later. Parallel to that, the limitations imposed by the DSSSD signal processing and data readout were also determined and the possibility to upgrade the readout system was evaluated by considering the available options on the market, able to process the 1536 channels from the six DSSSD detector modules. The ASIC-based GET system solved part of the limitations imposed by the Gassiplex system but on the other hand it presented other drawbacks for our application, such as mandatorily storing the full signal trace and thus leading to the need of a considerable amount of memory and an increase of the dead time. The solution that could best fit to our specifications was found in close collaboration with an industrial partner: the MMR board, a more flexible and higher performing electronics based on discrete components, processing both signal polarities and able to provide a trigger to the system. Furthermore, the upgrade of the signal processing and data acquisition was extended to the whole Compton camera setup, adapting the new frontend electronics designed initially for replacing the outdated ASIC-based modules of the scatterer also to the signal properties of the absorber scintillator and its segmented readout. The data streams from the two Compton camera components were merged. The detector components were enclosed in an upgraded newly designed version of Faraday cage, made of aluminum and with the inclusion of an active cooling device, which enabled a decrease of the DSSSD leakage current during online measurements. The first measurements with the upgraded full Compton camera system readout were performed offline and online, demonstrating the full compliance with the detector specifications while preserving the detector system's performance. The online measurements were executed at the Tandem accelarator in Garching, making use of a 20 MeV continuous proton beam and a 20 MeV pulsed deuteron beam, the latter allowing for time performance evaluation, hitting water and PMMA targets. The data throughput handled by the VME-based controller in use (Struck Innovative Systeme, model SiS3153) can reach up to 35 MB/s for each VME-based data receiver (VMMR module), which collects the data via optical links from the boards. This turns into a higher achievable data rate, which, in combination with the possibility to trigger on the scatter component of the system, allowed for an improvement of ~ 3 orders of magnitude in the ratio of acquired events in Compton coincidence from the system. The aim of these tests was to validate the new signal processing and data acquisition system at photon energy ranges and data rates of interest in the envisaged clinical scenario. However, taking into account the findings demonstrated for the DSSSD components, only the p-strip signals from these detectors were read out: a full data analysis and Compton imaging capability evaluation will be thus performed once an upgraded

version of DSSSD detectors will be installed in the system.

The investigated alternative Compton camera setup consisted of a detector arrangement based on a mono-layer scattering component. Given the excellent performance demonstrated for the monolithic $LaBr_3$(Ce) scintillator, the same detector was used as absorber component, whereas the scatter component of the system was replaced with one layer of pixelated 22 × 22 GAGG scintillator crystals (each of them 0.9 × 0.9 × 6 mm^3 separated by a 0.1 mm teflon layer) read out by an MPPC SiPM array. A proof of principle study was carried out using ^{137}Cs and ^{60}Co laboratory sources, revealing a system resolution of 2 mm, with a sub-mm accuracy. The angular resolution measure (ARM) value was found to be $\sim 8°$ at ^{137}Cs energy and $\sim 6°$ at ^{60}Co energies for simulated data, and around twice this amount for experimental data. The trend of improving performance as a function of the photon energy reflected the spatial and energy resolution performance of the monolithic $LaBr_3$(Ce) detector, which improves with increasing photon energy. The imaging capability of the system was evaluated in different geometrical scenarios, as a basis for further studies in the framework of a multi-modality imaging system, which will be discussed later.

9.2 Future perspectives

This section is dedicated to the future perspectives and envisaged plans which can be delineated for the Compton camera prototype setups which were characterized, consolidated and commissioned in this thesis work.

Speed performance of the position reconstruction algorithm for the monolithic scintillator

The ultimate goal of this project is to develop an imaging system, based on events acquired in Compton coincidence between two detector components, which can monitor the ion beam range online during the irradiation of a patient (in this case a small animal, given the field of view chosen for the system). Given this requirement, all procedures needed in order to retrieve position and energy information from the detector components and serving for the Compton imaging reconstruction, have to be performed online, without any postprocessing. The most time consuming analysis procedure is certainly the one needed for retrieving the photon interaction positions in the monolithic absorber. The k-NN algorithm is based on eventwise comparison and makes use of a "look-up-table" consisting of a reference library which contains 2D light amplitudes for 100 × 100 irradiation positions, regularly chosen with a step size of 0.5 mm, in order to scan the complete surface of the monolithic detector. Since each irradiation position contains at least 300 photopeak events and each event consists of a 2D light amplitude distribution built from the 256 or 64 PMT channels, the amount of data to be compared is quite relevant. The present situation requires a processing time, per photon interaction position reconstructed, of about 6 s and 2 s for a 256 and 64 PMT granularity scenario, respectively. An improvement was already achieved in terms of required processing memory (from $\sim 10^2$ GB to ~ 1 GB for the processing

of a full reference library), which permits to avoid the use of high performance computers (HPCcluster) and to pursue a more automatic procedure. However, for what concerns the processing time, considerable improvements could not be achieved. Given the structure of the data, new perspectives appeared in the direction of, for example, Deep Learning or Artificial Neural Network methods. In order to allow for first tests in this direction, the ^{137}Cs reference library for the $LaBr_3$(Ce) coupled to the H8500C PMT was acquired with the requirement of 600 events per position, since a large fraction of the available data will be needed for the training part of such networks. First steps in this direction are being performed, but are not part of this PhD thesis.

Realistic scenario for the incoming radiation in the monolithic absorber

So far, the method for determining the photon interaction position in the monolithic absorber, is based on an event by event comparison to a set of "ideal" data. Since the events contained in the 2D light amplitude reference library were obtained from a highly collimated (with a collimator opening of 1 mm) photon source hitting the detector's surface perpendicurarly, this procedure does not take into account possible incident angles different to 90° of the incoming photon, whose interaction position has to be reconstructed. In addition, the events acquired in coincidence from a Compton camera setup do not contain photopeak events, which on the other side are contained in the reference library. This may contribute to the uncertainties obtained in the interaction position reconstruction procedure and could be partly solved by setting up a calibration procedure which takes into account different incident photon angles as well. The second remark emerged when it was observed that the interaction positions reconstructed from unknown photon events acquired in a Compton setup were more homogeneously distributed when the last correction step applied to the raw data (see Sect. 6.3.2) was avoided. Furthermore, from simulation studies illustrated in [185], it was observed that with the present scatter component thickness, a considerable amount of high energy (> 1 MeV) electrons can reach the absorber. In addition, it can also happen that more than one photon is hitting the absorber in the same event time window. Since presently a set of reference 2D light distributions is not existing for this scenario, the acquisition of a set of reference data in a controlled (two-photons) or (electron plus photon) scenario is envisaged.

Spatial resolution of the monolithic scintillator at prompt-gamma ray energies

The spatial resolution of the monolithic $LaBr_3$(Ce) was extensively characterized for photon energies of 662 keV, 1173 keV and 1332 keV, which correspond to the photopeak energies of ^{137}Cs and ^{60}Co laboratory sources, respectively. Since the prompt-γ ray energy range of interest in the clinical scenario is between 3 and 6 MeV, further studies for the spatial resolution evaluation should be performed at higher energies. The unavailability of

laboratory sources in this energy range and the requirement of having a highly collimated photon beam makes this setup quite challenging. In [139] a measurement in this regard was envisaged through the GAMS6 setup at the Institute Laue-Langevin (ILL) in Grenoble, France. Unfortunately, the conditions for this measurement turned out to be not feasible due to the high photon background at lower energies, not allowing for the required collimation. This measurement may become possible at the upcoming γ-beam facility of the Extreme Light Infrastructure-Nuclear Physics (ELI-NP) facility at Bucharest [271], which will become operational in almost two years. An preservation or even further improvement of the spatial resolution is expected at higher energies, which, being considerably above the energy threshold for pair creation, should present a more confined light distribution.

Detectors' optical alignment

The newly designed Compton camera Faraday cage (see App. C) serves, in addition to the shielding functionality, also as a mechanical framework for the detector components which are mounted inside. However, the detector components are so far mounted on a millimetric accuracy scale using aluminum profile bars. Given the highly segmented DSSSD detectors and the relatively small field of view required for a small-animal irradiation scenario, there is therefore the need to improve the accuracy of the system arrangement to the order of a sub-mm scale. The foreseen plan is to implement a laser positioning system which would include a motorized translation stage for the detector positioning. This work will be included in the PhD thesis of T. Binder.

Compton camera efficiency

Given the limitations which were determined from the internal structure of the DSSSD modules, a new design for these detectors is required. A new stack of DSSSD detectors should maintain a high resistivity (> 10 kΩ cm) in order to avoid a high dark current in the silicon detectors and should possess improved interstrip properties. Furthermore, the detector thickness should be considered: a stack of six DSSSD, corresponding to a total thickness for the scattering material of 3 mm, is related to an ~ 1.5 % scattering probability for the photon events that should be detected by the Compton camera setup. This was a compromise dictated by the unavailability of thicker DSSSD detectors that could provide the required properties. A simulation study on the optimum number and thickness of the scattering layers in view of an optimized camera efficiency can be found in [185], revealing the preference for 1 mm DSSSD detectors. Since this thickness is still not available with the required quality, a compromise seems to be the use of 0.75 mm thick detectors instead of the 0.5 mm thick ones presently part of the LMU Compton camera. These can be purchased from CiS [191] based on a high resistivity material and foreseeing improved interstrip properties.

Multi-modality Compton camera

A characterization study performed for a second Compton camera setup based on γ-tracking in different geometrical configurations opened the discussion for different future applications. The camera showed a satisfactory spatial resolution of 2 mm with a relative detector distance of 50 mm and 200 mm, at different photon source energies. The performance of the camera improves with an increasing photon energy, with an angular resolution measure (ARM) comprised between $\sim 6°$ and 8°. Next steps of evaluation are being considered in the direction of a multi-modality device, which could combine the detection of PET and prompt-γ signals [4, 284]. With the combination of PET and Compton imaging, the detection of a single decay would in principle be enough to localize the source position. Large sensitivity could for example be expected for triple gamma emitters, such as ^{44}Sc (which emits a pair of 511 keV photons and a 1157 keV gamma ray almost simultaneously): the coincidence detection of a pair of 511 keV photons locates the source position along a line-of-response (LOR) and the source position can be then identified as one of the two intersection points of the LOR with a Compton cone after measuring the 1157 keV γ-ray.

APPENDIX A

List of publications and conference contributions

List of publications

- **Liprandi S.**, Takyu S., Aldawood S., Binder T., Dedes G., Kamada K., Lutter R., Mayerhofer M., Miani A., Mohammadi A., Nishikido F., Schaart D.R., Valencia Lozano I.I., Yoshida E., Yamaya T., Parodi K., Thirolf P.G.: *"Characterization of a Compton camera setup with monolithic $LaBr_3(Ce)$ absorber and segmented GAGG scatter detectors"*, in Proc. of IEEE Nuclear Science Symposium and Medical Imaging Conference (2017), to be published

- **Liprandi S.**, Mayerhofer M., Aldawood S., Binder T., Dedes G., Miani A., Schaart D.R., Valencia Lozano I.I., Parodi K. Thirolf P.G.: *"Sub-3mm spatial resolution from a large monolithic $LaBr_3(Ce)$ scintillator"*, Current Directions in Biomedical Engineering 3(2):655-659 (2017), DOI: https://doi.org/10.1515/cdbme-2017-0138

- Aldawood S., Thirolf P.G., Miani A., Böhmer M., Dedes G., Gernhäuser R., Lang C.,**Liprandi S.**, Maier L., Marinšek T., Mayerhofer M., Schaart D.R., Valencia Lozano I., Parodi K.: *"Development of a Compton Camera for prompt-gamma Medical Imaging"*, Radiation Physics and Chemistry (2016),
DOI: 10.1016/j.radphyschem.2017.01.024

- Aldawood S., Bortfeldt J., Böhmer M., Castelhano I., Dedes G., Enghardt W., Fiedler F., Gernhäuser R., Golnik C., Helmbrecht S., Hueso-González F., van der Kolff H., Kormoll T., Lang C., **Liprandi S.**, Lutter R., Maier L., Marinšek T., Pausch G., Petzoldt J., Pocevicius M., Römer K., Valencia Lozano I.I., Schaart D.R., Parodi K., Thirolf P.G.: *"Commissioning of a Compton camera for ion beam range verification via prompt γ detection using low-energy and clinical particle beams"*, Radiotherapy and Oncology 118:S2-S3 (2016), DOI:10.1016/S0167-8140(16)30005-6

- Valencia Lozano I.I., Dedes G., Aldawood S., **Liprandi S.**, Miani A., Zoglauer A., Lauber K., Thirolf P.G., Parodi K.: *"A compton camera prototype simulation study: Camera performance and first tests of range monitoring capabilities"*, in Proc. of IEEE Nuclear Science Symposium and Medical Imaging Conference (2016), DOI:10.1109/NSSMIC.2016.8069417

- Thirolf P.G., Aldawood S., Böhmer M., Bortfeldt J., Castelhano I., Dedes G., Fiedler F., Gernhäuser R., Golnik C., Helmbrecht S., Hueso-González F., Van Der Kolff H., Kormoll T., Lang C., **Liprandi S.**, Lutter R., Marinšek T., Maier L., Pausch G., Petzoldt J., Römer K., Schaart D.R. and Parodi K.: *"A Compton camera prototype for prompt gamma medical imaging"*, EPJ Web of Conferences 117, 05005 (2016), DOI: https://doi.org/10.1051/epjconf/201611705005

- Aldawood S., Castelhano I., Gernhäuser R., Van Der Kolff H., Lang C., **Liprandi S.**, Lutter R., Maier L., Marinšek T., Schaart D.R., Parodi K. and Thirolf P.G.: *"Comparative characterization study of a $LaBr_3$ scintillation crystal in two surface wrapping scenarios: absorptive and reflective"*, Frontiers and Oncology, 5:270 (2015), DOI:10.3389/fonc.2015.00270

Conference attendance and contributions

- *2018 IEEE Nuclear Science Symposium and Medical Imaging Conference*
  Contribution: *Monolithic $LaBr_3(Ce)$ absorber and segmented GAGG scatter detectors in a Compton camera arrangement for medical imaging*
  November 10-17, 2018 (Sydney, Australia)

- *49. Jahrestagung der Deutschen Gesellschaft für Medizinische Physik*
  Contribution 1: *Compact signal processing of a Compton camera system for medical imaging*
  Contribution 2: *Characterization of a Compton camera setup with monolithic $LaBr_3(Ce)$ absorber and segmented GAGG scatter detectors*
  September 19-22, 2017 (Nürnberg, Germany)

- *82. Jahrestagung der DPG und DPG-Frühjahrstagung*
  Contribution: *Compact signal processing of a Compton camera system for medical imaging*
  March 19-23, 2018 (Würzburg, Germany)

- *2017 IEEE Nuclear Science Symposium and Medical Imaging Conference*
  Contribution: *Characterization of a Compton camera setup with monolithic $LaBr_3(Ce)$ absorber and segmented GAGG scatter detectors*
  October 21-28, 2017 (Atlanta, USA)

- *Jahrestagung der BIOMEDIZINISCHEN TECHNIK und Dreiländertagung der MEDIZINISCHEN PHYSIK*

Contribution 1: *Optimization of a Compton camera prototype for particle beam range verification*
Contribution 2: *Sub-3mm spatial resolution from a large monolithic $LaBr_3(Ce)$ scintillator*
September 10-13, 2017 (Dresden, Germany)

- *81. Jahrestagung der DPG und DPG-Frühjahrstagung*
  Contribution: *Commissioning of the scatter component of a Compton camera consisting of a stack of Si strip detectors*
  March 27-31, 2017 (Münster, Germany)

- *47. Jahrestagung der Deutschen Gesellschaft für Medizinische Physik*
  Contribution: *Status of the development of a Compton camera prototype for ion beam range verification via prompt gamma imaging*
  September 7-10, 2016 (Würzburg, Germany)

- *80. Jahrestagung der DPG und DPG-Frühjahrstagung*
  Contribution: *Development of a Compton Camera prototype for prompt gamma medical imaging*
  March 14-18, 2016 (Darmstadt, Germany)

- *Alpa Symposium - Applications of Laser-driven Particle Acceleration*
  Contribution: *Development of a Compton camera prototype for prompt gamma medical imaging*
  November 19-21, 2015 (Venice, Italy)

- *IMPRS-MAP Workshop*
  Contribution: *Development of a Compton camera prototype for prompt gamma medical imaging*
  July 26-31, 2015 (Wildbad Kreuth, Germany)

- *Advanced Semiconductor Detectors for Medical Applications Symposium*
  February 13, 2015 (Munich, Germany)

- *79. Jahrestagung der DPG und DPG-Frühjahrstagung*
  Contribution: *Commissioning of the scatter component of a Compton camera consisting of a stack of Si strip detectors*
  March 23-27, 2015 (Heidelberg, Germany)

- *Symposium on Medical Imaging at Oncoray*
  September 2014 (Dresden, Germany)

APPENDIX B

PMT non-uniformity maps

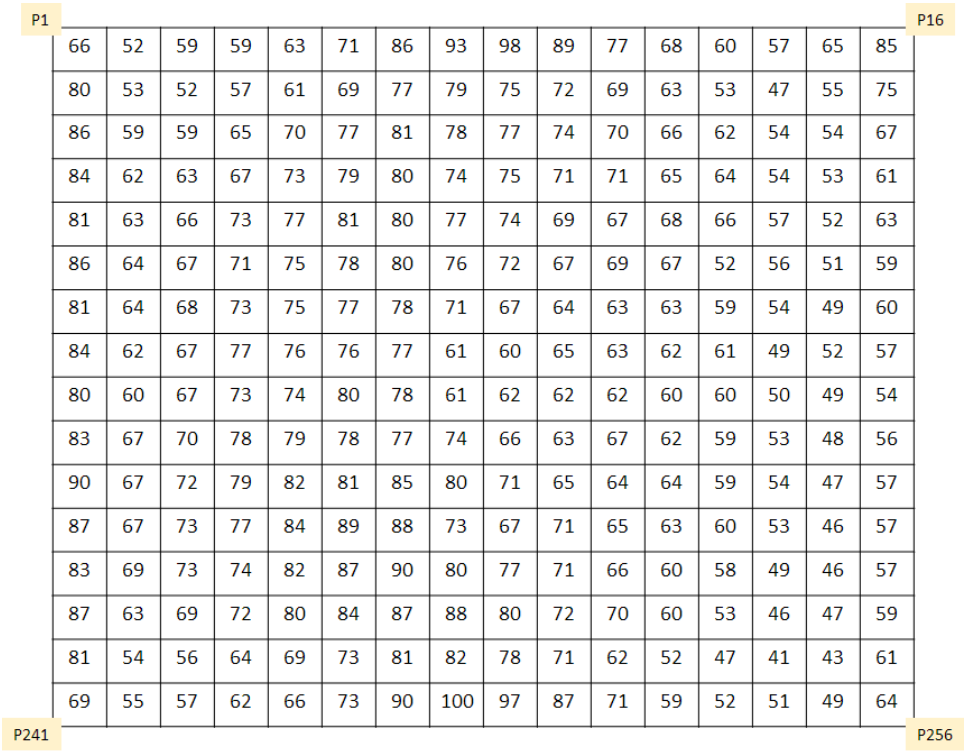

Figure B.1: PMT non-uniformity map for the H9500 PMT (crystal serial number: BA2480).

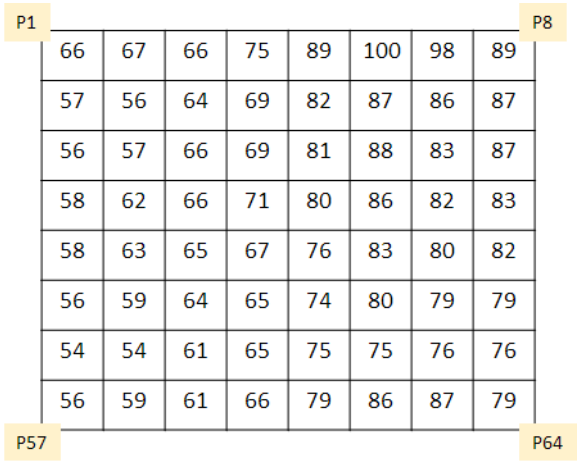

Figure B.2: PMT non-uniformity map for the H8500C PMT (crystal serial number: CB0609).

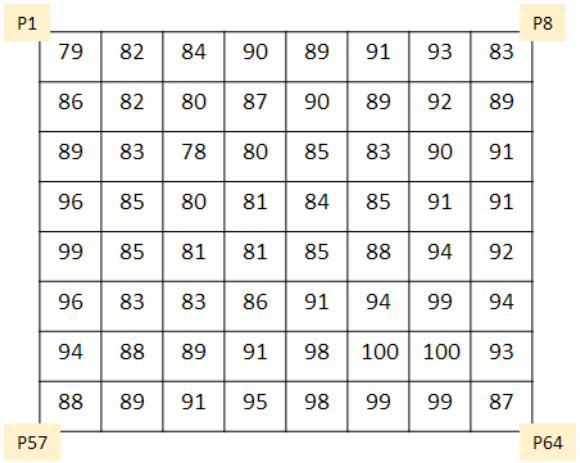

Figure B.3: PMT non-uniformity map for the H12700A-10 PMT (crystal serial number: GA1294).

APPENDIX C

Compton camera box mechanical drawing

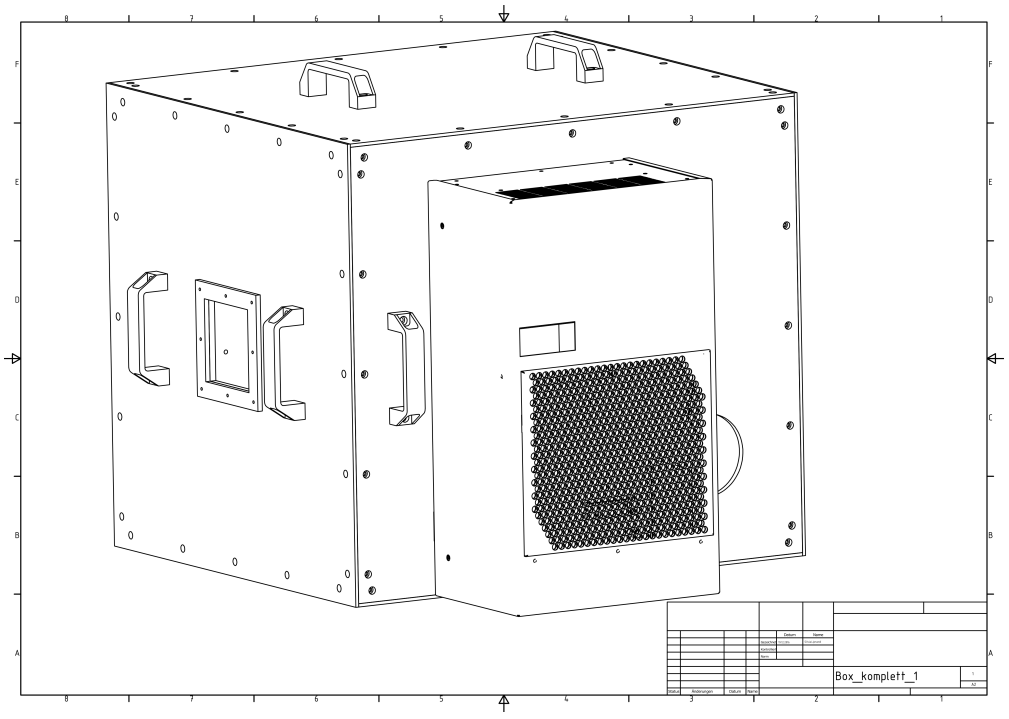

Figure C.1: Technical drawing of the Compton camera box

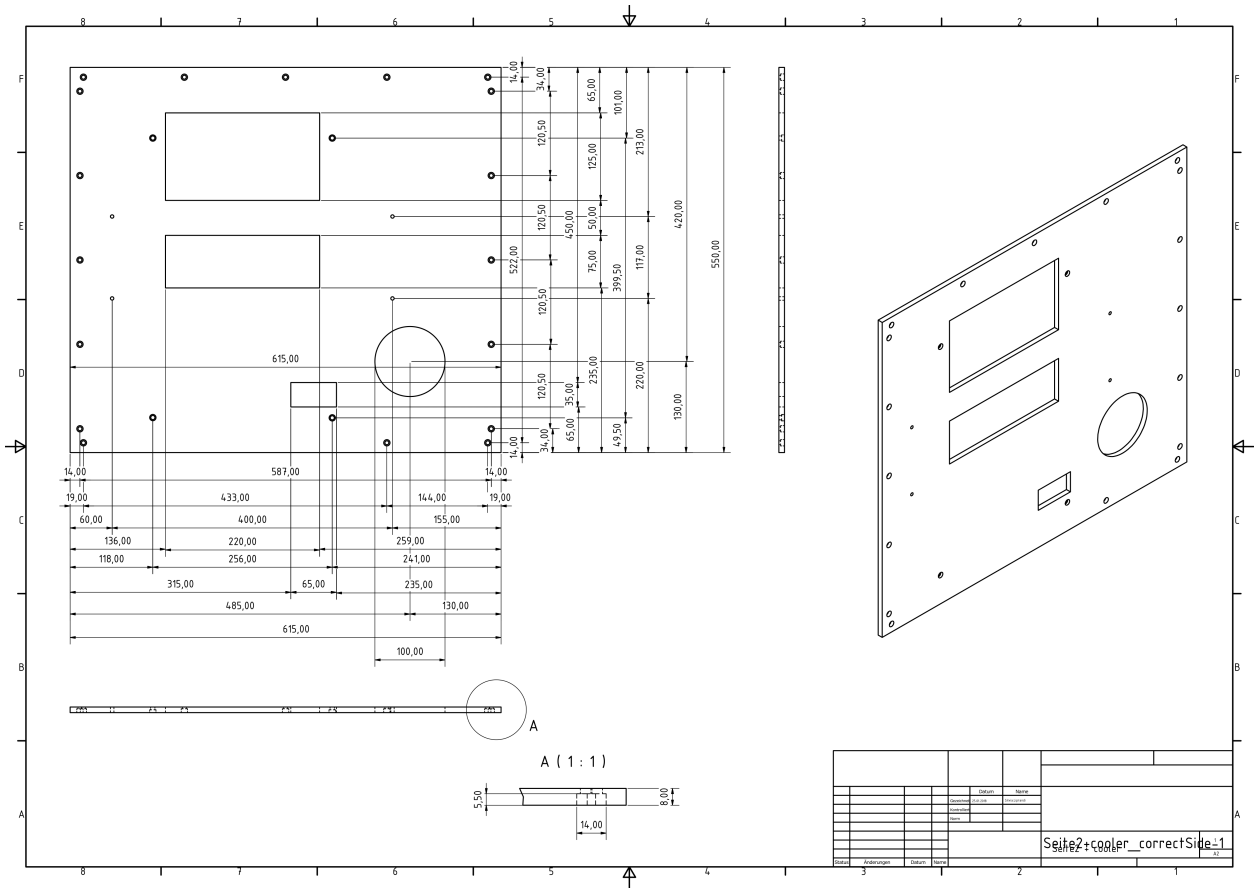

Figure C.2: Technical drawing of one lateral side of the Compton camera box, where the active cooling device is attached.

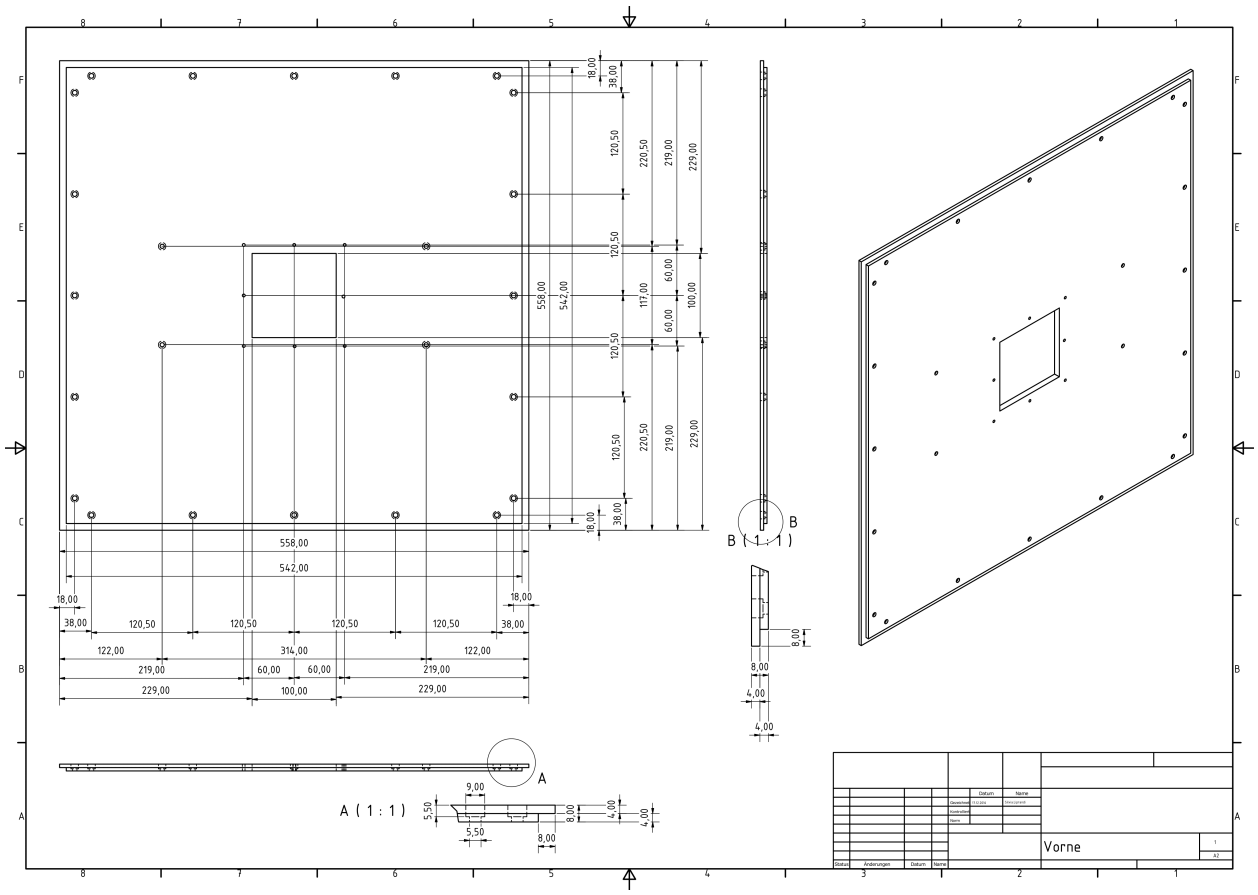

Figure C.3: Technical drawing of the front side of the Compton camera box, where the entrance window is located.

Bibliography

[1] J. M. Verburg and J. Seco, "Proton range verification through prompt gamma-ray spectroscopy," *Physics in Medicine and Biology*, vol. 59, no. 23, pp. 7089–7106, dec 2014. [Online]. Available: http://www.ncbi.nlm.nih.gov/pubmed/25365362http://stacks.iop.org/0031-9155/59/i=23/a=7089?key=crossref.2c380dcfa8360cb6e6defe62dd49f24a

[2] P. M. Martins, R. Dal Bello, A. Rinscheid, K. Roemer, T. Werner, W. Enghardt, G. Pausch, and J. Seco, "Prompt gamma spectroscopy for range control with CeBr3," *Current Directions in Biomedical Engineering*, vol. 3, no. 2, pp. 113–117, jan 2017. [Online]. Available: http://www.degruyter.com/view/j/cdbme.2017.3.issue-2/cdbme-2017-0023/cdbme-2017-0023.xml

[3] F. Hueso González, "Nuclear methods for real-time range verification in proton therapy based on prompt gamma-ray imaging," Ph.D. dissertation, Technical University Dresden, 2015. [Online]. Available: http://www.qucosa.de/fileadmin/data/qucosa/documents/20498/PhD{_}Thesis{_}FHG{_}public.pdf

[4] C. Lang, D. Habs, K. Parodi, and P. G. Thirolf, "Sub-millimeter nuclear medical imaging with high sensitivity in positron emission tomography using beta-gamma coincidences," *Journal of Instrumentation*, may 2013. [Online]. Available: http://arxiv.org/abs/1305.4261http://dx.doi.org/10.1088/1748-0221/9/01/P01008

[5] H. Paganetti, "Range uncertainties in proton therapy and the role of Monte Carlo simulations." *Physics in medicine and biology*, vol. 57, no. 11, pp. R99–117, jun 2012. [Online]. Available: http://www.ncbi.nlm.nih.gov/pubmed/22571913http://www.pubmedcentral.nih.gov/articlerender.fcgi?artid=PMC3374500

[6] "WHO — Cancer," 2017. [Online]. Available: http://www.who.int/topics/cancer/en/

[7] "Eurostat-cancer statistics." [Online]. Available: http://ec.europa.eu/eurostat/statistics-explained/index.php?title=Main{_}Page

[8] R. L. Siegel, K. D. Miller, and A. Jemal, "Cancer statistics, 2017," *CA: A Cancer Journal for Clinicians*, vol. 67, no. 1, pp. 7–30, jan 2017. [Online]. Available: http://www.ncbi.nlm.nih.gov/pubmed/28055103http://doi.wiley.com/10.3322/caac.21387

[9] American Cancer Society, "Radiation therapy principles," *American Cancer Society*, 2011.

[10] R. J. Klement and C. E. Champ, "Calories, carbohydrates, and cancer therapy with radiation: exploiting the five R's through dietary manipulation," *Cancer and Metastasis Reviews*, vol. 33, no. 1, pp. 217–229, mar 2014. [Online]. Available: http://www.ncbi.nlm.nih.gov/pubmed/24436017http://www.pubmedcentral.nih.gov/articlerender.fcgi?artid=PMC3988521http://link.springer.com/10.1007/s10555-014-9495-3

[11] "Radiation Therapy for Cancer - National Cancer Institute." [Online]. Available: https://www.cancer.gov/about-cancer/treatment/types/radiation-therapy

[12] "IMRT - Intensity-Modulated Radiation Therapy." [Online]. Available: https://www.radiologyinfo.org/en/info.cfm?pg=imrt

[13] F. Verhaegen and J. Seuntjens, "Monte Carlo modelling of external radiotherapy photon beams," *Physics in Medicine and Biology*, vol. 48, no. 21, pp. R107–R164, nov 2003. [Online]. Available: http://stacks.iop.org/0031-9155/48/i=21/a=R01?key=crossref.822c6a8bf68e8f985ca4f6b7effec995

[14] C. Reis and P. Nicolucci, "Assessment of radiotherapy photon beams: A practical and low cost methodology," *Radiation Physics and Chemistry*, vol. 131, pp. 60–65, feb 2017. [Online]. Available: https://www.sciencedirect.com/science/article/pii/S0969806X16306090

[15] B. Cai, O. L. Green, R. Kashani, V. L. Rodriguez, S. Mutic, and D. Yang, "A practical implementation of physics quality assurance for photon adaptive radiotherapy," *Zeitschrift für Medizinische Physik*, mar 2018. [Online]. Available: http://www.ncbi.nlm.nih.gov/pubmed/29550014http://linkinghub.elsevier.com/retrieve/pii/S0939388917300910

[16] C. DesRosiers, V. Moskvin, A. F. Bielajew, and L. Papiez, "150-250 MeV electron beams in radiation therapy," *Physics in Medicine and Biology*, vol. 45, no. 7, pp. 1781–1805, jul 2000. [Online]. Available: http://stacks.iop.org/0031-9155/45/i=7/a=306?key=crossref.32c79da60619831e49a487ca7ceff192

[17] W. C. Röntgen, "On a new kind of rays," *Science (New York, N.Y.)*, vol. 3, no. 59, pp. 227–31, feb 1896. [Online]. Available: http://www.ncbi.nlm.nih.gov/pubmed/17769966

[18] A. Taylor and M. E. B. Powell, "Intensity-modulated radiotherapy - what is it?" *Cancer Imaging*, vol. 4, no. 2, pp. 68–73, mar 2004. [Online]. Available: http://www.ncbi.nlm.nih.gov/pubmed/18250011http://www.pubmedcentral.nih.gov/articlerender.fcgi?artid=PMC1434586https://www.ncbi.nlm.nih.gov/pmc/articles/PMC1434586/

[19] R. R. Wilson, "Radiological Use of Fast Protons," *Radiology*, vol. 47, no. 5, pp. 487–491, nov 1946. [Online]. Available: http://www.ncbi.nlm.nih.gov/pubmed/20274616http://pubs.rsna.org/doi/10.1148/47.5.487

[20] D. E. Bonnett, "Current developments in proton therapy: a review," *Physics in Medicine and Biology*, vol. 38, no. 10, pp. 1371–1392, oct 1993. [Online]. Available: http://stacks.iop.org/0031-9155/38/i=10/a=001?key=crossref.2df456e7863cc9e1561d8dafaabf9784

[21] U. Amaldi, "History of hadrontherapy in the world and Italian developments," *Rivista Medica*, vol. 14, no. 1, 2008. [Online]. Available: https://indico.cern.ch/event/24728/attachments/424989/590019/RIVISTA{_}MEDICA{_}2008-14{_}1.pdf

[22] S. Braccini, "Scientific and Technological development of Hadrontherapy," *Proc. 11th Conf. Astroparticle, Space Physics, Radiation Interaction, Detectors and Medical Physics Application*, vol. 5, pp. 598–609, 2009. [Online]. Available: https://arxiv.org/ftp/arxiv/papers/1001/1001.0860.pdf

[23] T. Ohno, "Particle radiotherapy with carbon ion beams." *The EPMA journal*, vol. 4, no. 1, p. 9, mar 2013. [Online]. Available: http://www.ncbi.nlm.nih.gov/pubmed/23497542http://www.pubmedcentral.nih.gov/articlerender.fcgi?artid=PMC3598788

[24] H. Paganetti, C. X. Yu, and C. G. Orton, "Photon radiotherapy has reached its limit in terms of catching up dosimetrically with proton therapy," *Medical Physics*, vol. 43, pp. 4470–4472, jul 2016. [Online]. Available: http://www.ncbi.nlm.nih.gov/pubmed/27487862http://doi.wiley.com/10.1118/1.4954790

[25] A. Trofimov, P. L. Nguyen, J. J. Coen, K. P. Doppke, R. J. Schneider, J. A. Adams, T. R. Bortfeld, A. L. Zietman, T. F. DeLaney, and W. U. Shipley, "Radiotherapy Treatment of Early-Stage Prostate Cancer with IMRT and Protons: A Treatment Planning Comparison," *International Journal of Radiation Oncology*Biology*Physics*, vol. 69, no. 2, pp. 444–453, oct 2007. [Online]. Available: http://www.ncbi.nlm.nih.gov/pubmed/17513063http://www.pubmedcentral.nih.gov/articlerender.fcgi?artid=PMC2695934http://linkinghub.elsevier.com/retrieve/pii/S0360301607005068

[26] T. Bortfeld and W. Schlegel, "An analytical approximation of depth-dose distributions for therapeutic proton beams." *Physics in medicine and biology*, vol. 41, no. 8, pp. 1331–9, aug 1996. [Online]. Available: http://www.ncbi.nlm.nih.gov/pubmed/8858723

[27] D. Jette and W. Chen, "Creating a spread-out Bragg peak in proton beams," *Physics in Medicine and Biology*, vol. 56, no. 11, pp. 131–138, jun 2011. [Online]. Available: http://stacks.iop.org/0031-9155/56/i=11/a=N01?key=crossref.ac7eb3600afe78c672d5e07205b16a36

[28] J. H. Lawrence, C. A. Tobias, J. L. Born, R. K. McCombs, J. E. Roberts, H. O. Anger, B. V. Low-Beer, and C. B. Huggins, "Pituitary irradiation with high-energy proton beams: a preliminary report." *Cancer research*, vol. 18, no. 2, pp. 121–134, feb 1958. [Online]. Available: http://www.ncbi.nlm.nih.gov/pubmed/13511365

[29] W. D. Newhauser and R. Zhang, "The physics of proton therapy," *Physics in Medicine and Biology*, vol. 60, no. 8, pp. 155–209, apr 2015. [Online]. Available: http://stacks.iop.org/0031-9155/60/i=8/a=R155?key=crossref.e17ea27b3e09d2ae08a7471562523fb1

[30] C.-M. C. Ma and T. Lomax, *Proton and carbon ion therapy*. Taylor & Francis, 2013.

[31] "The Svedberg laboratory - Uppsala University." [Online]. Available: http://www.tsl.uu.se/about-tsl/history/protonterapi-60-ar/

[32] "PTCOG - Facilities in Operation." [Online]. Available: https://www.ptcog.ch/index.php/facilities-in-operation

[33] J. D. Slater, "Development and Operation of the Loma Linda University Medical Center Proton Facility," *Technology in Cancer Research & Treatment*, vol. 6, no. 4_suppl, pp. 67–72, aug 2007. [Online]. Available: http://www.ncbi.nlm.nih.gov/pubmed/17668955http://journals.sagepub.com/doi/10.1177/15330346070060S411

[34] M. Jermann, "Particle Therapy Statistics in 2014," *Int J Particle Ther*, vol. 2, no. 1, pp. 50–54, 2015. [Online]. Available: http://theijpt.org

[35] A. N. Schreuder, S. G. Hedrick, J. R. Renegar, T. J. Netherton, H. Chen, M. D. Blakey, M. E. Artz, B. H. Robison, A. G. Meek, and M. Fagundes, "A review of proton radiation therapy and the path to widespread clinical adoption," *Medical Physics International Journal*, vol. 4, no. 1, 2016. [Online]. Available: http://mpijournal.org/pdf/2016-01/MPI-2016-01-p035.pdf

[36] F. M. Wagner, B. Loeper-Kabasakal, and H. Breitkreutz, "Neutron medical treatment of tumours - A survey of facilities," *Journal of Instrumentation*, vol. 7, no. 3, 2012.

[37] F. Albertini, E. B. Hug, and A. J. Lomax, "Is it necessary to plan with safety margins for actively scanned proton therapy?" *Physics in Medicine and Biology*, vol. 56, no. 14, pp. 4399–4413, jul 2011. [Online]. Available: http://www.ncbi.nlm.nih.gov/pubmed/21709340http://stacks.iop.org/0031-9155/56/i=14/a=011?key=crossref.79bc965f9231438e4653528dcc301b14

[38] M. Goitein, "Calculation of the uncertainty in the dose delivered during radiation therapy," *Medical Physics*, vol. 12, no. 5, pp. 608–612, sep 1985. [Online]. Available: http://www.ncbi.nlm.nih.gov/pubmed/4046996http://doi.wiley.com/10.1118/1.595762

[39] A.-C. Knopf and A. Lomax, "In vivo proton range verification: a review," *Physics in Medicine and Biology*, vol. 58, no. 15, pp. R131–R160, aug 2013. [Online]. Available: http://www.ncbi.nlm.nih.gov/pubmed/23863203http://stacks.iop.org/0031-9155/58/i=15/a=R131?key=crossref.a4dce585277cdd2c3b0331cb1d3e7322

[40] U. Schneider, E. Pedroni, and A. Lomax, "The calibration of CT Hounsfield units for radiotherapy treatment planning," *Physics in Medicine and Biology*, vol. 41, no. 1, pp. 111–124, jan 1996. [Online]. Available: http://stacks.iop.org/0031-9155/41/i=1/a=009?key=crossref.7cef62664dbeba7f6a11f0639b13a9e8

[41] H. Paganetti, "Significance and Implementation of RBE Variations in Proton Beam Therapy," *Technology in Cancer Research & Treatment*, vol. 2, no. 5, pp. 413–426, oct 2003. [Online]. Available: http://www.ncbi.nlm.nih.gov/pubmed/14529306http://journals.sagepub.com/doi/10.1177/153303460300200506

[42] S. M. Holloway, M. D. Holloway, and S. J. Thomas, "A method for acquiring random range uncertainty probability distributions in proton therapy," *Physics in Medicine & Biology*, vol. 63, no. 1, p. 01NT02, dec 2017. [Online]. Available: http://www.ncbi.nlm.nih.gov/pubmed/29053110http://www.pubmedcentral.nih.gov/articlerender.fcgi?artid=PMC5802333http://stacks.iop.org/0031-9155/63/i=1/a=01NT02?key=crossref.3585096422fa64dc31524bbb24468cb4

[43] S. E. McGowan, N. G. Burnet, and A. J. Lomax, "Treatment planning optimisation in proton therapy," *The British Journal of Radiology*, vol. 86, no. 1021, p. 20120288, jan 2013. [Online]. Available: http://www.ncbi.nlm.nih.gov/pubmed/23255545http://www.pubmedcentral.nih.gov/articlerender.fcgi?artid=PMC4651068http://www.birpublications.org/doi/10.1259/bjr.20120288

[44] H. Paganetti and M. Goitein, "Radiobiological significance of beamline dependent proton energy distributions in a spread-out Bragg peak," *Medical Physics*, vol. 27, no. 5, pp. 1119–1126, may 2000. [Online]. Available: http://www.ncbi.nlm.nih.gov/pubmed/10841418http://doi.wiley.com/10.1118/1.598977

[45] J. B. Robertson, J. R. Williams, R. A. Schmidt, J. B. Little, D. F. Flynn, and H. D. Suit, "Radiobiological studies of a high-energy modulated proton beam

utilizing cultured mammalian cells." *Cancer*, vol. 35, no. 6, pp. 1664–1677, jun 1975. [Online]. Available: http://www.ncbi.nlm.nih.gov/pubmed/807318

[46] B. G. Wouters, G. K. Lam, U. Oelfke, K. Gardey, R. E. Durand, and L. D. Skarsgard, "Measurements of relative biological effectiveness of the 70 MeV proton beam at TRIUMF using Chinese hamster V79 cells and the high-precision cell sorter assay," *Radiation research*, vol. 146, no. 2, pp. 159–170, aug 1996. [Online]. Available: http://www.ncbi.nlm.nih.gov/pubmed/8693066

[47] A. C. Kraan, "Range Verification Methods in Particle Therapy: Underlying Physics and Monte Carlo Modeling," *Frontiers in Oncology*, vol. 5, p. 150, jul 2015. [Online]. Available: http://www.ncbi.nlm.nih.gov/pubmed/26217586http://www.pubmedcentral.nih.gov/articlerender.fcgi?artid=PMC4493660http://journal.frontiersin.org/Article/10.3389/fonc.2015.00150/abstract

[48] K. Parodi, "On- and off-line monitoring of ion beam treatment," *Nuclear Instruments and Methods in Physics Research Section A: Accelerators, Spectrometers, Detectors and Associated Equipment*, vol. 809, pp. 113–119, feb 2016. [Online]. Available: https://www.sciencedirect.com/science/article/pii/S0168900215008062

[49] J. C. Polf and K. Parodi, "Imaging particle beams for cancer treatment," *Physics Today*, vol. 68, no. 10, pp. 28–33, oct 2015. [Online]. Available: http://physicstoday.scitation.org/doi/10.1063/PT.3.2945

[50] K. Parodi and W. Assmann, "Ionoacoustics: A new direct method for range verification," *Modern Physics Letters A*, vol. 30, no. 17, p. 1540025, jun 2015. [Online]. Available: http://www.worldscientific.com/doi/abs/10.1142/S0217732315400258

[51] K. C. Jones, C. M. Seghal, and S. Avery, "How proton pulse characteristics influence protoacoustic determination of proton-beam range: simulation studies," *Physics in Medicine and Biology*, vol. 61, no. 6, pp. 2213–2242, mar 2016. [Online]. Available: http://www.ncbi.nlm.nih.gov/pubmed/26913839http://stacks.iop.org/0031-9155/61/i=6/a=2213?key=crossref.cb5065e308e4fb350843d9cebbf0a1ed

[52] J. Tada, Y. Hayakawa, K. Hosono, and T. Inada, "Time resolved properties of acoustic pulses generated in water and in soft tissue by pulsed proton beam irradiation-A possibility of doses distribution monitoring in proton radiation therapy," *Medical Physics*, vol. 18, no. 6, pp. 1100–1104, nov 1991. [Online]. Available: http://doi.wiley.com/10.1118/1.596618

[53] Y. Hayakawa, J. Tada, N. Arai, K. Hosono, M. Sato, T. Wagai, H. Tsuji, and H. Tsujii, "Acoustic pulse generated in a patient during treatment by pulsed proton radiation beam," *Radiation Oncology Investigations*, vol. 3, no. 1, pp. 42–45, 1995. [Online]. Available: http://doi.wiley.com/10.1002/roi.2970030107

[54] S. Kellnberger, W. Assmann, S. Lehrack, S. Reinhardt, P. Thirolf, D. Queirós, G. Sergiadis, G. Dollinger, K. Parodi, and V. Ntziachristos, "Ionoacoustic tomography of the proton Bragg peak in combination with ultrasound and optoacoustic imaging," *Scientific Reports*, vol. 6, no. 1, p. 29305, sep 2016. [Online]. Available: http://www.nature.com/articles/srep29305

[55] S. Lehrack, W. Assmann, D. Bertrand, S. Henrotin, J. Herault, V. Heymans, F. V. Stappen, P. G. Thirolf, M. Vidal, J. Van de Walle, and K. Parodi, "Submillimeter ionoacoustic range determination for protons in water at a clinical synchrocyclotron," *Physics in Medicine & Biology*, vol. 62, no. 17, pp. 20–30, aug 2017. [Online]. Available: http://www.ncbi.nlm.nih.gov/pubmed/28742053http://stacks.iop.org/0031-9155/62/i=17/a=L20?key=crossref.4976d1b3b58c839fa9340ebf7988948d

[56] S. K. Patch, M. Kireeff Covo, A. Jackson, Y. M. Qadadha, K. S. Campbell, R. A. Albright, P. Bloemhard, A. P. Donoghue, C. R. Siero, T. L. Gimpel, S. M. Small, B. F. Ninemire, M. B. Johnson, and L. Phair, "Thermoacoustic range verification using a clinical ultrasound array provides perfectly co-registered overlay of the Bragg peak onto an ultrasound image," *Physics in Medicine and Biology*, vol. 61, no. 15, pp. 5621–5638, aug 2016. [Online]. Available: http://stacks.iop.org/0031-9155/61/i=15/a=5621?key=crossref.3c3562cf92887ba59945ecfd9b75b2fb

[57] M. Ahmad, L. Xiang, S. Yousefi, and L. Xing, "Theoretical detection threshold of the proton-acoustic range verification technique," *Medical Physics*, vol. 42, no. 10, pp. 5735–5744, sep 2015. [Online]. Available: http://www.ncbi.nlm.nih.gov/pubmed/26429247http://www.pubmedcentral.nih.gov/articlerender.fcgi?artid=PMC4567582http://doi.wiley.com/10.1118/1.4929939

[58] W. Enghardt, P. Crespo, F. Fiedler, R. Hinz, K. Parodi, J. Pawelke, and F. Pönisch, "Charged hadron tumour therapy monitoring by means of PET," *Nuclear Instruments and Methods in Physics Research Section A: Accelerators, Spectrometers, Detectors and Associated Equipment*, vol. 525, no. 1-2, pp. 284–288, jun 2004. [Online]. Available: https://www.sciencedirect.com/science/article/pii/S0168900204004218

[59] X. Zhu and G. El Fakhri, "Proton therapy verification with PET imaging," *Theranostics*, vol. 3, no. 10, pp. 731–740, sep 2013. [Online]. Available: http://www.ncbi.nlm.nih.gov/pubmed/24312147http://www.pubmedcentral.nih.gov/articlerender.fcgi?artid=PMC3840408

[60] K. Parodi, T. Bortfeld, and T. Haberer, "Comparison Between In-Beam and Offline Positron Emission Tomography Imaging of Proton and Carbon Ion Therapeutic Irradiation at Synchrotron- and Cyclotron-Based Facilities," *International Journal of Radiation Oncology*Biology*Physics*, vol. 71, no. 3, pp. 945–956, jul 2008. [Online]. Available: http://www.ncbi.nlm.nih.gov/pubmed/18514787http://linkinghub.elsevier.com/retrieve/pii/S0360301608003374

[61] K. Parodi, P. Crespo, H. Eickhoff, T. Haberer, J. Pawelke, D. Schardt, and W. Enghardt, "Random coincidences during in-beam PET measurements at microbunched therapeutic ion beams," *Nuclear Instruments and Methods in Physics Research Section A: Accelerators, Spectrometers, Detectors and Associated Equipment*, vol. 545, no. 1-2, pp. 446–458, jun 2005. [Online]. Available: https://www.sciencedirect.com/science/article/pii/S0168900205005759

[62] D. W. Litzenberg, D. A. Roberts, M. Y. Lee, K. Pham, A. M. Vander Molen, R. Ronningen, and F. D. Becchetti, "On-line monitoring of radiotherapy beams: Experimental results with proton beams," *Medical Physics*, vol. 26, no. 6, pp. 992–1006, jun 1999. [Online]. Available: http://www.ncbi.nlm.nih.gov/pubmed/10436901http://doi.wiley.com/10.1118/1.598491

[63] H. D. Maccabee, U. Madhvanath, and M. R. Raju, "Tissue activation studies with alpha-particle beams," *Physics in Medicine and Biology*, vol. 14, no. 2, p. 304, apr 1969. [Online]. Available: http://stacks.iop.org/0031-9155/14/i=2/a=304?key=crossref.c6821772a39cafdcde7c176fe29cbfc8

[64] F. Pönisch, K. Parodi, B. G. Hasch, and W. Enghardt, "The modelling of positron emitter production and PET imaging during carbon ion therapy." *Physics in medicine and biology*, vol. 49, no. 23, pp. 5217–32, dec 2004. [Online]. Available: http://www.ncbi.nlm.nih.gov/pubmed/15656273

[65] K. Parodi, H. Paganetti, H. A. Shih, S. Michaud, J. S. Loeffler, T. F. DeLaney, N. J. Liebsch, J. E. Munzenrider, A. J. Fischman, A. Knopf, and T. Bortfeld, "Patient Study of In Vivo Verification of Beam Delivery and Range, Using Positron Emission Tomography and Computed Tomography Imaging After Proton Therapy," *International Journal of Radiation Oncology*Biology*Physics*, vol. 68, no. 3, pp. 920–934, jul 2007. [Online]. Available: http://www.ncbi.nlm.nih.gov/pubmed/17544003http://www.pubmedcentral.nih.gov/articlerender.fcgi?artid=PMC2047826http://linkinghub.elsevier.com/retrieve/pii/S036030160700377X

[66] W. Enghardt, K. Parodi, P. Crespo, F. Fiedler, J. Pawelke, and F. Pönisch, "Dose quantification from in-beam positron emission tomography," *Radiotherapy and Oncology*, vol. 73, pp. S96–S98, dec 2004. [Online]. Available: https://www.sciencedirect.com/science/article/pii/S0167814004800240

[67] "FLUKA (FLUktuierende KAskade) code." [Online]. Available: http://www.fluka.org/fluka.php

[68] K. Parodi, A. Ferrari, F. Sommerer, and H. Paganetti, "Clinical CT-based calculations of dose and positron emitter distributions in proton therapy using the FLUKA Monte Carlo code," *Physics in Medicine and Biology*, vol. 52, no. 12, pp. 3369–3387, jul 2007. [Online]. Available: http://www.ncbi.nlm.nih.gov/pubmed/17664549http://www.pubmedcentral.nih.

gov/articlerender.fcgi?artid=PMC2292644http://stacks.iop.org/0031-9155/52/i=12/a=004?key=crossref.15f59e86385403401a1e9c3359c1e69d

[69] "Geant4 - A simulation toolkit." [Online]. Available: https://geant4.web.cern.ch/

[70] I. Pshenichnov, I. Mishustin, and W. Greiner, "Distributions of positron-emitting nuclei in proton and carbon-ion therapy studied with GEANT4," *Physics in Medicine and Biology*, vol. 51, no. 23, pp. 6099–6112, dec 2006. [Online]. Available: http://www.ncbi.nlm.nih.gov/pubmed/17110773http://stacks.iop.org/0031-9155/51/i=23/a=011?key=crossref.2ba2d869cb5d630e6b094d05957b99c5

[71] J. Ziegler, "SRIM & TRIM." [Online]. Available: http://www.srim.org/

[72] W. Tuckwell and E. Bezak, "Calculation of the positron distribution from 15O nuclei formed in nuclear reactions in human tissue during proton therapy," *Physics in Medicine and Biology*, vol. 52, no. 9, pp. 2483–2498, may 2007. [Online]. Available: http://www.ncbi.nlm.nih.gov/pubmed/17440247http://stacks.iop.org/0031-9155/52/i=9/a=010?key=crossref.74b8c8402ddd58a358179336e9faa81c

[73] Los Alamos National Laboratory, "MCNP - A General Monte Carlo N-Particle Transport Code." [Online]. Available: https://mcnp.lanl.gov/

[74] E. Seravalli, C. Robert, J. Bauer, F. Stichelbaut, C. Kurz, J. Smeets, C. Van, N. Ty, D. R. Schaart, I. Buvat, K. Parodi, and F. Verhaegen, "Monte Carlo calculations of positron emitter yields in proton radiotherapy," *Phys. Med. Biol. Phys. Med. Biol*, vol. 57, no. 57, pp. 1659–1673, 2012. [Online]. Available: http://iopscience.iop.org/0031-9155/57/6/1659

[75] C. H. Min, X. Zhu, B. A. Winey, K. Grogg, M. Testa, G. El Fakhri, T. R. Bortfeld, H. Paganetti, and H. A. Shih, "Clinical Application of In-Room Positron Emission Tomography for In Vivo Treatment Monitoring in Proton Radiation Therapy," *International Journal of Radiation Oncology*Biology*Physics*, vol. 86, no. 1, pp. 183–189, may 2013. [Online]. Available: http://www.ncbi.nlm.nih.gov/pubmed/23391817http://www.pubmedcentral.nih.gov/articlerender.fcgi?artid=PMC3640852http://linkinghub.elsevier.com/retrieve/pii/S0360301612039065

[76] K. Parodi, T. Bortfeld, W. Enghardt, F. Fiedler, A. Knopf, H. Paganetti, J. Pawelke, G. Shakirin, and H. Shih, "PET imaging for treatment verification of ion therapy: Implementation and experience at GSI Darmstadt and MGH Boston," *Nuclear Instruments and Methods in Physics Research Section A: Accelerators, Spectrometers, Detectors and Associated Equipment*, vol. 591, no. 1, pp. 282–286, jun 2008. [Online]. Available: https://www.sciencedirect.com/science/article/pii/S0168900208004580

[77] K. Parodi, W. Enghardt, and T. Haberer, "In-beam PET measurements of $\beta+$ radioactivity induced by proton beams," *Physics in Medicine and Biology*, vol. 47,

no. 1, pp. 21–36, jan 2002. [Online]. Available: http://stacks.iop.org/0031-9155/47/i=1/a=302?key=crossref.6d14d2bfaacdb35beba2797e8928940d

[78] Y. Iseki, H. Mizuno, Y. Futami, T. Tomitani, T. Kanai, M. Kanazawa, A. Kitagawa, T. Murakami, T. Nishio, M. Suda, E. Urakabe, A. Yunoki, and H. Sakai, "Positron camera for range verification of heavy-ion radiotherapy," *Nuclear Instruments and Methods in Physics Research Section A: Accelerators, Spectrometers, Detectors and Associated Equipment*, vol. 515, no. 3, pp. 840–849, dec 2003. [Online]. Available: https://www.sciencedirect.com/science/article/pii/S0168900203023106

[79] T. Nishio, T. Ogino, K. Nomura, and H. Uchida, "Dose-volume delivery guided proton therapy using beam on-line PET system," *Medical Physics*, vol. 33, no. 11, pp. 4190–4197, oct 2006. [Online]. Available: http://www.ncbi.nlm.nih.gov/pubmed/17153398http://doi.wiley.com/10.1118/1.2361079

[80] T. Yamaya, T. Inaniwa, E. Yoshida, F. Nishikido, K. Shibuya, N. Inadama, and H. Murayama, "Simulation studies of a new OpenPET geometry based on a quad unit of detector rings," *Physics in Medicine and Biology*, vol. 54, no. 5, pp. 1223–1233, mar 2009. [Online]. Available: http://www.ncbi.nlm.nih.gov/pubmed/19182323http://stacks.iop.org/0031-9155/54/i=5/a=008?key=crossref.179765f1387a6e8b560696c83136780c

[81] H. Tashima, T. Yamaya, E. Yoshida, S. Kinouchi, M. Watanabe, and E. Tanaka, "A single-ring OpenPET enabling PET imaging during radiotherapy," *Physics in Medicine and Biology*, vol. 57, no. 14, pp. 4705–4718, jul 2012. [Online]. Available: http://www.ncbi.nlm.nih.gov/pubmed/22750792http://stacks.iop.org/0031-9155/57/i=14/a=4705?key=crossref.04fdc6242a702be3045781283b3f3474

[82] B. Kozlovsky, R. J. Murphy, and R. Ramaty, "Nuclear Deexcitation GammaRay Lines from Accelerated Particle Interactions," *The Astrophysical Journal Supplement Series*, vol. 141, no. 2, pp. 523–541, aug 2002. [Online]. Available: http://stacks.iop.org/0067-0049/141/i=2/a=523

[83] J. Smeets, "Prompt gamma imaging with a slit camera for real time range control in particle therapy," Ph.D. dissertation, Université Libre de Bruxelles, 2012. [Online]. Available: https://webcache.googleusercontent.com/search?q=cache:WlAcCK38RocJ:https://dipot.ulb.ac.be/dspace/bitstream/2013/209624/1/2c3d9b18-b34c-4d7a-8c46-2cd8e45cf8a4.txt+{&}cd=4{&}hl=it{&}ct=clnk{&}gl=de

[84] K. Parodi, P. Crespo, H. Eickhoff, T. Haberer, J. Pawelke, D. Schardt, and W. Enghardt, "Random coincidences during in-beam PET measurements at microbunched therapeutic ion beams," *Nuclear Instruments and Methods in Physics Research Section A: Accelerators, Spectrometers, Detectors and Associated*

Equipment, vol. 545, no. 1-2, pp. 446–458, jun 2005. [Online]. Available: https://www.sciencedirect.com/science/article/pii/S0168900205005759

[85] F. Stichelbaut and Y. Jongen, "Verification of the proton beam position in the patient by the detection of prompt gamma rays emission," *39th Meeting of the Particle Therapy Co-Operative Group (San Francisco)*, 2003. [Online]. Available: https://www.ptcog.ch/archive/steering{_}committee{_}docs/ptcog39-2003/2003{_}PTCOG{_}39{_}Abstracts.pdf

[86] C.-H. Min, C. H. Kim, M.-Y. Youn, and J.-W. Kim, "Prompt gamma measurements for locating the dose falloff region in the proton therapy," *Applied Physics Letters*, vol. 89, no. 18, p. 183517, oct 2006. [Online]. Available: http://aip.scitation.org/doi/10.1063/1.2378561

[87] E. Testa, M. Bajard, M. Chevallier, D. Dauvergne, F. L. Foulher, J. C. Poizat, C. Ray, M. Testa, N. Freud, and J. M. Létang, "Monitoring the Bragg peak location of 73 MeV/u carbon ions by means of prompt γ-ray measurements," *Applied Physics Letters*, vol. 93, pp. 1–10, sep 2008. [Online]. Available: http://arxiv.org/abs/0809.0185http://dx.doi.org/10.1063/1.2975841

[88] C. Hyeong Kim, C. Hee Min, and J. Guen Park, "Development of an Array-Type Prompt Gamma Detection System for the Online Measurement of the Range of the Proton Beam in a Patient: a Monte Carlo Feasibility Study," *Journal of the Korean Physical Society*, vol. 52, no. 3, pp. 888–891, 2008. [Online]. Available: https://www.researchgate.net/publication/252238213

[89] C. H. Min, H. R. Lee, C. H. Kim, and S. B. Lee, "Development of array-type prompt gamma measurement system for in vivo range verification in proton therapy," *Medical Physics*, vol. 39, no. 4, pp. 2100–2107, mar 2012. [Online]. Available: http://www.ncbi.nlm.nih.gov/pubmed/22482631

[90] M. Testa, "Physical measurements for ion range verification in charged particle therapy," Ph.D. dissertation, Université Claude Bernard Lyon, 2010. [Online]. Available: https://tel.archives-ouvertes.fr/tel-00566188/document

[91] F. Roellinghoff, A. Benilov, D. Dauvergne, G. Dedes, N. Freud, G. Janssens, J. Krimmer, J. M. Létang, M. Pinto, D. Prieels, C. Ray, J. Smeets, F. Stichelbaut, and E. Testa, "Real-time proton beam range monitoring by means of prompt-gamma detection with a collimated camera," *Physics in Medicine and Biology*, vol. 59, no. 5, pp. 1327–1338, mar 2014. [Online]. Available: http://stacks.iop.org/0031-9155/59/i=5/a=1327?key=crossref.57e15f5df434c06e9367303d85ff24a9

[92] J.-W. Kim and Jong-Won, "Pinhole Camera Measurements of Prompt Gamma-rays for Detection of Beam Range Variation in Proton Therapy," *Journal of the Korean Physical Society*, vol. 55, no. 4, pp. 1673–1676, oct 2009. [Online]. Available: http://www.jkps.or.kr/journal/DOIx.php?id=10.3938/jkps.55.1673

[93] J. Smeets, F. Roellinghoff, G. Janssens, I. Perali, A. Celani, C. Fiorini, N. Freud, E. Testa, and D. Prieels, "Experimental Comparison of Knife-Edge and Multi-Parallel Slit Collimators for Prompt Gamma Imaging of Proton Pencil Beams," *Frontiers in Oncology*, vol. 6, p. 156, jun 2016. [Online]. Available: http://www.ncbi.nlm.nih.gov/pubmed/27446802http://www.pubmedcentral.nih.gov/articlerender.fcgi?artid=PMC4921459http://journal.frontiersin.org/Article/10.3389/fonc.2016.00156/abstract

[94] J. Smeets, F. Roellinghoff, D. Prieels, F. Stichelbaut, A. Benilov, P. Busca, C. Fiorini, R. Peloso, M. Basilavecchia, T. Frizzi, J. C. Dehaes, and A. Dubus, "Prompt gamma imaging with a slit camera for real-time range control in proton therapy," *Physics in Medicine and Biology*, vol. 57, no. 11, pp. 3371–3405, jun 2012. [Online]. Available: http://www.ncbi.nlm.nih.gov/pubmed/22572603http://stacks.iop.org/0031-9155/57/i=11/a=3371?key=crossref.cbb392ae153f40350872c31cf8c5ed3f

[95] I. Perali, A. Celani, L. Bombelli, C. Fiorini, F. Camera, E. Clementel, S. Henrotin, G. Janssens, D. Prieels, F. Roellinghoff, J. Smeets, F. Stichelbaut, and F. V. Stappen, "Prompt gamma imaging of proton pencil beams at clinical dose rate," *Physics in Medicine and Biology*, vol. 59, no. 19, pp. 5849–5871, oct 2014. [Online]. Available: http://stacks.iop.org/0031-9155/59/i=19/a=5849?key=crossref.d1c598721e0b970b36f1c8a6ad1dd1a1

[96] "XGLab - X and Gamma Ray Electronics." [Online]. Available: https://www.xglab.it/

[97] "IBA (Ion Beam Application)." [Online]. Available: https://iba-worldwide.com/

[98] I. Perali, "A Prompt Gamma Camera for Real-time Range Control in Proton Therapy," Ph.D. dissertation, Politecnico di Milano, 2015. [Online]. Available: http://www.infn.it/thesis/thesis{_}dettaglio.php?tid=10003

[99] "OncoRay: National Center for Radiation Research in Oncology Dresden." [Online]. Available: http://doi.wiley.com/10.1002/mp.12670

[100] C. Richter, G. Pausch, S. Barczyk, M. Priegnitz, I. Keitz, J. Thiele, J. Smeets, F. V. Stappen, L. Bombelli, C. Fiorini, L. Hotoiu, I. Perali, D. Prieels, W. Enghardt, and M. Baumann, "First clinical application of a prompt gamma based in vivo proton range verification system," *Radiotherapy and Oncology*, vol. 118, no. 2, pp. 232–237, feb 2016. [Online]. Available: http://www.ncbi.nlm.nih.gov/pubmed/26774764http://linkinghub.elsevier.com/retrieve/pii/S0167814016000074

[101] M. Priegnitz, S. Barczyk, L. Nenoff, C. Golnik, I. Keitz, T. Werner, S. Mein, J. Smeets, F. Vander Stappen, G. Janssens, L. Hotoiu, F. Fiedler, D. Prieels, W. Enghardt, G. Pausch, and C. Richter, "Towards clinical application: prompt gamma imaging of passively scattered proton fields with a knife-edge slit camera,"

Physics in Medicine and Biology, vol. 61, no. 22, pp. 7881–7905, nov 2016. [Online]. Available: http://www.ncbi.nlm.nih.gov/pubmed/27779120http://stacks.iop.org/0031-9155/61/i=22/a=7881?key=crossref.142532baa3a9efe94e4b27e9ecade18a

[102] L. Nenoff, M. Priegnitz, G. Janssens, J. Petzoldt, P. Wohlfahrt, A. Trezza, J. Smeets, G. Pausch, and C. Richter, "Sensitivity of a prompt-gamma slit-camera to detect range shifts for proton treatment verification," *Radiotherapy and Oncology*, vol. 125, no. 3, pp. 534–540, dec 2017. [Online]. Available: http://www.ncbi.nlm.nih.gov/pubmed/29113697http://linkinghub.elsevier.com/retrieve/pii/S0167814017326531

[103] A. Studen, "Compton Camera with Position-Sensivite Silicon Detectors," Ph.D. dissertation, University of Ljubjana, 2005.

[104] A. C. Zoglauer, "First Light for the Next Generation of Compton and Pair Telescopes," Ph.D. dissertation, Technical University Munich, 2005. [Online]. Available: http://megalibtoolkit.com/documents/Zoglauer{_}PhD.pdf

[105] W. Lee and T. Lee, "A compact Compton camera using scintillators for the investigation of nuclear materials," 2010. [Online]. Available: www.elsevier.com/locate/nima

[106] D. Everett, J. Fleming, R. Todd, and J. Nightingale, "Gamma-radiation imaging system based on the Compton effect," *Proceedings of the Institution of Electrical Engineers*, vol. 124, no. 11, p. 995, 1977. [Online]. Available: http://digital-library.theiet.org/content/journals/10.1049/piee.1977.0203

[107] M.-H. Richard, "Design study of a Compton camera for prompt-gamma imaging during ion beam therapy," Ph.D. dissertation, Université Claude Bernard Lyon, 2009. [Online]. Available: https://tel.archives-ouvertes.fr/file/index/docid/744844/filename/Thesis{_}MHR{_}Comptoncamera{_}FINAL2.pdf

[108] F. Roellinghoff, M. H. Richard, M. Chevallier, J. Constanzo, D. Dauvergne, N. Freud, P. Henriquet, F. Le Foulher, J. M. Létang, G. Montarou, C. Ray, E. Testa, M. Testa, and A. H. Walenta, "Design of a Compton camera for 3D prompt-γ imaging during ion beam therapy," *Nuclear Instruments and Methods in Physics Research, Section A: Accelerators, Spectrometers, Detectors and Associated Equipment*, vol. 648, no. SUPPL. 1, pp. 20–23, 2011.

[109] J. Krimmer, J.-L. Ley, C. Abellan, J.-P. Cachemiche, L. Caponetto, X. Chen, M. Dahoumane, D. Dauvergne, N. Freud, B. Joly, D. Lambert, L. Lestand, J. M. Létang, M. Magne, H. Mathez, V. Maxim, G. Montarou, C. Morel, M. Pinto, C. Ray, V. Reithinger, E. Testa, and Y. Zoccarato, "Development of a Compton camera for medical applications based on silicon strip and scintillation detectors," 2015. [Online]. Available: http://dx.doi.org/10.1016/j.nima.2014.11.042

[110] M. H. Richard, M. Dahoumane, D. Dauvergne, M. De Rydt, G. Dedes, N. Freud, J. Krimmer, J. M. Letang, X. Lojacono, V. Maxim, G. Montarou, C. Ray, F. Roellinghoff, E. Testa, and A. H. Walenta, "Design study of the absorber detector of a compton camera for on-line control in ion beam therapy," *IEEE Transactions on Nuclear Science*, vol. 59, no. 5 PART 1, pp. 1850–1855, 2012.

[111] M. Fontana, D. Dauvergne, J. M. Létang, J. L. Ley, and E. Testa, "Compton camera study for high efficiency SPECT and benchmark with Anger system," *Physics in Medicine and Biology*, vol. 62, no. 23, pp. 8794–8812, 2017.

[112] C. Golnik, D. Bemmerer, W. Enghardt, F. Fiedler, F. Hueso-González, G. Pausch, K. R\ömer, H. Rohling, S. Sch\öne, and W. L., "Tests of a Compton imaging prototype in a monoenergetic 4.44 MeV photon field-a benchmark setup for prompt gamma-ray imaging devices Related content." [Online]. Available: http://iopscience.iop.org.emedien.ub.uni-muenchen.de/article/10.1088/1748-0221/11/06/P06009/pdf

[113] H. Rohling, M. Priegnitz, S. Schoene, A. Schumann, W. Enghardt, F. Hueso-González, G. Pausch, and F. Fiedler, "Requirements for a Compton camera for in-vivo range verification of proton therapy," *Physics in Medicine and Biology*, vol. 62, no. 7, pp. 1–20, 2017.

[114] "Instituto de Física Corpuscular —." [Online]. Available: http://webific.ific.uv.es/web/

[115] G. Llosá, M. Trovato, J. Barrio, A. Etxebeste, E. Muñoz, C. Lacasta, J. F. Oliver, M. Rafecas, C. Solaz, and P. Solevi, "First Images of a Three-Layer Compton Telescope Prototype for Treatment Monitoring in Hadron Therapy," *Frontiers in Oncology*, vol. 6, no. February, pp. 2–7, 2016. [Online]. Available: http://journal.frontiersin.org/Article/10.3389/fonc.2016.00014/abstract

[116] E. Muñoz, J. Barrio, A. Etxebeste, P. G. Ortega, C. Lacasta, J. F. Oliver, C. Solaz, and G. Llosá, "Performance evaluation of MACACO: A multilayer Compton camera," *Physics in Medicine and Biology*, vol. 62, no. 18, pp. 7321–7341, 2017.

[117] "The University of Maryland — A Preeminent Public Research University." [Online]. Available: https://www.umd.edu/

[118] M. McCleskey, W. Kaye, D. S. Mackin, S. Beddar, Z. He, and J. C. Polf, "Evaluation of a multistage CdZnTe Compton camera for prompt γ imaging for proton therapy," *Nuclear Instruments and Methods in Physics Research, Section A: Accelerators, Spectrometers, Detectors and Associated Equipment*, vol. 785, pp. 163–169, 2015.

[119] E. Draeger, D. Mackin, S. Peterson, H. Chen, S. Avery, S. Beddar, and J. C. Polf, "3D prompt gamma imaging for proton beam range verification," *Physics in Medicine and Biology*, vol. 63, no. 3, 2018.

[120] S. Kabuki, K. Hattori, R. Kohara, E. Kunieda, A. Kubo, H. Kubo, K. Miuchi, T. Nakahara, T. Nagayoshi, H. Nishimura, Y. Okada, R. Orito, H. Sekiya, T. Shirahata, A. Takada, T. Tanimori, and K. Ueno, "Development of Electron Tracking Compton Camera using micro pixel gas chamber for medical imaging," *Nuclear Instruments and Methods in Physics Research, Section A: Accelerators, Spectrometers, Detectors and Associated Equipment*, vol. 580, no. 2, pp. 1031–1035, 2007.

[121] C. Lang, "Design of a Compton camera for medical imaging and characterization of its components," Ph.D. dissertation, Ludwig-Maximilians Universität München, 2015.

[122] J. M. Verburg, "Reducing range uncertainty in proton therapy," Ph.D. dissertation, Eindhoven University of Technology, 2015. [Online]. Available: https://gray.mgh.harvard.edu/images/documents/PhDThesis{_}JMVerburg{_}Web{_}20150912.pdf

[123] J. M. Verburg, H. A. Shih, and J. Seco, "Simulation of prompt gamma-ray emission during proton radiotherapy," *Physics in Medicine and Biology*, vol. 57, no. 17, pp. 5459–5472, sep 2012. [Online]. Available: http://stacks.iop.org/0031-9155/57/i=17/a=5459?key=crossref.f7379f4c051114a9e93cba8e0c849d11

[124] "TALYS - Simulation of nuclear reactions." [Online]. Available: http://www.talys.eu/home/

[125] "EMPIRE - Nuclear Reaction Model Code." [Online]. Available: https://nucleus.iaea.org/Pages/nuclear-reaction-model-code.aspx

[126] P. Dyer, D. Bodansky, A. G. Seamster, E. B. Norman, and D. R. Maxson, "Cross sections relevant to gamma-ray astronomy: Proton induced reactions," *Physical Review C*, vol. 23, no. 5, pp. 1865–1882, may 1981. [Online]. Available: https://link.aps.org/doi/10.1103/PhysRevC.23.1865

[127] Lang, Werntz, Crannell, Trombka, and Chang, "Cross sections for production of the 15.10-MeV and other astrophysically significant gamma-ray lines through excitation and spallation of C-12 and O-16 with protons." *Physical review. C, Nuclear physics*, vol. 35, no. 4, pp. 1214–1227, apr 1987. [Online]. Available: http://www.ncbi.nlm.nih.gov/pubmed/9953888

[128] K. T. Lesko, E. B. Norman, R. M. Larimer, and S. G. Crane, "Measurements of Cross Sections Relevant to γ-Ray Line Astronomy," in *Genesis and Propagation of Cosmic Rays*. Dordrecht: Springer Netherlands, 1988, pp. 375–379. [Online]. Available: http://www.springerlink.com/index/10.1007/978-94-009-4025-3{_}24

[129] A. Belhout, J. Kiener, A. Coc, J. Duprat, C. Engrand, C. Fitoussi, M. Gounelle, A. Lefebvre-Schuhl, N. de Séréville, V. Tatischeff, J.-P. Thibaud, M. Chabot, F. Hammache, and H. Benhabiles-Mezhoud, "γ-ray production by proton and α-particle induced reactions on C-12, O-16, Mg-24, and Fe,"

Physical Review C, vol. 76, no. 3, p. 034607, sep 2007. [Online]. Available: https://link.aps.org/doi/10.1103/PhysRevC.76.034607

[130] J. Narayanaswamy, P. Dyer, S. R. Faber, and S. M. Austin, "Production of 6.13 MeV gamma rays from the O-16 (p, p' γ) O-16 reaction at 23.7 and 44.6 MeV," *Physical Review C*, vol. 24, no. 6, pp. 2727–2730, dec 1981. [Online]. Available: https://link.aps.org/doi/10.1103/PhysRevC.24.2727

[131] J. Kiener, M. Berheide, N. L. Achouri, A. Boughrara, A. Coc, A. Lefebvre, F. de Oliveira Santos, and C. Vieu, "γ -ray production by inelastic proton scattering on 16O and 12C," *Physical Review C*, vol. 58, no. 4, pp. 2174–2179, oct 1998. [Online]. Available: https://link.aps.org/doi/10.1103/PhysRevC.58.2174

[132] H. Benhabiles-Mezhoud, J. Kiener, J.-P. Thibaud, V. Tatischeff, I. Deloncle, A. Coc, J. Duprat, C. Hamadache, A. Lefebvre-Schuhl, J.-C. Dalouzy, F. de Grancey, F. de Oliveira, F. Dayras, N. de Séréville, M.-G. Pellegriti, L. Lamia, and S. Ouichaoui, "Measurements of nuclear γ -ray line emission in interactions of protons and α particles with N, O, Ne, and Si," *Physical Review C*, vol. 83, no. 2, pp. 1–15, feb 2011. [Online]. Available: https://link.aps.org/doi/10.1103/PhysRevC.83.024603

[133] G. Pausch, J. Petzoldt, M. Berthel, W. Enghardt, F. Fiedler, C. Golnik, F. Hueso-Gonzalez, R. Lentering, K. Romer, K. Ruhnau, J. Stein, A. Wolf, and T. Kormoll, "Scintillator-Based High-Throughput Fast Timing Spectroscopy for Real-Time Range Verification in Particle Therapy," *IEEE Transactions on Nuclear Science*, vol. 63, no. 2, pp. 664–672, apr 2016. [Online]. Available: http://ieeexplore.ieee.org/document/7454861/

[134] C. Golnik, F. Hueso-González, A. Müller, P. Dendooven, W. Enghardt, F. Fiedler, T. Kormoll, K. Roemer, J. Petzoldt, A. Wagner, and G. Pausch, "Range assessment in particle therapy based on prompt γ-ray timing measurements," *Physics in Medicine and Biology*, vol. 59, no. 18, pp. 5399–5422, sep 2014. [Online]. Available: http://www.ncbi.nlm.nih.gov/pubmed/25157685http://stacks.iop.org/0031-9155/59/i=18/a=5399?key=crossref.5437fcd3059992135ec2113679c7dad6

[135] F. Hueso-González, W. Enghardt, F. Fiedler, C. Golnik, G. Janssens, J. Petzoldt, D. Prieels, M. Priegnitz, K. E. Römer, J. Smeets, F. Vander Stappen, A. Wagner, and G. Pausch, "First test of the prompt gamma ray timing method with heterogeneous targets at a clinical proton therapy facility," *Physics in Medicine and Biology*, vol. 60, no. 16, pp. 6247–6272, aug 2015. [Online]. Available: http://stacks.iop.org/0031-9155/60/i=16/a=6247?key=crossref.3382b95c39af8f8ab69e65cd74102dff

[136] J. Petzoldt, K. E. Roemer, W. Enghardt, F. Fiedler, C. Golnik, F. Hueso-González, S. Helmbrecht, T. Kormoll, H. Rohling, J. Smeets, T. Werner, and G. Pausch, "Characterization of the microbunch time structure of proton pencil beams at a clinical treatment facility," *Physics in*

Medicine and Biology, vol. 61, no. 6, pp. 2432–2456, mar 2016. [Online]. Available: http://www.ncbi.nlm.nih.gov/pubmed/26943881http://stacks.iop.org/0031-9155/61/i=6/a=2432?key=crossref.aec8e6b7c5d2cb451f86b9566b73f416

[137] T. Werner, J. Berthold, W. Enghardt, F. Hueso-gonzález, T. Kögler, J. Petzoldt, C. Richter, A. Rinscheid, K. Römer, K. Ruhnau, J. Smeets, J. Stein, A. Straessner, A. Wolf, and G. Pausch, "Range Verification in Proton Therapy by Prompt Gamma-Ray Timing (PGT): Steps towards Clinical Implementation," pp. 8–10, 2017.

[138] "CALA - Centre for Advanced Laser Applications: Mainpage." [Online]. Available: https://www.cala-laser.de/

[139] S. Aldawood, "Commissioning of a Compton camera for medical imaging," Ph.D. dissertation, Ludwig-Maximilians Universität München, 2016. [Online]. Available: https://edoc.ub.uni-muenchen.de/20304/13/Aldawood{_}Saad.pdf

[140] "MPPC (multi-pixel photon counters) — Hamamatsu Photonics." [Online]. Available: https://www.hamamatsu.com/eu/en/4004.html

[141] G. F. Knoll, *Radiation Detection and Measurement*, 4th ed. John Wiley & Sons, Inc, 2010.

[142] E. B. Podgoršak, *Radiation Physics for Medical Physicists*, 2nd ed. Springer, 2010. [Online]. Available: http://dx.doi.org/10.1007/978-1-4614-2146-7{_}2

[143] E. Rutherford, "The Scattering of α and β Particles by Matter and the Structure of the Atom," *Philosophical Magazine*, vol. 21, no. 6, pp. 669–688, 1991.

[144] N. Bohr, "On the constitution of atoms and molecules," vol. 26, no. 6, pp. 1–25, 1913.

[145] H. Bethe, "Zur Theorie des Durchgangs schneller Korpuskularstrahlen durch Materie," *Annalen der Physik*, vol. 5, pp. 325–400, 1930.

[146] U. Fano, "Penetration of protons, alpha particles, and mesons," *Annual Reviews Nuclear Science*, vol. 13, pp. 1–67, 1963.

[147] E. B. Podgorsak, *Radiation physics for medical physicists*.

[148] "National Institute of Standards and Technology — NIST." [Online]. Available: https://www.nist.gov/

[149] M. J. Berger, M. Inokuti, H. H. Anderson, H. Bichsel, J. A. Dennis, D. Powers, S. M. Seltzer, and J. E. Turner, "Report 37," *Journal of the International Commission on Radiation Units and Measurements*, vol. os19, no. 2, 1984. [Online]. Available: https://academic.oup.com/jicru/article/2923758/Report

[150] M. J. Berger and S. M. Seltzer, "Tables of energy losses and ranges of electrons and positrons," National aeronautics and space administration, Tech. Rep., 1964. [Online]. Available: https://ntrs.nasa.gov/archive/nasa/casi.ntrs.nasa.gov/19650002905.pdf

[151] M. Krim, N. Harakat, A. Khouaja, J. Inchaouh, M. Mesradi, H. Chakir, A. Kartouni, A. Marouane, M. Benjelloun, S. Boudhaim, M. Fiak, M. Bouhssa, and Z. Houssni, "Method for range calculation based on empirical models of proton in liquid water: Validation study using Monte-Carlo method and ICRU data ." *International Journal of Scientific & Engineering Research*, vol. 8, no. 3, pp. 728–735, 2017.

[152] G. Molière, "Theorie der streuung schneller geladenen Teilchen I Einzelstreuung am abgeschirmten Coulomb-Feld," *Zeitschrift für Naturforschung*, no. 2a, pp. 133–145, 1947.

[153] ——, "Theorie der Streuung schneller geladenen Teilchen II Mehrfach- und Vielfachstreuung," *Zeitschrift für Naturforschung*, no. 3a, pp. 78–97, 1948.

[154] W. T. Scott, "The theory of small-angle multiple scattering of fast charged particles," *Reviews of Modern Physics*, vol. 35, no. 2, pp. 231–313, 1963.

[155] D. E. Groom and S. R. Klein, "Passage of particles through matter," *The European Physical Journal C*, vol. 15, no. 1-4, pp. 163–173, mar 2000. [Online]. Available: http://www.springerlink.com/index/10.1007/BF02683419

[156] Particle Data Group, "Atomic Nuclear Properties." [Online]. Available: http://pdg.lbl.gov/2017/AtomicNuclearProperties/index.html

[157] "LISE++ : Exotic Beam Production." [Online]. Available: http://lise.nscl.msu.edu/lise.html

[158] T. Tabata, R. Ito, and S. Okabe, "Generalized semiempirical equations for the extrapolated range of electrons," *Nuclear Instruments and Methods*, vol. 103, pp. 85–91, 1972.

[159] M. F. L'Annunziata, *Radioactivity : Introduction and History, From the Quantum to Quarks.* Elsevier Science, 2016.

[160] R. D. Evans, *The Atomic Nucleus.* Tata McGraw-Hill Publishing Company LTD., 1955.

[161] A. H. Compton, "A quantum theory of the scattering of X-rays by light elements," *The Physical Review*, vol. 21, no. 5, pp. 483–502, 1923. [Online]. Available: https://journals.aps.org/pr/pdf/10.1103/PhysRev.21.483

[162] "Compton scattering calculator." [Online]. Available: https://web-docs.gsi.de/{~}stoe{_}exp/web{_}programs/compton/index.php

[163] O. Klein and Y. Nishina, "Über die Streuung von Strahlung durch freie Elektronen nach der neuen relativistischen Quantendynamik von Dirac," *Zeitschrift für Physik*, vol. 52, no. 11-12, pp. 853–868, 1929. [Online]. Available: https://link-springer-com.emedien.ub.uni-muenchen.de/content/pdf/10.1007{%}2FBF01366453.pdf

[164] J. W. Du Mond, "Compton modified line structure and its relation to the electron theory of solid bodies," *Physical Review*, vol. 33, no. 5, pp. 643–658, 1929.

[165] R. Ribberfors, "Relationship of the relativistic Compton cross section to the momentum distribution of bound electron states," *Physical Review B*, vol. 12, no. 6, pp. 2067–2074, 1975.

[166] A. Zoglauer and G. Kanbach, "Doppler broadening as a lower limit to the angular resolution of next generation Compton telescopes," *Proceeding of SPIE - The International Society for Optical Engineering*, pp. 1302–1309, 2003. [Online]. Available: http://public.lanl.gov/mkippen/actsim/papers/Doppler{_}SPIE2002{_}Proceedings.pdf

[167] "Insulator — physics — Britannica.com." [Online]. Available: https://www.britannica.com/science/insulator

[168] A. S. Sedra and K. C. Smith, *Microelectronic Circuits*, 5th ed. Oxford University Press, 2004, vol. 37. [Online]. Available: www.oup.com

[169] R. Eisberg and R. Resnick, *Quantum Physics of Atoms, Molecules, Solids, Nuclei, and Particles*. John Wiley and Sons, 1985. [Online]. Available: http://www.wiley-vch.de/en/areas-interest/natural-sciences/quantum-physics-of-atoms-molecules-solids-nuclei-and-particles-978-0-471-87373-0

[170] M. Miura-Mattausch and H. Mattausch, *The physics and modeling of MOSFETS: surface-potential model HiSIM*, internatio ed. World Scientific, 2008. [Online]. Available: http://books.google.com/books?hl=en{&}lr={&}id=q5vK3B0adloC{&}oi=fnd{&}pg=PR5{&}dq=The+Physics+and+Modeling+of+MOSFETs{&}ots=-oUhrzeRJq{&}sig=foHVRMNQsk0nk6jHEuoPBrnsATg

[171] H. Spieler, *Semiconductor Detector Systems*, 1st ed. Oxford Science Publications, 2005.

[172] W. Shockley, *Electrons and holes in semiconductors*, V. Nostrand, Ed. Princeton, 1950. [Online]. Available: http://linkinghub.elsevier.com/retrieve/pii/0016003251911027

[173] H. Ibach and H. Lüth, *Solid state physics - an introduction to principles of material science*, 2nd ed. Springer, 1996.

[174] S. Sze and K. N. Kwok, *Physics of semiconductor devices*, 3rd ed. John Wiley and Sons Publication, 2013.

[175] V. Kulibaba, N. Maslov, S. Potin, and A. Starodubtsev, "Interstrip resistance of a semiconductor microstrip detector," Tech. Rep. 39, 2001. [Online]. Available: https://www.kipt.kharkov.ua/conferences/ihepnp/17workshop{_}res/N5/60{_}5.pdf

[176] M. Frautschi, M. Hoeferkamp, and S. Seidel, "Capacitance measurements of double-sided silicon microstrip detectors," *Nuclear Instruments and Methods in Physics Research Section A: Accelerators, Spectrometers, Detectors and Associated Equipment*, vol. 378, no. 1-2, pp. 284–296, aug 1996. [Online]. Available: https://www.sciencedirect.com/science/article/pii/0168900296004676

[177] B. M. Wilamowski and J. D. Irwin, *Fundamentals of Industrial Electronics*, 2nd ed., T. Group and Francis, Eds. CRC Press, 2011.

[178] T. J. Sobering, "Noise in Electronic Systems," *SDE Consulting*, 1999. [Online]. Available: http://www.k-state.edu/ksuedl/publications/Technote4-NoiseinElectronicSystems.pdf

[179] F. Hooge, "1/f Noise is no surface effect," *Physics Letters A*, vol. 29, no. 3, pp. 139–140, 1969.

[180] "Saint-Gobain." [Online]. Available: https://www.saint-gobain.com/en

[181] "Scionix: Dedicated Scintillation Detectors." [Online]. Available: https://scionix.nl/

[182] "C&A Corporation." [Online]. Available: http://www.c-and-a.jp/index.html

[183] "Photomultiplier Tubes," Hamamatsu Photonics, Tech. Rep., 2007.

[184] "Introduction to SiPM," sensL, sense light, Tech. Rep., 2011. [Online]. Available: https://www.sensl.com/downloads/ds/TN-IntrotoSPMTech.pdf

[185] I. I. Valencia Lozano, "Prompt gamma imaging based on Compton camera detector systems for range verification in proton therapy treatments," Ph.D. dissertation, Ludwig-Maximilians Universität München, 2018.

[186] "MEGAlib — The Medium-Energy Gamma-ray Astronomy library." [Online]. Available: http://megalibtoolkit.com/home.html

[187] Y. Toko, N. Aoyama, K. Watanabe, K. Sakamori, and K. Endo, "Experimental Study of a Si/CdTe Semiconductor Compton Camera for the Next Generation of Gamma-ray Astronomy," Ph.D. dissertation, University of Tokyo, 2008.

[188] P. Bloser, J. Ryan, M. McConnell, J. Macri, R. Andritschke, G. Kanbach, and A. Zoglauer, "The MEGA project: Science goals and hardware development," *New Astronomy Reviews*, vol. 50, pp. 619–623, 2006. [Online]. Available: http://linkinghub.elsevier.com/retrieve/pii/S1387647306000832

[189] R. Brun and F. Rademakers, "ROOT - An object oriented data analysis framework," *Nuclear Instruments and Methods in Physics Research A*, vol. 389, pp. 81–86, 1997.

[190] CERN, "ROOT a Data analysis Framework." [Online]. Available: https://root.cern.ch/

[191] "CiS :: Forschungsinstitut für Mikrosensorik und Photovoltaik GmbH." [Online]. Available: https://cismst.org/profil/willkommen/

[192] Mesytec GmbH, "MHV-4 module."

[193] "Micron Semiconductor Ltd." [Online]. Available: http://www.micronsemiconductor.co.uk/

[194] Saint Gobain, "Brillance Scintillators Performance Summary," Tech. Rep., 2009.

[195] S. Aldawood, I. Castelhano, R. Gernhäuser, H. Van Der Kolff, C. Lang, S. Liprandi, R. Lutter, L. Maier, T. Marinšek, D. R. Schaart, K. Parodi, and P. G. Thirolf, "Comparative Characterization Study of a LaBr3(Ce) Scintillation Crystal in Two Surface Wrapping Scenarios: Absorptive and Reflective," *Frontiers in Oncology*, vol. 5, no. December, pp. 1–9, 2015. [Online]. Available: http://journal.frontiersin.org/Article/10.3389/fonc.2015.00270/abstract

[196] B. D. Milbrath, R. C. Runkle, T. W. Hossbach, W. R. Kaye, E. A. Lepel, B. S. McDonald, and L. E. Smith, "Characterization of alpha contamination in lanthanum trichloride scintillators using coincidence measurements," *Nuclear Instruments and Methods in Physics Research A*, vol. 547, pp. 504–510, 2005.

[197] F. G. Quarati, I. V. Khodyuk, C. W. Van Eijk, P. Quarati, and P. Dorenbos, "Study of 138La radioactive decays using LaBr3 scintillators," *Nuclear Instruments and Methods in Physics Research, Section A: Accelerators, Spectrometers, Detectors and Associated Equipment*, vol. 683, pp. 46–52, 2012. [Online]. Available: http://dx.doi.org/10.1016/j.nima.2012.04.066

[198] S. Chu, L. Ekström, and R. Firestone, "The Lund / LBNL Nuclear Data Search." [Online]. Available: http://nucleardata.nuclear.lu.se/toi/

[199] K. S. Shah, "Cerium Bromide scintillation crystal," 2008.

[200] K. S. Shah, J. Glodo, W. Higgins, E. V. D. Van Loef, W. W. Moses, S. E. Derenzo, and M. J. Weber, "CeBr 3 scintillators for gamma-ray spectroscopy," *IEEE Transactions on Nuclear Science*, vol. 52, pp. 3157–3159, 2004.

[201] W. M. Higgins, A. Churilov, E. van Loef, J. Glodo, M. Squillante, and K. Shah, "Crystal growth of large diameter LaBr3:Ce and CeBr3," *Journal of Crystal Growth*, vol. 310, pp. 2085–2089, 2008.

[202] L. M. Fraile, H. Mach, V. Vedia, B. Olaizola, V. Paziy, E. Picado, and J. M. Udías, "Fast timing study of a CeBr 3 crystal: Time resolution below 120 ps at 60 Co energies," *Nuclear Inst. and Methods in Physics Research A*, vol. 701, pp. 235–242, 2013. [Online]. Available: http://dx.doi.org/10.1016/j.nima.2012.11.009

[203] P. Guss, M. Reed, D. Yuan, A. Reed, and S. Mukhopadhyay, "CeBr3 as a room-temperature, high-resolution gamma-ray detector," *Nuclear Instruments and Methods in Physics Research A*, vol. 608, pp. 297–304, 2009. [Online]. Available: http://dx.doi.org/10.1016/j.nima.2009.06.096

[204] F. G. A. Quarati, P. Dorenbos, J. Van Der Biezen, A. Owens, M. Selle, L. Parthier, and P. Schotanus, "Scintillation and detection characteristics of high-sensitivity CeBr3 gamma-ray spectrometers," *Nuclear Instruments and Methods in Physics Research A*, vol. 729, pp. 596–604, 2013. [Online]. Available: http://dx.doi.org/10.1016/j.nima.2013.08.005

[205] S. Holland, "High resolution low background CeBr3 scintillators," 2016. [Online]. Available: www.scionix.nl

[206] Hamamatsu Photonics K.K., "Photomultiplier H9500 SERIES," 2015.

[207] ——, "Photomultiplier H8500 SERIES / H10966 SERIES," 2018.

[208] ——, "Photomultiplier H12700 SERIES," 2018.

[209] Saint Gobain, "Data sheet BC-630 Silicone Grease," Tech. Rep., 2013. [Online]. Available: https://www.crystals.saint-gobain.com/sites/imdf.crystals.com/files/documents/bc-630.pdf

[210] K. Zeitelhack, A. Elhardt, J. Friese, R. Gernhäuser, J. Homolka, A. Kastenmüller, P. Kienle, H.-J. Körner, P. Maier-Komor, M. Münch, W. Przygoda, W. Schön, A. Ulrich, and J. Wieser, "The HADES RICH detector," *Nuclear Instruments and Methods in Physics Research A*, vol. 433, pp. 201–206, 1999. [Online]. Available: https://ac-els-cdn-com.emedien.ub.uni-muenchen.de/S016890029900371X/1-s2.0-S016890029900371X-main.pdf?{_}tid=d5bdef0a-9075-41f0-8d67-fbd031f55723{&}acdnat=1532163379{_}d20673bcf57f65c8a7a89ea79bd614e4

[211] A. Kastenmüller, M. Böhmer, J. Friese, R. Gernhäuser, J. Homolka, P. Kienle, H. J. Körner, D. Maier, M. Münch, C. Theurer, and K. Zeitelhack, "Fast detector readout for the HADES-RICH," *Nuclear Instruments and Methods in Physics Research A*, vol. 433, no. 1, pp. 438–443, 1999.

[212] J. Bortfeldt, "Development of Floating Strip Micromegas Detector," Ph.D. dissertation, Ludwig-Maximilians Universität München, 2014. [Online]. Available: http://link.springer.com/10.1007/978-3-319-18893-5

[213] "GASSIPLEX, a 16 integrated channels front-end analog amplifiers with multiplex serial readout." [Online]. Available: http://www-subatech.in2p3.fr/fr/

[214] E. L. Holzman, "Wideband measurement of the dielectric constant of an FR4 substrate using a parallel-coupled microstrip resonator," *IEEE Transactions on Microwave Theory and Techniques*, vol. 54, no. 7, pp. 3127–3130, 2006.

[215] "MEGTRON 6 High Speed, Low Loss Multi-layer Materials." [Online]. Available: https://www.matrixelectronics.com/products/panasonic/megtron-6/

[216] J. Santiard, W. Beusch, S. Buytaert, C. Enz, E. Heijne, P. Jarron, F. Krummenacher, K. Marent, and F. Piuz, "Gasplex a low noise analog signal processor for readout of gaseous detectors," *European Organization for Nuclear Research*, 1994.

[217] "Texas Instruments." [Online]. Available: http://www.ti.com/{#}

[218] P. Baron and E. Delagnes, "AGET , a Front End ASIC for Active Time Projection Chamber Data Sheet," 2013.

[219] S. Anvar, P. Baron, B. Blank, J. Chavas, E. Delagnes, F. Druillole, P. Hellmuth, L. Nalpas, J. L. Pedroza, J. Pibernat, E. Pollacco, A. Rebii, N. Usher, and A.-T. collaboration, "AGET, the GET front-end ASIC, for the readout of the time projection chambers used in nuclear physic experiments," in *IEEE Nuclear Science Symposium Conference Record*, 2012, pp. 745–749.

[220] E. Pollacco, S. Anvar, H. Baba, P. Baron, D. Bazin, C. Belkhiria, B. Blank, J. Chavas, P. Chomaz, E. Delagnes, F. Druillole, P. Hellmuth, C. Huss, E. Galyaev, B. Lynch, W. Mittig, T. Murakami, L. Nalpas, J. L. Pedroza, R. Raabe, J. Pibernat, B. Raine, A. Rebii, A. Taketani, F. Saillant, D. Suzuki, N. Usher, and G. Wittwer, "GET: A Generic Electronic System for TPCs for Nuclear Physics Experiments," *Physics Procedia*, vol. 37, pp. 1799–1804, 2012.

[221] "MicroTCA® — PICMG." [Online]. Available: https://www.picmg.org/openstandards/microtca/

[222] "PICMG — Open Modular Computing Standards." [Online]. Available: https://www.picmg.org/

[223] "AdvancedMC® — PICMG." [Online]. Available: https://www.picmg.org/openstandards/advanced-mezzanine-card/

[224] RS Components, "ISO-TECH IPS 2303 power supply." [Online]. Available: http://docs-asia.electrocomponents.com/webdocs/0956/0900766b80956d06.pdf

[225] "Samtec." [Online]. Available: https://www.samtec.com/

[226] "Mesytec - Detector Readout Systems." [Online]. Available: https://www.mesytec.com/

[227] V. Beck, "Signal Processing of Double-Sided Silicon Strip Detectors with an ASIC-based Data Acquisition Test System," 2017.

[228] T. Schmidt, "Performance examination of GET-ASIC-based signal processing with external preamplifiers," 2017.

[229] "SIS3153 USB3.0 and Ethernet to VME interface." [Online]. Available: http://www.struck.de/sis3153.html

[230] R. Schneider, "MMR System: Multi-channel Readout," 2018. [Online]. Available: https://www.mesytec.com/

[231] ——, "MMR Multi-plexed Readout - hardware features," 2018. [Online]. Available: https://www.mesytec.com/

[232] ——, "VMMR-8/16," 2018. [Online]. Available: https://www.mesytec.com/

[233] "High-speed ground plane header."

[234] "Low-profile through-hole header."

[235] "MCFD-16." [Online]. Available: https://www.mesytec.com/products/nuclear-physics/MCFD-16.html

[236] "MQDC-32." [Online]. Available: https://www.mesytec.com/products/nuclear-physics/MQDC-32.html

[237] "MTDC-32." [Online]. Available: https://www.mesytec.com/products/nuclear-physics/MTDC-32.html

[238] "Quad Coincidence Logic Unit - Mod. N455." [Online]. Available: http://www.caen.it/csite/CaenProd.jsp?parent=12{&}idmod=105{#}

[239] "Quad Coincidence Logic Unit - Mod. 429A." [Online]. Available: http://www-esd.fnal.gov/esd/catalog/main/lcrynim/429a-spec.htm

[240] J. Hoffmann, N. Kurz, and M. Richter, "TRIVA 5, VME Trigger Module," 2009. [Online]. Available: https://www.gsi.de/fileadmin/EE/Module/TRIVA/triva5{_}5.pdf

[241] "RIO 3 Power Pc." [Online]. Available: http://fpsalmon.usc.es/genp/doc/DAQ/rio3{_}8064{_}datasheet.pdf

[242] H. Essel and N. Kurz, "The general purpose data acquisition system MBS," *IEEE Transactions on Nuclear Science*, vol. 47, no. 2, pp. 475–478, 1999. [Online]. Available: http://ieeexplore.ieee.org/document/842672/

[243] R. Lutter, O. Schaile, K. Schöffel, K. Steinberger, P. Thirolf, and C. Broude, "MARaBO OU - A MBS and ROOT Based Online / Offline Utility," *IEEE Transactions on Nuclear Science*, vol. 47, no. 2, pp. 280–283, 2000. [Online]. Available: https://ieeexplore.ieee.org/abstract/document/846164/

[244] "MARaBOU Data Acquisition." [Online]. Available: https://www-old.mll-muenchen.de/marabou/htmldoc/

[245] O. Schaile, "HistPresent - Easy interactive analysis within the ROOT framework," Tech. Rep., 2005. [Online]. Available: https://homepages.physik.uni-muenchen.de/{~}Otto.Schaile/hpr.pdf

[246] F. Lüke and R. Schneider, "mvme - mesytec VME Data Acquisition," 2018. [Online]. Available: https://www.mesytec.com/

[247] "mesytec - MSI-8." [Online]. Available: https://www.mesytec.com/products/nuclear-physics/MSI-8.html

[248] "V785 / ADCs (Peak Sensing) — CAEN." [Online]. Available: http://www.caen.it/csite/CaenProd.jsp?parent=11{&}idmod=37

[249] "GG8000 Octal Gate and Delay Generator — Products — AMETEK ORTEC." [Online]. Available: https://www.ortec-online.com/products/electronics/delays-gates-and-logic-modules/gg8020

[250] "N638 / Translators — CAEN." [Online]. Available: http://www.caen.it/csite/CaenProd.jsp?parent=12{&}idmod=385

[251] "DT5800 / Digital Detector Emulator — CAEN." [Online]. Available: http://www.caen.it/csite/CaenProd.jsp?idmod=837{&}parent=59

[252] D. Bortoletto, A. Garfinkel, A. Hardman, K. Hoffman, T. Keaffaber, N. Shaw, and G. Stanley, "Capacitance measurements of double-metal double-sided silicon microstrip detectors," *Nuclear Instruments and Methods in Physics Research Section A: Accelerators, Spectrometers, Detectors and Associated Equipment*, vol. 383, no. 1, pp. 104–109, dec 1996. [Online]. Available: https://www.sciencedirect.com/science/article/pii/S0168900296006638

[253] "BC-418, BC-420, BC-422 — Products — Saint-Gobain Crystals." [Online]. Available: https://www.crystals.saint-gobain.com/products/bc-418-bc-420-bc-422-bc-422q

[254] "Photomultiplier Tubes Catalogue."

[255] R. Viegas, "Optimization study of the performance of a LaBr3 monolithic scintillator in a Compton camera system," Master's thesis, University of Coimbra, 2018.

[256] P. L. Reeder and D. C. Stromswold, "Performance of Large NaI(Tl) Gamma-Ray Detectors Over Temperature -50°C to +60°C," Tech. Rep., 2004. [Online]. Available: https://www.pnnl.gov/main/publications/external/technical{_}reports/PNNL-14735.pdf

[257] T. M. Binder, "Evaluation of new Components for the Absorber Detector of the Garching Compton Camera Prototype," Master's thesis, Ludwig-Maximilians Universität München, 2017.

[258] E. Fix and J. Hodges, "Discriminatory analysis, nonparametric discrimination: Consistency properties," 1951. [Online]. Available: http://www.dtic.mil/dtic/tr/fulltext/u2/a800276.pdf

[259] M. C. Maas, D. J. Van Der Laan, D. R. Schaart, J. Huizenga, J. C. Brouwer, P. Bruyndonckx, S. Léonard, C. Lemaître, and C. W. E. Van Eijk, "Experimental characterization of monolithic-crystal small animal PET detectors read out by APD arrays," *IEEE Transactions on Nuclear Science*, vol. 53, no. 3, pp. 1071–1077, 2006.

[260] D. J. van der Laan, M. C. Maas, H. W. de Jong, D. R. Schaart, P. Bruyndonckx, C. Lemaître, and C. W. van Eijk, "Simulated performance of a small-animal PET scanner based on monolithic scintillation detectors," *Nuclear Instruments and Methods in Physics Research A*, vol. 571, pp. 227–230, 2007.

[261] D. R. Schaart, H. T. Van Dam, S. Seifert, R. Vinke, P. Dendooven, H. Löhner, and F. J. Beekman, "A novel, SiPM-array-based, monolithic scintillator detector for PET," *Physics in Medicine and Biology*, vol. 54, no. 11, pp. 3501–3512, 2009.

[262] H. T. Van Dam, S. Seifert, R. Vinke, P. Dendooven, H. Löhner, F. J. Beekman, and D. R. Schaart, "Improved nearest neighbor methods for gamma photon interaction position determination in monolithic scintillator PET detectors," *IEEE Transactions on Nuclear Science*, vol. 58, no. 5, pp. 2139–2147, 2011.

[263] "DT5800 / Digital Detector Emulator — CAEN." [Online]. Available: http://www.caen.it/csite/CaenProd.jsp?idmod=837{&}parent=59

[264] "Hamamatsu Photonics." [Online]. Available: https://www.hamamatsu.com/jp/en/index.html

[265] Plansee, "DENSIMET ® and INERMET ® Tungsten Alloys," Tech. Rep. [Online]. Available: https://www.baymevbm.de/media/fp/13da846fe69{_}Produkte{_}und{_}Werkstoffe.pdf

[266] "WHS Sondermetalle." [Online]. Available: https://www.whs-sondermetalle.de/de/

[267] "Hartmetall-Gesellschaft." [Online]. Available: https://www.hmtg.de/

[268] M. Mayerhofer, "Optimizing the spatial resolution of the monolithic LaBr3 absorbing scintillator of the Garching Compton-camera prototype," Master's thesis, University of Hamburg / LMU Munich, 2017.

[269] A. Miani, "Determination of the spatial resolution of a monolithic scintillator in a Compton camera system with MeV range photons," Master's thesis, Università degli Studi di Milano / LMU Munich, 2016.

[270] S. Liprandi, M. Mayerhofer, S. Aldawood, T. Binder, G. Dedes, A. Miani, D. R. Schaart, I. I. Valencia Lozano, K. Parodi, and P. G. Thirolf, "Sub-3mm spatial resolution from a large monolithic LaBr3(Ce) scintillator," *Current Directions in Biomedical Engineering*, vol. 3, no. 2, 2017.

[271] "ELI-NP — Extreme Light Infrastructure - Nuclear Physics." [Online]. Available: http://www.eli-np.ro/

[272] M. Kawula, S. Liprandi, T. Binder, M. Mayerhofer, K. Parodi, and P. G. Thirolf, "Creation of an integrated platform for spatial resolution determination in a monolithic scintillator," *Poster presentation at the Deutsche Physikalische Gesellschaft conference*, 2018.

[273] A. Gostojić, V. Tatischeff, J. Kiener, C. Hamadache, J. Peyré, N. Karkour, D. Linget, L. Gibelin, X. Lafay, X. Grave, N. Dosme, E. Legay, S. Blin, and P. Barrillon, "Characterization of LaBr3:Ce and CeBr3 calorimeter modules for 3D imaging in gamma-ray astronomy," *Nuclear Instruments and Methods in Physics Research Section A: Accelerators, Spectrometers, Detectors and Associated Equipment*, vol. 832, pp. 24–42, oct 2016. [Online]. Available: https://www-sciencedirect-com.emedien.ub.uni-muenchen.de/science/article/pii/S0168900216305861

[274] "Tandem-Beschleuniger - Maier-Leibnitz-Laboratorium - LMU München." [Online]. Available: https://www.bl.physik.uni-muenchen.de/tandem/index.html

[275] Picotech, "PT-104 Data Logger," 2013. [Online]. Available: https://www.picotech.com/download/manuals/usbpt104.en-2.pdf

[276] "Fuhrmeister GmbH." [Online]. Available: https://www.fuhrmeister-gmbh.de/

[277] D. Pelte and D. Schwalm, *In-beam gamma-ray spectroscopy with heavy ions*, North Holland Publishing, Ed. North-Holland Pub. Co., 1982. [Online]. Available: https://inis.iaea.org/search/searchsinglerecord.aspx?recordsFor=SingleRecord{&}RN=14791070

[278] "National Institute of Radiological Sciences." [Online]. Available: http://www.nirs.qst.go.jp/ENG/index.shtml

[279] "Shin-Etsu Chemical Homepage." [Online]. Available: https://www.shinetsu.co.jp/en/

[280] W. Chaiphaksa, P. Limkitjaroenporn, H. J. Kim, and J. Kaewkhao, "The mass attenuation coefficients, effective atomic numbers and effective electron densities for GAGG:Ce and CaMoO4scintillators," *Progress in Nuclear Energy*, vol. 92, pp. 48–53, 2016. [Online]. Available: http://dx.doi.org/10.1016/j.pnucene.2016.06.010

[281] S. Takyu, S. Liprandi, F. Nishikido, A. Mohammadi, E. Yoshida, S. Aldawood, T. Binder, M. Mayerhofer, R. Lutter, I. I. V. Lozano, G. Dedes, K. Kamada, K. Parodi, P. G. Thirolf, and T. Yamaya, "Development of a DOI-based Compton camera for nuclear medicine application," 2017.

[282] S. Aldawood, P. G. Thirolf, A. Miani, M. Böhmer, G. Dedes, R. Gernhäuser, C. Lang, S. Liprandi, L. Maier, T. Marinšek, M. Mayerhofer, D. R. Schaart, I. V. Lozano, and K. Parodi, "Development of a Compton Camera for prompt-Gamma Medical Imaging," *Radiation Physics and Chemistry*, vol. 40, pp. 190–197, 2017.

[283] S. Liprandi, S. Takyu, S. Aldawood, T. Binder, G. Dedes, K. Kamada, R. Lutter, M. Mayerhofer, A. Miani, A. Mohammadi, F. Nishikido, D. R. Schaart, I. I. V. Lozano, E. Yoshida, T. Yamaya, K. Parodi, and P. G. Thirolf, "Characterization of a Compton camera setup with monolithic LaBr3(Ce) absorber and segmented GAGG scatter detectors," in *IEEE NSS-MIC Conference Proceeding*, vol. 3, 2017, pp. 3–6.

[284] T. Yamaya, E. Yoshida, H. Tashima, Y. Okumura, M. Suga, N. Kawachi, K. Kamada, and K. Parodi, "Concrete realization of the whole gamma imaging concept," in *IEEE NSS-MIC Conference Proceeding*, 2017, pp. 7–9.

Acknowledgements

The conclusion of my journey as a PhD student is a very important step for me, as a scientist and as a person, and many people contributed in different ways to the achievement of this step. First of all my deep gratitude goes to PD Dr. Peter Thirolf for the continuous support he was always available to provide. In this four years I learned with your guidance and your passion for physics a whole fascinating world. I am grateful because I have learned a lot from you, under many point of view. Thank you for all the interesting discussions and for giving me the freedom to scientifically grow. Danke. Thanks to Prof. Dr. Katia Parodi for having given me the honor to work in this Department. For being a brilliant scientist able to inspire other people, but also a great person. And thanks for giving a bit of italian touch to our Department. I am grateful to Rudi Lutter for his constant kindness combined with a great knowledge which was always a support when needed. Thanks as well to Otto Schaile which, of equal kindness, was a guru on root related topics. Thanks to Dr. Mohammad Safari for the great and very efficient help during the last months of my PhD for the simulations and images reconstruction in MEGAlib. And thanks to Ingrid as well for all the work and discussions on the use of MEGAlib for the Compton camera prototype. The work presented in this thesis was possible also thanks to the electronics and mechanical workshop of LMU: thanks to Mr. Krapfl and Mr. Öhm for their work. Special thanks to the staff member of the MLL Tandem accelerator for their assistance and support during all the beam times. I am also happy that I had the possibility to know Robert Schneider from Mesytec. Thanks for all the discussions and suggestions, they were always interesting and helpful. A super special thanks goes to my great Compton camera team for sharing scientific work and social life: thanks to Saad for introducing me to the initial system, being a big brother during his time in Munich and still close even if geographically distant. Thanks to Tim for being a valuable colleague, for all the time and fun spent together and for introducing me to funny bavarian movies. Special thanks to all present and past students which worked with me: Rita, for being so diligent and so cute at the same time, Maria, I am happy to have made possible the prolongation of your stay here and proud of you. Agnese, Michael, Tim, Giovanni, Thorsten, Vincent, it was a fortune and a great pleasure to have you here. Thanks to Benedict for being a perfect office mate (and a perfect bottle and Nature journal collector), and to Lars for having shared some

lunch-brunch together. To all friends and sharers of joy and suffer of the PhD journey: among the many people I could have found on my way here, I am so happy to have found you guys and to have shared not only scientific experience but also a great time together. Juliana, Franz, Basti, Thomas, Matthias, Ingrid, Basti. And thanks to Chiara, for simply being here, to Vassia for being always a sweet friend, to Elettra for her crazy cuteness, to Theresa and Ludovica for having found you on my way. Without mentioning all the names, thanks for the nice discussions to any other member of the Department and for the nice time we spent together. I would like to express my deep gratitude also to the whole group of Prof. Dr. Taiga Yamaya: Dr. Akram Mohammadi, Dr. Nishikido Fumihiko and all the others for the great work we did together even though there are thousands of kilometres between us. Special thanks to Dr. Sodai Takyu, for your kindness, the experiments together, the skype calls and the fruitful discussions. Thanks to Prof. Dr. Yamaya for being a great leader and scientist but also a nice person to discuss with. In italiano vorrei ringraziare le persone che dall'Italia (e non) mi hanno sempre supportato (e sopportato). Grazie agli amici di sempre che ci sono e ci saranno. Grazie dal profondo del mio cuore alla mia famiglia, per essere cosi bella da farmi sentire sempre serena dentro di me. Grazie mamma e papi per avermi sempre supportato con tutto l'amore del mondo, questo mi ha permesso di arrivare fin qui. E grazie al mio Luchino, per essere sempre rimasto carino anche se ormai é lui il fratellone fra i due. E per essere un fratello su cui si puó contare. Mio adorato Davide, ringraziarti in poche righe sulla pagina finale della mia sudata tesi di dottorato non é possibile. Sono passati ormai anni dal nostro primo incontro sui banchi del Polimi, e il tuo supporto, la tua stima e il tuo amore non sono mai mancati. Semplicamente grazie per esserci, mi rendi una persona migliore.